Space-Time Characterisation and Adaptive Processing of Ionospherically-Propagated HF Signals

GIUSEPPE AURELIANO FABRIZIO

Thesis submitted for the degree of

Doctor of Philosophy

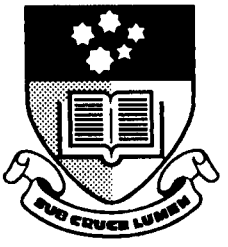

Department of Electrical and Electronic Engineering
Faculty of Engineering
The University of Adelaide
Adelaide, South Australia

July 2000

Contents

Abstract

This thesis is concerned with the mathematical characterisation and adaptive processing of narrowband high frequency signals received by a very wide aperture antenna array after reflection from the ionosphere. A major component of this research focuses on the experimental validation of space-time signal processing models for the complex (amplitude and phase) data received when a far-field source is propagated by a single-hop mid-latitude ionospheric path. Deterministic and statistical signal models are described and validated in terms of the accuracy with which they can represent the characteristics of complex-valued wavefields received by a 2.8 km long uniform linear array over time intervals in the order of a few seconds and a few minutes respectively.

The second major component of this research quantifies the effect of ionospheric propagation on the interference cancellation performance of various adaptive beamforming schemes. The improvements in output signal-to-noise ratio gained by adaptive beamforming relative to conventional beamforming are statistically quantified and compared with predictions made by a multi-sensor HF channel model. Degradations in performance caused by instrumental uncertainties are also considered and signal processing techniques which compensate for the relevant hardware imperfections are proposed and experimentally tested.

Declaration

This work contains no material that has been accepted for the award of any other degree or diploma in any university or other teritary institution and, to the best of my knowledge and belief, contains no material previously published or written by another person, except where due reference has been made in the text.

I give consent to this copy of my thesis, when deposited in the University Library, being available for loan and photocopying.

Signature

Date 21 July 2000

Acknowledgements

This thesis has been made possible thanks to the technical and moral support of numerous people.

I would like to thank my principal supervisor, Professor Doug Gray, of the Electrical and Electronic Engineering Department at The University of Adelaide, for continually encouraging me to deepen my understanding of signal processing and for providing invaluable guidance in times of need.

My co-supervisors, Dr Mike Turley and Dr Stuart Anderson, of the Defence Science and Technology Organisation, Australia for their willingness to assist me throughout the candidature by sharing their experience in the fields of signal processing and ionospheric propagation whenever it was sought.

The Surveillance Systems Division of the Defence Science and Technology Organisation, and particularly Dr Malcolm Golley (former Chief of the High Frequency Radar Division) for allowing me the opportunity to pursue my interests in this field of research.

The Centre for Sensor Signal and Information Processing in Adelaide for the use of their facilities as well as the opportunity to meet and interact with internationally recognised researchers. In particular, Professor Yuri Abramovich, for passing on his wealth of experience and research methodologies during the initial stages.

To the technical and administration staff of the above-mentioned organisations for their performance of countless tasks which saved me time and energy and to my friends outside work for their enjoyable company. Lastly, I would like to express my gratitude to my family for their unconditional love and support. I dedicate this thesis to my family.

List of Figures

List of Tables

Abbreviations

ACS	Auto-Correlation Sequence
AM	Amplitude Modulated
AR	Auto-Regressive
ARMA	Auto-Regressive Moving-Average
CD	Coherently Distributed
CPI	Coherent Processing Interval
CSF	Channel Scattering Function
DOA	Direction-of-Arrival
FA	Fitting Accuracy
FMCW	Frequency Modulated Continuous Waveform
FMS	Frequency Management System
HF	High Frequency
ID	Incoherently Distributed
LCMV	Linearly Constrained Minimum Variance
LS	Least Squares
MA	Moving-Average
MF	Matched-Field
MFA	Model Fitting Accuracy
ML	Maximum Likelihood
MODE	Method of Direction Estimation
MSC	Magnitude Squared Coherence
MUSIC	MUltiple SIgnal Classification
MVDR	Minimum Variance Distortionless Response

OTH	Over-the-Horizon
PDF	Probability Density Function
PRF	Pulse Repetition Frequency
PRI	Pulse Repetition Interval
PSD	Power Spectral Density
SLC	Sidelobe Canceller
SMI	Sample Matrix Inverse
SNR	Signal-to-Noise Ratio
STAP	Space-Time Adaptive Processing
SVD	Singular Value Decomposition
ULA	Uniform Linear Array
WFA	Wavefront Analysis

Symbols

$*$	Complex conjugate
$\alpha(\Delta t)$	Temporal correlation coefficient of ionospheric channel
$\beta(\Delta d)$	Spatial correlation coefficient of ionospheric channel
λ	Carrier wavelength
$\mathbf{P}_z$	Projection operator onto the range space of the matrix $\mathbf{Z}$
$\mathbf{Q}_n$	Matrix containing noise-subspace eigenvectors
$\mathbf{Q}_s$	Matrix containing signal-subspace eigenvectors
$\mathbf{U}_s$	Matrix containing signal-subspace SVD left singular vectors
$\mathbf{V}_s$	Matrix containing signal-subspace SVD right singular vectors
Λ_n	Diagonal matrix containing noise-subspace eigenvalues
Λ_s	Diagonal matrix containing signal-subspace eigenvalues
Σ_s	Diagonal matrix containing SVD singular values
θ	Cone angle-of-arrival
$\mathbf{i}_k(t)$	Array snapshot corresponding to interference
$\mathbf{n}_k(t)$	Array snapshot corresponding to noise
$\mathbf{s}(\theta)$	Steering vector or array response vector for a ULA
$\mathbf{s}_k(t)$	Array snapshot corresponding to signal
$\mathbf{v}(\Delta f)$	Complex phasor corresponding to a uniformly sampled cisoid
$\mathbf{x}_k(t)$	Array snapshot for the received data
$\mathbf{x}_k^{[n]}(t)$	n^{th} element of array snapshot
$\vec{\mathbf{k}}$	Wavenumber vector
$\vec{\mathbf{r}}$	Position vector
B_s	Spatial bandwidth of ionospheric channel

B_t	Temporal bandwidth of ionospheric channel
c	Speed of light in free space
d	Ground distance between transmitter and receiver
$E\{\cdot\}$	Statistical expectation
f_b	Bandwidth of linear FMCW
f_c	Carrier frequency
f_p	Pulse repetition frequency of linear FMCW
g_r	Group range of ionospheric propagation path
H	Hermitian or conjugate transpose
h_v	Virtual ionospheric height of reflection
k	Range sample index $k = 1, 2, .., K$
l	Fast-time sample index $l = 1, 2, .., L$
n	Receiver number $n = 1, 2, .., N$
r_e	Radius of the earth
T	Transpose
t	Pulse repetition interval index $t = 1, 2, ..P$
T_s	Sampling period of the A/D converter
$Tr\{\cdot\}$	Trace

Glossary

Array manifold The collection of all of array steering vectors or array response vectors.

Array snapshot A vector containing the complex-valued samples recorded at a particular time instant or frequency bin by the receivers of the array

Beamforming Spectral analysis of the received array snapshots to estimate the direction-of-arrival and/or the waveform of coherent and incoherent signals received by the array

Beampattern The magnitude of the spatial transfer function presented by the beamformer in the array to a far-field source

Coning For off-boresight sources, the coning effect causes the azimuth of the source perceived with a ULA to appear closer to boresight as the elevation angle of incidence increases.

Distributed signal A statistical signal with a continuously distributed (i.e., non-discrete) spatial, temporal or space-time power density function.

Doppler processing Spectral analysis of the data received from one PRI to another to estimate the Doppler frequency distribution of the received coherent signals

Fast-time samples The time domain samples recorded in a particular receiver within the PRI

Fine structure The complex-valued space-time distortions imposed on a particular signal mode by irregularities in the ionospheric reflection process

Gross structure The gross structure of a narrowband ionospherically-propagated signal is determined by the superposition of monochromatic plane waves whose parameters best fit the spatial and temporal properties of the prevailing signal modes

Group range The group-range of a mode is the propagation path length from transmitter to receiver assuming the mode travels this path at the speed of light in free space

Main array A 2.8 km long narrowband uniform linear array known as the Jindalee OTH radar receiving array

Mode For single-hop propagation, a mode is a signal reflected from a localised region of an ionospheric layer. Different signal modes may be reflected from well-separated points within the same ionospheric layer or from distinct ionospheric layers. By definition (in this thesis), different single-hop modes can be resolved from one another in time-delay when the group-range resolution is 5 km.

Oblique sounder A system used to determine the mode content of a HF link as a function of operating frequency.

Range processing Spectral analysis of the data received during the PRI to estimate the time-delay distribution of the received coherent signals

Ray A monochromatic plane wave with a fixed amplitude, initial phase, Doppler frequency and direction-of-arrival.

Receiver mismatch Receiver mismatch occurs when the difference between the frequency responses of two or more receivers in the array varies across the passband of interest

Slow-time samples The samples recorded from one PRI to another over the CIT at a particular range cell

Spatial structure The spatial structure of a signal refers to the gain and phase relationship between the receiver outputs rather than their absolute value

Weight vector A vector containing the complex-valued weights used to beamform the received array snapshots

Publications

1. S J Anderson, Y I Abramovich, and G A Fabrizio. Stochastic constraints in nonstationary hot clutter cancellation. In *IEEE International Conference on Acoustics, Speech and Signal Processing (ICASSP97)*, pages 3753–3756, Munich, Germany, April 1997.

2. Y I Abramovich, G A Fabrizio, S J Anderson, D A Gray, and M D Turley. Nonstationary HF interference rejection in adaptive arrays. In *Proc. RADAR-97*, Edinburgh, UK, 1997.

3. G A Fabrizio, Y I Abramovich, D A Gray, S J Anderson, and M D Turley. Adaptive cancellation of nonstationary interference in HF antenna arrays. *IEE Proceedings Radar, Sonar and Navigation*, 145(1):19–24, February 1998.

4. G A Fabrizio, D A Gray, M D Turley, and S J Anderson. Adaptive correction of HF antenna arrays for nonstationary interference rejection. In *Proceedings of the International Radar Symposium*, pages 1165–1175, Munich, Germany, September 1998.

5. G A Fabrizio, D A Gray, M D Turley, and S J Anderson. Modelling the spatial characteristics of ionospherically propagated HF signals. In *Proceedings of the International Radar Symposium*, pages 1187–1197, Munich, Germany, September 1998.

6. G A Fabrizio, D A Gray, and M D Turley. Using sources of opportunity to estimate digital compensation for receiver mismatch in HF arrays. In *Proceedings of the Fifth International Symposium on Signal Processing and its Applications (ISSPA99)*, volume 2, pages 855–858, Brisbane, Australia, August 1999.

7. G A Fabrizio, D A Gray, and M D Turley. Parametric localisation of space-time distributed sources. In *IEEE International Conference on Acoustics, Speech and Signal Processing (ICASSP 2000)*, pages 3097–3100, Istanbul, Turkey, June 2000.

8. G A Fabrizio, D A Gray, and M D Turley. Using sources of opportunity to estimate digital compensation for receiver mismatch in HF arrays. *Accepted for publication in IEEE Transactions on Aerospace and Electronic Systems*, 2000.

CHAPTER 1

Introduction

1.1 Introduction

Over-the-horizon (OTH) radars are used to perform early warning surveillance across very wide areas in a cost-effective manner. Unlike traditional line-of-sight radars which can only see as far as the horizon, skywave OTH radars reflect high frequency signals (3-30 MHz) off the ionosphere to monitor both ship and aircraft movements around the curvature of the earth. This inherently simple concept allows skywave OTH radar systems to detect and track targets at ranges of up to 3000 km.

The Jindalee skywave over-the-horizon radar, constructed near Alice Springs in Central Australia, is currently used for surveillance of Australia's north and north-western coastline regions. The location and coverage of the Jindalee OTH radar and two other OTH radars being developed at Laverton, Western Australia, and Longreach, Queensland are shown in Figure 1.1. The coverage of a ground-based microwave radar in the vicinity of Darwin is also illustrated for comparison.

The successful operation of OTH radars such as Jindalee requires research in a variety of different fields. Important areas of research extend from the physics of the ionosphere to the design of antennas and computer hardware as well as software for signal processing and frequency management. This thesis is concerned with research in the field of signal processing to enhance the capabilities of Jindalee and other OTH radars.

The current chapter introduces the basic operational principles of OTH radar and discusses the high frequency signal environment, a brief overview of signal processing and frequency management for the Jindalee OTH radar is also included. Areas which require further investigation are then described to motivate the specific research undertaken in this thesis. The chapter concludes with a summary of the key contributions.

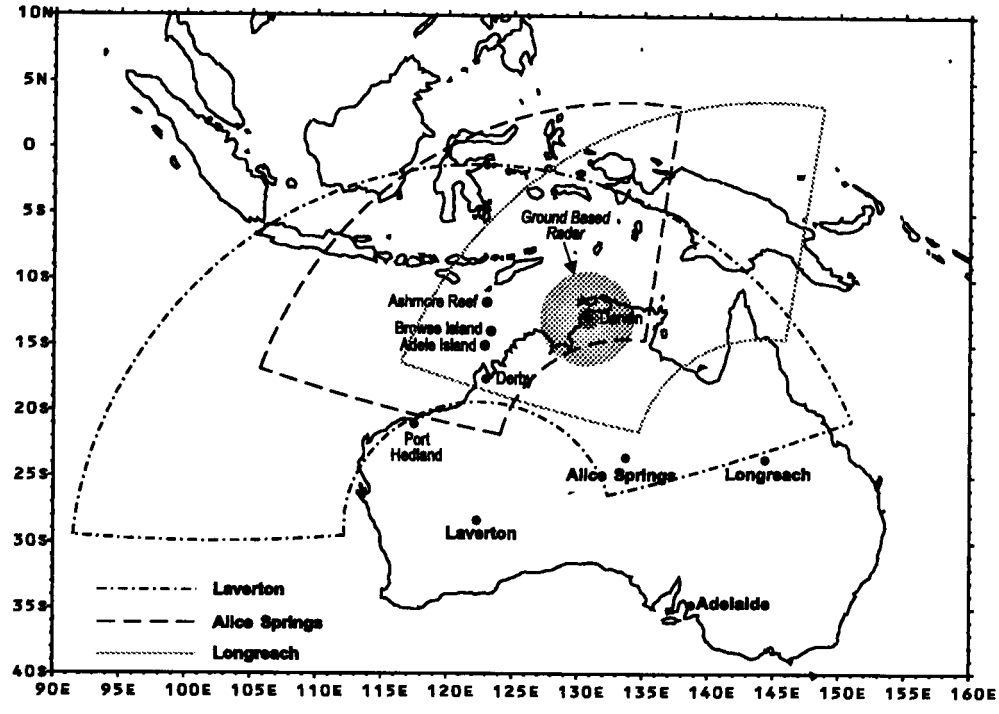

Figure 1.1: Location and coverage of the Jindalee OTH radar (Alice Springs) and two additional OTH radars nearing completion at Laverton and Longreach. The surveillance area of the ground-based microwave (line-of-sight) radar close to Darwin is also shown for comparison.

1.2 Principle of operation and signal environment

The principle of operation for a high frequency (HF) OTH skywave radar is illustrated in Figure 1.2. Turning this inherently simple concept into a useful and reliable surveillance tool creates many significant and serious technical challenges. These challenges arise from uncertainties in the ionospheric reflection process as well as the ability of this mechanism to propagate a host of other unwanted signals which can potentially mask the target signal of interest.

The signals received by an OTH radar can be categorised as either coherent signals or incoherent signals, as indicated by the flow-chart in Figure 1.3. Coherent signals originate from the transmitted radar signal and may be classified as either distributed backscatter from extended areas of terrain or sea-surface (clutter returns) or localised backscatter from aircraft or ships (target echoes) as well as meteors (meteor echoes). Incoherent signals are present irrespective of whether the transmitter is on or off and may be classified as either man-made (interference) or naturally occurring (background noise).

Naturally occurring background noise is either of galactic origin (e.g., stars) or atmospheric origin (e.g., lightning discharges), the spectral and spatial distribution of background noise can vary markedly as a function of time. Man-made interference may be regarded as either unintentional (e.g., electrical machinery) or intentional (e.g., AM radio stations). Interference received from man-made sources is often highly directional and more powerful than background noise. Due to the large number of users, a significant pro-

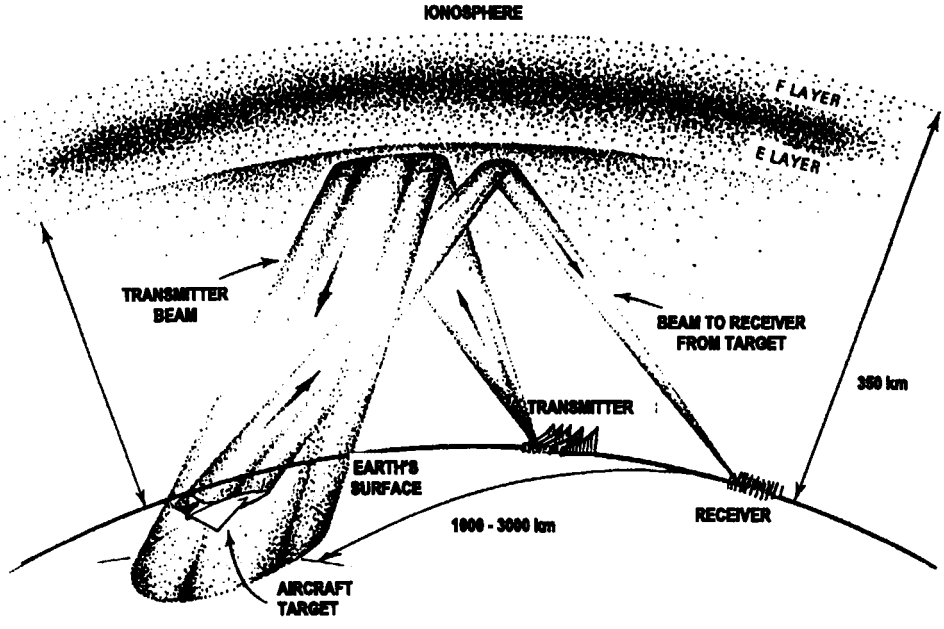

Figure 1.2: Principle of operation for a high frequency skywave over-the-horizon radar (E-layer propagation is illustrated for the case of aircraft detection)

portion of the HF band is frequently occupied by man-made interference. Although not shown in Figure 1.3, the radar receiver introduces its own unintentional noise contribution which is commonly referred to as internal receiver noise.

Since the Jindalee receiver site is well isolated from the transmitter site and from urban areas, the coherent and incoherent signals which reach the Jindalee receiver array are almost exclusively propagated via the ionosphere. As a result, the properties of the composite signal received by the radar are not only determined by the nature of the co-channel signals but also by the characteristics of the ionospheric circuits which link the various signal sources to the receiver array at the selected operating frequency. The composite signal environment which the radar must contend with is largely determined by the choice of operating frequency which in turn influences the effectiveness of signal processing. For this reason, a combination of judicious signal processing and real-time frequency management are essential for operational OTH radar systems.

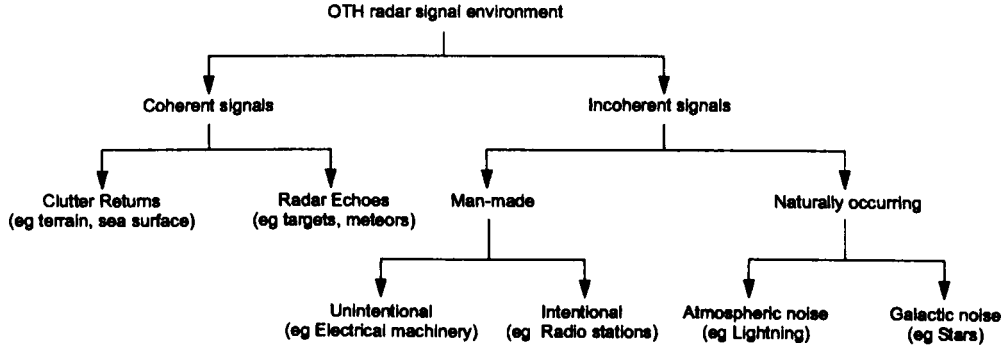

Figure 1.3: Composite signal environment for high frequency OTH radar

1.3 Signal processing and frequency management

A conventional signal processing scheme which can be used to detect and estimate the azimuth, range and Doppler frequency of target echoes from the received composite signal has been described in (Lees 1987) while the capabilities and limitations of this scheme are quantitatively discussed for the Jindalee OTH radar in (Sinnott 1987). The essential features of the conventional signal processing scheme are overviewed with reference to the Jindalee OTH radar in this section to introduce the fundamental capabilities and limitations of this facility.

The frequency management system (FMS) described by (Earl and Ward 1986) was developed to provide the Jindalee OTH radar with real-time advice on the most appropriate choice of operating frequency for the radar mission at hand. The main considerations which drive the frequency selection process are stated briefly in this section to expose some significant technical tradeoffs as a lead into the motivation for research.

1.3.1 Radar waveform

The Jindalee transmitter array pictured in Figure 1.4 radiates a saw-tooth linear sweep frequency modulated continuous waveform (FMCW) in a narrowband frequency channel selected by adjusting the carrier frequency and bandwidth of the linear FM pulse. This radar signal illuminates the surveillance region for a designated period of time known as the coherent processing interval (CPI) or dwell time during which a specified number of linear FM pulses or FMCW sweeps are emitted.

The Jindalee receiver array pictured in Figure 1.5 makes use of a synchronised copy of the transmitted waveform to demodulate or down-convert the received signals prior to analog-to-digital conversion. The digital samples acquired by the receiver array during a radar dwell are range processed, beamformed and Doppler processed to detect and estimate the geographical location and radial velocity of targets within the surveillance region.

1.3.2 Range processing

A down-converted radar echo has a frequency during the linear FM pulse repetition interval (PRI) which is linearly dependent on the time-delay or group-range of the signal path associated with the scatterer that gives rise to it. Range processing aims to resolve the received radar echoes into different time-delay or group-range bins by applying a Fast Fourier Transform (FFT) to the digital data acquired within each PRI.

The range resolution is inversely proportional to the bandwidth of the transmitted FMCW signal which is limited in practice by the availability of clear (unused) frequency channels and the dispersive properties of the ionosphere. The range resolution is typically between 3-30 km for OTH radar while the range accuracy and range coverage are typically

between 10-40 km and 1000-3000 km respectively (Sinnott 1987). The range accuracy is primarily limited by uncertainties in the height and tilt of the ionosphere at the signal reflection point(s) while the range coverage is limited by the maximum usable frequency (the frequency beyond which the signal passes through the ionosphere) as well as other environmental factors.

1.3.3 Beamforming

The aim of beamforming is to receive signals which are incident from a specified array "look" direction while attenuating signals incident from other directions as much as possible. A radar echo or interference signal originating from a point source in the far-field of the array can, in the ideal case of *specular* reflection from the ionosphere, be represented as a plane wave incident from a certain azimuth and elevation. For a uniform linear array (ULA) such as Jindalee, a plane wave narrowband signal sampled at a particular time instant by the receivers in the array will exhibit a spatial frequency dependent on the signal direction-of-arrival (azimuth and elevation) and the inter-sensor spacing in wavelengths. As a result, signals arriving with the same time-delay or group-range may be resolved in azimuth by applying an FFT across the aperture (i.e., to the receiver outputs) at each range bin.

The aperture of the Jindalee receiver array spans approximately 2.8 km and the azimuthal resolution (which is inversely proportional to the array aperture in wavelengths) varies between 0.2-2.0 degrees over the HF band. The azimuth accuracy is in the order of 1-5 degrees (Sinnott 1987) and is limited by the same ionospheric uncertainties as the range accuracy although both bearing and range accuracy can usually be improved through the recognition of ground features such as land-sea boundaries. The azimuth coverage is roughly 45 degrees either side of the array boresight and is limited by ambiguities arising when the inter-sensor spacing is greater than half the operating wavelength.

1.3.4 Doppler processing

A radar echo from a moving target has a frequency that is Doppler shifted in comparison with clutter returns from the same azimuth and group-range due to the target's radial component of velocity relative to the ground or sea-surface. The target's Doppler shift manifests itself as a regular phase progression in the temporal samples recorded in each receiver from one PRI to another. The rate of phase progression (i.e., Doppler frequency) is determined by the carrier frequency and the target's radial component of velocity.

Doppler processing aims to resolve target echoes and clutter returns with the same azimuth and group-range into different Doppler frequency bins by applying an FFT to the temporal samples recorded from one PRI to another during the dwell. The Doppler resolution is determined by the inverse of the duration of the CPI which is typically in the order of a few seconds for aircraft detection. Although a longer CPI is expected to

Figure 1.4: The Jindalee OTH radar transmitter site at Harts Range (100 km north-east of Alice Springs)

yield better Doppler resolution and more coherent gain of target signal energy, a very long CPI becomes impractical when targets are maneuvering quickly and many surveillance regions need to be monitored. As the CPI is lengthened it may additionally be required to correct for temporal distortions imposed by the ionosphere on backscattered signals (Anderson and Abramovich 1998).

1.3.5 Frequency management

The ionosphere is a dynamic and spatially inhomogeneous propagation medium with frequency dependent characteristics. As a result, the quality of radar signal propagation from the point of view of target detection varies as a function of time, geography and operating frequency. To enhance OTH radar performance, the operating frequency needs be chosen in real-time so as to optimise the probability of detecting targets located in the geographical area of interest. The reader is referred to (Earl and Ward 1986) for an excellent description of the methods and the equipment used for frequency management in the Jindalee OTH radar.

One of the most influential factors driving the choice of operating frequency in OTH radar is the target signal-to-noise ratio (SNR). A technique known as backscatter sounding is used to estimate the signal power backscattered from the surveillance region as a function of frequency. These measurements are combined with measurements of the noise power spectral density to yield an estimate of the signal-to-noise ratio in different frequency channels across the HF band. The FMS system also monitors channel occupancy

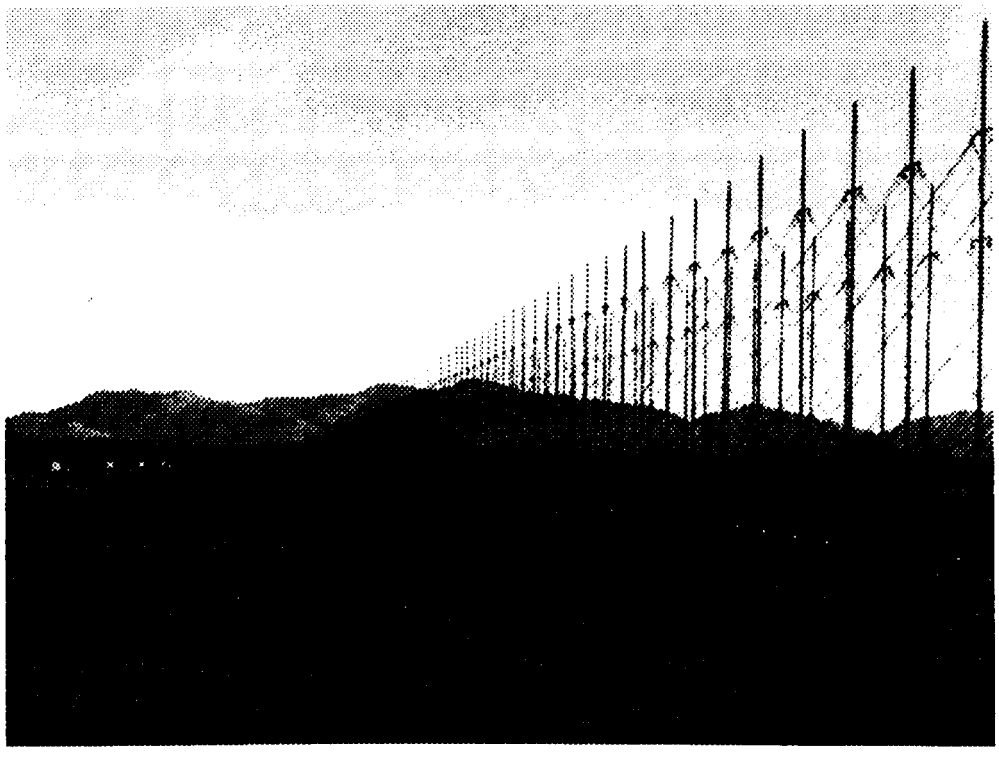

Figure 1.5: The Jindalee OTH radar receiver site at Mt Everard (40 km north-west of Alice Springs)

so that frequency channels which are free of strong radio frequency interference (RFI) from other users can be identified as potential candidates for radar operation. The SNR criterion for frequency channel evaluation is most important for aircraft detection since the targets are typically detected against noise rather than clutter. Aircraft of fighter size or larger can be detected by OTH radar, but detection becomes progressively more difficult as the operating frequency decreases as this is typically associated with a decrease in the radar cross section of the target and an increase in the background noise power.

The ionospheric propagation medium usually exhibits a stratified nature which often results in a HF signal being reflected by a number of different ionospheric layers. As a result, the received signal is often a superposition of multiple components or signal modes which propagate along different ionospheric paths between the transmitter and receiver. Different signal modes may experience different ionospherically-induced Doppler shifts and Doppler spreads so the superposition of multiple modes tends to broaden the clutter occupied region of Doppler space which can in turn obscure targets moving at a low radial speed. An oblique sounder and mini-radar are employed in the FMS to respectively provide information on the mode content and spectral characteristics of a HF link as a function of operating frequency. The Doppler spectrum criterion for frequency channel evaluation is especially relevant to ship detection where the targets are not travelling fast and must often be detected against clutter rather than noise. Depending upon the sea state (which also contributes to the Doppler spectrum characteristics of backscattered signals) it is possible to detect steel-hulled ships of ocean-going size.

1.4 Motivation for research

The relatively low computational complexity of conventional (FFT-based) beamforming is a major advantage for antenna array systems which are required to operate in real-time using computer hardware with relatively limited processing capacity. However, a significant disadvantage of the conventional beamformer is that it allows strong interference signals to leak through the sidelobes of the beampattern and obscure the relatively weaker target echoes in a significant number of beam steer directions. When conventional beamforming is used this deleterious situation can only be avoided by selecting clear frequency channels which are not occupied by other users.

To find clear frequency channels, an omni-directional (whip) antenna is used at the receiver site to monitor the spectral occupancy of the HF band in real-time. The power spectral density of interference-plus-noise signals is measured in adjacent narrowband frequency channels across a selectable portion of the spectrum so that, in accordance with broadcasting regulations, different frequency channels can be classified as either forbidden, occupied or clear of other users. Aside from the performance benefits of operating on clear frequency channels it is noted that Jindalee has a policy of non-interference with other users.

Due to the heavy usage of the HF band there are often times at which the availability of suitable clear frequency channels is significantly diminished. Such circumstances are quite common at night time when the ionosphere is especially prone to allowing very long distance propagation of radio waves. High user congestion in the HF band has the potential to severely degrade OTH radar performance as it limits the scope which the frequency management system has for optimising the selection of operating frequency. More specifically, frequency channels which are optimum in terms of target signal reception may contain powerful co-channel interference while the clear frequency channels, typically found at the high end of the spectrum, may be inappropriate for radar signal propagation to the geographical area of interest.

Dramatic advances have been made over the past two decades in the fields of computer technology, antenna array hardware and adaptive array signal processing. As a result, adaptive beamforming is now a more attractive and feasible alternative with respect to conventional beamforming in operational antenna array systems. In the context of OTH radar, adaptive beamforming provides a means for removing co-channel interference in frequency channels which are potentially suitable for radar operation.

In the HF environment, interference signals are received by the array after reflection from the ionosphere which is a dynamic and spatially inhomogeneous propagation medium. Despite the vast amount of theoretical research and computer simulations published on the subject of array signal processing, there are very few experimental studies which have quantitatively analysed the effect of ionospheric propagation on the interference cancellation performance of various adaptive beamforming algorithms. Moreover, it

is currently unclear how more effective adaptive beamforming algorithms should be designed and optimised for different HF interference and noise scenarios. This is partly due to the lack of *experimentally verified* multi-sensor (space-time) signal processing models of the ionospheric reflection process which can distort the structure HF signals over time intervals commensurate with the CPI of OTH radar.

A major component of the thesis is devoted to the development of mathematical models that represent the space-time characteristics of ionospherically-propagated HF signals received by a very wide aperture antenna array. The central aim of this component is to determine the domain of validity for the different models and to quantify the fidelity with which they can predict the characteristics of ionospherically-propagated signal-fields received by the array. A secondary component of this thesis is concerned with evaluating the interference cancellation performance of various adaptive beamforming schemes relative to the conventional beamformer by experiment and simulation using the previously derived models. This component also involves the identification and compensation of hardware related aspects which can limit adaptive beamformer performance in practice.

The research work presented in this thesis is particularly relevant to development of OTH radar systems which treat signal processing and frequency management as a global optimisation problem. To enhance target detection, future OTH radar systems will be required to measure the spatial properties of co-channel interference across the HF band so that the choice of operating frequency and adaptive beamforming algorithm can be optimised jointly in order to provide the best possible output SNR in the beam steer directions considered important for surveillance.

1.5 Main contributions

The process of signal reflection from each ionospheric layer is by no means mirror like and can induce appreciable distortions upon individual propagation modes. A wave interference model for the "fine structure" of an ionospheric mode has been proposed by various investigators but the ability of this model to represent real wavefields over typical OTH radar CPI has not been experimentally quantified.

> **The second chapter experimentally quantifies the accuracy with which space-time wave interference models can represent the complex-valued wavefields received from ionospheric modes on a mid-latitude path by a very wide aperture antenna array over a typical OTH radar CPI.**

The dynamic nature of the ionosphere causes changes in the wavefields of ionospheric modes with respect to time. It has been shown that for narrow signal bandwidths in the order of 10 kHz and short time intervals in the order of 10 minutes the temporal proper-

ties or Doppler spectrum of a quiet mid-latitude ionospheric channel may be adequately described by a stationary statistical model. Despite its importance to the HF interference rejection problem, the incorporation of the spatial properties (DOA spectrum) of ionospheric channels in a statistically stationary space-time generalisation of this model has not received as much attention in terms of theoretical derivation and experimental validation.

The third chapter develops a space-time stationary statistical model of the ionospheric channel based on the scattering of radio waves from a dynamic and spatially irregular ionospheric plasma and experimentally validates the ability of such a model to represent the observed mode wavefields in a statistical sense.

The deterministic and statistical ionospheric channel models referred to above may be combined into a generalised parametric space-time signal processing model which can be used to simulate the complex-valued samples received from coherent and incoherent HF signals propagated via the ionosphere. In the case of interference, the different propagation modes cannot be isolated in time-delay to facilitate the estimation of model parameters associated with each propagation mode. The ability to estimate these model parameters is considered important for future FMS systems which may be required to quantify the directional characteristics of co-channel interference.

The fourth chapter proposes a novel closed-form space-time parameter estimation technique based on the generalised mathematical model of the ionospheric channel that estimates the parameters of individual signal modes optimally according to the least squares criterion in a computationally attractive manner when the different modes cannot be resolved in time-delay.

The costs associated with the operational implementation of adaptive beamformers in preference to conventional beamformers can only be justified in terms of the resulting performance improvement which is usually measured in terms of signal-to-interference plus noise ratio (SINR) at the beam output. Although adaptive beamforming has been applied in many diverse practical applications, the uniqueness of the HF environment requires a specific study into the performance improvement which can be achieved by different adaptive beamforming schemes. In addition, the experimental performance of adaptive beamformers operating on a very wide aperture HF antenna array has not previously been compared with that predicted by multi-sensor signal processing models of the ionospheric channel(s) which propagate the interference in terms of output SINR distributions.

The fifth chapter evaluates the experimental performance of various adaptive beamforming schemes relative to the conventional beamformer and assesses the ability of a statistically stationary space-time signal processing model to forecast the relative output SINR distributions observed in practice.

Differences in the analog transfer functions of the receivers in the array is an instrumental factor known as receiver mismatch which can severely limit the effectiveness of interference suppression by means of adaptive beamforming. While the problem of calibrating for uncertainties in the array manifold with HF sources of opportunity has already been researched, the complementary problem of using HF sources of opportunity to estimate digital compensation for receiver mismatch has (to the author's knowledge) not been addressed in the context of HF arrays.

The sixth chapter introduces a new signal processing algorithm which is capable of estimating digital corrections for receiver mismatch using HF interference sources of opportunity, the effectiveness of the proposed technique is experimentally demonstrated by using a radio broadcast of opportunity to compensate for real receiver mismatch.

The main body of the thesis is completed with the conclusions in chapter 7, this is followed the appendices and bibliography. The numbers in parentheses refer to publications as listed on page xxv.

CHAPTER 2

Wave interference model

A HF signal which propagates beyond the line-of-sight is often reflected from multiple points within the ionosphere. A popular model for the signal resulting at the receiver consists of a superposition of multiple plane waves which emanate from the different ionospheric reflection points. The principle aim of this chapter is to quantitatively assess the virtues and limitations of the wave interference model in both the spatial and temporal domain using experimental data collected by a very wide aperture antenna array.

Section 2.1 contains background information and a literature survey on the subject of wave interference in ionospheric propagation, this section serves to highlight areas of research which require further exploration as well as to introduce and motivate the specific experimental study undertaken in this chapter. The experimental facility and procedure used to collect data for this study are described in section 2.2, this is followed by a preliminary analysis of the data in section 2.3. The purpose of this analysis is to quantify the essential spatial and temporal characteristics of the HF link under study, these characteristics include the mean direction-of-arrival and Doppler shift of each signal mode propagated during the experiment.

A mathematical space-time model of HF signals reflected by the ionosphere is derived in section 2.4, this model is based on the wave interference principle and mathematically relates the experimental setup to the theoretically expected antenna array measurements. Section 2.5 discusses a parameter estimation technique which can be applied to this model and proposes a measure for assessing the accuracy with which the estimated signal model can represent the experimental data. Wave interference signal models are estimated from experimental data recorded on a mid-latitude ionospheric circuit in section 2.6, the accuracy with which these models can represent the space-time complex-valued samples of real HF signal-fields recorded by the array is also quantitatively assessed.

2.1 Literature review

To present a concise literature review relevant to this particular study it is necessary to define the nature of this research in more detail. This particular research is devoted to the study of one-way oblique ionospheric circuits which propagate signals from a distant HF emitter to a receiving antenna array. The study of point-to-point ionospheric circuits is important for HF communication and HF direction finding systems and is currently of great relevance to the problem of interference rejection in OTH radar. Within this framework, the present work is concerned with the ionospheric propagation of narrowband signals which typically have bandwidths in the order of tens of kilohertz and are not significantly affected by the dispersive properties of the ionosphere. Although wideband HF systems exist, it is worth noting that most HF arrays operate on narrowband signals and this includes the Jindalee OTH radar receiving array.

2.1.1 Background

A wide variety of high frequency (HF) systems rely on the ionosphere as a propagation medium for the transmission/reception of HF signals over distances well beyond the line-of-sight. Examples include HF communication links for transferring data or speech over long distances, direction finding networks for locating the position of distant HF emitters and OTH radars for detecting and tracking the movements of remote aircraft. In practice, the performance of HF systems utilising the ionosphere depends not only on the choice of operating parameters but also upon the characteristics of the propagation medium or ionospheric channel.

The ionosphere is typically composed of multiple reflecting layers so in this medium propagation is usually by multipath components or signal modes. Due to the spatially inhomogeneous and dynamic nature of the ionosphere, the process of signal reflection from each layer is by no means "mirror-like" and can at times induce appreciable distortion on individual signal modes. Both of these ionospheric propagation effects (i.e., multipath and individual signal mode distortion) are generally not entirely predictable and have the potential to impair system performance.

System performance can often be enhanced through the use of judicious signal processing algorithms which are designed to remove undesired signals and to provide compensation for the contaminating effects which the ionospheric reflection process has imparted on the desired signal structure. Modern signal processing algorithms are usually designed and optimised on the basis of mathematical models for the received signals, and not surprisingly, the practical effectiveness of model-based algorithms is largely determined by the fidelity with which the assumed data model represents the actual characteristics of the signal-field as it is seen by the antenna sensor(s). For this reason, users of HF systems are interested in analysing and modeling the characteristics of ionospherically-propagated sig-

nals measured by their sensor(s), particularly those characteristics which can potentially limit the performance of their systems.

A relatively simple signal-field model results when each ionospheric layer is considered as a smooth "copper sheet" reflector of radio waves, in this case the signal received from a far-field source is modelled as a superposition of plane waves each of which can be parameterised by a complex amplitude, direction of propagation (azimuth and elevation), Doppler shift and polarisation state. Such a model represents what may be referred to as the "gross" structure of an ionospherically-propagated signal, in many respects, this deterministic model plays a central role in the development of many signal detection and signal parameter estimation algorithms.

The reflecting layers of the ionosphere are known to contain randomly changing irregularities in electron density which induce distortions on the ideal signal structure assumed in the case of specular reflection. Ionospherically-induced distortions can influence the amplitude, phase and polarisation state of a signal mode. The spatial and temporal departures of a signal mode from an ideal (specularly reflected) plane wave due to these distortions gives each propagating mode its "fine" structure. A variety of different models have been proposed to explain the fine structure of ionospheric modes, a popular model describes fine structure as a superposition of a small number of sub-modes or rays which have similar Doppler frequencies and closely spaced directions of arrival. The various rays in this model are presumed to result from relatively few specular reflection points within an ionospheric layer that move over time.

The combination of experimental and mathematical techniques used to estimate the parameters of interest for each component ray are collectively referred to as wavefront analysis (WFA) techniques. In practice, WFA has traditionally been applied to decompose the gross structure of composite signal wavefields by assuming that each propagation mode undergoes specular reflection. The lack of analysis on isolated ionospheric modes has led to much debate regarding the ability of the wave interference model to additionally represent fine structure. Although the literature review encompasses both gross and fine structure analysis, it is emphasised that the focus of this experimental study is to quantify the ability of the wave interference model to represent the *fine structure* of signal modes propagated over a one-hop mid-latitude ionospheric circuit.

2.1.2 Studies of gross structure

In the multipath ionospheric environment it is often assumed that the gross structure of the signal-field can be modelled as a superposition of plane waves corresponding to the different modes of propagation. Most HF array systems are required to estimate the direction-of-arrival (DOA) of the incident propagation modes in order to partially or fully satisfy their operational objective. The DOA estimation problem provides a suitable vehicle for discussing previous experimental studies based on gross structure models of

ionospheric propagation and the practical difficulties which have been encountered in estimating the parameters of these models (i.e., the directions-of-arrival of real ionospheric modes).

HF array systems initially used interferometry or classical beamforming techniques to estimate the mode directions-of-arrival. A major obstacle encountered by these systems was that many array apertures were not always large enough to resolve the different propagation modes. As a result, the initial emphasis was more on avoiding the deleterious effects of multipath propagation rather than to resolve the different modes. Wavefront testing methods were developed by Treharne (1967) and more recently in (Warrington, Thomas and Jones 1990) so that estimates of the emitter DOA in HF direction finding systems were only taken at times when the received wavefront closely resembled a plane wavefront. These techniques, which rely on relative fading between modes to give times of quasi-unimodal propagation, severely restrict the situations under which data can be acquired and are therefore of limited utility (Hayden 1961).

A class of so-called superresolution algorithms were developed in the field of array signal processing to enhance the resolution capabilities of sensor arrays. The MUltiple SIgnal Classification (MUSIC) superresolution algorithm, originally developed by (Schmidt 1979), sparked tremendous interest in this area and led to the development and analysis of different superresolution algorithms. Despite the vast quantity of published theoretical analysis and computer simulation results on superresolution algorithms, there has been comparatively little reported on the ability of such algorithms to resolve the directions-of-arrival of different propagation modes in the HF environment.

A 16 element linear antenna array with an aperture of 120 m was used by (Creekmore, Bronez and Keizer 1993) to estimate the DOA of propagation modes originating from known AM radio broadcasts of opportunity. MUSIC and three other superresolution techniques were used to resolve the number of ionospherically-propagated modes assumed to propagate from each source. The authors concluded that the propagation modes appeared to be "spatially extended" due to temporal variations in the ionosphere. In other words, the discrete planar wavefront model assumed by the adopted superresolution techniques did not appear to be strictly valid in practice. This propagation effect, which arises due to the fine structure of the ionospheric reflection process, significantly complicated the process of identifying the correct number of modes and associating a single bearing per mode as both quantities appeared to fluctuate with respect to time.

An irregular two-dimensional array with 8 elements and an effective aperture of about 8 wavelengths was used by (Tarran 1997) to determine the azimuth and elevation of signal modes which propagated from a known transmitter over a 1235 km mid-latitude path. The MUSIC algorithm was used to estimate the direction-of-arrival of two dominant modes at a rate of 30 azimuth-elevation bearings per second. The resulting azimuth-elevation scatter plot demonstrates spreads in the order of a few degrees for each of the modes in both dimensions, this led the author to conclude that ionospheric reflection can cause very

rapid and significant fluctuations in the mode bearings. These results provided further evidence that a plane wave of fixed direction-of-arrival is not always a good model for individual signal modes even over short periods of time.

A regular 6 element circular array of 50 m diameter was used by (Moyle and Warrington 1997) to estimate the directions-of-arrival of the modes which propagated over a controlled 778 km mid-latitude ionospheric circuit. The ionospheric circuit was controlled in the sense that oblique sounding methods were used to identify the mode structure which prevailed for the path at the time of recording. Although three distinct propagation modes were resolved in range by the ionogram at the operating frequency, the application of MUSIC and a number of other superresolution algorithms were unable to resolve the directions-of-arrival of all three propagation modes. The authors concluded that the inability to resolve all three modes may have been due to the poorly matched reception channels in the array and the relatively small aperture.

A 7-element V-shaped array with a greatest dimension of 350 m was used by (Zatman and Strangeways 1994) to resolve multi-moded HF transmissions of opportunity. The MUSIC and Direction of Arrival by Signal Elimination (DOSE) algorithms were described in (Zatman and Strangeways 1994) and applied to estimate the azimuth and elevation angles of the various ionospheric modes. While neither algorithm performed consistently well, it was concluded that the inability of MUSIC to consistently resolve the propagation modes was possibly due the high correlation existing between the different modes, the additive noise present in the data and the effects of mutual coupling between the antenna elements.

A uniform linear array (ULA) with an aperture of 1.4 km was used in (3) to intercept two high signal-to-noise radio interference sources of opportunity. One of these sources was received over a controlled mid-latitude ionospheric path while the other source propagated to the array via the typically perturbed equatorial ionosphere. To resolve the potentially correlated modes, the outputs of 16 well calibrated digital receivers were considered in groups of 12 receivers in order to form the spatially smoothed MUSIC spectra as described by (Pillai 1989). On the controlled circuit it was demonstrated that spatial smoothing significantly improved the ability of MUSIC to resolve two identified propagation modes which were highly correlated over the observation interval. A time-sequence of MUSIC spectra were evaluated at a rate of 60 Hz to show the temporal variation of the mode directions-of-arrival during a typical OTH radar CPI of approximately 4.2 seconds. The experimental results demonstrated a smooth temporal variation of the mode DOA's for both of the sources, these variations were in the order one degree for the modes propagated via the equatorial ionosphere and fractions of a degree for the modes propagated on the mid-latitude path.

It is clear from the experimental results reported in the literature that estimating the gross structure of an ionospherically-propagated wavefield requires well-calibrated wide aperture arrays, low noise levels and in many cases the use of superresolution techniques

which are insensitive to inter-mode correlations. While the above-mentioned system attributes are frequently necessary for resolving different ionospheric propagation modes, the practical effectiveness of these systems relies on the accuracy of the assumed gross structure model (i.e., a known number of specularly reflected signal modes). It is evident that the presence of mode fine structure has posed significant problems in the resolution of signal-fields presumed to obey this relatively simple propagation model, and moreover, the deleterious effects of fine structure are amplified by the increased system sensitivity required to achieve the initial objective of gross-structure model parameter estimation. Many HF systems stand to benefit from a more detailed understanding of mode fine structure, this is especially true for modern very wide aperture HF antenna arrays such as Jindalee where great care has been taken to reduce the influence of array imperfections, site errors and noise. The desire to improve the operational performance of such arrays has led investigators to study the fine structure of ionospheric modes.

2.1.3 Studies of fine structure

The first experimental investigation on mode fine structure with a very wide aperture array was conducted by (Sweeney 1970). This study made use of a 2.5 km uniform linear array (ULA) to sample the amplitude and phase of ionospheric modes propagated over a 2550 km mid-latitude path. The ULA was composed of 8 non-overlapping subarrays with each subarray consisting of 32 vertical whip antennas spaced 10 m apart. The 32 vertical whips in each subarray were connected to an analog beamformer to form a subarray output, the 8 subarray outputs were sampled by 8 well calibrated digital receivers to allow digital beamforming.

A linear FMCW waveform was used in one experiment to separate the different propagation modes on the basis of time-of-arrival. Classical digital beamforming and range processing was carried out via a two-dimensional Discrete Fourier Transform (DFT) to compute the azimuth-range power spectral density of the different modes. The same experimental setup was adopted to separate the modes on the basis of Doppler shift using CW signals. A two-dimensional DFT was implemented over space and time to compute the azimuth-Doppler power spectral density of the different modes. The principle objective of the analysis was to examine the discreteness of the received modes in azimuth, range and Doppler. Particular attention was paid to the spatial dimension as the primary objective of the analysis was to determine the extent to which ionospheric propagation and fine structure degrades the azimuthal pattern properties of a very wide aperture array. While single-hop modes appeared discrete in azimuth, range and Doppler to the resolution of the array, it was noticed that double-hop modes exhibited considerable spread in all three dimensions. Based on these results, the author concluded that for single-hop modes the presence of mode fine structure did not significantly degrade the beampattern properties and hence the "performance" of a very wide aperture antenna array. The au-

thor postulated that the observed spreading on double-hop modes was being caused by intermediate ground reflection from very rough (mountainous) terrain at the mid-point of the path.

The performance of a very wide aperture antenna array has a different meaning when the received signal represents interference rather than the signal of interest and is to be removed by means of adaptive processing rather than conventional processing. When the signal represents interference the effect of fine structure is observed close to the relatively steep "nulls" of the beampattern rather than across the flatter main lobe. In this case, the performance is related to the interference power at the beamformer output which is expected to be very sensitive to variations in the spatial structure of each propagation mode.

The effect of mode fine structure on the interference cancellation performance of adaptive beamformers in a very aperture antenna array was reported in (3). The experimental facility and data collected for this investigation was previously summarised in the section on gross structure. The interference cancellation performance of the sample matrix inverse adaptive beamforming technique (Reed, Mallet and Brennan 1974) was found to depend significantly upon the rate at which the spatial filtering weights were updated. When the weights were updated very quickly the cancellation performance was degraded by about 4 dB relative to its optimum level due to the limited number of samples available for estimating the beamformer. On the other hand, if the weights were updated too slowly (at a rate slower than once per second) the cancellation performance was degraded by up to 5 dB relative to the optimum level for one source due to the presence of mode fine structure. The authors concluded that temporal variations in the spatial structure of ionospherically-propagated signal modes has the potential to severely degrade the interference cancellation performance of adaptive beamformers in very wide aperture antenna arrays.

Another experimental study of fine structure using a very wide aperture antenna array was carried out by (Rice 1973). In this investigation, a 32 element uniform linear array with an aperture of approximately 1.2 km was used to measure the phase-only spatial structure of ionospheric modes propagated over a 911 km mid-latitude path. Different modes were resolved on the basis of time-of-arrival using an FMCW waveform and measurements from an oblique sounder were analysed to identify the propagation modes for the circuit.

The unwrapped phase-fronts received from six propagation modes were plotted side by side and exhibited varying degrees of phase non-linearity across the aperture. In particular, the phase-front of a mode reflected from the F2-layer was much more linear than those observed for modes reflected by lower ionospheric layers during the same time interval. The author concluded that the mechanism leading to distorted phase-fronts is associated with phenomena near the height of reflection, rather than diffraction effects arising from the passage of rays through lower height regions where the other modes

are reflected. The author attributed the non-linear mode phase-fronts to within mode wave interference effects. This interpretation considers each mode as being composed of a number of sub-modes which have nearly the same transit time (unresolved in range) and slightly different angles of arrival. Changes in the mode phase-fronts with respect to time were observed at one minute intervals in (Rice 1976), these temporal variations indicate that the sub-modes have different Doppler characteristics.

The wave interference interpretation of fine structure is supported by measurements made at vertical incidence by (Felgate and Golley 1971). The authors used an array of 89 elements to fill a circular area with a diameter of approximately 1 km. A waveform with a 70 microsecond pulse duration and a repetition frequency of 50 Hz was used to separate and identify the propagation modes according to their different times of arrival. The amplitude pattern produced by each mode over the ground was sampled at regular time intervals and presented as an intensity modulated photographic display. Periodic fringe patterns consisting of alternate bright and dark bands were frequently observed for individual modes. The authors suggested that the regularity of these fringe patterns was produced by the interference between a small number of discrete rays returned from different specular reflection points within the ionospheric layer. The motion of fringes over the ground with respect to time was attributed to changes in either the horizontal or vertical position of these specular reflection points which changes the phase relationship between the different rays.

The assumption that a mode consists of a small number of specularly reflected rays with similar Doppler shifts and closely spaced angles of arrival was also assumed by (Clark and Tibble 1978). An 8 element vertical antenna array 74 m high was used to measure the elevation angles of arrival of CW ionospheric modes separated on the basis of Doppler shift. It was found that the elevation angles of certain modes fluctuated in a sinusoidal fashion by more than 5 degrees during a 90 second interval.The authors commented that such results seemed unrealistic and that the most probable explanation for the large excursions in elevation angle was their inability to resolve the rays comprising the fine structure of these modes.

2.1.4 Significance of research relative to previous work

The wave interference model of mode fine structure suggested in the literature is derived from idealised physical principles and is supported by a number of above-mentioned experimental investigations. Such a model has the advantage of being mathematically tractable and it allows the data to be interpreted from a physical perspective which is more readily understood when the number of rays is small.

From the literature review it is evident that an analysis is yet to be carried out which attempts to estimate the spatial and temporal parameters of these rays and then compares the simulated wavefield with measurements of the actual wavefield recorded by an antenna

array. A quantitative measure of the match between the simulated and experimental array data can be used to assess the accuracy of the model in a manner that is general and not dependent on any particular signal processing application. The current research aims to quantify the accuracy with which the wave interference model can represent mode wavefield samples received in the spatial and temporal domain by a very wide aperture antenna array operated with typical OTH radar parameters.

2.2 Experimental facility and data collection

The experimental facility used to collect data for this study includes a very wide aperture antenna array equipped with a multi-channel digital receiver, an oblique sounder and a test transmitter located in the far-field of the array. The relevant characteristics of these three systems and the procedure used for data collection are described below.

2.2.1 Experimental facility

The very wide aperture receiver array of the Jindalee OTH radar is located at 23.523(S) and 133.678(E), near Alice Springs in Central Australia. The Jindalee receiver is a uniform linear array (ULA) which spans an aperture of approximately 2.8 km and is oriented with boresight at an azimuth of 324.20 degrees clockwise from true North. Figure 1.5 shows a picture of the Jindalee receiving array which is often referred to more simply as the main array.

The main array is composed of 462 dual-fan antenna elements, each dual-fan element consists of a pair of vertical monopole antennas that are 6 m high and positioned 3 m apart in a line perpendicular to that of the main array. A 2.4 m fixed length cable is inserted into the rear monopole to introduce a time delay designed such that the summation of the monopole outputs (with the rear monopole output inverted by 180 degrees) yields a front-to-back directivity ratio which is traded off over the HF band. The schematic diagram in Figure 2.1 illustrates this fixed length cable along with other components in the signal path extending from the dual-fan antennas to one of the digital receivers.

The 462 dual-fan antenna elements are grouped into 32 uniformly spaced subarrays, each subarray is composed of 28 consecutive dual-fan elements which are shared with neighboring subarrays (i.e., a 50 % overlap with each adjacent subarray). All of the subarrays are connected to an analog beamforming network and can be steered to look in a prescribed azimuthal direction. As indicated in Figure 2.1, analog beamforming is performed by switching the outputs of the 28 dual-fan elements through a (Dolph-Chebychev) tapering weight and a suitably adjusted delay-line before summing the resultant signals in a combiner to form the subarray output.

The 32 subarray outputs are then passed through a low noise amplifier and a length of cable which connects the amplified subarray output to its respective digital receiver.

The low noise amplifier controls the signal level entering the receivers to ensure that the received data is limited by external noise rather than internal noise and that the signal level is appropriate for the dynamic range of the A/D converter. The run of cable which connects each amplifier output to a digital receiver is of known nominal length and depends upon the distance between the subarray and the multi-channel digital receiver. The radio frequency (RF) signal entering the receivers is first mixed or deramped with a linearly swept frequency modulated continuous waveform (FMCW) of selectable carrier frequency and bandwidth. The deramped signal is translated to an intermediate frequency (IF) and bandpass filtered before being translated to baseband by a 50 MHz local oscillator and digitised at approximately the Nyquist rate by an analog-to-digital (A/D) converter.

Each reception channel of the array is matched across the receiver passband by injecting a calibration signal at the port located immediately behind each subarray. The frequency response of each reception channel is measured at the required resolution over the passband of interest and digital corrections are applied to compensate for any differences in the channel transfer functions. Obviously, the radiation patterns of the subarrays cannot be measured and calibrated with this scheme. It is noted that great care has been taken in the design of the main array to minimise the influence of mutual coupling and sensor position errors, a ground screen has also been laid over a significant area below the array to stabilize the impedance of the antenna elements.

The test transmitter or beacon is a vertical whip antenna located at 12.436(S) and 130.907(E), near Darwin in the Northern Territory. The test transmitter and the main array are separated by a ground distance of approximately 1265 km. The great circle azimuth of the test transmitter is approximately 21.97 degrees when measured clockwise relative to the boresight of the main array. A communications link between the two sites makes it possible to control the beacon remotely from the receiver site, an important aspect of this connection is that the timing and characteristics of the FMCW signal emitted by the beacon can be synchronized with those of the waveform generator in the main array. Such a capability allows the absolute time delay and hence group range of the ionospherically-propagated signal modes to be estimated.

The oblique sounder makes use of the co-operative beacon near Darwin and a separate subarray located at the Jindalee receiver site to provide information regarding the mode content of this mid-latitude path. The data recorded by the oblique sounder can be used to estimate the time-delay associated with different propagation modes and to identify the ionospheric layers which reflected them. The oblique sounder is independently operated by the Jindalee Frequency Management System (FMS) which routinely records oblique incidence ionograms for this particular ionospheric circuit. The FMS subarray used for oblique sounding is nominally the same as those used in the main array and is located about 100 m behind the main array with the same boresight direction. Although not shown in Figure 2.1, digital recordings made by the main array and the FMS subarray were stored on magnetic tape in the field to allow off-line data processing.

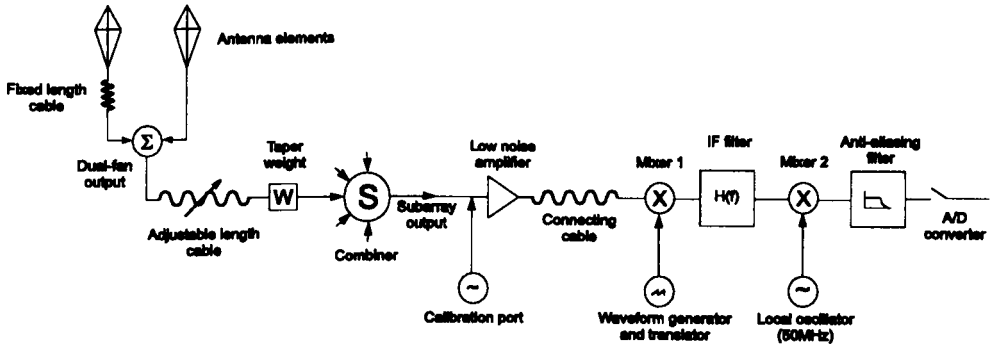

Figure 2.1: Hardware architecture of a reception channel in the Jindalee array

2.2.2 Data collection

The standard technique for observing the mode structure of an ionospheric propagation circuit as a function of operating frequency is that of oblique sounding (Davies 1990). The method used to record oblique incidence ionograms for the current study is quantitatively described by (Earl and Ward 1986) but some essential features are repeated here for convenience.

On the present system, the remote beacon transmits a linear FMCW signal which sweeps over a selectable portion of the HF band at a rate of 100 kHz per second. The signal transmitted by the beacon is received in the main beam of the FMS subarray and is mixed or deramped with a synchronized version of the transmitted signal. After filtering and down-conversion, the instantaneous frequency of the baseband signal corresponding to a particular mode is linearly dependent upon the time-delay or group range associated with the ionospheric path it has taken.

Signal modes which arrive after sufficiently different time-delays are separated into different frequency bins by performing digital spectral analysis (FFT) or range processing on blocks of data acquired during a specified time interval. In the oblique sounder, range processing estimates the power-delay profile of the signals received over successive data segments where each segment is acquired over a time interval of approximately 0.6 seconds. As the emitted signal sweeps at a rate of 100 kHz per second to interrogate different portions of the HF band, the effective bandwidth of digital samples received during a particular data segment is close to 60 kHz which translates to a group range resolution of approximately 5 km for a one way path.

After spectral analysis, a clean-up algorithm is used to remove interference originating from other users in the HF band. The peaks in the resulting range spectra which are above a pre-set threshold are detected for each data segment and displayed as an oblique incidence ionogram with frequency on the horizontal axis and group range or time-delay on the vertical axis. The oblique incidence ionogram pertaining to this study was collected on 1 April 1998 at 06:23 UT. This ionogram is displayed in Figure 2.2 and is discussed in section 2.3.

The experiment involving the main antenna array was conducted immediately prior to

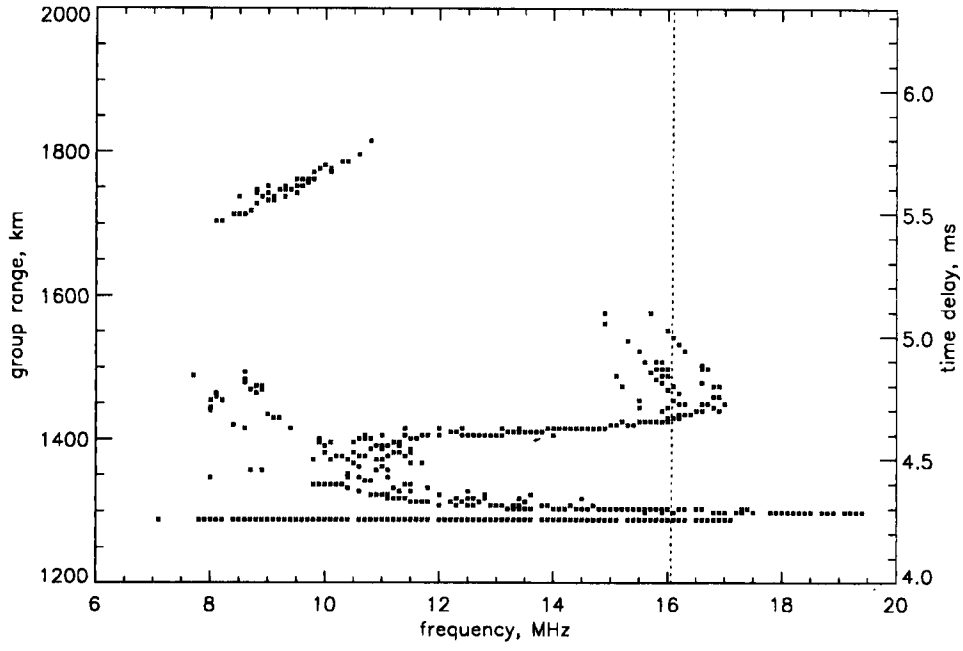

Figure 2.2: Oblique incidence ionogram indicating the mode content for the Darwin to Alice Springs ionospheric circuit as a function of carrier frequency in the HF band on 1 April 1998 at 06:23 UT.

recording the ionogram. In this experiment, the main array was synchronised to receive a narrowband FMCW signal emitted by the beacon in the main lobe of each subarray pattern. The narrowband FMCW signal was linearly swept over a 20 kHz bandwidth at a rate of 60 sweeps per second with a fixed carrier frequency of 16.110 MHz. Clear channel advice from the Jindalee FMS system was used to check that the 20 kHz channel with a centre frequency of 16.110 MHz was free of co-channel interference from other users.

Digital data were recorded by the main array as a sequence of coherent processing intervals (CPI) or "dwells". Each dwell of data is recorded in approximately 4.2 seconds during which a total of 256 phase coherent FMCW sweeps are emitted and received by the system. Adjacent dwells are separated by an inter-dwell gap of about 0.5 seconds to allow tape recording of the acquired digital data. A total of 47 dwells were recorded during the experiment between 06:17 and 06:21 UT on 1 April 1998.

The A/D samples recorded within each FMCW sweep are often referred to as fast-time samples (Griffiths 1996). A total of 320 fast-time samples were collected for each sweep in each receiver, these samples were range processed to form frequency domain samples or range samples. The 20 kHz signal bandwidth yields a group range resolution of 15 km for a one way path, this resolution was traded off to about 20 km in order to control range sidelobes with the Hanning window. The propagation modes of interest appear over a finite coverage in group range so only a portion of the range spectrum needs to be retained for further processing. In this case, a total of 42 range samples covering a range depth of 615 km between 1055 and 1670 km were retained for further processing.

A propagation mode normally appears discrete in group range when the resolution is in the order of 20 km, and quite often, this resolution is sufficiently high to resolve different propagation modes into separate range bins. The ability of the array to isolate signals received from the different propagation modes into different range bins enables the space-time characteristics of these modes to be studied individually. The space-time characteristics of a particular propagation mode can be studied by analysing the data recorded across different receivers and from one sweep to another in the range bin that contains the mode of interest. The temporal sequence of a range sample from one sweep to another are collectively known as slow-time samples (Griffiths 1996), these samples provide information regarding the Doppler characteristics of propagation modes. The slow-time samples recorded by the different receivers within a particular FMCW sweep are collectively referred to as an array snapshot which provides information regarding the spatial characteristics of propagation modes.

The above-mentioned data were collected by exploiting some unique features of the Jindalee receiver array and the oblique sounder system. It is evident from the literature review that the very wide aperture arrays used in previous work on mode fine structure did not have the same characteristics as the Jindalee array. One of these arrays (Rice 1973) was only able to sample the phase of the signal-field while the other (Sweeney 1970) had comparatively fewer antenna elements and receivers to sample the spatial properties of these fields. The data collected by the current system is arguably of the highest quality for the purpose of analysing mode fine structure.

2.3 Preliminary data analysis

A preliminary analysis of the experimental data collected by the oblique sounder and the main antenna array is performed in this section to quantify some important gross and fine structure features of the ionospheric circuit under study. More specifically, data from the oblique sounder is interpreted to determine the number of propagation modes and to identify the ionospheric layers which reflected them. Once the mode content of the HF link has been determined, the power, time-delay, direction of arrival and Doppler shift of each resolved propagation mode are estimated as mean values over the period of data collection.

Variations in the spatial structure of individual signal modes over short time intervals are detected by means of coherence measures to show the existence of mode fine structure. The chosen coherence measures also indicate the degree of departure exhibited by the received mode wavefronts relative to the plane wave model of best fit. Care is taken to distinguish between observations which are potentially caused only by measurement errors and noise with those that are at least partly attributable to physical phenomena occurring in the ionosphere.

2.3.1 Mode content of the HF link

The oblique incidence ionogram shown in Figure 2.2 was recorded by the FMS oblique sounder to determine the mode content of the Darwin-to-Alice Springs ionospheric circuit at 06:23 UT on 1 April 1998. This type of ionogram measures the time delay taken by different ionospheric modes to propagate between the test transmitter and the receiver site as function of operating frequency. The estimate of a mode time-delay is often converted to a distance known as the group path or group range by assuming that the mode travels at the speed of light in free space. Comprehensive information on the measurement and interpretation of oblique incidence ionograms can be found in the texts by (McNamara 1991) and (Davies 1990).

Perhaps the most obvious aspect of the ionogram in Figure 2.2 is that the mode content changes as a function of operating frequency. The gradual variation in the number and group range of the propagation modes with respect to frequency clearly illustrates the dispersive nature of the ionosphere within the HF band. For a narrowband signal, the mode content is estimated as the point(s) of intersection between the ionogram trace and a line drawn vertically at the operating frequency. The ionogram in Figure 2.2 resolves five distinct propagation modes at group ranges of 1290, 1300, 1430, 1475 and 1540 km when the operating frequency is 16.110 MHz. This frequency coincides with that used in the main antenna array experiment.

To identify the ionospheric layers responsible for propagation it is required to calculate the virtual ionospheric height of reflection for each resolved mode. By assuming a spherical earth and specular reflection from a concentric ionospheric layer it is possible to show that the virtual ionospheric height of reflection h_v is given by,

$$h_v = \frac{g_r \sin[d/2r_e + \arcsin(2r_e \sin(d/2r_e)/g_r)]}{2\sin(d/2r_e)} - r_e \tag{2.1}$$

where $r_e = 6270$ km is the Earth's radius, $d = 1265$ km is the ground distance of the path and g_r (km) is the group range of the mode estimated by the ionogram. Using this relationship the virtual heights corresponding to the five resolved propagation modes are calculated as 99, 122, 303, 349 and 408 km respectively.

The lowest reflecting layer with a virtual height of 99 km is identified as mid-latitude sporadic-E. This relatively thin layer which typically has a thickness of approximately 5 km normally forms at altitudes between 90-110 km and is often characterised by a flat trace with respect to frequency in the ionogram. The occurrence of this layer is irregular or sporadic in time and is thought to originate from the concentration of metallic ions produced by burnt out meteors. Amongst other features, the sporadic-E layer is characterised by a relatively high ionisation density that forms into clouds so it often has a patchy nature horizontally (Barnes 1990). Further information regarding the physical makeup and characteristics of sporadic-E as well as other ionospheric layers can be found

in the text by (Davies 1990).

The ionospheric layer with a virtual height of 122 km also exhibits a flat trace with respect to frequency in the ionogram and is therefore identified as a second reflection from possibly the same mid-latitude sporadic-E layer. It is reasonable to ask how two reflections from the same ionospheric layer can arrive with different time-delays or group ranges. A possible explanation is that a signal can be reflected from a point in the ionosphere which is not on the great circle plane defined by the two sites and therefore travels a further distance compared to the signal resolved at a lower group range. This situation may arise in the sporadic-E layer due to a reflection from a different cloud of ionisation which is off the great circle plane.

The remaining modes are propagated by the F-region where reflection may occur from the F1-layer at altitudes between 140-210 km or the F2-layer at heights above 210 km. The layers in the F-region are produced largely by ultra-violet (UV) ionising radiation from the sun with wavelengths ranging very roughly between 17-80 nm (Budden 1985). One aspect of ionospheric propagation that occurs in all regions but is most noticeable in the F-region is the magneto-ionic splitting of a signal into an ordinary (o) ray and an extraordinary (x) ray. In addition, each of these rays can propagate via two different paths known as the high (H) angle and low (L) angle paths. A detailed mathematical treatment of magneto-ionic splitting in the ionosphere is covered in the text by (Budden 1985) while a concise description of the origin of the high and low angle paths can be found in (Davies 1990).

The propagation mode with a group range of 1430 km and a virtual height of 303 km is made up of the ordinary and extraordinary magneto-ionic components in low angle path of the F2-layer. These two magneto-ionic components cannot be resolved by the oblique sounder and their superposition generally produces a resultant wave with elliptical polarisation. The plane of polarisation of the resultant wave rotates when the relative phase path between the two magneto-ionic components changes as a result of motions in the ionosphere. This rotation is known as Faraday rotation and typically manifests itself as deep and quasi-periodic fading of the resultant signal in both the spatial and temporal domain.

The propagation mode with a group range of 1475 km and virtual height of 349 km corresponds to the ordinary magneto-ionic component in the high angle path of the F2-layer. The mode with the largest group range of 1540 km and virtual height of 408 km is the extraordinary magneto-ionic component in the high angle path of the same layer. The ordinary and extraordinary components have counter-rotating polarisations, the polarisation of the ordinary wave rotates clockwise at the operating frequency when viewed in the direction of wave propagation while the extraordinary component rotates anti-clockwise at the same rate. It is noted that the original linearly polarised signal is represented by the superposition of equal amplitude ordinary and extraordinary components with circular polarisations and zero initial phase difference. In the high angle path of the F2-

layer it is evident that the two magneto-ionic components experience markedly different retardations or penetration depths into the ionosphere, this phenomenon which allows the oblique sounder to resolve the components is due to the anisotropic nature of the ionosphere caused by the Earth's magnetic field.

Double-hop modes which involve an intermediate ground reflection or mixed modes which consist of reflections from two or more ionospheric layers have also been observed on this link but were not present at the time of recording at a frequency of 16.110 MHz. Ionospheric modes may be represented in standard notation, as recommended by (Davies 1990), with the one-hop sporadic-E reflection denoted by $1E_s$ and a double-hop reflection written as $2E_s$. The one-hop F2-layer reflection in the low angle path is represented by $1F_2$ while the resolved ordinary and extraordinary magneto-ionic components in the high angle path are referred to by $1F_2(o)$ and $1F_2(\mathrm{x})$ respectively.

2.3.2 Power, angle-of-arrival and Doppler shift

The mean signal-to-noise ratio of each resolved mode over the period of data collection is estimated from the power-delay profile shown in Figure 2.3. This power-delay profile was calculated by averaging the range power spectra recorded in 30 receivers and 256 PRI of each dwell over the entire data set consisting of 47 dwells. In other words, the range power spectrum shown in Figure 2.3 represents an average of $256 \times 30 \times 47$ different realisations. It is noted that 30 of the 32 available reception channels were analysed for this data as two adjacent reception channels at one end of the array were not properly calibrated.

The locations of the peaks in the power-delay profile are consistent with the group ranges of the modes resolved by the oblique sounder. The four peaks in Figure 2.3 appear at group ranges of 1290, 1435, 1480 and 1540 km, as compared to the five modes resolved at group ranges of 1290, 1300, 1430, 1475 and 1540 km by the ionogram. The group range resolution of the power-delay profile measured by the main array is in the order of 20 km which is not high enough to resolve the two sporadic-E reflections at group ranges of 1290 and 1300 km. The remaining modes which are propagated via the F-region have been resolved by the main array and appear discrete in group range. The discrete character of this power-delay profile indicates that the group ranges of all modes do not change by more than the group range resolution of the main array (20 km) throughout the data collection period (4 minutes). The mean SNR corresponding to mode(s) represented by each peak of the power-delay profile is estimated as the ratio between the magnitude of the peak and the background noise level which is estimated from the flat portion of the spectrum in the vicinity of range cell number seven. In ascending order of group-range, the propagation modes have SNR's of approximately 34.5, 40.5, 34.0 and 20.0 dB.

The gross structure of the mode wavefields sampled by the main array is illustrated for a particular dwell by two dimensional (space-time) intensity modulated displays in

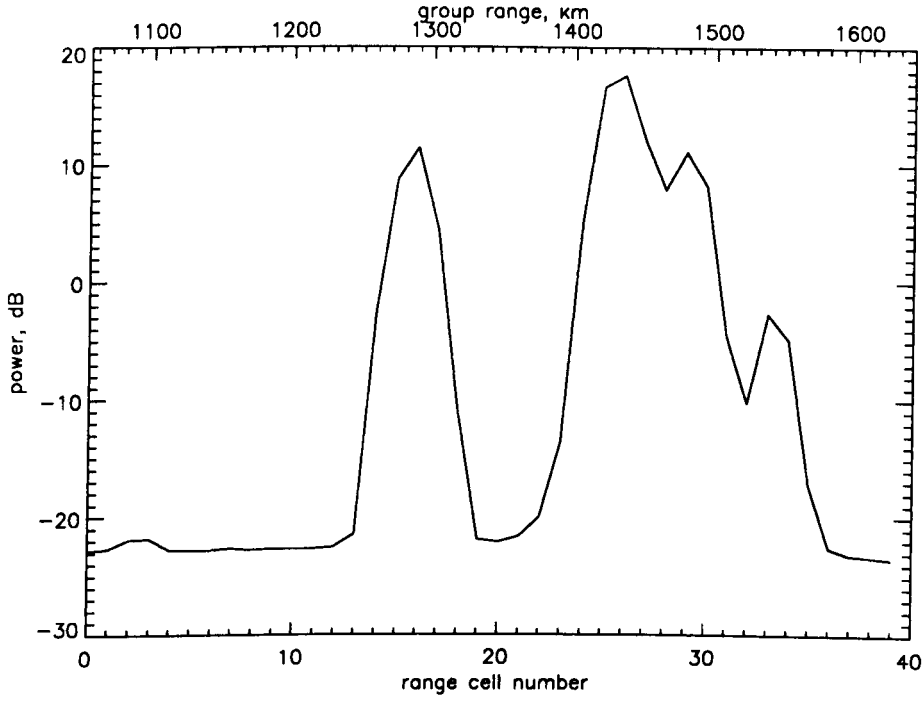

Figure 2.3: Average power-delay profile (range power spectrum) recorded for the Darwin-to-Alice Springs ionospheric link by the main array at f_c=16.110 MHz on 1 April 1998 between 06:17 and 06:21 UT

Figures 2.4 to 2.7. These displays illustrate the real component of the complex-valued mode wavefield received in the range cells corresponding to a peak in the power-delay profile. Each display consists of 256 consecutive array snapshots recorded by 30 receivers during a coherent processing interval of approximately 4.2 seconds.

The highly non-planar wavefronts observed in Figure 2.4 are expected because the wavefield in this range cell results from a superposition of unresolved sporadic-E modes which most likely have different directions-of-arrival. In addition, each sporadic-E mode may be contaminated by ionospherically-induced distortions over this time interval such as the phase fluctuations observed by Abramovich, Anderson, Frazer and Solomon (1995). Wavefronts which are much more planar are observed for the $1F_2$ mode in Figure 2.5 where the real component of the wavefield resembles a two-dimensional sinusoid. The spatial frequency of the sinusoid is related to the cone angle-of-arrival of the mode with respect to the sub-array steer direction whereas the temporal frequency is related to the Doppler shift imparted by the ionosphere. Figures 2.6 and 2.7 display the real wavefields of the $1F_2(o)$ and $1F_2(x)$ magneto-ionic components respectively. While the $1F_2(o)$ mode exhibits relatively planar wavefronts it is apparent that the ionospheric reflection process has distorted the wavefronts of the $1F_2(x)$ mode. Moreover, such distortions can be attributed to the presence of irregularities in the ionosphere because a single magneto-ionic component (i.e., the extraordinary ray of the F_2-layer high angle path) has been isolated for study and is not contaminated by other components which are theoretically expected for a smooth ionospheric layer.

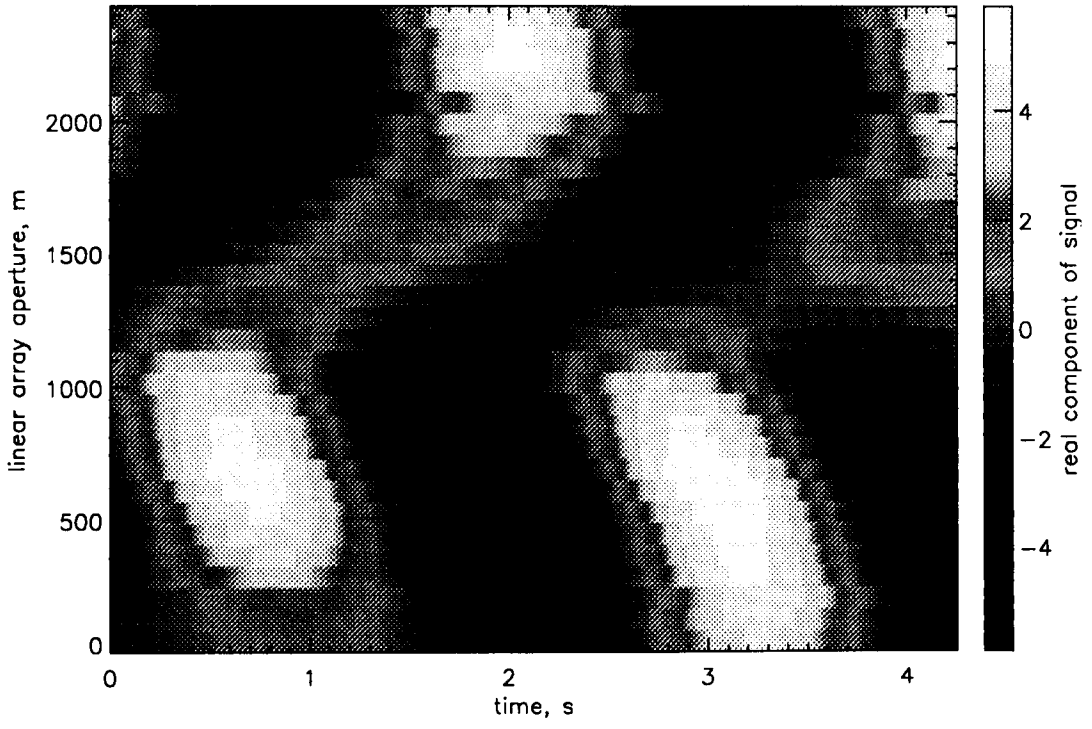

Figure 2.4: Real component of the $1E_s$ mode signal-field sampled in space and time by the main array (range cell $k = 16$)

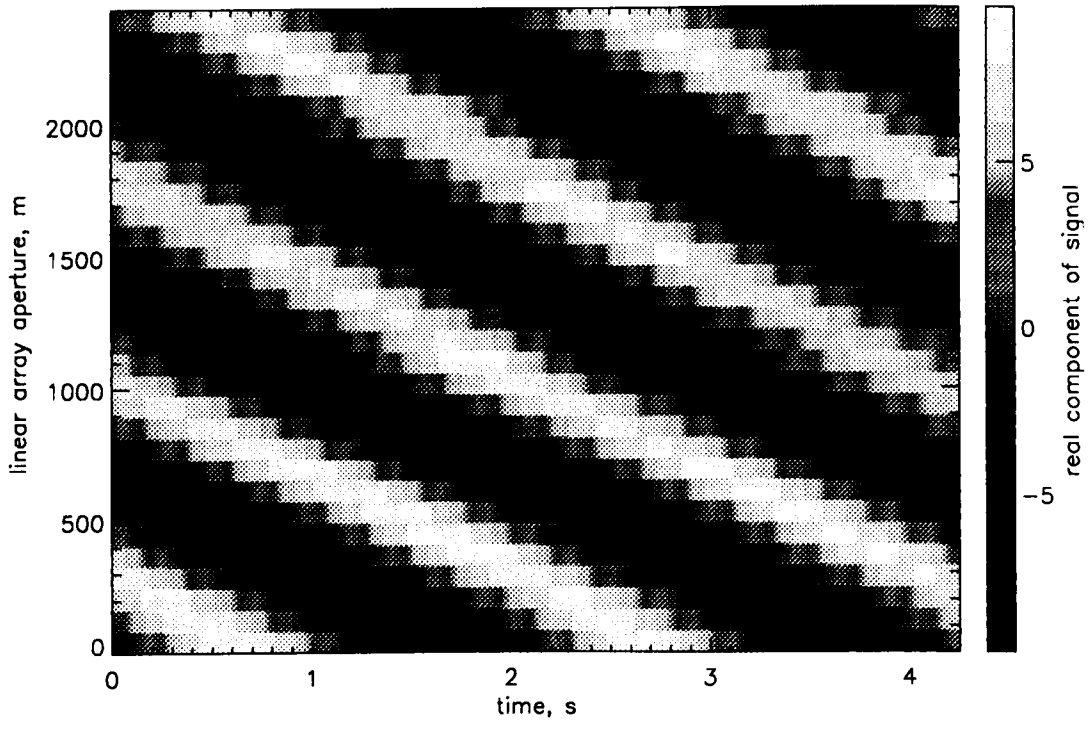

Figure 2.5: Real component of the $1F_2$ mode signal-field samples in space and time by the main array (range cell $k = 26$)

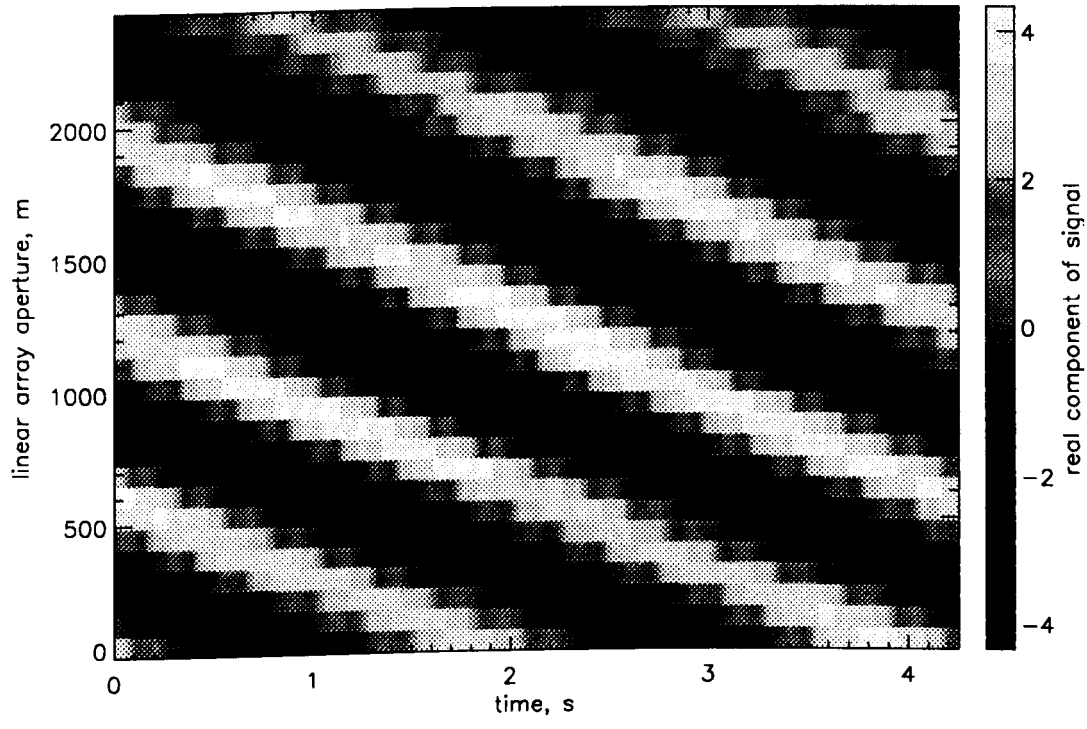

Figure 2.6: Real component of the $1F_2(o)$ mode signal-field sampled in space and time by the main array (range cell $k = 29$)

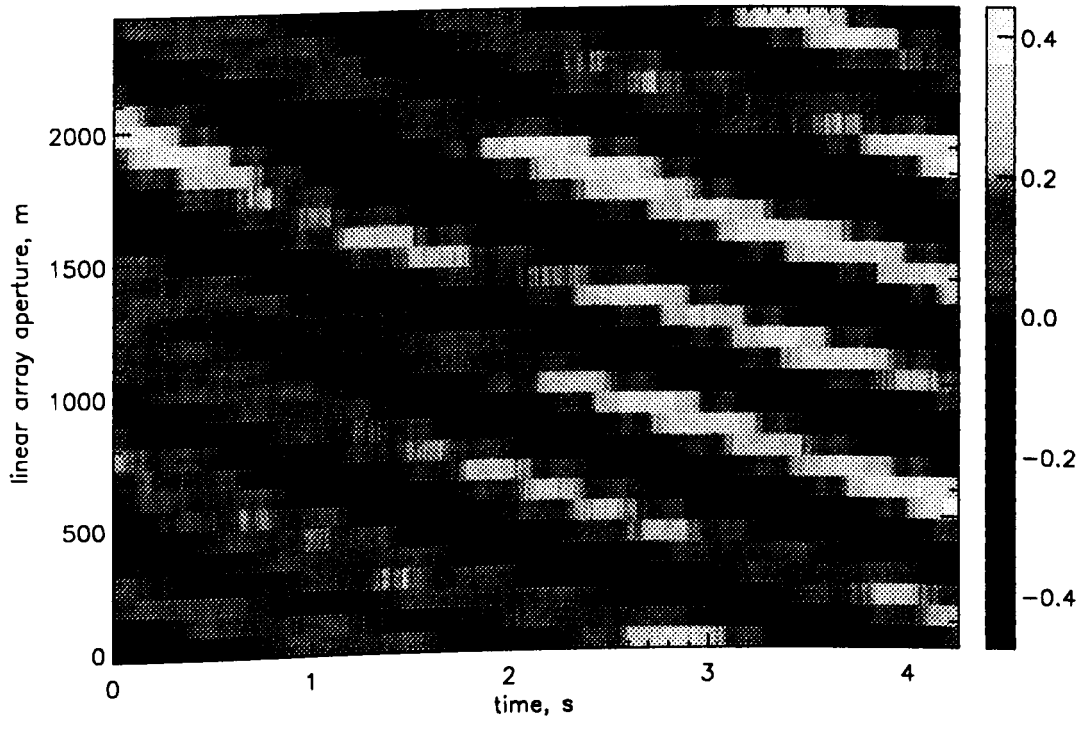

Figure 2.7: Real component of the $1F_2(x)$ mode signal-field samples in space and time by the main array (range cell $k = 33$)

The mean cone angle-of-arrival and Doppler shift of the propagation modes can be estimated from the array data by using conventional beamforming and Doppler processing methods. For a given range cell (k), the angular power spectrum $p_x(k,\theta)$ and Doppler power spectrum $p_y(k,\Delta f)$ are derived from the spatial and temporal sample covariance matrices of the data respectively. It should be noted that the angular spectrum is in terms of the cone angle-of-arrival while the Doppler spectrum relates to temporal variations in the phase path of a particular mode caused by movements of the effective ionospheric reflection point.

The unbiased sample spatial covariance matrix estimated for the k^{th} range cell in a particular dwell or coherent processing interval (CPI) is denoted by $\hat{\mathbf{R}}_x(k)$ and is given by,

$$\hat{\mathbf{R}}_x(k) = \frac{1}{P}\sum_{t=1}^{P} \mathbf{x}_k(t)\mathbf{x}_k^H(t) \tag{2.2}$$

where $P = 256$ is the number of PRI averaged over a CPI of 4.2 seconds, H denotes the Hermitian operator (conjugate transpose) and $\mathbf{x}_k(t)$ is the $N = 30$ dimensional array snapshot vector recorded at the k^{th} range cell and t^{th} PRI. The sample spatial covariance matrices computed in different dwells are then averaged together to form a sample spatial covariance matrix $\bar{\mathbf{R}}_x(k)$ which contains the mean spatial second order statistics of the data in the k^{th} range cell over the data collection interval ($\approx$ 4 minutes). The mean angular power spectrum $p_x(k,\theta)$ is then computed as,

$$p_x(k,\theta) = \frac{\mathbf{s}^H(\theta)\bar{\mathbf{R}}_x(k)\mathbf{s}(\theta)}{N^2}\ ,\ \mathbf{s}(\theta) = [1\ e^{j2\pi\Delta d\sin\theta/\lambda}\cdots e^{j2\pi(N-1)\Delta d\sin\theta/\lambda}]^T \tag{2.3}$$

where $\mathbf{s}(\theta)$ is the N-dimensional array steering vector for a cone angle θ. To determine the mean Doppler spectrum let the D-dimensional complex vector $\mathbf{y}_k(n,t,\Delta t)$ contain the slow-time samples recorded in the n^{th} receiver and the k^{th} range cell starting at the t^{th} PRI with consecutive samples being spaced by Δt PRI. This vector can be written as,

$$\mathbf{y}_k(n,t,\Delta t) = [\mathbf{x}_k^{[n]}(t)\ \mathbf{x}_k^{[n]}(t+\Delta t)\cdots\mathbf{x}_k^{[n]}(t+(D-1)\Delta t)]^T \tag{2.4}$$

where $\mathbf{x}_k^{[n]}(t)$ is the output of the n^{th} receiver at the k^{th} range cell and t^{th} PRI. The temporal sample covariance matrix estimated for the k^{th} range cell in a particular dwell is denoted by $\hat{\mathbf{R}}_y(k)$ and is given by,

$$\hat{\mathbf{R}}_y(k) = \frac{1}{N(P-D\Delta t+1)}\sum_{n=1}^{N}\sum_{t=1}^{P-D\Delta t+1} \mathbf{y}_k(n,t,\Delta t)\mathbf{y}_k^H(n,t,\Delta t) \tag{2.5}$$

where the temporal snapshots have been averaged in sliding window fashion within a receiver over slow time (t) and then across the different receivers (n). Note that the

sliding window average makes use of all samples in the dwell whereas the non-overlapped average results in the samples spaced by less than Δt PRI being missed. As before, these matrices are averaged over different dwells to form the mean sample temporal covariance matrix $\bar{\mathbf{R}}_y(k)$ which is used to evaluate the mean Doppler power spectrum $p_y(k, \Delta f)$ as,

$$p_y(k, \Delta f) = \frac{\mathbf{v}^H(\Delta f)\bar{\mathbf{R}}_y(k)\mathbf{v}(\Delta f)}{D^2}, \quad \mathbf{v}(\Delta f) = [1 \; e^{j2\pi\Delta f/f_p'} \ldots e^{j2\pi(D-1)\Delta f/f_p'}]^T \tag{2.6}$$

where the D-dimensional vector $\mathbf{v}(\Delta f)$ is the complex frequency phasor corresponding to a Doppler shift of Δf Hz observed with an effective pulse repetition frequency of $f_p' = f_p/\Delta t$ Hz ($f_p = 60$ Hz).

Figures 2.8 to 2.11 show the angular and Doppler power spectra resulting in the range cells containing the signal modes ($k = 16, 26, 29, 33$) when the parameters $N = 30$, $P = 256$, $D = 30$, $\Delta t = 6$ were used and 47 dwells of data were averaged. The mean cone angle-of-arrival and Doppler shift of the signal received in each range cell are estimated as the location of the maxima in the corresponding angular and Doppler power spectra respectively, these estimates and are listed in Table 2.1.

Mode	g_r, km	h_v, km	SNR, dB	Δf, Hz	θ, deg
$1E_s$	1290	99	34.5	0.42	21.9
$1F_2$	1430	122	40.5	0.44	20.8
$1F_2(o)$	1475	304	34.0	0.46	20.5
$1F_2(x)$	1540	409	20.0	0.53	19.9

Table 2.1: Parameters describing the gross structure of the Darwin-to Alice Springs HF link on 1 April 1998 between 06:17-06:21 UT

If the signal received in each range cell containing a signal mode were a monochromatic plane wave, as would be the case for specular ionospheric reflection, the global maxima of the angular and Doppler power spectra are expected to be the same when the contribution due to additive noise can be neglected. Under such conditions, the value of the maximum coincides with that of the corresponding peak in the power-delay profile and the sidelobe structure of both spectra would appear undisturbed. To some extent, this description seems to fit the characteristics of the spectra plotted for the $1F_2$ and $1F_2(o)$ modes in Figures 2.9 and 2.10 respectively.

However, this description does not accurately portray the characteristics of the spectra plotted in Figures 2.8 and 2.11 which correspond to the $1E_s$ and $1F_2(x)$ modes respectively. In the case of Figure 2.8 the observed discrepancy is thought to arise mainly due to the superposition of two sporadic-E modes which have very similar Doppler shifts but different angles-of-arrival. It is worth noting that the two sporadic-E modes are almost but not completely resolved in angle-of-arrival by the classical beamformer. In the case of Figure 2.11, the irregular sidelobes and lower maximum of the angular power spectrum is attributable to the significant non-planarity and temporal variability of the received

wavefronts caused by the movement of ionospheric irregularities in the vicinity of the $1F_2(x)$ mode reflection region during the period of data collection.

2.3.3 Fine structure of ionospheric modes

Experimental measurements made by (Rice 1976) and (Sweeney 1970) on a very wide aperture array indicate that a mode wavefront can often be regarded as having a more or less planar large-scale structure with some degree of amplitude and phase corrugations superimposed. These corrugations may be viewed as the spatial modulation imparted by the ionosphere on the underlying planar wavefront which would have resulted in the case of specular reflection.

Neither of the two above-mentioned analyses explicitly studied the time-evolution of the complex-valued mode wavefronts over time intervals comparable with the coherent integration time of OTH radar. Moreover, the signal bandwidths and PRI used in both analyses (approximately 100 kHz and 1 second respectively) are quite different to those typically used in OTH radar applications (less than 20 kHz and approximately 0.02 seconds respectively).

A very wide aperture array analysis of the complex-valued mode wavefronts measured with a PRI of less than 0.02 seconds over CPI in the order of a few seconds has not been carried out previously and is the subject of the current investigation on fine structure. The principle objective is to detect and quantify variations in the spatial structure of a mode wavefront where the term "spatial structure" refers to the gain and phase relationship between the receiver outputs rather than their absolute value. A measure of the variation in spatial structure with respect to time should ideally be independent of time-invariant gain and phase mismatches between the receivers as well as temporal modulations which give rise to the mean Doppler shift and Doppler spread.

A quantitative measure of the similarity between the spatial structure of two complex array snapshots recorded in the k^{th} range cell at PRI t and $t + \Delta t$ can be defined as the following magnitude squared coherence (MSC) function.

$$\xi_k(\Delta t) = \frac{|\mathbf{x}_k^H(t)\mathbf{x}_k(t+\Delta t)|^2}{\mathbf{x}_k^H(t)\mathbf{x}_k(t)\ \ \mathbf{x}_k^H(t+\Delta t)\mathbf{x}_k(t+\Delta t)} \quad , \quad 0 \leq \xi_k(\Delta t) \leq 1 \tag{2.7}$$

The MSC is unity when the snapshots $\mathbf{x}_k(t)$ and $\mathbf{x}_k(t+\Delta t)$ are related by a complex scalar (i.e., have the same spatial structure) and is zero when the two snapshots are orthogonal. A value between these two extremes indicates the degree to which the spatial structure of the complex snapshot has changed over Δt PRI which translates to a time interval of $\tau = \Delta t / f_p$ seconds ($f_p = 60$ Hz). Unlike the RMS phase deviation measure used by (Rice 1976), the MSC takes both the amplitude and phase of the mode wavefronts into account and the condition of unit MSC is not influenced by time-invariant array manifold errors or the temporal phase rotation introduced by the Doppler shift.

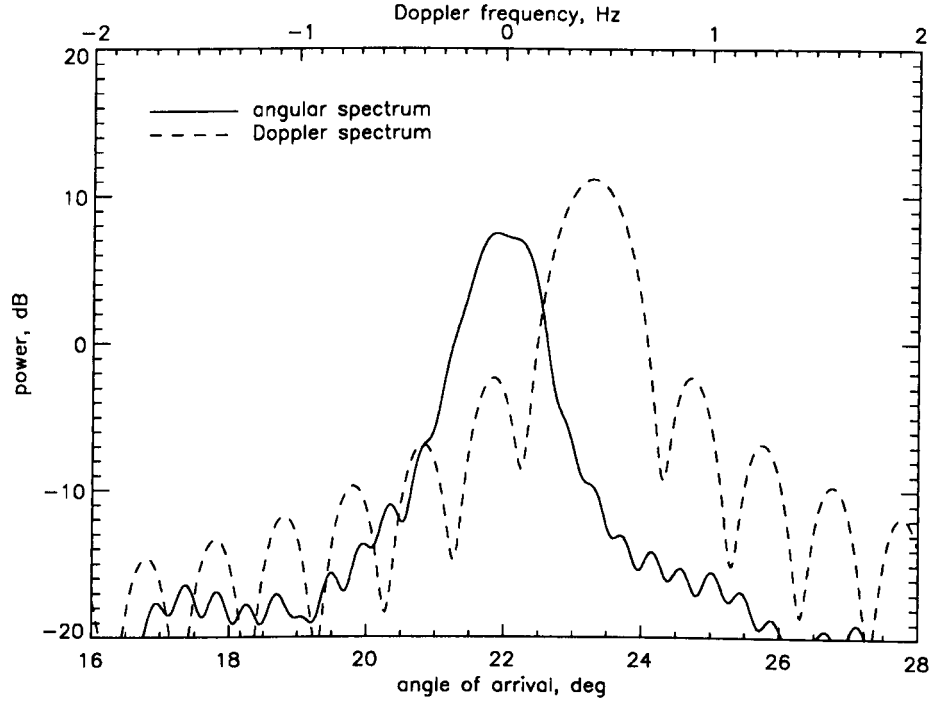

Figure 2.8: Conventional Doppler and Angle-of-Arrival spectrum for the $1E_s$ mode

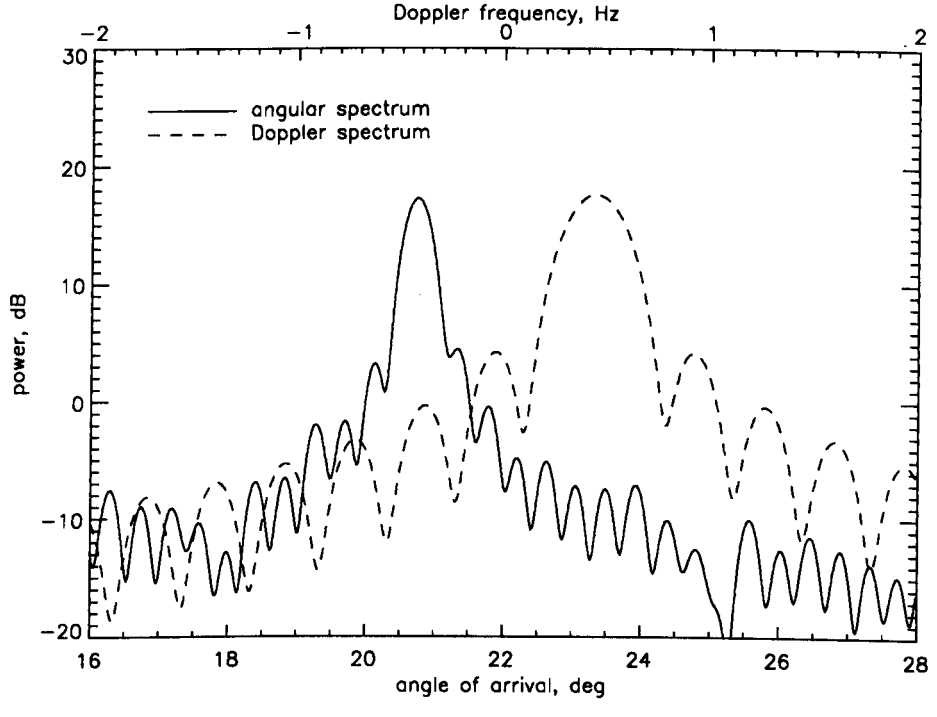

Figure 2.9: Conventional Doppler and Angle-of-Arrival spectrum for the $1F_2$ mode

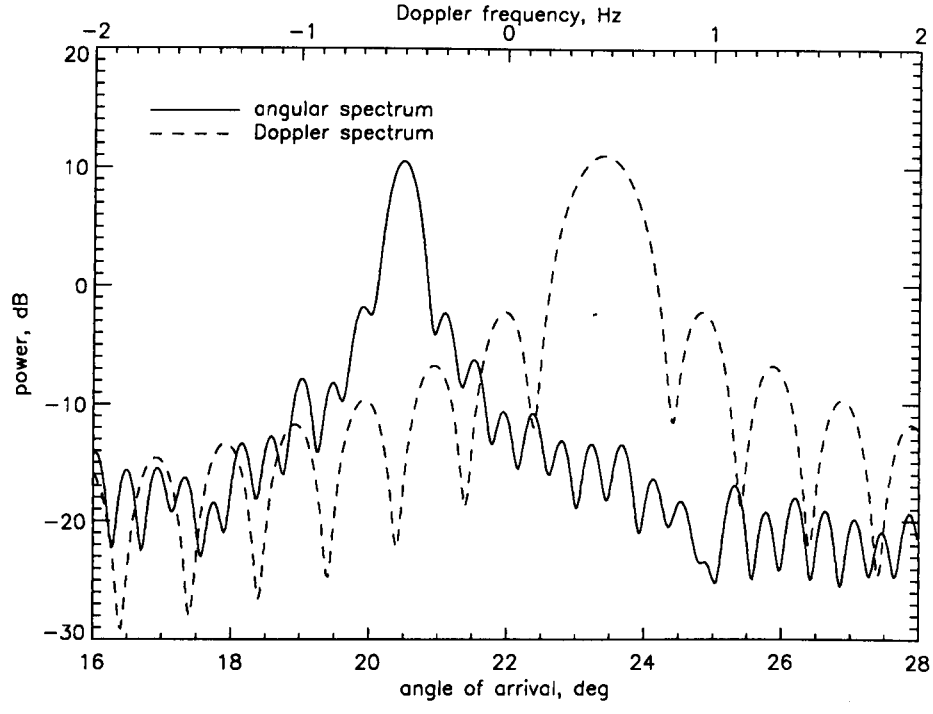

Figure 2.10: Conventional Doppler and Angle-of-Arrival spectrum for the $1F_2(o)$ mode

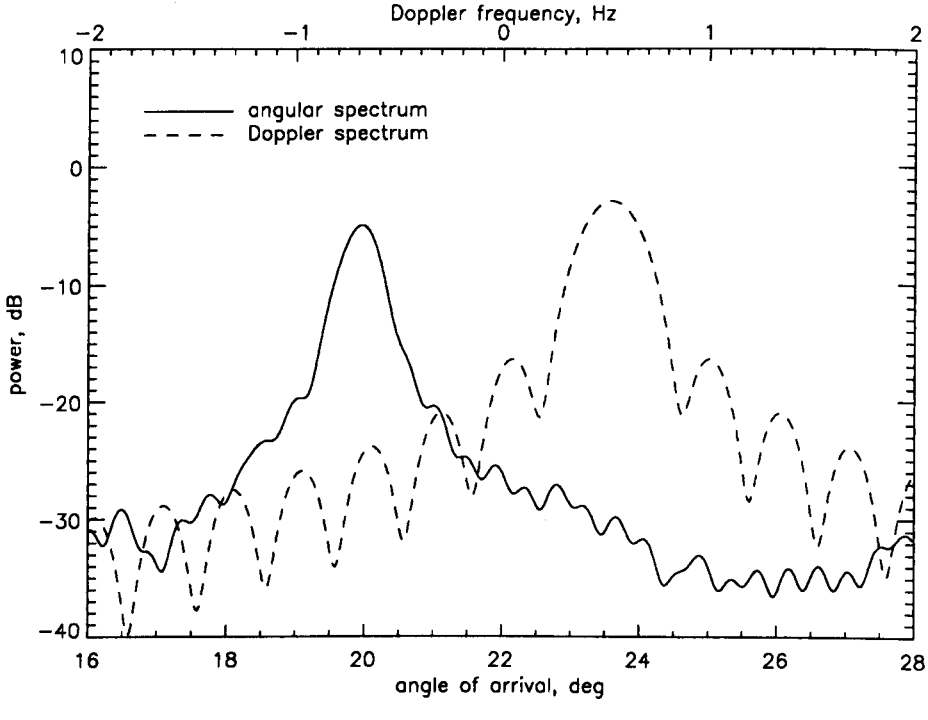

Figure 2.11: Conventional Doppler and Angle-of-Arrival spectrum for the $1F_2(x)$ mode

Figures 2.12 to 2.15 show the cumulative distributions of the MSC values evaluated for different modes and time intervals τ. These distributions were obtained by evaluating MSC for all pairs of array snapshots separated by $\tau = \Delta t/f_p$ seconds in 47 dwells of data with each dwell containing $P = 256$ snapshots. The minimum temporal separation of $\tau = 1/60$ seconds is represented by curve 1 in these figures and may be regarded as a quasi-instantaneous measure of the MSC, the MSC distributions at longer temporal separations of 1, 2 and 3 seconds are represented by curves 2, 3 and 4 respectively.

A comparison of the different curves in each figure clearly demonstrates that the MSC is highly dependent on temporal separation. If the spatial structure of each mode were time-invariant over such intervals the MSC distributions would not depend on the temporal separation. The significantly lower MSC values observed as the temporal separation increases suggests that the spatial structure of the received snapshots changes appreciably over time intervals as short as one second.

For example, 99 percent of the MSC values evaluated for the $1F_2(o)$ mode lie above 0.95 at the minimum temporal separation (curve 1 in Figure 2.14). For the same mode and data set, approximately 70 percent of the MSC values lie below 0.95 when the temporal separation is increased to 3 seconds (curve 4 in Figure 2.14). On the basis of this result, one may be 99 percent confident that 70 percent of the array snapshots separated by a time interval of $\tau = 3$ seconds do not exhibit the same similarity in spatial structure as those separated by a quasi-instantaneous interval of $\tau = 1/60$ seconds.

These results demonstrate that for very short temporal separations the mode wavefronts remain essentially the same but as the temporal separation increases from a fraction of a second to a few seconds the dissimilarity between the mode wavefronts gradually increases. Although these figures quantitatively measure changes in the spatial structure of the received wavefronts with respect to temporal separation they provide no information regarding the nature of these changes. It is useful to understand whether such changes are caused by shifts in the mean angle-of-arrival of the wavefront or whether they primarily arise due to variations in the amplitude and phase corrugations.

An alternative MSC function, formulated in Eqn.(2.8), investigates the temporal behaviour of the plane wave which best fits the received signal wavefronts and the degree of planarity exhibited by these wavefronts.

$$\rho_k(t,\theta) = \frac{|\mathbf{s}^H(\theta)\mathbf{x}_k(t)|^2}{\mathbf{s}^H(\theta)\mathbf{s}(\theta)\ \mathbf{x}_k^H(t)\mathbf{x}_k(t)} \quad , \quad 0 \leq \rho_k(t,\theta) \leq 1 \tag{2.8}$$

The value of θ which maximises $\rho_k(t,\theta)$ at time t is denoted by θ_{max} and represents the angle-of-arrival of the plane wave which best fits the array snapshot $\mathbf{x}_k(t)$ in a least squares sense. The maximum value $\rho_k(t,\theta_{max})$ is a measure of the goodness of fit between the array snapshot $\mathbf{x}_k(t)$ and the *best fitting plane wave*, in simple terms this measure indicates the size of the amplitude and phase crinkle on the wavefront. Note that $\rho_k(t,\theta_{max})$ is the same as the peak output of the normalised conventional beamformer at time t. A value

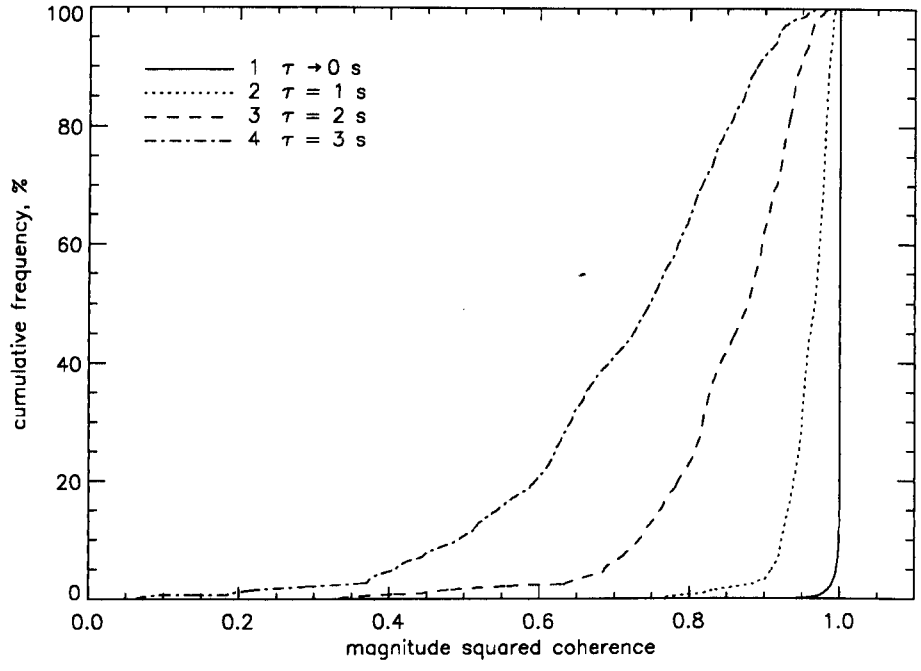

Figure 2.12: Cumulative distribution of the MSC for the $1E_s$ mode

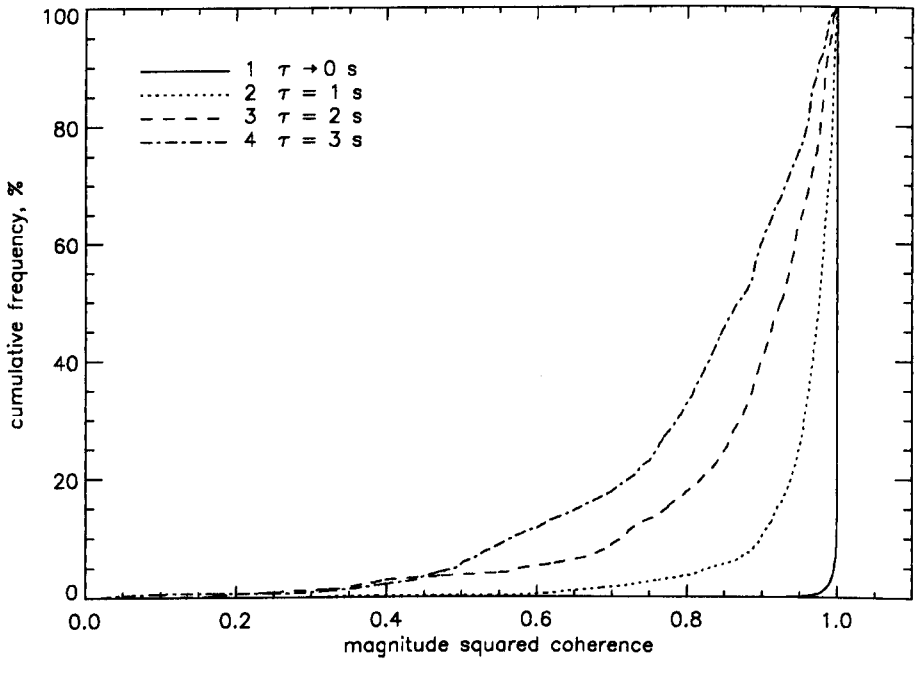

Figure 2.13: Cumulative distribution of the MSC for the $1F_2$ mode

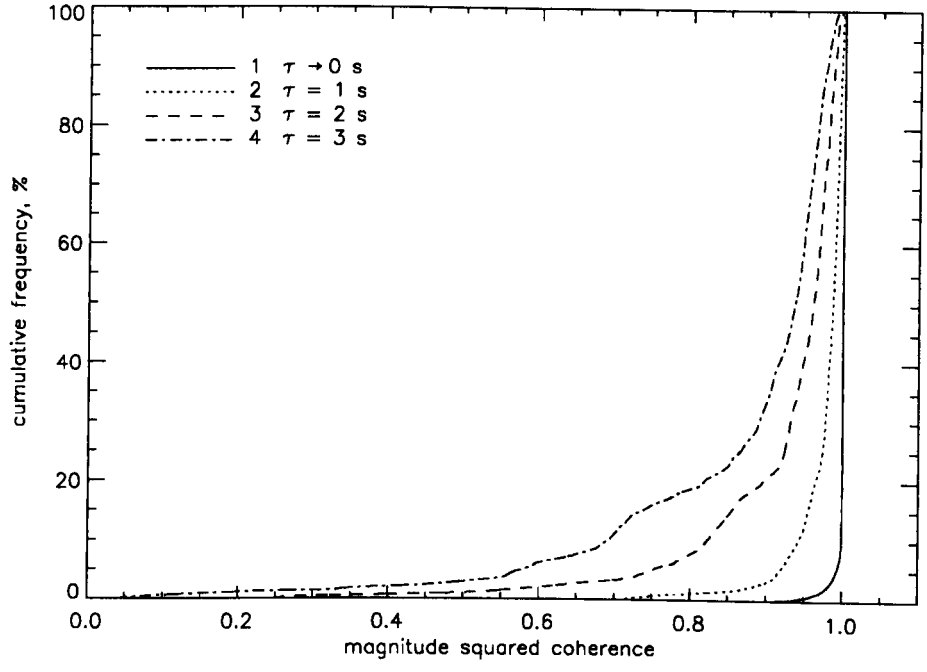

Figure 2.14: Cumulative distribution of the MSC for the $1F_2(o)$ mode

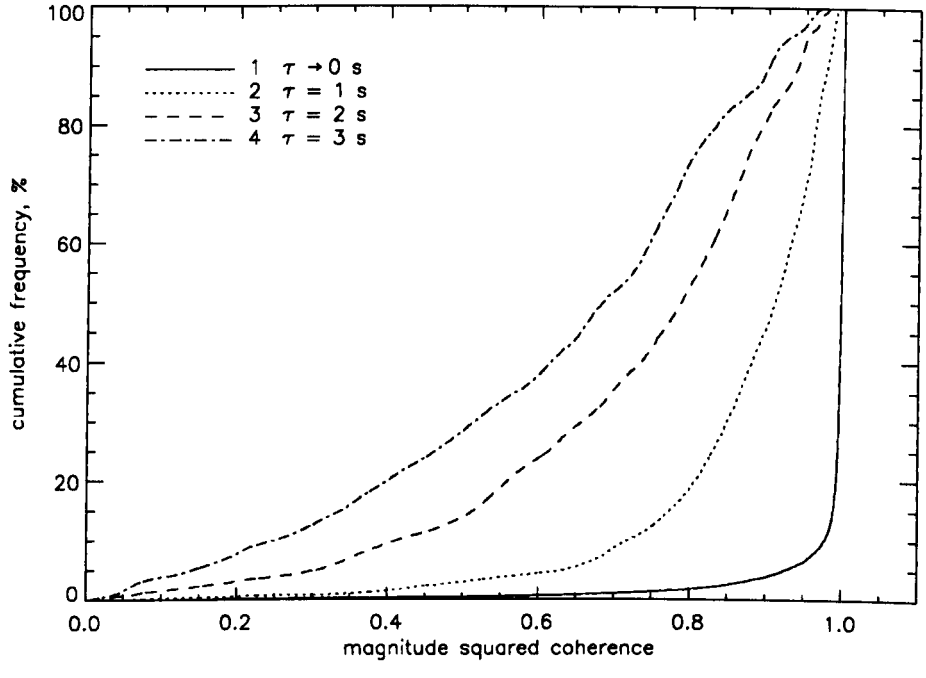

Figure 2.15: Cumulative distribution of the MSC for the $1F_2(x)$ mode

near unity indicates an almost planar wavefront while lower values indicate the degree of departure from a planar wavefront.

The quantities θ_{max} and $\rho_k(t, \theta_{max})$ are evaluated for each mode and plotted in Figures 2.16 to 2.19 as a function of slow time t. A sequence of four dwells (recorded with an inter-dwell gap of approximately 0.5 seconds) is shown to illustrate the temporal behaviour of these quantities over times scales beyond typical OTH radar CPI. The scales are different on these figures in order to clearly show the variation of the above-mentioned quantities for each mode.

With the exception of Figure 2.16, which corresponds to the unresolved sporadic-E modes, the value of $\rho_k(t, \theta_{max})$ is reasonably close to unity which supports the view of essentially planar wavefronts. It is noted that the plane waves which best fit the mode wavefronts remain relatively constant in angle-of-arrival over intervals in the order of a few seconds. It is also apparent that the degree of fit between these plane waves and the received snapshots fluctuates smoothly over time. This indicates that the amplitude and phase modulations imparted on the plane wave of best fit change gradually or in a correlated manner when observed at a temporal resolution of 1/60 seconds (i.e., from one PRI to another).

The value of $\rho_k(t, \theta_{max})$ is expected to be less than unity even if the external signal is a perfect plane wave as a result of additive noise and the potential presence of array manifold errors. Variations due to additive noise are random in nature and superimpose on the smoother variations caused by the physical processes evolving in the ionosphere, this superposition is most evident in the Figure 2.19 which corresponds to the mode with lowest signal-to-noise ratio and is hardly noticeable in the other figures. Array manifold errors are assumed to be fixed over such time intervals so the smooth variations in $\rho_k(t, \theta_{max})$ are attributable to spatial distortions induced by the ionospheric reflection process on each mode. The precise form of the variations in $\rho_k(t, \theta_{max})$ differ substantially from one mode to another, this qualitatively indicates that the spatial distortions induced on a signal mode reflected from a particular ionospheric region is not so dependent on those induced by other regions.

The collection of results on fine structure presented in this section confirm the view that a mode wavefront can be pictured as having an essentially planar spatial structure with some degree of amplitude and phase corrugations superimposed. More importantly, the analysis undertaken in this section has yielded additional information regarding the time-evolution of these wavefronts recorded over time intervals commensurate with the typical OTH radar CPI. The experimental results suggest that the underlying planar wavefront of a mode does not vary significantly over time intervals in the order of a few seconds whereas the size and shape of the wavefront corrugations evolve in a smooth or correlated manner. This leads to the interpretation that the ionospheric reflection process induces changing amplitude and phase distortions about a mean plane wavefront which become progressively de-correlated from each other over time.

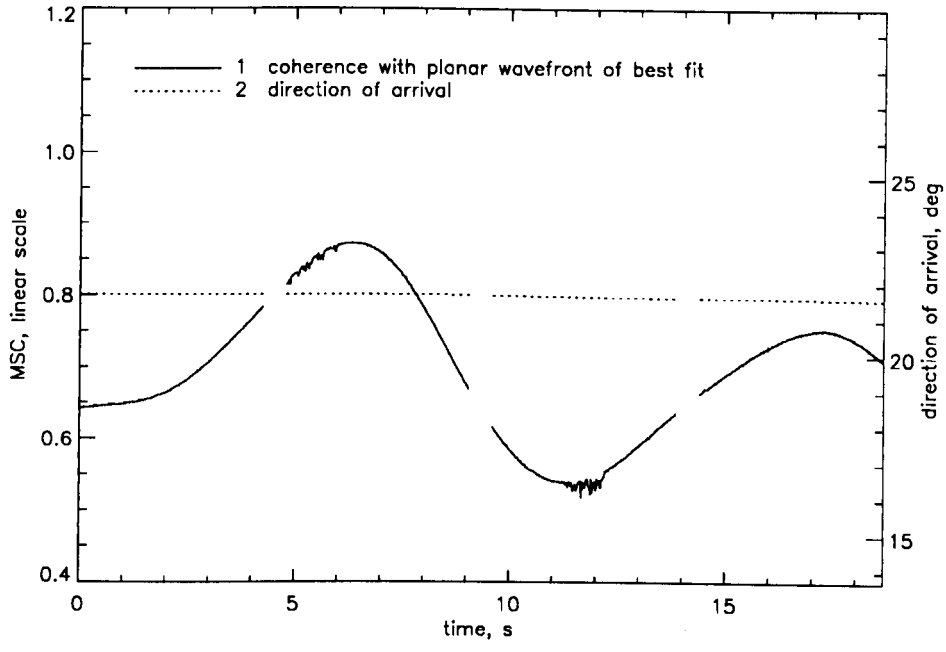

Figure 2.16: Analysis of planarity for the array snapshot $\mathbf{x}_k(t)$ containing the $1E_s$ mode ($k = 16$)

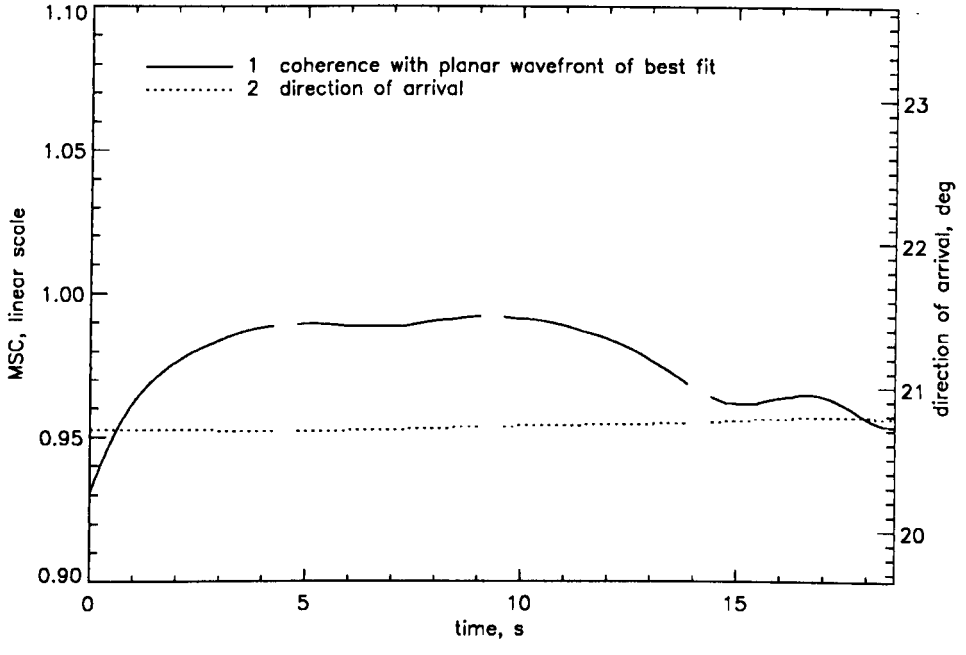

Figure 2.17: Analysis of planarity for the array snapshot $\mathbf{x}_k(t)$ containing the $1F_2$ mode ($k = 26$)

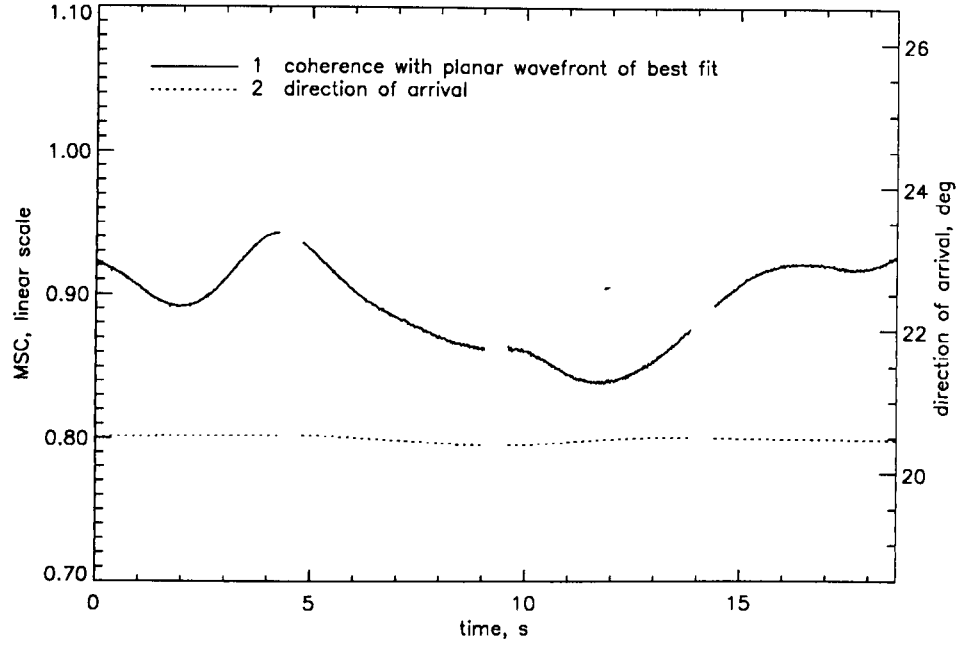

Figure 2.18: Analysis of planarity for the array snapshot $\mathbf{x}_k(t)$ containing the $1F_2(o)$ mode ($k = 29$)

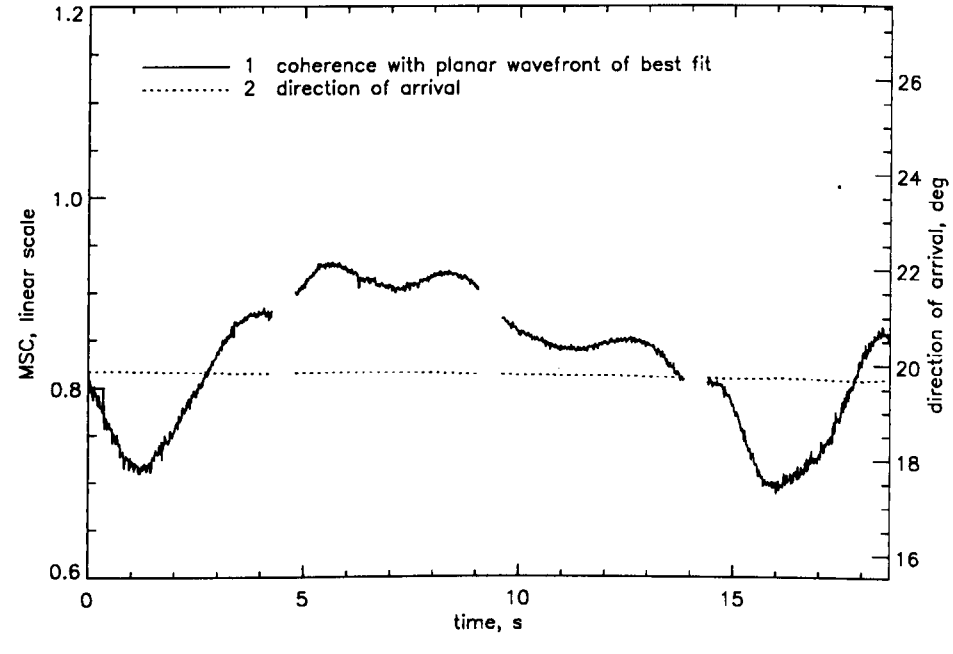

Figure 2.19: Analysis of planarity for the array snapshot $\mathbf{x}_k(t)$ containing the $1F_2(x)$ mode ($k = 33$)

2.4 Multi-sensor HF signal model

The purpose of this section is to derive a wave interference signal model which, under standard assumptions and approximations, mathematically describes the complex envelope of the digital signal-field samples recorded by the main array in the experiment. A mathematical model which represents the gross structure of the signal-field received over typical OTH radar CPI is developed first. This space-time model assumes specular reflection from each ionospheric layer and represents the complex envelope of the raw (unprocessed) digital signal-field samples acquired by the main array. The range formed version of this signal processing model is then derived and extended to incorporate mode fine structure.

2.4.1 Raw data model

The model in this section is derived by assuming that the ionospheric reflection process which gives rise to each propagation mode is specular. In addition, the effects of instrumental and site errors are neglected in order to derive a space-time model which represents the digital signal-field samples acquired by an ideal antenna array. Imperfections such as mutual coupling, sensor position errors, non-identical sensor radiation patterns and improperly calibrated receivers can subsequently be incorporated into the model if required.

The complex envelope of the digital space-time samples received due to the m^{th} propagation mode is modeled as,

$$g_m(l,t,n) = A_m \exp\left(j2\pi\{\Delta u_m l T_s + \Delta f_m t/f_p\} + j\{\boldsymbol{k}_m \cdot \boldsymbol{r}_n + \gamma(\tau_m)\}\right) \qquad (2.9)$$

where $g_m(l,t,n)$ for $m = 1,2,..,M$ represents the ionospherically-reflected FMCW mode wavefield digitised at the l^{th} fast-time sample and t^{th} PRI in the n^{th} receiver of the main array after the deramping and filtering stages described in section 2.2.1. The physical significance associated with each term in Eqn.(2.9) is explained below and justification is provided for any approximation made in the derivation of this model.

The fast-time digital samples acquired during a pulse repetition interval (PRI) are indexed by the integer $l = 0,2,..,L-1$ ($L = 320$) and correspond to the raw A/D samples *prior* to range processing. To distinguish between fast-time samples recorded in different PRI the integer $t = 0,2,..,P-1$ ($P = 256$) is used to index the particular PRI within the coherent processing interval (CPI). The indices l and t are used to reference the digital samples collected in the temporal domain whereas the index $n = 0,2,..,N-1$ ($N = 32$) relates to the spatial domain and is used to identify the particular receiver within the array.

The terms T_s, f_p and τ_m respectively denote the fast-time sampling period in seconds, the pulse repetition frequency (PRF) in Hertz and the time-delay taken by the m^{th} signal mode to travel from the transmitter to the reference receiver in the array at the beginning

of the CPI ($l = 0, t = 0$). A convenient choice for the reference receiver is the first one ($n = 0$) which is taken to be the leftmost receiver of the main array when observed in the boresight direction. The parameters for the experiment were $T_s = 52$ microseconds and $f_p = 60$ Hz, the time-delay τ_m taken by a single-hop mode to propagate over the ground distance of 1265 km typically ranges between $4 - 6$ milliseconds.

Within the PRI, the frequency of a deramped and filtered FMCW signal mode is proportional to the time delay associated with the ionospheric path traveled by the mode. This frequency is denoted by Δu_m and is given by,

$$\Delta u_m = \frac{f_b \tau_m}{LT_s} \tag{2.10}$$

where $f_b = 20$ kHz is the FMCW sweep bandwidth and $LT_s = 1/f_p$ is the duration of the PRI in seconds. This group-range dependent frequency manifests itself as a regular phase progression on the complex envelope of the fast-time samples recorded for a particular mode within each sweep. In Eqn.(2.9), this regular phase progression is represented by the term $e^{j2\pi\Delta u_m l T_s}$.

A smooth ionospheric layer may exhibit regular motion with respect to time which imposes a Doppler shift on the reflected mode. The Doppler shift imposed by the regular motion of the ionosphere on the m^{th} mode is denoted by Δf_m and is given by,

$$\Delta f_m = \frac{2 v_m f_c}{c} \tag{2.11}$$

where $f_c = 16.110$ MHz is the carrier frequency, $c = 3.0 \times 10^8$ m/s is the speed of light in free space and v_m is the effective component of velocity of the reflection point. A positive Doppler shift indicates that the effective reflection point is moving "downwards" (i.e., shortening the phase path of the mode with respect to time) while the reverse applies when the Doppler shift is negative.

In practice, the effective velocity v_m of the reflection point is typically less than 10 m/s for quiet mid-latitude paths which corresponds to a Doppler shift of 1 Hz at a carrier frequency of 15 MHz. Over a 4.2 second CPI the effective displacement of the reflection point due to such motion is 42 m which results in a differential time-delay of $\delta\tau_m = 1.4$ ns between the beginning and end of the CPI. The time-bandwidth product $\delta\tau_m f_b \ll 1$ is much less than unity so the Doppler effect is accurately described by a phase shift for each FMCW signal mode over the CPI. The ionospherically imparted Doppler shift manifests itself as a regular phase progression from one sweep to another over the CPI, in Eqn.(2.9) this regular phase progression is represented by the term $e^{j2\pi\Delta f_m t/f_p}$.

The change in group range of a signal mode due to ionospheric movements over the CPI is in the order of tens of metres and is extremely small compared with the 20 km range resolution of the main array. Consequently, the term Δu_m is assumed to be fixed over a 4.2 second dwell interval. In the above example, it would take over 15 minutes

before the change in ionospheric "height" caused by a regular movement of the layer can be resolved in group range by the main array.

The phase of the m^{th} mode at the beginning of the CPI relative to that of the transmitted waveform is denoted by $\gamma(\tau_m)$. This initial phase depends on the mode time-delay and determines the starting phase relationship between the modes. The value of $\gamma(\tau_m)$ is determined by the phase path of the ionospheric circuit which links the transmitter to the reference receiver in the array at the beginning of the CPI.

$$\gamma(\tau_m) = e^{j2\pi\{f_c\tau_m + \frac{f_b\tau_m^2}{LT_s}\}} \tag{2.12}$$

The scalar A_m is a attenuation factor which accounts for all losses in the mode amplitude occurring between the transmitter and receiver. This term includes propagation distance loss described by the inverse square law, absorption of mode energy by the ionosphere and changes imposed on the incident mode amplitude by the reception channels of the array. For the moment it is assumed that the reception channels are identical so that A_m is independent of receiver number (n).

The relationship between digital samples acquired simultaneously in different receivers may be described using the three-dimensional coordinate system in Figure 2.20. The uniform linear array is aligned along the x-axis with the reference antenna sensor at the origin and the remaining identical antenna sensors equally spaced by a distance of Δd metres. A plane wave signal originating from a far-field source is incident upon the ULA from an azimuth angle α and an elevation angle β after specular reflection from the ionosphere.

In the main array the spacing between adjacent subarray centres is $\Delta d = 84$ m while the great circle azimuth of the transmitting source utilised in this experiment is $\alpha = 22$ degrees relative to boresight. The elevation angle of incidence β depends on the height of reflection in the ionosphere and typically varies between $5 - 35$ degrees for single-hop modes on the 1265 km mid-latitude path being investigated.

Let $\boldsymbol{k}_m = \frac{2\pi}{\lambda}\boldsymbol{u}(\alpha_m, \beta_m)$ be defined as the three-dimensional wavenumber vector corresponding to the m^{th} propagation mode where $\boldsymbol{u}(\alpha_m, \beta_m)$ is a three-dimensional unit vector in the propagation direction of the incident wave and $\lambda = c/f_c$ is the carrier wavelength.

The relative phase of the carrier component of the signal between the reference receiver and other receivers is calculated as the inner product $\boldsymbol{k}_m \cdot \boldsymbol{r}_n$ where $\boldsymbol{r}_n$ is the position vector of the n^{th} receiver, as defined in Eqn.(2.13).

$$\boldsymbol{k}_m = \frac{2\pi}{\lambda}\begin{bmatrix} \cos\beta_m \sin\alpha_m \\ \cos\beta_m \cos\alpha_m \\ \sin\beta_m \end{bmatrix}, \quad \boldsymbol{r}_n = \begin{bmatrix} n\Delta d \\ 0 \\ 0 \end{bmatrix} \tag{2.13}$$

The differential time-delay observed for the m^{th} signal mode when received at the two ends

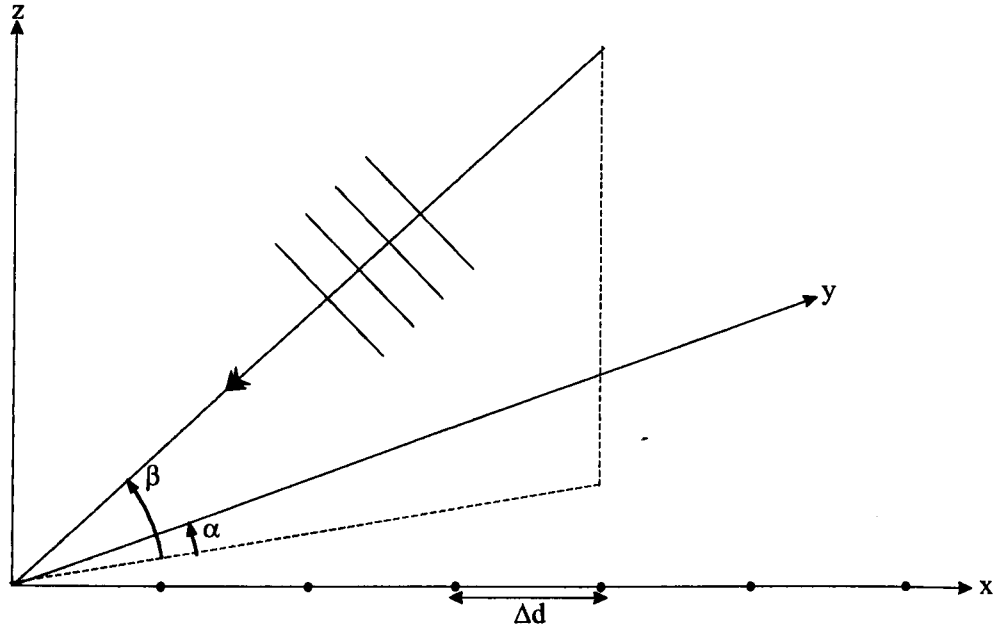

Figure 2.20: Three dimensional co-ordinate system showing a plane wave incident from azimuth α and elevation β on a ULA aligned along the x-axis.

of the array is given by $\boldsymbol{u}(\alpha_m, \beta_m) \cdot \boldsymbol{r}_{N-1}/c = (N-1)\Delta d \cos\beta_m \sin\alpha_m / c$ which is in the order of $2-3$ microseconds for $\alpha_m = 22$ degrees, $\beta = 5-35$ degrees and $N = 32$ subarrays. The time-bandwidth product corresponding to the differential delay across the array is much less than unity for a bandwidth of $f_b = 20$ kHz so the narrowband assumption is justified for the FMCW signal used in this experiment. For the m^{th} propagation mode, the phase relationship between the digital samples recorded at different receivers of the uniform linear array is given by,

$$\boldsymbol{k}_m \cdot \boldsymbol{r}_n = \frac{2\pi}{\lambda} n \Delta d \cos\beta_m \sin\alpha_m = \frac{2\pi}{\lambda} n \Delta d \sin\theta_m \tag{2.14}$$

and is included as the term $e^{j\boldsymbol{k}_m \cdot \boldsymbol{r}_n}$ in Eqn.(2.9). As indicated by Eqn.(2.14), the measured phase difference can be interpreted in terms of a single cone angle-of-arrival θ_m which is subtended by the mode wave-vector and the x-axis. If the cone angle is used as an estimate of the source azimuth, then for off-boresight sources, this interpretation results in the apparent azimuth angle of the source shifting towards the array boresight as the elevation angle increases. This effect is referred to as coning and often allows different propagation modes originating from a single source to be resolved in cone angle θ_m with a ULA.

The derivation of the mathematical model used to represent the digital samples received by the main array due to a single specularly reflected propagation mode has been described. In a multipath environment the received signal results from a superposition of M modes. Let $\mathbf{x}_l(t)$ be a complex N-dimensional vector which represents the array snapshot recorded at the l^{th} fast-time sample in the t^{th} PRI, and denote $\mathbf{x}_l^{[n]}(t)$ as the n^{th} element of this vector (i.e. the n^{th} receiver output). In general, the digital signal-field

samples received under the above-mentioned gross structure assumptions and approximations can be written as the superposition of M modes and uncorrelated additive noise $\mathbf{n}_l^{[n]}(t)$.

$$\mathbf{x}_l^{[n]}(t) = \sum_{m=1}^{M} g_m(l,t,n) + \mathbf{n}_l^{[n]}(t) \tag{2.15}$$

The additive noise is often modelled as temporally and spatially white with the following second order statistics,

$$E\{\mathbf{n}_{l_1}^{[n_1]}(t_1)\mathbf{n}_{l_2}^{[n_2]*}(t_2)\} = \sigma_n^2\, \delta(l_1 - l_2)\, \delta(t_1 - t_2)\, \delta(n_1 - n_2) \tag{2.16}$$

where $E\{\cdot\}$ is the statistical expectation operator and $\delta(\cdot)$ is the Kronecker delta function.

2.4.2 Range processed data model

Range processing is performed by taking the Fast Fourier Transform of the shaded fast-time samples collected in each PRI of each receiver. The contiguous set of FFT outputs or range samples retained for further processing are denoted by $\mathbf{x}_k^{[n]}(t)$ and indexed according to the range bin number $k = 0, 2, .., K-1$ ($K = 42$). Although l and k are indices it is possible to adhere to this notation without ambiguity as the exclusive use of either k or l for this index in the following treatment implicitly declares whether raw A/D samples or range samples are considered. Taking the (range processing) FFT of Eqn.(2.15) yields,

$$\mathbf{x}_k^{[n]}(t) = \sum_{m=1}^{M} g_m(t,n)\, W(\frac{k}{LT_s} - \Delta u_m) + \mathbf{n}_k^{[n]}(t) \tag{2.17}$$

where $g_m(t,n)$ is a space-time cisoid given by Eqn.(2.18), $\mathbf{n}_k^{[n]}(t)$ is the FFT output arising from the additive noise sequence $\mathbf{n}_l^{[n]}(t)$ and the frequency domain function $W(\cdot)$ is the normalised Fourier Transform of the Hanning window used to taper the fast-time samples such that $W(0) = 1$.

$$g_m(t,n) = c_m \exp\left(j2\pi\{\Delta f_m t/f_p + n\Delta d \sin\theta_m/\lambda\}\right) \tag{2.18}$$

When the group ranges of the modes are sufficiently different the various space-time waveforms $g_m(t,n)$ can be effectively separated into different range cells. This separation is effective providing the range sidelobes corresponding to the neighboring modes do not cause significant interference (e.g., are below the noise level) at the range cell most closely matched to the group range of the mode to be analysed.

In practice, the actual wavefield sampled at such a range cell will deviate to some degree from the idealised model of a two-dimensional (space-time) complex sinusoid. Reasons for such departures include mode fine structure, incompletely resolved propagation modes

as well as instrumental and site errors. The main array has been carefully designed to minimise instrumental and site errors so when signals reflected from different ionospheric layers are effectively resolved in range the dominant factor responsible for the observed departures between the idealised model and the recorded data is expected to be mode fine structure.

The ionosphere can also exhibit large-scale latitudinal and longitudinal gradients or tilts which shift the mode direction-of-arrival (azimuth and elevation) relative to that which is expected for a smooth and horizontally level reflecting layer. The influence of ionospheric tilts on the mode bearings has been mathematically treated by (Gething 1991) and may be used to interpret mismatches between the expected and estimated cone angle-of-arrival.

2.4.3 Fine structure model

It is known that a smooth ionospheric layer can theoretically propagate four rays over a one-way oblique circuit. As discussed in section 2.3.1, these rays consist of two pairs of magneto-ionic components known as the high angle and low angle rays (Davies 1990). The four theoretically expected rays are not usually resolvable in time-delay using a group-range resolution of 5 km (except near the maximum useable frequency) but in some cases a single magneto-ionic component can be isolated for study. When a single magneto-ionic component can be isolated, the presence of fine structure can only arise from the presence and movement of electron density irregularities in the ionosphere near the region of signal reflection. When two or more of the theoretically expected rays remain unresolved, the appearance of fine structure in the resultant signal arises partially due to the superposition of different rays and potentially the influence of ionospheric irregularities on each ray.

Experimental results from several different analysis described in the literature review indicate that individual propagation modes are frequently composed of a small number of (presumably specular) components or "sub-modes" with different Doppler frequency shifts and closely spaced directions-of-arrival. It has been conjectured that each sub-mode originates from a different specular reflection point within the ionospheric layer. In a smooth layer these sub-modes may correspond to the four theoretically expected reflections or a subset of them, whereas for a single magneto-ionic component, these sub-modes may originate from physically separated reflection points caused by the roughness of a perturbed ionospheric layer.

Both interpretations of the sub-modes leads to a specularly reflected wave interference model of fine structure, the interference between different waves causing within mode fading in both the spatial and temporal domain. In the wave interference model of mode fine structure, the space-time samples received from the m^{th} mode are represented by a

superposition of R_m rays,

$$g_m(t,n) = \sum_{r=1}^{R_m} c_r \exp\left(j2\pi\{\Delta f_r t/f_p + n\Delta d \sin\theta_r/\lambda\}\right) \tag{2.19}$$

where the various terms for each ray $r = 1, 2, .., R_m$ in Eqn.(2.19) are defined in analogous fashion to those in Eqn.(2.18). Now if k_m is the range cell most closely matched to the m^{th} mode and the different modes are well resolved in range the digital space-time samples received in this range cell by the array can be approximated as,

$$\mathbf{x}_{k_m}^{[n]}(t) \approx g_m(t,n) + \mathbf{n}_{k_m}^{[n]}(t) \tag{2.20}$$

where $g_m(t,n)$ is given by Eqn.(2.19) with $R_m > 1$ for fine structure and $R_m = 1$ for gross structure. From a mathematical point of view the distinction between the gross and fine structure of an *individual* propagation mode resolved in range is that the latter contains more than one term in the wave interference model. The physical origin of the extra terms which model fine structure may tentatively be interpreted from the theory of ionospheric propagation and measurements made by oblique sounders.

The wave interference model in Eqn.(2.20) is deterministic while it is known that the Doppler shift, direction-of-arrival and other parameters of a real ionospheric mode change as a function of time. It is noted that the scope of such a model is to represent the space-time characteristics of the propagation mode(s) received by an array over typical OTH radar coherent integration times in the order of a few seconds. The ray parameters are required to be updated in order for such a model to track temporal variations in the ionospheric circuit being probed.

2.5 Parameter estimation

The purpose of this section is to describe the procedure used for estimating the wave interference model parameters and to propose criteria for quantitatively assessing the capability of such a model to represent the fine structure of real ionospheric modes. More specifically, the objective is to estimate the cone angle-of-arrival, Doppler frequency, and complex amplitude of the constituent rays and to evaluate the degree to which the superposition of these rays fits the mode wavefields sampled in space and time by the main array.

Section 2.5.1 briefly overviews some commonly used methods for estimating the ray parameters while section 2.5.2 describes the parameter estimation technique selected for this analysis in more detail. Criteria for assessing the accuracy with which the estimated wave interference model represents the experimentally recorded wavefields are also proposed in section 2.5.2.

2.5.1 Selection of parameter estimation technique

The problem of resolving a wavefield received for a particular propagation mode into a number of constituent rays is a challenging one in the HF environment because the rays are likely to have almost the same Doppler shifts and be very closely spaced in angle-of-arrival. Two rays with the same Doppler shift but different angles-of-arrival will produce a non-planar wavefront at the receivers which does not change over time. On the other hand, two rays with the same angle-of-arrival but different Doppler shifts will produce a plane wave which exhibits temporal fading. In general, the rays can have slightly different angles-of-arrival and Doppler shifts which results in time-varying and non-planar wavefronts. This qualitative interpretation is consistent with the quantitative analysis made on the wavefronts corresponding to different propagation modes in section 2.3.3.

Classical spectral estimation techniques based on the FFT algorithm are generally considered the most robust and computationally efficient spectral estimation techniques. The term spectral estimation is used here rather than frequency estimation because unlike many high resolution methods the classical estimator also indicates the power of the sinusoids present in the data. One disadvantage of these estimators is that the structure of the sidelobes is data-independent and the leakage of strong signals through these sidelobes has the potential to mask a relatively weaker signal in the main lobe. Another disadvantage is the main lobe width which prevents the resolution of two or more frequency components that are mutually spaced closer than the reciprocal of the data record duration.

The distorting impact of sidelobe leakage is evident in all classical spectra plotted in Figures 2.8 to 2.11, while the resolution limitations caused by the main lobe width is perhaps most apparent in the angular spectrum of Figure 2.8 where two modes were known to be present but are not completely resolved in angle-of-arrival. The main lobe width and sidelobe leakage of the classical spectral estimator are the major shortcomings which makes this technique unsuitable for estimating the fine structure parameters of the experimentally recorded wavefields.

The minimum variance distortionless response (MVDR) spectral estimator was developed by (Capon 1969) to improve the resolution of closely spaced components, particularly in the spatial domain where the amount of data is often limited due to the small number of available receivers. In the spatial domain the SMI estimate of the MVDR spectrum $p_{mv}(k,\theta)$ is computed as,

$$p_{mv}(k,\theta) = [\mathbf{s}^H(\theta)\hat{\mathbf{R}}_x^{-1}(k)\mathbf{s}(\theta)]^{-1} \tag{2.21}$$

where $\hat{\mathbf{R}}_x(k)$ is the sample spatial covariance matrix. The MVDR spectral estimator can also be applied in the temporal domain by replacing $\hat{\mathbf{R}}_x(k)$ with $\hat{\mathbf{R}}_y(k)$ and $\mathbf{s}(\theta)$ with $\mathbf{v}(\Delta f)$ in Eqn.(2.21). The location of significant peaks in the MVDR spectrum represent the estimates of angle-of-arrival or Doppler frequency while their magnitude is linearly proportional to the power of the corresponding sinusoidal component.

Other methods based on linear prediction are described by (Marple 1987) but the best frequency resolution and frequency estimation characteristics have in the literature been attributed to a class of techniques based on the eigen-structure of the sample covariance matrix. The basis for improved performance, especially at lower signal-to-noise ratios, is the division of the information in the sample covariance matrix into two vector subspaces, one a signal subspace and the other a noise subspace. The tremendous interest in subspace approaches has arisen mainly from the introduction of the MUltiple SIgnal Classification (MUSIC) algorithm by (Schmidt 1981).

Since the introduction of MUSIC, a variety of other superresolution algorithms have been proposed and are reported as having certain advantages with respect to one another. A summary of these algorithms and an exhaustive list of references to their original source can be found in (Krim and Viberg 1996). The maximum likelihood (ML) algorithm and the method of direction estimation (MODE) for uniform linear arrays are two high performance parametric methods which can outperform MUSIC when two or more rays are coherent or highly correlated over the observation interval (Krim and Viberg 1996).

However, the ML method is computationally intensive relative to MUSIC, and perhaps more importantly, its convergence to the globally optimum estimates of the signal frequencies cannot be guaranteed. The MODE algorithm has comparable computational effort to MUSIC, and like MUSIC, this approach has been extended to address the joint two dimensional (space-time) frequency estimation problem (Li, Stoica and Zheng 1997). Although there is no definitive way of deciding on the best estimator for the application at hand, it was decided that MUSIC would be used as it provides an overall compromise between resolution power, computational complexity and the ability to perform joint space-time analysis. In addition, so-called spatial smoothing techniques (Pillai 1989) can be applied to improve the performance of the MUSIC estimator in the presence of correlated multipath signals.

2.5.2 Space-Time MUSIC

There are a number of reasons for attempting to estimate the spatial and temporal frequencies of the rays in the wave interference model jointly rather than separately. Perhaps the most significant reason is that space-time processing allows the various rays to be discriminated simultaneously in two dimensions rather than only in one at a time. For example, two rays with almost identical Doppler shifts may not be resolved in the temporal domain but if their angles-of-arrival are sufficiently different it is theoretically possible to resolve the two rays as different peaks in the space-time domain.

When the rays can be resolved separately in the temporal and spatial domain the problem of correctly pairing the angle-of-arrival and Doppler frequency estimates for each ray still remains. Another advantage of joint space-time processing is that pairing occurs automatically since each ray is resolved and localised in a two-dimensional (space-time)

co-ordinate system. The disadvantage of joint space-time processing is the extra computational effort arising from the use of covariance matrices with higher dimensionality and the larger amount of data required to estimate such matrices accurately. Another disadvantage is that a two-dimensional space must be searched instead of two one-dimensional spaces. To describe the space-time MUSIC technique let $\mathbf{x}_k(s,t)$ be an N_s-dimensional array snapshot vector recorded by N_s receivers of the main array starting at receiver number s where $s = 0, 1, .., N - N_s$ and $N > N_s$. Unlike the N-dimensional array snapshot vector $\mathbf{x}_k(t)$ which contains all the receiver outputs at the k^{th} range cell and t^{th} PRI, the N_s-dimensional vector $\mathbf{x}_k(s,t)$ contains the outputs of a subset of adjacent receivers in the array with the first element corresponding to the output of receiver number s. The (N_sN_t)-dimensional space-time data vector $\mathbf{z}_k(s,t,\Delta t)$ is then formed by stacking the N_s-dimensional array snapshots $\mathbf{x}_k(s,t)$ recorded at N_t slow-time samples that are equally spaced by a interval of Δt PRI. It is assumed that the values of N_s and N_t are chosen to ensure identifiability.

$$\mathbf{z}_k(s,t,\Delta t) = [\mathbf{x}_k^T(s,t)\ \mathbf{x}_k^T(s,t+\Delta t)\cdots\mathbf{x}_k^T(s,t+(N_t-1)\Delta t)]^T \tag{2.22}$$

The space-time data vector $\mathbf{z}_k(s,t,\Delta t)$ can be expressed in the following compact form according to the wave interference model of fine structure presented in section 2.4.3.

$$\mathbf{z}_k(s,t,\Delta t) = \mathbf{A}(\boldsymbol{\varphi})\mathbf{s}_k(t) + \mathbf{n}_k(s,t,\Delta t) \tag{2.23}$$

Before defining the terms $\mathbf{A}(\boldsymbol{\varphi})$ and $\mathbf{s}_k(t)$ in Eqn.(2.23), it is noted that in Eqn.(2.19) the number of rays used to model the fine structure of a particular mode was denoted by R_m where the subscript m indicated the dependence between the number of rays and the particular mode being modeled. As this analysis deals with the wavefields recorded in different range cells k, rather than the those produced by different modes (which may not be resolved in range) another notation is used. To make this notation as simple as possible, it is assumed that the wave interference model for range cell k contains M rays even though strictly speaking the value of M changes as function of k. Using the simplified notation, the $N_sN_t \times M$ space-time steering matrix $\mathbf{A}(\boldsymbol{\varphi})$ is parameterised by the angles-of-arrival and Doppler frequencies of the M rays contained in the parameter vector $\boldsymbol{\varphi} = [\theta_1\ \theta_2\cdots\theta_M\ \Delta f_1\ \Delta f_2\cdots\Delta f_M]^T$.

$$\mathbf{A}(\boldsymbol{\varphi}) = [\mathbf{a}(\theta_1,\Delta f_1)\ \mathbf{a}(\theta_2,\Delta f_2)\cdots\mathbf{a}(\theta_M,\Delta f_M)] \tag{2.24}$$

This matrix is composed of the (N_sN_t)-dimensional space-time signal steering vectors $\mathbf{a}(\theta,\Delta f)$ defined as the Kronecker product ($\otimes$) between the N_s-dimensional spatial steering vector $\mathbf{s}(\theta)$ and the N_t-dimensional temporal frequency vector $\mathbf{v}(\Delta f)$.

$$\mathbf{a}(\theta,\Delta f) = \mathbf{s}(\theta)\otimes\mathbf{v}(\Delta f) \tag{2.25}$$

The M-dimensional signal vector $\mathbf{s}_k(t)$ contains the complex waveforms $g_m(k,t,s)$ recorded for each ray at the starting receiver (s).

$$\mathbf{s}_k(t) = [g_1(k,t,s)\; g_2(k,t,s) \cdots g_M(k,t,s)]^T \tag{2.26}$$

The space-time vector of uncorrelated white noise $\mathbf{n}_k(s,t,\Delta t)$ is constructed in analogous fashion to Eqn.(2.22) and represents the additive noise component of the space-time vector $\mathbf{z}_k(s,t,\Delta t)$.

Traditionally, the space-time covariance matrix used to compute the MUSIC spectrum is estimated by using the full array aperture (i.e., all receivers) and averaging the outer products of the resulting space-time data vectors recorded over the coherent processing interval. When two or more rays are coherent or have the same Doppler shift (i.e., rays with the same Doppler frequency have a fixed gain and phase relationship over time at each point in space and are therefore coherent) the use of this matrix in the MUSIC algorithm fails to yield consistent estimates of the angles-of-arrival and Doppler shifts of the rays. This occurs as a result of a rank deficiency in the dimension of the signal subspace, the mathematical reasons for the failure of MUSIC under these circumstances is discussed in detail by (Pillai 1989). To rectify this situation, which may well occur in the current practical application, the idea of spatial smoothing described by (Shan, Wax and Kailath 1985) can be employed to "de-correlate" the rays while preserving both the angular and Doppler information.

A so called forward-backward spatial smoothing scheme is used to form an alternative N_sN_t-dimensional sample space-time matrix $\hat{\mathbf{R}}_z(k)$.

$$\hat{\mathbf{R}}_z(k) = \sum_{t=0}^{P'}\sum_{s=0}^{N'} \mathbf{z}_k(s,t,\Delta t)\mathbf{z}_k^H(s,t,\Delta t) + \mathbf{J}\mathbf{z}_k^*(s,t,\Delta t)\mathbf{z}_k^T(s,t,\Delta t)\mathbf{J} \tag{2.27}$$

where $P' = P - N_t\Delta t$, $N' = N - N_s$ and $\mathbf{J}$ is the square $N_sN_t \times N_sN_t$-dimensional exchange matrix with ones on the anti-diagonal and zeros elsewhere. The exact space-time covariance matrix $\mathbf{R}_z(k)$ for the fine structure model is derived by substituting Eqn.(2.23) into Eqn.(2.27) and taking the statistical expectation $E\{\cdot\}$ of the resulting expression.

$$\mathbf{R}_z(k) = \mathbf{A}(\varphi)\mathbf{S}_k\mathbf{A}^H(\varphi) + \sigma_n^2\mathbf{I} \tag{2.28}$$

The M by M matrix $\mathbf{S}_k$ is referred to as the spatially smoothed source covariance matrix; the true source covariance matrix being defined as $E\{\mathbf{s}_k(t)\mathbf{s}_k^H(t)\}$. While the true source covariance matrix is not full rank when two or more signals are coherent it can be shown that the rank of the spatially smoothed source covariance matrix increases by one with probability one for each spatial average (Pillai 1989). It is this property which is exploited by the spatial smoothing scheme that allows MUSIC to yield consistent estimates of the ray parameters when two or more rays are coherent or highly correlated. The cost of

spatial smoothing is that the effective aperture of the array is reduced which leads to a decrease in azimuthal resolution and a reduction in the maximum number of signals which can be resolved.

Assuming $\mathbf{A}(\varphi)\mathbf{S}_k\mathbf{A}^H(\varphi)$ is of full rank (i.e., of rank M), the eigen-decomposition of the exact space-time covariance matrix $\mathbf{R}_z(k)$ can be expressed as

$$\mathbf{R}_z(k) = \mathbf{Q}_s\mathbf{\Lambda}\mathbf{Q}_s^H + \sigma_n^2\mathbf{Q}_n\mathbf{Q}_n^H \tag{2.29}$$

where the M columns of $\mathbf{Q}_s$ and the $N_sN_t - M$ columns of $\mathbf{Q}_n$ are the eigenvectors spanning the signal and noise subspaces respectively while the diagonal matrix $\mathbf{\Lambda} = diag[\lambda_1\ \lambda_2 \cdots \lambda_M]$ contains the M largest eigenvalues corresponding to the principal or signal subspace eigenvectors. As the eigenvectors spanning the noise subspace are orthogonal to those in the signal subspace, the signal vectors are also mutually orthogonal to the noise subspace eigenvectors. In other words, $\mathbf{Q}_n^H\boldsymbol{a}(\theta, \Delta f) = 0$ if $\theta = \theta_m$ and $\Delta f = \Delta f_m$ for a particular ray $m = 1, 2, .., M$. The parameter pairs $(\theta_m, \Delta f_m)$ corresponding to the M rays are the only possible parameter pairs which can satisfy this condition of orthogonality because any collection of different space-time signal vectors $\mathbf{a}(\theta, \Delta f)$ forms a linearly independent set (i.e., the manifold has a Vandermonde structure).

The spatially smoothed MUSIC "spectrum" $p_{mu}(\theta, \Delta f)$ is computed from the noise subspace $\hat{\mathbf{Q}}_n$ derived from the sample space-time covariance matrix $\hat{\mathbf{R}}_z(k)$.

$$p_{mu}(\theta, \Delta f) = \frac{\mathbf{a}^H(\theta, \Delta f)\mathbf{a}(\theta, \Delta f)}{\mathbf{a}^H(\theta, \Delta f)\hat{\mathbf{Q}}_n\hat{\mathbf{Q}}_n^H\mathbf{a}(\theta, \Delta f)} \tag{2.30}$$

Although $p_{mu}(\theta, \Delta f)$ is not a true spectrum it typically exhibits sharp peaks in the vicinity of the true angles-of-arrival and Doppler shifts of the complex sinusoids (cisoids) present in the data. The locations of the peaks in the two-dimensional MUSIC spectrum correspond to the estimates of the ray angles-of-arrival and Doppler shifts. These angles-of-arrival and Doppler shifts are represented by the *estimated* parameter vector $\hat{\varphi}$.

The magnitude of the peaks in the MUSIC spectrum should not be interpreted as the power of the rays, but the angles-of-arrival and Doppler frequencies estimated by MUSIC can be used to estimate the amplitude and initial phase of each ray by a least squares procedure. Let the NP-dimensional vector $\mathbf{z}_k$ contain all the space-time data recorded within the CPI,

$$\mathbf{z}_k = [\mathbf{x}_k^T(0)\ \mathbf{x}_k^T(1) \cdots \mathbf{x}_k^T(P)]^T \tag{2.31}$$

and the $NP \times M$ matrix $\mathbf{A}(\hat{\varphi})$ contain the estimated space-time signal vectors. The M-dimensional vector of ray complex amplitudes $\hat{\mathbf{c}}_k$ is estimated so as to minimise the

residual error power according to the following least squares criterion,

$$\hat{\mathbf{c}}_k = \text{argmin}\|\mathbf{z}_k - \mathbf{A}(\hat{\boldsymbol{\varphi}})\mathbf{c}_k\|^2 \tag{2.32}$$

where $\|\cdot\|^2$ represents the squared Euclidean norm also known as the Frobenius norm $\|\cdot\|_F$. Note that the M complex-valued elements of $\hat{\mathbf{c}}_k$ represents both the amplitude and initial phase of the M rays in the wave interference model of the wavefield received in the k^{th} range cell. The solution to Eqn.(2.32) can be expressed in closed form and is given by,

$$\hat{\mathbf{c}}_k = \mathbf{A}^+(\hat{\boldsymbol{\varphi}})\mathbf{z}_k = [\mathbf{A}^H(\hat{\boldsymbol{\varphi}})\mathbf{A}(\hat{\boldsymbol{\varphi}})]^{-1}\mathbf{A}^H(\hat{\boldsymbol{\varphi}})\mathbf{z}_k \tag{2.33}$$

where $\mathbf{A}^+(\hat{\boldsymbol{\varphi}})$ denotes the Moore-Penrose pseudo-inverse of $\mathbf{A}(\hat{\boldsymbol{\varphi}})$.

After the model order is selected and the ray parameters are estimated by applying the procedure described above to experimental data it is then necessary to quantify the accuracy with which the model fits the experimental data. It may also be of interest to quantify the ability of the model to represent experimental data recorded outside the spatial and temporal intervals used for the estimation of the various ray parameters. In any case, a quantitative measure of the match between the simulated signal-field and the received space-time data is required to evaluate the performance of the wave interference model as well as to establish criteria for accepting or rejecting its validity.

A measure of modelling performance that is relatively simple to calculate and of intuitive appeal is the ratio of the energy in the residual modelling error to that of the experimental data. This measure is referred to as the model fitting accuracy (MFA) and is calculated in the manner described by Eqn.(2.34) where the k subscript has been dropped for notational convenience.

$$\text{MFA} = 1 - \frac{\|\mathbf{z} - \mathbf{A}(\hat{\boldsymbol{\varphi}})\hat{\mathbf{c}}\|^2}{\|\mathbf{z}\|^2} \tag{2.34}$$

The space-time signal model $\hat{\mathbf{z}} = \mathbf{A}(\hat{\boldsymbol{\varphi}})\hat{\mathbf{c}}$ is considered a satisfactory representation of the received data $\mathbf{z}$ when the MFA is sufficiently close to its upper limit of 100 percent. The meaning of the term "sufficiently close" should be defined with respect to the signal-to-noise ratio since the MFA will be less than 100 percent even if the signal model exactly replicates the signal component of the received data due to the presence of additive noise. From Eqn.(2.34) it is relatively simple to show that the expected value of the MFA for perfect signal modelling and uncorrelated additive noise is given by SNR/(SNR+1) where SNR is the signal-to-noise ratio. For the high SNR data used in this analysis, the MFA will most likely be limited by signal modeling errors rather than additive noise. The purpose of the following section is to experimentally quantify the MFA in the range cells corresponding to the peaks of the power-delay profile in Figure 2.3.

2.6 Experimental results

The purpose of this section is to decompose mode fine structure into relatively few specularly reflected rays and to determine the accuracy with which the superposition of these rays can represent the space-time signal-field samples recorded from ionospherically propagated modes by a very wide aperture antenna array over a typical OTH radar coherent integration time (CIT).

This section begins with a description of the space-time MUSIC analysis procedure and presents experimental results which demonstrate the ability of this algorithm to resolve the fine structure of individual propagation modes. The accuracy with which the superposition of rays estimated by the space-time MUSIC algorithm can represent the complex-valued mode wavefield samples is then quantified as a function of the number of assumed rays and the particular CIT of data analysed.

2.6.1 MUSIC analysis procedure

The parameter estimation technique described in section 2.5 requires the model order, or the number of rays, to be specified along with the spatial and temporal dimensions of the data vector used for covariance matrix estimation. A method based on information theory was developed by (Wax and Kailath 1985) and uses the eigenvalues of the sample covariance matrix to estimate the number of rays. Although such a method is applicable in this analysis it should be kept in mind that the objective is to determine how well a small number of rays can represent the data rather than to use the potentially high number rays indicated by these methods to model the data very accurately.

A model involving a very large number of rays can be constructed to portray mode fine structure very accurately but such a complex model is perhaps of limited utility for two reasons. One reason is that the physical significance of the various factors which contribute to the observed data characteristics is more readily understood when the data can be satisfactorily represented with a small number of rays. Secondly, and perhaps more importantly, a model with lower order is mathematically more tractable for the design and theoretical analysis of signal processing algorithms. At the other extreme, a one-ray model is mathematically very simple but results obtained with such models must be interpreted with caution as they may not be representative of the HF environment. Ideally, models of intermediate complexity are of most practical benefit because they are challenging enough to allow the performance of different algorithms to be meaningfully ranked but not so challenging as to defeat all algorithms.

The question then arises as to what constitutes the specific meaning of the term "relatively few rays" or "a small number of rays" which has been used up until now. Two and three ray wavefields were synthesised by (Gething 1991) in order to compare the performance of different WFA methods. The same model orders were adopted by

(Rice 1982) to analytically derive probability density functions for a defined measure of wavefront planarity. In this section the ability of the wave interference model to represent real wavefields using up to four rays is analysed. The major justification for going to four rays is that it coincides with the number of rays that are theoretically expected after reflection from a single smooth ionospheric layer.

The space-time MUSIC algorithm with spatial averaging was described in section 2.5.2 using arbitrary parameters for the number of receivers (N_s), the number of temporal taps (N_t) and the spacing between adjacent taps (Δt). Along with the model order M, these parameters need to be specified in order to form either one-dimensional or two-dimensional (space-time) MUSIC spectra from a particular coherent integration time of data.

Although larger values of N_s, N_t and Δt improve resolution they also increase the dimensionality of the covariance matrix which must be estimated from a finite set of space-time samples. A covariance matrix of larger dimension is not estimated as well and contains a higher level of statistical noise which increases the variance of the MUSIC spectrum estimates. Using data from multiple dwells to stabilise these estimates is not a preferred option in practice because there is a greater chance of the ray parameters changing over a longer observation interval. Other drawbacks associated with the use of very large covariance matrices include the much higher computational complexity, which is proportional to the cube of the data vector dimension, and the greater potential to encounter problems with numerical stability of the routines used to perform eigen-decomposition.

There are no definite guidelines for the selection of data vector dimensions, especially when the signal environment is not known apriori. In this analysis, the space-time MUSIC spectra were estimated using $N_s = 16$ receivers, $N_t = 16$ temporal taps and $\Delta t = 12$ PRI (i.e., a 0.2 second tap spacing). For a dwell of data, these parameters were considered to represent a tradeoff between the resolution and variance of the space-time MUSIC estimator. The spatial-only MUSIC spectrum is obtained by setting $N_t = 1$ and keeping $N_s = 16$ while the temporal-only version is computed by setting $N_s = 1$ and keeping $N_t = 16$, $\Delta t = 12$.

2.6.2 Resolving mode fine structure

To demonstrate the experimental application of one and two dimensional MUSIC the problem of resolving the fine structure of the $1E_s$ mode received during a particular dwell is considered, the real component of the space-time wavefield analysed in this example was previously illustrated in Figure 2.4.

Curves 2 and 3 in Figure 2.21 illustrate the spatial-only MUSIC spectra evaluated with $N_s = 16$ assuming a model order of four and five rays respectively. It is observed that the four peaks resolved for $M = 4$ become broader when $M = 5$ is assumed but a fifth peak is not generated, this suggests the presence of four dominant rays in the wavefield which can be resolved in angle-of-arrival by MUSIC. Curve 1 in Figure 2.21

shows the *unsmoothed* MUSIC spectrum corresponding to the same experimental data, this spectrum is derived by selecting the dimension of the spatial covariance matrix as the total number of receivers in the array. In this case $N_s = N = 30$ so the spatial covariance matrix is estimated by averaging the array snapshots received over time (i.e., spatial averaging is not performed). Curve 4 in Figure 2.21 relates to the right vertical axis and represents the MVDR spectrum evaluated according to Eqn.(2.21), this spectrum was evaluated by using the same spatially smoothed sample spatial covariance matrix as that used to compute the two MUSIC spectra represented by Curves 2 and 3.

A comparison of Curve 2 and Curve 4 in Figure 2.21 illustrates that the spatial-only MUSIC algorithm can resolve four closely spaced rays while the MVDR only resolves three. Note that the presence of the fourth ray is indicated (but not resolved) by a slight bulge in the MVDR spectrum which would not be expected if this fourth ray were not present. A comparison of Curve 1 and Curve 2 in Figure 2.21 illustrates the benefit of spatial averaging, the dramatic improvement in the MUSIC spectrum after spatial smoothing allows four rays to be resolved. The poor performance of the standard (unsmoothed) MUSIC algorithm in this example suggests the presence of highly correlated arrivals over the observation interval. This observation points to the presence of rays with very similar Doppler shifts.

For the same wavefield, curves 1, 2 and 3 in Figure 2.22 illustrate the temporal-only MUSIC spectra which results when a model order of one, two and three rays is assumed respectively. All three MUSIC spectra relate to the left vertical axis and were evaluated using the sample temporal covariance matrix parameters $N_t = 16$ and $\Delta t = 12$. Curve 4 relates to the right vertical axis and represents the MVDR spectrum evaluated from the same sample temporal covariance matrix. Despite four rays being resolved in spatial domain only two rays are resolved in the Doppler domain by MUSIC. The inability of temporal-only MUSIC to resolve more than two rays is consistent with the previous suggestion that some of the rays have very similar Doppler shifts.

The MVDR spectrum is sometimes called a high-resolution estimator but it cannot resolve the two rays resolved by MUSIC in Figure 2.22, this is another illustration of the relatively superior frequency estimation performance of the MUSIC super-resolution algorithm. Nevertheless, the MVDR spectrum is useful because it indicates that most of the received power lies in the range of Doppler frequencies between 0.4-0.6 Hz. If four dominant rays were present then the Doppler frequencies of these rays are expected to be within this range, this statement will be qualified later when the space-time MUSIC algorithm is applied.

The discrepancy between the number of rays resolved in angle-of-arrival and Doppler frequency creates a problem when it comes to interpreting the wavefield by means of assigning a spatial and temporal frequency for each ray. This real data example serves to illustrate the principal motivation for using space-time MUSIC rather than estimating the parameters by calculating two separate one-dimensional MUSIC spectra. The space-time

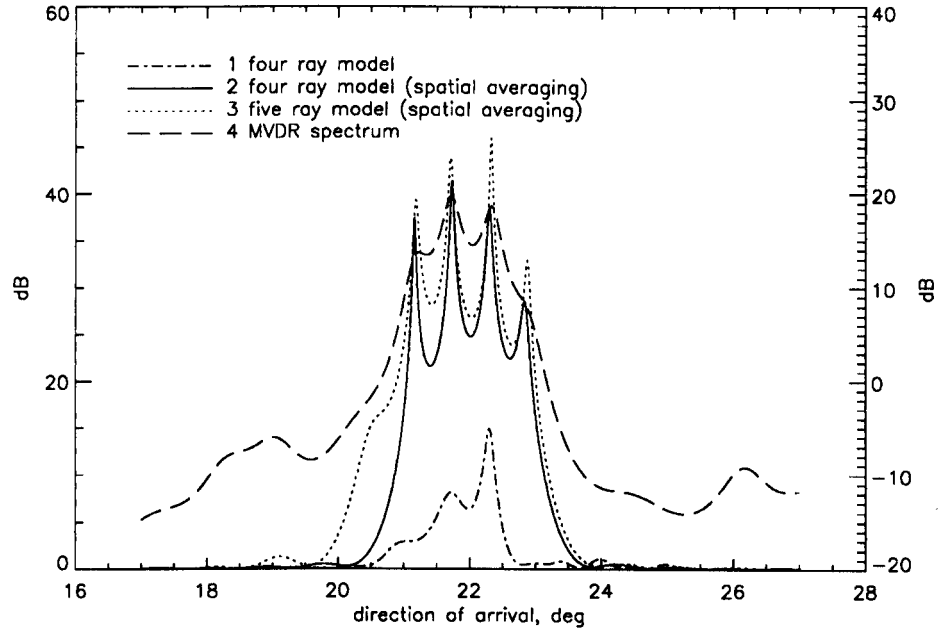

Figure 2.21: Spatial MUSIC spectra for the $1E_s$ mode ($k = 16$). The angles-of-arrival corresponding to the four peaks in Curve 2 are 21.2, 21.7, 22.3 and 22.8 degrees.

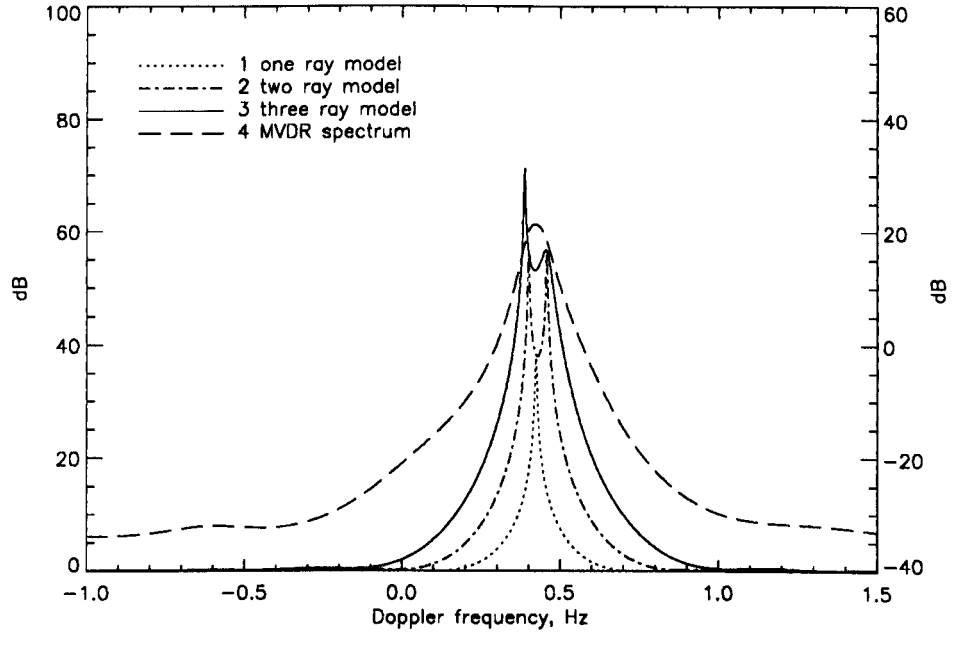

Figure 2.22: Temporal MUSIC spectra for the $1E_s$ mode ($k = 16$). The Doppler frequencies corresponding to the two peaks in Curve 2 are 0.40 and 0.46 Hertz.

MUSIC spectrum derived from the same $1E_s$ mode wavefield using $N_s = 16$, $N_t = 16$, $\Delta t = 12$ and assuming four rays is shown as a three dimensional surface plot in Figure 2.23.

The parameters of the four rays resolved by the space-time MUSIC spectrum in Figure 2.23 are listed in Table 2.2, this includes the amplitudes and initial phase of each ray which were estimated by the least squares procedure described in section 2.5. Note that the location of each peak resolved by the temporal-only and spatial-only MUSIC spectra is consistent with one of the four peaks resolved in the space-time MUSIC spectrum. The space-time MUSIC spectrum also confirms that three of the four rays have almost identical Doppler shifts, these rays were not resolved by temporal-only MUSIC but were resolved by the smoothed spatial-only and space-time MUSIC algorithm due to their different angles-of-arrival.

Figure 2.31 shows the real component of a wavefield generated with the ray parameters estimated for the $1E_s$ mode in Table 2.2. On visual inspection, this wavefield is very similar to the experimentally recorded one shown in Figure 2.4. A quantitative comparison between the real and simulated complex wavefields is made in terms of the fitting accuracy measure defined in section 2.5. In this example, the estimated four ray interference model yields a fitting accuracy of 96 percent.

From a physical perspective, the two rays with cone angles-of-arrival less than the great circle azimuth of the test transmitter (22 degrees) may correspond to the ordinary and extraordinary magneto-ionic components reflected by a particular cloud of enhanced sporadic-E ionisation. The pair of rays with cone angles-of-arrival larger than 22 degrees are assumed to be reflected from a different cloud of enhanced sporadic-E ionisation. Although it cannot be proven by this analysis, these two rays may correspond to the ordinary and extraordinary magneto-ionic components reflected at points in the $1E_s$ layer located at great circle azimuths *larger* than 22 degrees with respect to the array boresight since the coning effect only serves to shift the apparent azimuth of a received signal closer to boresight.

Examples of the space-time MUSIC spectra resulting for the $1F_2$, $1F_2(o)$ and $1F_2(x)$ modes are shown in Figures 2.24 to 2.26. For each mode, the model order was chosen to represent the number of rays which were frequently required to yield a fitting accuracy greater than 90 percent over the entire data set consisting of 47 dwells (each dwell being 4.2 seconds in duration). The ray parameters estimated from these space-time MUSIC spectra, to be discussed below, are also listed in Table 2.2. Figures 2.27 to 2.30 summarise the results of this experimental analysis by showing the fitting accuracy achieved for each mode as a function of the number of rays and the particular dwell of data analysed.

Some dwell numbers in Figures 2.27 to 2.30 do not contain a measurement for each model order because the number of peaks resolved by the space-time MUSIC spectrum does not always coincide with the assumed number of rays. This situation may arise when the model order is overestimated or if the ray parameters change slightly during the coherent integration time. The fitting accuracy is not displayed when the number of

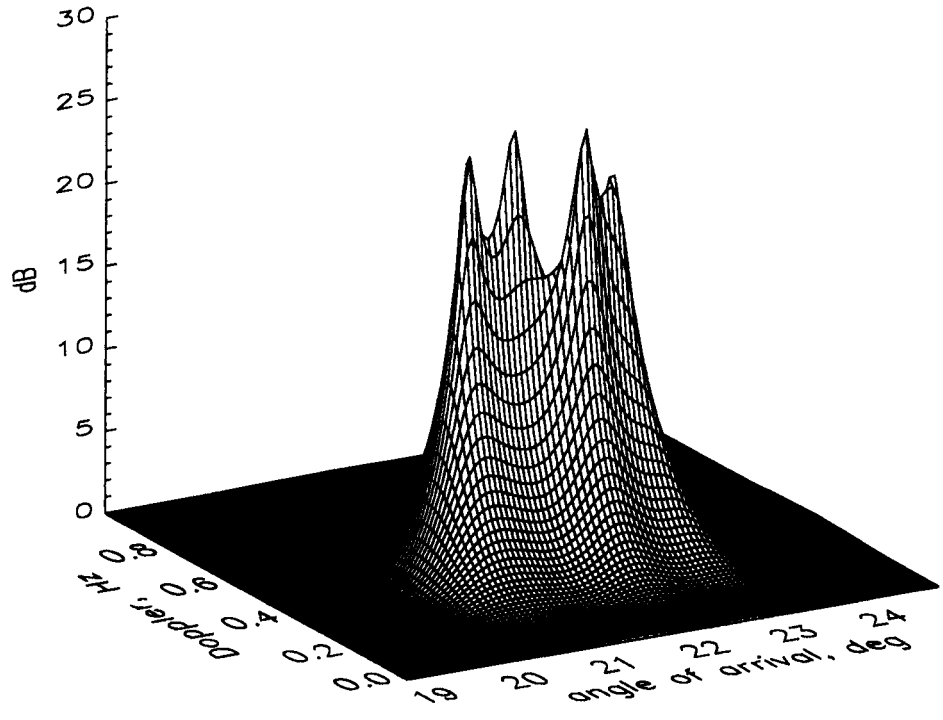

Figure 2.23: Space-time MUSIC spectrum for the $1E_s$ mode assuming four rays

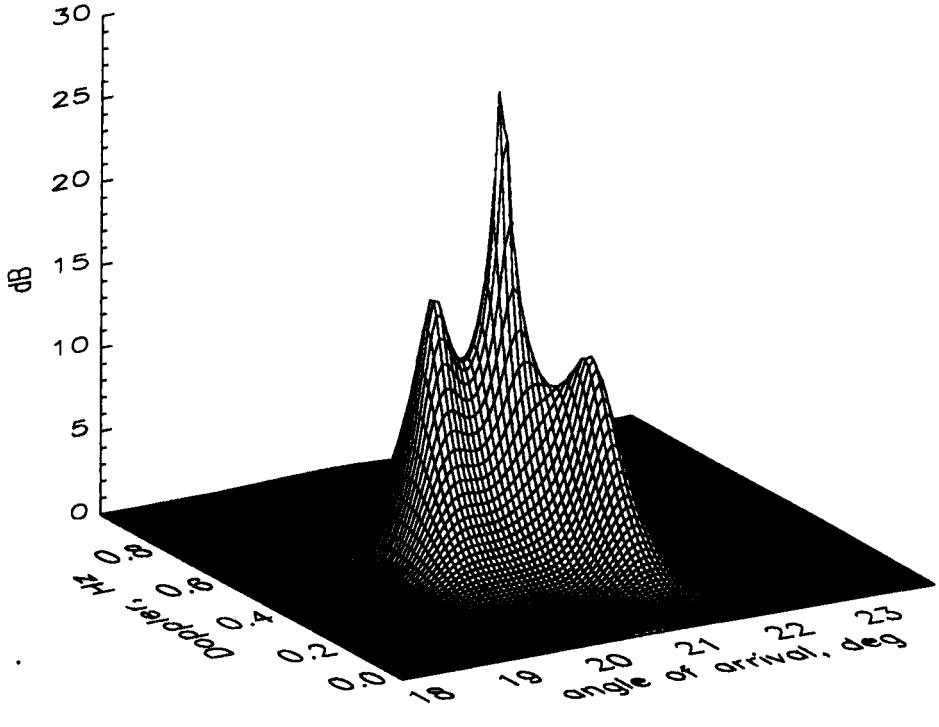

Figure 2.24: Space-time MUSIC spectrum for the $1F_2$ mode assuming three rays

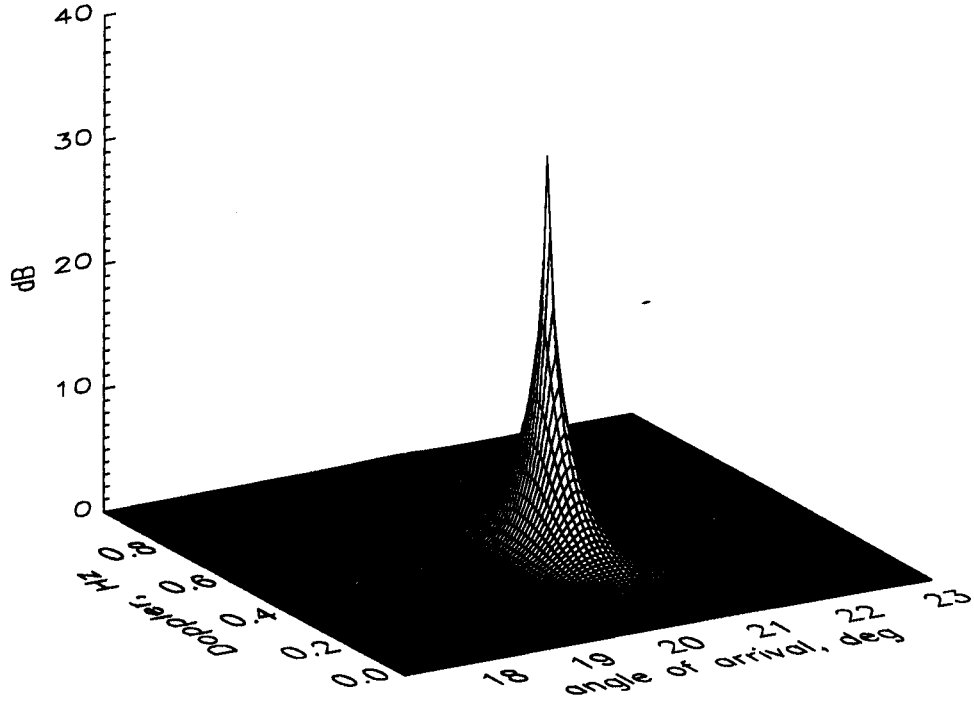

Figure 2.25: Space-time MUSIC spectrum for the $1F_2(o)$ mode assuming one ray

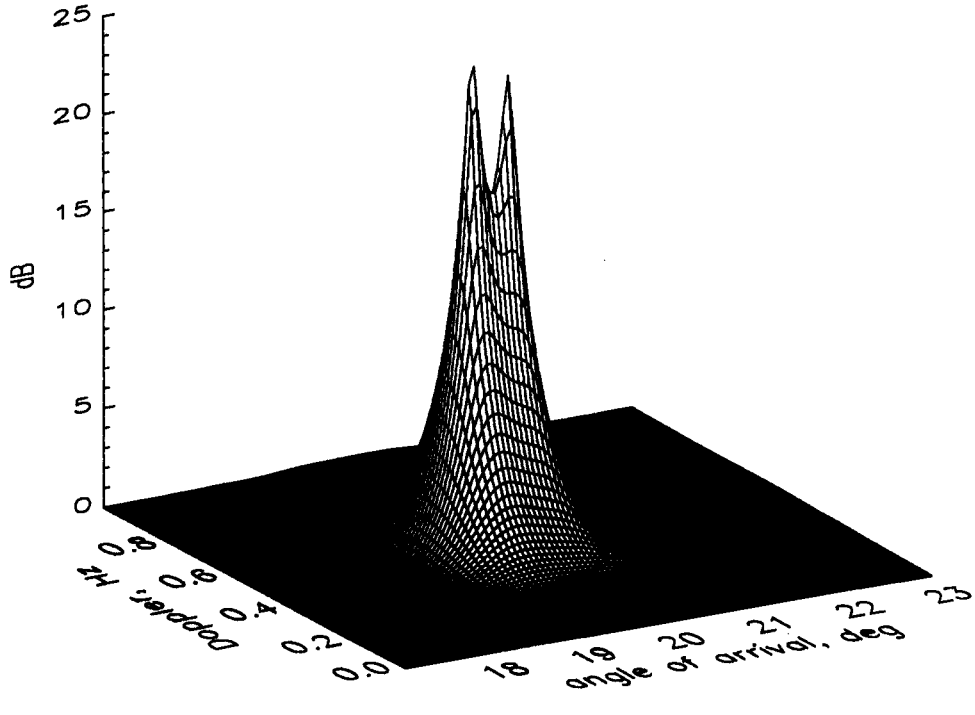

Figure 2.26: Space-time MUSIC spectrum for the $1F_2(x)$ mode assuming two rays

Mode	Angle-of-arrival, deg	Doppler, Hz	Magnitude, linear	Phase, deg
$1E_s$ ray 1	21.2	0.43	1.10	77.3
$1E_s$ ray 2	21.7	0.44	2.57	−174.8
$1E_s$ ray 3	22.4	0.40	2.16	−8.78
$1E_s$ ray 4	22.8	0.43	0.65	−127.4
$1F_2$ ray 1	20.1	0.50	0.54	141.4
$1F_2$ ray 2	20.7	0.48	2.76	54.5
$1F_2$ ray 3	21.3	0.37	0.64	104.7
$1F_2(o)$ ray 1	20.4	0.48	3.93	−50.0
$1F_2(x)$ ray 1	19.7	0.51	0.67	61.4
$1F_2(x)$ ray 2	20.1	0.52	0.88	160.8

Table 2.2: Ray parameters estimated from the space-time MUSIC spectra of the $1E_s$, $1F_2$, $1F_2(o)$ and $1F_2(x)$ modes.

peaks does not agree with the assumed model order but it is important to note that the failure of MUSIC to resolve the expected number of peaks does not imply that a wave interference model having the assumed number of rays cannot adequately represent the data. For example, the assumption of two and three rays for the $1F_2$ mode in dwell 22 gives rise to one and two peaks respectively so the symbols corresponding to these model orders do not appear at dwell number 22 in Figure 2.28. However, the fitting accuracy achieved by the two resolved rays when three rays were assumed was 93 percent.

At least two rays are expected for the $1F_2$ mode since this mode is theoretically composed of both the ordinary and extraordinary rays in the low angle path. Inspection of Figure 2.28 reveals that three rays are resolved more often than two rays for this mode, and at times, a three ray model yields a significantly better fitting accuracy compared with the two ray model. For example, the three ray model depicted by the space-time MUSIC spectrum of Figure 2.24 led to a fitting accuracy of 95 percent as compared to 87 percent for a two ray model. When a third ray is resolved it is thought to account for ionospheric irregularities in F-region possibly caused by the passage of travelling ionospheric disturbances.

In the absence of ionospheric irregularities a one-ray model is expected to provide a very accurate description of the wavefield produced by a single magneto-ionic component. As shown in Figure 2.29, this was found to be the case for the $1F_2(o)$ mode in most of the data dwells analysed. A high fitting accuracy using a single ray also indicates that the ULA has an array manifold which is accurately matched at the carrier frequency to the one theoretically expected in the absence of instrumental and site errors. In the example of Figure 2.25, a single ray provided a fitting accuracy of 95 percent for the $1F_2(o)$ mode.

Figure 2.30 shows that a single ray is not able to represent the $1F_2(x)$ mode wavefields as well as those of the $1F_2(o)$ mode. The extraordinary magneto-ionic component is reflected from a different region in the F_2-layer which on this occasion appears to be comparatively more disturbed than the region which reflects the ordinary magneto-ionic

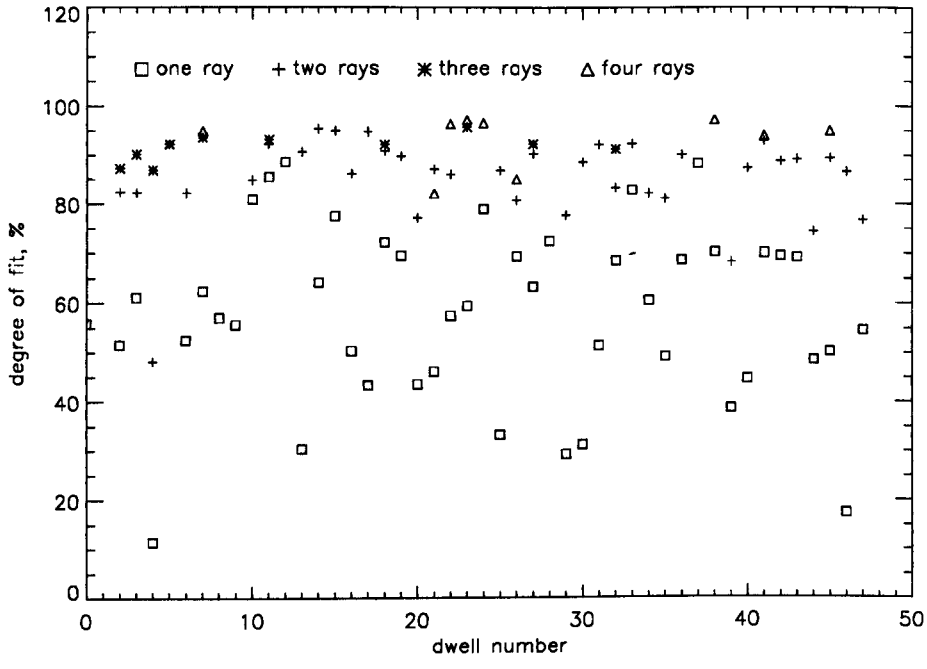

Figure 2.27: Fitting accuracy for the $1E_s$ mode

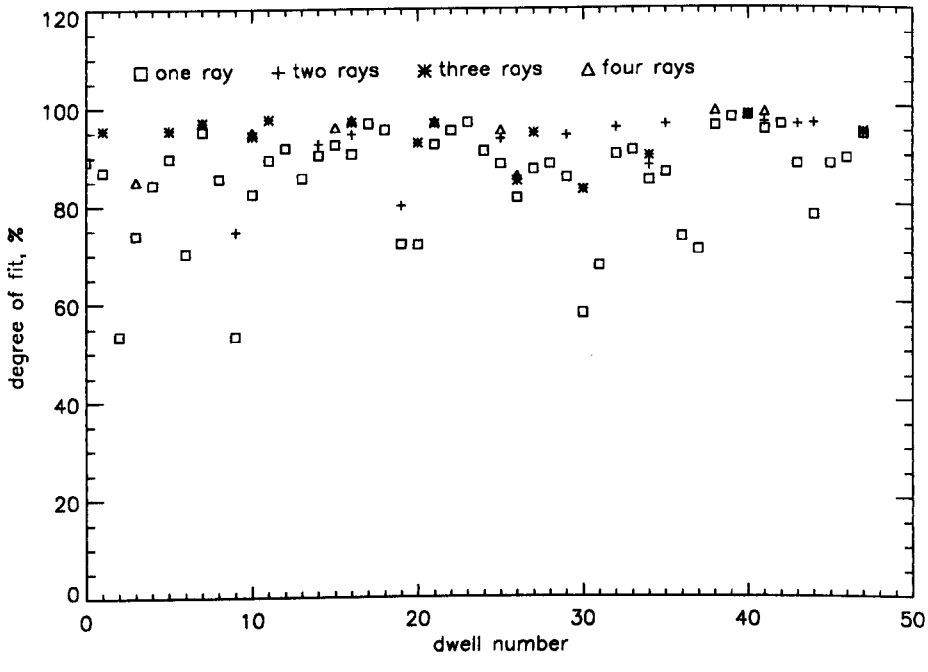

Figure 2.28: Fitting accuracy for the $1F_2$ mode

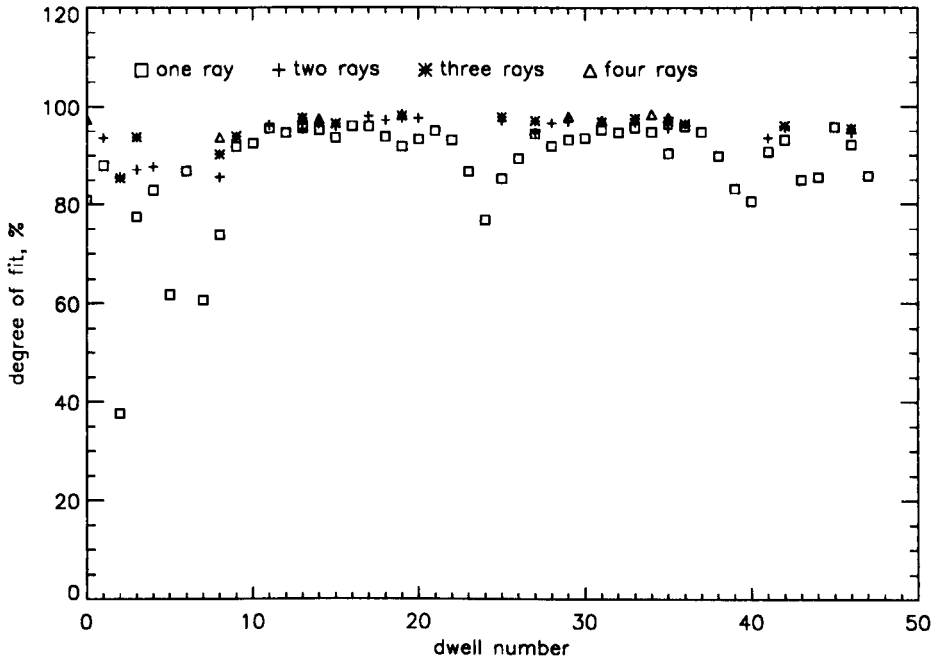

Figure 2.29: Fitting accuracy for the $1F_2(o)$ mode

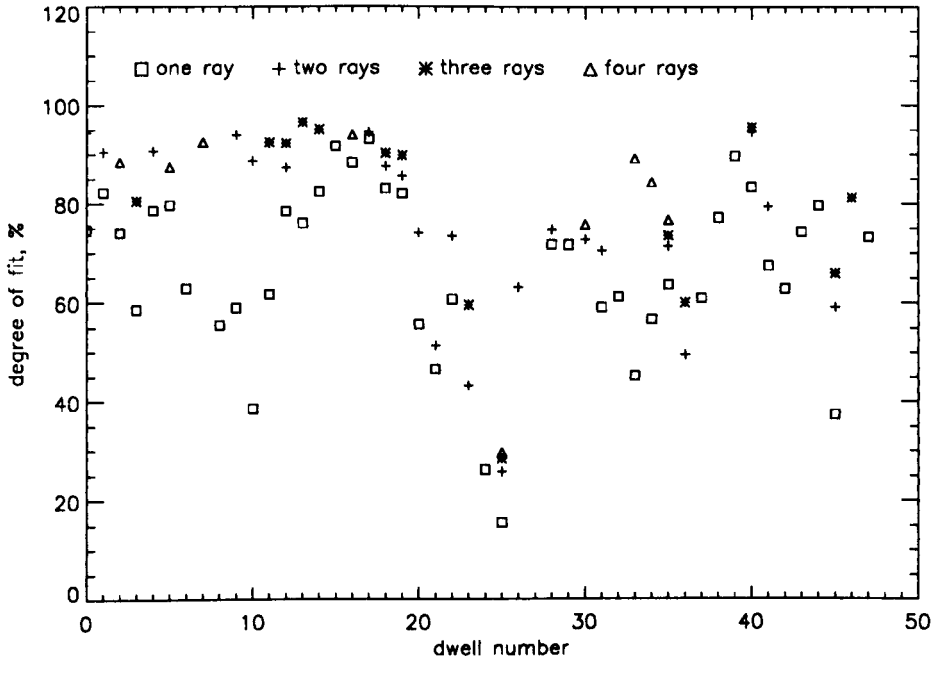

Figure 2.30: Fitting accuracy for the $1F_2(x)$ mode

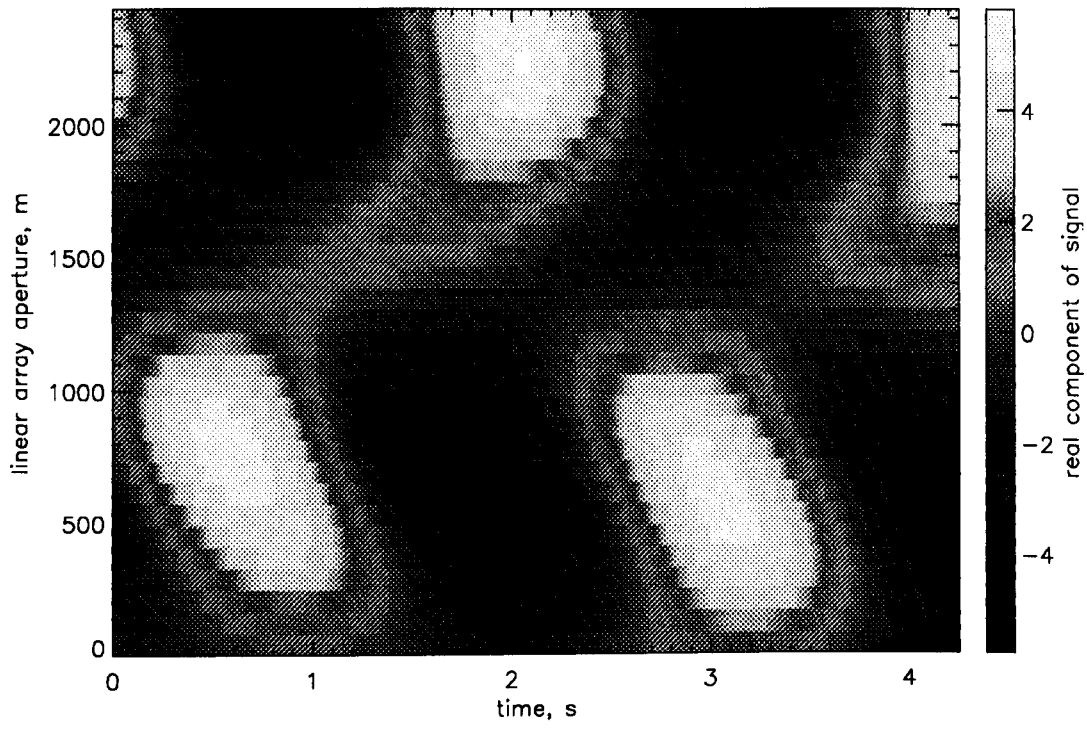

Figure 2.31: Real component of the space-time wavefield simulated for the $1E_s$ mode using the estimated four ray model

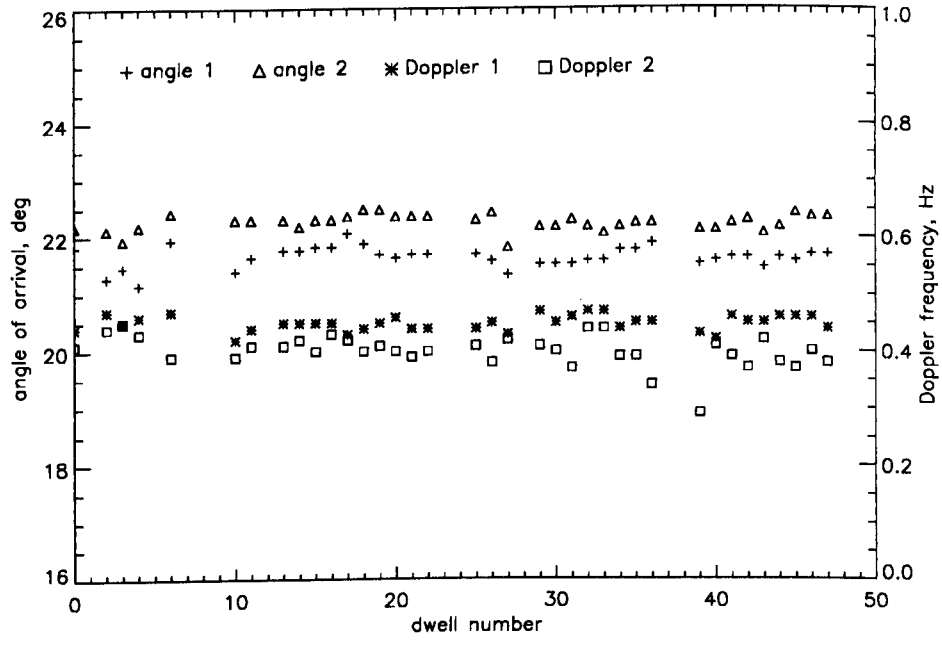

Figure 2.32: Dwell to dwell variation of the estimated angles-of-arrival and Doppler shifts of a two ray model for the $1E_s$ mode

component. For the $1F_2(x)$ mode it was found that two or more rays were often needed to yield fitting a accuracy above 90 percent. Two rays were resolved more often than three or four rays for this particular mode and the fitting accuracy achieved by two rays was usually considerably higher than that for one ray. For example, the two ray model corresponding to the spectrum in Figure 2.26 resulted in a fitting accuracy of 94 percent whereas a one ray model only fitted the data to an accuracy of 82 percent.

To illustrate the time-variation of ray parameters from one dwell to another consider the two ray representation of the $1E_s$ mode. Figure 2.32 shows the variation in the estimated cone angles-of-arrival and Doppler shifts of the two rays for dwells in which the fitting accuracy was greater than 85 percent. The time-variation of the ray angles-of-arrival is in the order of 0.5 degrees over the 47 dwells analysed while the Doppler shifts vary by approximately 0.1 Hz. The observed variation in ray parameters from dwell to dwell is expected due to the movement of the effective reflection points in the ionosphere over time intervals in the order of a few minutes.

2.7 Chapter summary

The fine structure of signal modes reflected from different layers in the ionosphere is considered by some investigators to result from a superposition of relatively few specularly reflected rays having similar Doppler shifts (to account for the observed temporal fading) and closely spaced angles-of-arrival (to account for the observed spatial fading). However, the resolution of a complex valued space-time mode wavefield into a number of component rays with a very wide aperture antenna array has not previously been carried out and reported in the open literature. As a result, quantitative information regarding the ability of such a model to represent the mode wavefields received by a very wide aperture array over typical OTH radar CPI was not previously available.

After some preliminary investigations which were used to illustrate the characteristics of the received wavefront distortions and their time-evolution, the MUSIC space-time superresolution algorithm was used in this chapter to resolve the fine structure of ionospheric modes recorded by the Jindalee receiving array on a controlled mid-latitude propagation path. Quantitative measures were developed to assess the accuracy with which the model was able to represent the experimentally recorded wavefields, the physical significance of the various resolved rays was also tentatively interpreted on the basis of oblique incidence ionograms recorded for the path.

The experimental results indicate that over time intervals in the order of a few seconds the ionospheric modes recorded by the Jindalee array could be represented to fitting accuracies above 90 percent using four rays or less over a large percentage of the data set analysed. However, time-variation of the ray parameters were observed from one dwell to another as a result of motions in the ionosphere. These variations imply that as the CPI increases the number of rays required to maintain a certain modelling accuracy will also

increase. As a consequence, the deterministic ray interference model is not suitable for representing the characteristics of a complete data set received over an interval of a few minutes.

CHAPTER 3

Stationary statistical model

In applications such as OTH radar it is useful to have an accurate model for the space-time complex (amplitude and phase) fading of HF signals reflected by a single ionospheric layer over time intervals which *exceed* a few seconds. For reasons mentioned in the previous chapter, a deterministic wave interference characterisation of such fading processes becomes inconvenient and difficult to interpret intuitively when the time interval is lengthened to a few minutes. If the complex fading process can be treated as a stationary random process over such time periods it is then possible to conveniently model the space-time characteristics of the received data in a statistical sense. This chapter is devoted to the development and experimental validation of space-time statistical models for HF signals which are received over a period of a few minutes by a very wide aperture antenna array after a single-hop oblique ionospheric reflection. The principle motivation is to develop models which accurately portray the second order statistics of the received signals with relatively few parameters that can be easily interpreted intuitively and extrapolated if required to estimate system performance.

Section 3.1 contains background information and a literature review on the use of statistical models for characterising HF signals returned to the ground by the ionosphere. Both empirical and physical models of HF signals reflected from a random ionosphere are considered and special attention is paid to statistical models which have been validated by experimental data analysis. In section 3.2, space-time statistical models of the fading process are derived from physical principles to describe the reflection of HF signals from a "random" ionosphere. This physical interpretation of the fading process may also be used to explain the connection between the deterministic wave interference model and the stationary statistical models. It is emphasised that the verification of the physics itself is beyond the scope of this research which is primarily concerned with comparing the statistical properties of the model against those of the received signals. The hypothesis tests used to accept or reject the proposed statistical models from realisations of the data are described in section 3.3 while the model validation criteria associated with these tests are applied to experimental data in section 3.4.

3.1 Literature Review

The background information in section 3.1.1 explains the relative advantages and shortcomings of using statistical models to represent the characteristics of ionospherically propagated HF signals rather than deterministic wave interference models. Section 3.1.2 contains a review of the statistical HF signal models reported in the literature, the physical and empirical models considered are those which can be used to describe the statistical properties of the reflected wavefields measured by either a single antenna over time or by a collection of spatially separated antenna sensors over space and time. Section 3.1.3 provides motivation for conducting further research regarding the *space-time* statistical properties of HF signals reflected by a single ionospheric layer and explains its significance in terms of the construction of realistic multi-sensor HF signal processing models.

3.1.1 Background

A HF signal returned to the ground by a single ionospheric layer has an amplitude and phase which is found to fluctuate over space and time with respect to the ideal case of specular reflection (i.e., a plane wave with a constant direction-of-arrival and Doppler shift). This observation leads to the conclusion that an individual layer in the ionosphere must have properties which are time varying and cannot be considered uniform on the horizontal plane. In other words, what is usually thought of as a single plane wave must in reality be a collection of waves scattered by the presence and movement of irregularities in the ionosphere.

In the previous chapter, a superposition of relatively few plane waves with different angles-of-arrival and Doppler shifts was used to model the complex fading of HF signals reflected by individual ionospheric layers over time intervals in the order of a few seconds. Although the wave interference model was often able to accurately represent the experimentally observed space-time fading processes with less than four components, it was found that the parameters of this model changed or "aged" significantly as the observation interval was increased beyond a few seconds. Consequently, over time intervals of a few minutes an accurate representation of these fading processes can only be obtained by regularly updating the model parameters or by increasing the model order. Both of these alternatives lead to a specification of the fading process which becomes quite complex and difficult to understand intuitively when the time intervals of interest extend well beyond a few seconds. For this reason, the wave interference model may be inappropriate in applications which require a complete data set received over several minutes to be characterised in a concise manner (i.e., with relatively few parameters) that can be readily interpreted intuitively.

From both physical interpretation and experimental data analysis it is evident that the fading produced on the ground by the ionospheric reflection process is better treated as

a random process rather than a deterministic process when the length of the observation interval exceeds a few seconds. Unlike the wave interference model, the fading produced by a random process is not completely predictable so it cannot be described in exact terms. Such processes are usually specified in terms of their statistical properties and one of the most important features of a random fading process from this point of view is its auto-correlation function in the dimensions of space, time or space-time.

If the statistical properties, which are governed by the joint probability density function of the fading process, are time-invariant within the observation interval then the processes is said to be *temporally stationary*, and if these properties are the same when measured at different positions in space within a particular region then the process is said to be *spatially homogeneous*. A random process is referred to as *spatially stationary* if the joint density of the observations made at two locations separated by a fixed distance and direction is independent of absolute location within a particular region of space. When this density function depends only on the distance between two points and not the relative orientation of one from the other the process is referred to as *isotropic*.

The HF signal fading processes produced by reflection from a single ionospheric layer are known to be nonstationary in frequency, time and space but if attention is restricted to narrowband signals of bandwidths less then 20 kHz, time intervals in the order of a few minutes and apertures not larger than a few kilometres, then it is more likely that the wavefield samples collected by an antenna array can be adequately described by a stationary complex-valued space-time random process. The statistical characterisation of signals with such bandwidths, over these time intervals and spatial extents is of great relevance and potential importance to the operation of OTH radar systems. Such models are useful not only for the purpose of frequency management (i.e., the task of optimising the selection of operating frequency and bandwidth from a number of available frequency channels) but also for guiding the design and optimisation of adaptive array signal processing algorithms which can enhance target detection in the presence of both coherent and incoherent interference.

Statistical models of random signals can be broadly categorised as either empirical models, which are formulated solely on the basis of experimental data analysis, or physical models which are derived from consideration of the physical phenomena assumed to give rise to the observed data characteristics. Experimentally validated empirical models have already been developed to describe the *temporal-only* characteristics of HF signals reflected by individual ionospheric layers. These stationary statistical models describe the fading in amplitude and phase as a complex Gaussian process which is fully characterised by its second order statistics (i.e., the temporal auto-correlation function or power spectral density). In these models, which will be described in the next section, the fading process is described by an even power spectral density function which is parameterised by two numbers; the mean Doppler shift and the Doppler spread.

The advantage of such a representation is that it concisely provides a user with a

direct indication of the expected system performance as in most cases target detection and spectrum estimation are intimately linked. As far as the HF reflection channel is concerned, an analogous space-time statistical model of HF signals reflected by individual ionospheric layers is yet to be experimentally validated. Such a model is of paramount importance in guiding the design and optimisation of spatial-only and space-time adaptive processing algorithms. For this reason, this chapter is devoted to the development and experimental validation of space-time statistical models for HF signals propagated by a single-hop mid-latitude oblique ionospheric path.

3.1.2 Statistical models of HF signals

A vast quantity of measurements have been published on the propagation of HF signals by ionospheric reflection. It is therefore necessary to establish a crude sorting scheme which can be used to classify such measurements. For example, have the measurements been made at one antenna or at multiple spaced antennas and has the amplitude and/or phase of the wavefield been recorded. Other important factors which influence the data characteristics is the rate and spatial separation at which measurements are taken and whether they arise from a single magneto-ionic component, a single mode or two or more superimposed modes. In general, the characteristics of the measurements will also depend on whether observations are made on a one-hop or multi-hop ionospheric path, whether the E, Es or F layer is involved in signal reflection and if the geographic location of the path is in the mid-latitude, auroral or equatorial region.

The CCIR report (CCIR 1970) contains a comprehensive list of references to experimental and theoretical results on the subject of amplitude fading at a single antenna. In many studies, the amplitude of the received signal at different times is treated as a random variable and assigned a probability density function. Experimental evidence suggests that amplitude fading records obtained over intervals in the order of a few minutes have samples whose distribution can be approximated fairly closely by the Rayleigh distribution or the Nakagami-Rice distribution, see (Barnes 1992) for example. The Rayleigh distribution is actually a special case of the Nakagami-Rice distribution when there is no steady or deterministic amplitude component in the received signal. Both of these parametric distributions have generally been accepted as being representative of amplitude fading under a wide variety of conditions.

A model of the probability density function for the received signal amplitude is necessary but not sufficient to construct a satisfactory representation of the received signal. As far as the amplitude is concerned, some specification of the correlation between different samples is often required to model the fading rate of the signal. In the CCIR report (CCIR 1970) the auto-correlation function of the amplitude fluctuations is assumed to have a Gaussian form and the fading period is defined as the standard deviation of the Gaussian auto-correlation function which best fits the observed measurements. Under

multimode conditions, values in the range of 0.5 to 2.5 seconds are typical (CCIR 1970), whereas for a single magneto-ionic component, fading periods in the order of minutes can be found (Balser and Smith 1962).

Measurements of the *spatial* correlation between amplitude fluctuations received simultaneously at spaced antennas were made by (Balser and Smith 1962) over a 1600 km mid-latitude path. A pulsed waveform was used to separate the different propagation modes and the amplitude of the wavefield were sampled by a uniform linear array composed of 6 whip antennas spaced 610 m apart. For single modes it was found that the diversity distance, defined as the spatial separation at which the correlation coefficient falls to 0.5, was in the order of 40 wavelengths for one-hop paths and 10 wavelengths for multi-hop paths. As pointed out by (Sweeney 1970), these values correspond to an angular spread of about 0.2 degrees and 1 degree respectively.

These measurements, and earlier ones referenced in (Booker, Ratcliffe and Shinn 1950), have led researchers to picture a single ionospheric mode as a single ray specularly reflected by a smooth ionosphere surrounded by a cone of rays produced by the roughness of the ionosphere. The former is often referred to as the specular or coherent component by analogy with specular reflection from a mirror while the latter is known as the diffracted or incoherent component which is scattered by irregular reflection from a rough surface. The coherence ratio of a particular mode is defined as the ratio of the power in the specular component to that in the diffracted components and is a measure of the size of the amplitude and phase "crinkles" in the downcoming wavefronts.

Several investigators have estimated the coherence ratio of ionospheric modes using either amplitude measurements at one antenna or phase difference measurements between two spaced antennas. When a specular component is present the amplitude is assumed to be distributed according to the Nakagami-Rice density function which is parameterised by the power of the steady component relative to that of the random components (i.e., the coherence ratio). A more sensitive technique for estimating the coherence ratio is based on the theory of phase measurements at spaced receivers (Whale and Gardiner 1966). Starting from the Nakagami-Rice distribution, the authors derived curves for the standard deviation of the phase difference measured at two spaced receivers in terms of the coherence ratio and the generalised spatial auto-correlation function of the diffracted components.

A summary of the experimental measurements of coherence ratio can be found in (Gething 1991) with references to the original papers. For example, (Bramley 1951) quoted the square root of the coherence ratio $b = 2.5$ as being fairly typical while (Hughes and Morris 1963) calculated values ranging from $b = 0.4$ to $b = 1.9$, although in the latter case CW signals were used and the data may have contained more than one propagation mode. A more recent analysis by (Warrington et al. 1990) concluded that the coherence ratio $B = b^2$ was between 0 and 7 under "approximately single moded propagation" but values greater than 40 were estimated when the same data was interpreted as specular

component with a *variable* direction-of-arrival plus a cone of diffracted components. It is noted that the estimates of coherence ratio vary quite markedly from one analysis to another. This observation prompted (Gething 1991) to comment that "even allowing for the expected variability of the ionosphere from day to day, results obtained by various investigators do not seem entirely consistent".

In the investigation by (Boys 1968) it was inferred that there is, strictly speaking, no specular component but only a group of rays coming from very similar directions with no common phase history. In other words, (Boys 1968) regarded the true coherence ratio as zero which implies that the reflected signal is considered as a completely scattered wave whose spatial correlation function depends on the angular power spectrum of the diffracted components scattered by the roughness of the ionosphere. This view was supported by experimental measurements of a Radio Australia broadcast at 17.870 MHz which was propagated by a one-hop reflection from the F2-layer over a 2700 km mid-latitude path. Phase measurements were made at 10 vertical whip antennas spaced approximately 50 metres apart with a central antenna providing the phase reference. Over a five minute interval (Boys 1968) noted that the plane wave of best fit to the data did not wander in direction-of-arrival. The author concluded that over such time intervals the characteristics of the received wavefield are best expressed in terms of the angular power spectrum of the wavefront distortions. This power spectrum was assumed to have a Gaussian form and the standard deviation was found to be between 0.1 to 0.3 degrees.

A purely statistical representation of the reflected wave is consistent with the theory developed by (Booker et al. 1950). The authors thought of the ionosphere as an irregular screen or diffraction grating which randomly varies the re-radiated electric field distribution just beyond the horizontal surface of the screen. It was mathematically deduced that the generalised spatial auto-correlation function of the electric field received on a parallel plane a finite distance away from the screen (say on the ground) is the same as that of the electric field distribution which gives rise to it (i.e., that just beyond the horizontal surface of the screen). In other words, the angular power spectrum of the wavefield received on the ground is given by the Fourier transform of the spatial auto-correlation function of the electric field irregularities just beyond the rough diffracting screen.

A phase changing screen is the usual condition as far as the ionosphere is concerned (Whale and Gardiner 1966). As explained by (Boys 1968), a variation in the electron density causes a change in the real part of the refractive index only and this causes a change in phase. Since the number of irregularities is large, the emergent wave is considered to have a randomly varying phase with a constant amplitude at all points which is, of course, the description of an idealised phase screen. From a physical view point, a phase changing screen seems realistic as most of the irregularities occur in the E and F regions where the collision frequency and hence the attenuation are small (Boys 1968). Alternatively, the presence of irregularities is viewed by (Bowhill 1961) as forming a "buckled" specular reflector which acts as a phase screen for normally (and obliquely)

incident waves. At oblique incidence the phase change it causes on the wave is reduced by a factor of $\cos\theta_i$ where θ_i is the angle relative to normal incidence. This is related to the phenomenon that an optical surface becomes more nearly a specular reflector at grazing incidence ($\theta_i \rightarrow 90$ degrees), the author notes that the same effect is observed for radio waves.

Most authors have concentrated on ionospheric models which are phase changing screens, but it should be noted that the theory of diffraction from an irregular ionosphere in (Booker et al. 1950) is based on a *single* ionospheric pass or reflection. Signals from very distant sources usually involve multiple ionospheric reflections and intermediate scattering from terrain or sea-surface. Such signals do not satisfy the requirements of this theory and are therefore not expected to obey models derived from it. It is commonly assumed that the two-dimensional spatial auto-correlation function of the phase screen irregularities has a two-dimensional Gaussian form, as in (Bramley 1955) and (Bowhill 1961) for example. In the special case of an isotropic screen, this function is only dependent on distance and not direction along the screen. It is noted that in these theoretical studies little if any consideration is given to the type of ionosphere which would produce such irregularities and the proposed spatial models were not validated against experimental measurements.

Using the theory developed by (Booker et al. 1950) it is possible to define a *characteristic* size or length of irregularities as the distance between two points on the ground for which the generalised auto-correlation of the wavefield falls to a value of 0.5 (Briggs and Phillips 1950). In the study by (Briggs and Phillips 1950), three receivers placed at the corners of an isoceles right angled triangle with side 130 m were used to observe the amplitude fading of "single echoes" of a pulse transmitter reflected by the ionosphere at vertical incidence. By assuming that fading was predominantly due to a diffraction pattern of constant form which drifts over the ground at a constant velocity, the temporal auto-correlation function at the receivers was translated into a spatial auto-correlation function from which irregularity scale sizes in the order of 100-200 m were estimated for the F-region.

The first rigorous experimental confirmation of a stationary statistical model for the temporal amplitude and phase characteristics of narrowband signals propagated over a period of a few minutes across a mid-latitude ionospheric path was published by (Watterson, Juroshek and Bensema 1970). The authors used formal hypothesis tests to show that the baseband signal received in a single channel may be described by a zero mean complex Gaussian process that produces Rayleigh amplitude fading. This is in accordance with a completely scattered wave since the Nakagami-Rice distribution tends to the Rayleigh density when there is no steady or specular component. The temporal modulation processes imposed by the ionosphere on different ionospheric modes (i.e., reflections from different ionospheric layers or regions) were found to be statistically independent. The observed amplitude and phase fluctuations induced by the HF channels were characterised by their Doppler spectrum which was shown to be, in general, the sum of two Gaussian

functions of frequency, one for each magneto-ionic component.

3.1.3 Significance of research relative to previous work

It is evident from the literature review that much attention has been focussed in either the temporal domain or the spatial domain and that the only experimentally validated statistical model of ionospherically propagated HF signals is for single receiver systems (Watterson et al. 1970). A *space-time* statistical model of the amplitude and phase of narrowband signals reflected by different layers in the ionosphere has, as yet, not been experimentally confirmed. Such a model would be of particular value in the design and analysis of spatial-only or space-time adaptive processing algorithms which are becoming increasingly popular in practical HF antenna array systems. Hence, the purpose of this chapter is to develop and experimentally validate a space-time statistical model of the ionospheric reflection channel. Such a model is required to express the space-time statistical characteristics of the HF channel in a concise manner which can be interpreted from both signal processing and physical perspectives.

The question then arises as to the connection between the wave interference model used to characterise short data sets (in the order of a few seconds) and the stationary statistical models used to characterise longer data sets lasting a few minutes. To provide a possible answer it is instructive to compare the physical interpretation of both models. A common interpretation for the different specular components in the wave interference model is that they originate from spatially separated reflection points in a particular ionospheric layer that are effectively smooth over at least one Fresnel zone. Whereas the common physical interpretation of the statistical model is that signal reflection occurs over a single localised region of an ionospheric layer, rather than at a number spatially separated points, and that over this region the layer exhibits a degree of roughness rather than being effectively smooth over at least one Fresnel zone.

At a particular time instant the phase screen which is equivalent to the irregular structure of the ionosphere in the latter interpretation may be resolved into its spatial Fourier components. Each (two-dimensional) spatial frequency component in the spectral decomposition of the surface gives rise to its own specular component which is reflected in a direction determined by the spatial frequency of the field disturbance at the screen. If the so-called "buckles" of the irregular ionospheric surface do not vary rapidly with distance in any direction then only a few spatial frequency components are required to accurately approximate the character of the buckles and hence the equivalent phase screen of the surface. The dominant spatial frequency components which approximate this structure at a particular time will each radiate a specular component; these superimpose with one another to produce a wave interference fading pattern on the ground.

As the surface changes with time its character will be represented by different spatial frequency components. However, the structure of such a surface evolves slowly with time

over a few seconds as signals received from isolated modes over such intervals are almost coherent for quiet mid-latitude conditions. It is therefore plausible that over a period of a few seconds the spatial frequency components which dominate the form of the surface at a particular time instant remain approximately constant and the time-evolution of the surface is described by a combination of these components with different relative phases. The relative phases are determined by the differential Doppler shifts associated with these components which may also be considered more or less regular over these relatively short time intervals. This explanation is a possible interpretation of the space-time wave interference model in terms of reflection from a slowly evolving spatially irregular surface.

Over longer periods of time, in the order of a few minutes, the surface will be described by a large number of different spatial frequency components which radiate energy over a distribution of directions. If such a signal can be treated as a statistically stationary signal over the observation interval then the probability density function of the radiated components in direction-of-arrival and Doppler shift forms the space-time power density of the signal. Apart from this qualitative explanation of the connection between the wave interference and statistical wavefield models, it is noted that the available data cannot be used to make definite conclusions about the different *physical interpretations* of the wave interference model. Consequently, the verification of the physical origin of the wave interference model and its hypothesised connection to the statistical models is beyond the scope of this research.

3.2 Ionospheric reflection of radio waves

The aim of this section is to propose a physical model for the space-time statistical properties of HF signals which are propagated over long distance oblique paths by reflection from the ionosphere. Such a model allows the space-time statistical properties of the reflected wavefield received by an array of antennas on the ground to be related to the physical characteristics of the ionospheric reflection process. The physical model is based on the theory which governs the reflection and transmission of transverse electromagnetic waves from an interface between two media; one free space and the other ionospheric plasma.

HF signals reflected by the ionosphere are known to fluctuate in amplitude and phase with respect to time and space. The fading observed on the ground is produced by the time-evolution of irregular ionospheric structures which give rise to signal reflection. Section 3.2.1 proposes a physical model of the ionospheric reflection process which can be used to determine the spatial structure of the wavefield received on the ground after reflection from an irregular ionosphere of constant form. The time evolution of the irregular ionospheric structure which produces fading on the ground is considered in Section 3.2.2 to derive the generalised space-time auto-correlation function of the received signal-field in terms of the statistical parameters which describe the ionospheric reflection process.

3.2.1 Reflection from an irregular ionosphere

In the experimental situation of interest, a "point source" transmitter illuminates a volume of ionosphere and after a single-hop reflection the signal is returned to the ground where an array of antennas samples the amplitude and phase of the reflected wavefield. The aim of this section is to derive a mathematical expression which describes the wavefield produced on a plane which contains the receiving antenna array by an irregular ionospheric structure of *constant form*. In practice this constant structure represents a snapshot of the ionosphere at a particular instant in time.

It is worth mentioning that the mathematical expressions describing the received signal-fields in this section are not derived from a strictly physical perspective. The physical concepts introduced to derive these expressions may be regarded as analogous replacements of the true physics occurring in the ionosphere, this more simplistic approach is frequently used for the purpose of deriving mathematical models of the received signal-fields. In other words, this section does not attempt to describe the physics which is actually occurring to produce the received signal-fields but rather to use some well-known analogous physical concepts to derive models for the received signal-fields and their space-time second order statistics.

3.2.1.1 Qualitative description of the reflection process

In the absence of *large-scale* horizontal gradients in the electron concentration profile the received signal will be reflected from a region of ionosphere near the mid-point of the path between the transmitter and receiver. Even if the ionosphere in this region were horizontally uniform the variation in plasma density with altitude may give rise to more than one solution for the elevation angle of incidence of the transmitted signal which is totally internally reflected towards the receiver. Stated another way, the condition of total internal reflection may be satisfied at the path mid-point at a number of more or less discrete ionospheric heights within the continuum of heights which are illuminated by the intersection of the transmit and receive antenna elevation radiation patterns.

For a horizontally smooth ionospheric layer it is shown by (Davies 1990) that two solutions exist over a single-hop oblique path when a model of the plasma density height profile is assumed and the effect of the earth's magnetic field is neglected. These two solutions are known as the high and low angle rays, these rays have different angles of incidence and are reflected from different virtual heights in the ionosphere. For fixed transmitter and receiver locations, the difference in the virtual reflection heights depends on the plasma density profile and the frequency of operation. In very thin layers, such as sporadic-E for example, the high and low angle rays travel nearly identical paths as the two solutions for the elevation angle of incidence converge to a single ray solution, while in thicker layers, such as the F-layer, this is not always the case so the virtual reflection heights of the high and low angle rays may be quite different. This section considers

these solutions separately and for each ray it aims to represent the wavefield reflected by a horizontally irregular ionosphere of constant form rather than a smooth ionosphere.

In the vicinity of the path mid-point, where signal reflection towards the receiver effectively occurs, the iso-ionic contours of the ionosphere may not be horizontally uniform so the plasma particles which reflect a particular ray will be distributed at different heights over a region of space. If this reflection region were regarded as an iso-ionic plasma surface it is reasonable to imagine that at a particular time instant the height of different points on such a surface varies in some manner about a mean horizontal plane of finite extent. This horizontal plane is imagined to be at some mean height above the ground with its "centre" at the path mid-point, experimental results suggest that the dimensions of its sides are typically in the order of a few kilometers for relatively stable ionospheric conditions (Gething 1991). Regular vertical movement of the mean horizontal plane with respect to time may be interpreted as imposing a mean Doppler shift on the signal while changes in the spatial structure of the irregular reflection surface about this horizontal plane causes the signal received on the ground to fluctuate or fade.

For oblique paths spanning a long ground distance (greater than 1000 km), the separation between the transmitter and the reflection region is much greater than the spatial extent of this region so the signal incident upon the reflecting surface may be regarded as a plane wave. This surface may be uneven in height close to the path mid-point due to wave-like disturbances and the presence of electron density irregularities in the ionosphere. Moreover, the shape of the surface may change in an unpredictable or random manner with time due to the motion of these wave-like disturbances and irregularities.

When the surface changes in a random way it will cause random fluctuations in the signal received on the ground. In order to relate the statistical properties of the received signal to those of the reflecting surface it is first necessary to develop an equation which expresses the wavefield on the ground for a given realisation of the surface (i.e., for the spatial structure of the surface "frozen" at an instant in time). In this problem, the interface at which the incident wave is reflected may be described by a position vector $\vec{r}_s = [x, y, z_s(x, y)]$ where the roughness of the reflecting iso-ionic surface is described by the plasma displacement function $z_s(x, y)$. Specular reflection will occur from a flat surface xy-plane (i.e., $z_s(x, y) = 0$). The interaction between the incident wave and the plasma in regions of ionosphere below the reflecting surface $z < z_s(x, y)$ is neglected while the region above the surface $z > z_s(x, y)$ does not influence the wave which is assumed to be totally internally reflected by a thin layer of plasma of constant electron density at heights $z_s(x, y) - \eta < z < z_s(x, y) + \eta$.

Experimental evidence suggests that the plasma displacements $z_s(x, y)$ in the surface are highly correlated on a spatial scale greater than one wavelength for quiet mid-latitude ionospheric conditions since the wavefronts received from *individual modes* on such circuits generally exhibit a high degree of planarity, as demonstrated by the analysis in chapter 2. Furthermore, significant changes in the structure of this surface only occur over time-scales

greater than about 0.1 second since over smaller intervals the signal returned at a point on the ground is observed to be almost coherent. In simple terms, previous data analysis suggests that the reflecting surface does not have much structure over distances less than one wavelength and that over time periods commensurate with the radar pulse repetition interval the structure of the surface may be considered to be of constant form. These characteristics may not be accurate in ionospheric regions near the equator or auroral zones as measurements made on such paths indicate that the ionosphere is significantly more disturbed than it is in quiet mid-latitude areas.

3.2.1.2 Mathematical representation of the reflected field

Consider a linearly polarised transverse electromagnetic wave with wave vector $\vec{k}_i$ propagating in a direction that is incident at an angle θ_i with respect to the normal of the xy-plane. The electric field $\vec{E}_i(\vec{r}_s)$ which is incident on the reflecting surface at position $\vec{r}_s$ is then given by,

$$\vec{E}_i(\vec{r}_s) = \vec{E} \exp(-j\vec{k}_i \cdot \vec{r}_s) \tag{3.1}$$

where $\vec{E}$ represents the electric field intensity phasor in the vicinity of the surface after the path loss from the transmitter (inverse square law) has been taken into account. Boundary conditions apply at the surface and assuming there is no transmitted wave it follows that the reflection factor of the tangential component of electric field is $\Gamma = -1$. In other words, the plasma surface behaves like an irregular metal sheet and the *reflected* field distribution $\vec{E}_r(\vec{r}_s)$ *at the surface* is then given by,

$$\vec{E}_r(\vec{r}_s) = \vec{E} \exp(j\vec{k}_r \cdot \vec{r}_s) \tag{3.2}$$

where $\vec{k}_r$ is the wave-vector of the reflected wave such that the angle-of-incidence equals the angle-of-reflection $\theta_i = \theta_r$. The angular spectrum of the reflected signal is given by the spatial Fourier transform of the re-radiated electric field distribution over the surface. Using this result, the electric field resulting at some point $\vec{r}$ on the ground can be expressed as a superposition of plane waves combined with amplitudes and phases determined by the Fourier coefficients.

Evaluation of the spatial Fourier transform over an irregular time-varying surface is not mathematically tractable for the purpose of determining the statistical properties of the reflected wavefield. An alternative approach is to translate the plasma displacements $z_s(x, y)$ occurring at a given time into equivalent phase shifts on a field which is re-radiated from the mean horizontal plane. In other words, the idea is to replace the time-varying irregular plasma surface by flat "phase screen" fixed in the xy-plane which imposes a space and time varying phase modulation on the re-radiated field at each point on the screen that is determined by the prevailing plasma displacement at that point.

As the separation between the reflecting surface and the receiver array is much larger than the spatial extent of the surface, the field contribution received on the ground from each radiating current element on the surface is that which propagates over a very narrow spread of directions centred about $\vec{k}_r$ (i.e., the direction of the specular reflection corresponding to the transmitter and receiver locations). Moreover, the surface is assumed to have a relatively flat character so most of the energy scattered near the path mid-point will be in the direction of specular reflection. For propagation in the direction of $\vec{k}_r$, a radiating plasma element with a displacement $z_s(x,y)$ normal to the xy-plane can be replaced by an identical element which is on the xy-plane at position $\vec{r}_{xy} = [x,y,0]^T$ and phase shifted by $\exp(-j\frac{2\pi}{\lambda} z_s(x,y)\cos\theta_i)$. This transformation is only strictly valid for a point which is far from the radiating surface and in the direction of specular reflection since $z_s(x,y)\cos\theta_i$ is the difference in path length between the actual and substituted plasma elements to such a point. After this transformation, the wavefield received by an array on the ground can be thought of as arising from a radiating phase screen in the xy-plane with a re-radiated electric field distribution given by,

$$\vec{E}_r(\vec{r}_{xy}) = \vec{E} e^{-j\frac{2\pi}{\lambda} f(\vec{r}_{xy},\theta_i)} \exp(j\vec{k}_r \cdot \vec{r}_{xy}) \tag{3.3}$$

where the position vector $\vec{r}_{xy}$ spans the phase screen which is of finite spatial extent in xy-plane and $f(\vec{r}_{xy},\theta_i) = z_s(x,y)\cos\theta_i$. As described by (Booker et al. 1950), the angular spectrum of the reflected signal $P(\vec{k})$ is given by the spatial Fourier transform of the electric field distribution $\vec{E}_r(\vec{r}_{xy})$ which is re-radiated by the phase screen. As the original plasma surface is assumed to have no structure of size less than one wavelength it follows that the re-radiated field distribution has no spatial frequency component greater than the reciprocal of one wavelength. If these components were to exist they would radiate evanescent waves (Booker et al. 1950) which propagate only a short distance away from the screen and may be neglected as far as their contribution to the field measured on the ground is concerned. When evanescent waves are neglected, the angular spectrum of waves $P(\vec{k})$ which propagate with wave-vector $\vec{k}$ can be calculated according to the spatial Fourier transform in Eqn.(3.4).

$$P(\vec{k}) = \int_{screen} \vec{E}_r(\vec{r}_{xy}) e^{-j\vec{k}\cdot\vec{r}_{xy}} d\vec{r}_{xy} = \vec{E} \int_{screen} e^{-j\frac{2\pi}{\lambda} f(\vec{r}_{xy},\theta_i)} e^{-j(\vec{k}-\vec{k}_r)\cdot\vec{r}_{xy}} d\vec{r}_{xy} \tag{3.4}$$

In the case of a perfectly flat reflecting surface of constant dielectric susceptibility the function $f(\vec{r}_{xy},\theta_i) = 0$. As the dimensions of the screen are much larger than the wavelength λ, the angular spectrum of the re-radiated wave tends to the delta function $P(\vec{k}) \to \delta(\vec{k}_r)$ when $f(\vec{r}_{xy},\theta_i) = 0$ which corresponds to a specular reflection of the incident wave. It is also evident that the effect of the plasma displacements on the angular spectrum depends on the angle of incidence θ_i because for a given plasma displacement the amount of phase modulation is determined by θ_i through the relationship $f(\vec{r}_{xy},\theta_i) = z_s(x,y)\cos\theta_i$. As the

ray tends towards grazing incidence ($\theta_i \rightarrow 90$ degrees) the phase modulation imparted by plasma displacements is reduced by a factor of $\cos\theta_i$ which makes the reflecting plasma surface appear relatively less rough to the wave which becomes more nearly specularly reflected.

Once the angular spectrum of the reflected signal is known for a certain plasma disturbance, it is possible to represent the signal-field received by an array in the plane $z = z_g$ on the ground by a superposition of plane waves.

$$\vec{E}_r(\vec{r}_g) = \int P(\vec{k}) e^{j\vec{k}\cdot\vec{r}_g} d\vec{k} \quad , \quad \vec{r}_g = [x, y, z_g] \tag{3.5}$$

For over-the-horizon propagation the only field measured by the array is the reflected field $\vec{E}_r(\vec{r}_g)$ as there is no line of sight between the transmitter and receiver. For a wave-vector with components $\vec{k} = [k_x \; k_y \; k_z]^T$ it is possible to substitute $\vec{k} \cdot \vec{r}_g = \vec{k} \cdot \vec{r}_{xy} + k_z z_g$ into Eqn.(3.5) to yield,

$$\vec{E}(\vec{r}_g) = \int Q(\vec{k}, z_g) e^{j\vec{k}\cdot\vec{r}_{xy}} d\vec{k} \quad , \quad \vec{r}_{xy} = [x, y, 0] \tag{3.6}$$

where $Q(\vec{k}, z_g) = P(\vec{k}) e^{jk_z z_g}$. It is evident from Eqn.(3.6) that $Q(\vec{k}, z_g)$ represents the spatial Fourier transform of the of field existing in the plane $z = z_g$ which contains the antenna array. As $z_g \rightarrow \infty$ the electric field intensity observed on such a plane is referred to as the Fraunhoffer pattern in diffraction studies. The Fresnel pattern, which corresponds more nearly to that formed by an ionospherically reflected radio wave on the ground, is that which is produced on a parallel plane at a finite distance z_g away from the screen. The relationship between the spatial Fourier transform of the field at the phase screen and that on a parallel plane a finite distance away from this screen will be exploited in the next section to derive models for the generalised space-time auto-correlation function of the field received by the array.

3.2.2 Reflection from a time-varying irregular ionosphere

The aim of this section is to extend the previous analysis to deal with a time-varying irregular ionospheric structure and to determine the statistical properties of the wavefield received on the ground in terms of the statistical properties of this structure. It is shown in this section that the generalised *space-time* auto-correlation of the Fresnel diffraction pattern is, under certain conditions, the same as that of the field distribution at the screen which gives rise to it. The analysis proceeds similarly to that which was undertaken in (Booker et al. 1950) for the spatial-only auto-correlation function of the electric field produced on a plane a finite distance away from a two dimensional random diffracting screen.

3.2.2.1 Space-time second order statistics of received signal

To take temporal changes of the irregular surface into account the quantity $P(\vec{k},t)$ is introduced and defined as the angular spectrum of the wave-field which results from the time-varying surface $z_s(x,y,t)$ and phase screen function $f(\vec{r}_{xy},\theta_i,t) = z_s(x,y,t)\cos\theta_i$. This angular spectrum is calculated according to Eqn.(3.4) by substituting $P(\vec{k},t)$ for $P(\vec{k})$ and $f(\vec{r}_{xy},\theta_i,t)$ for $f(\vec{r}_{xy},\theta_i)$. The relationship $Q(\vec{k},t) = P(\vec{k},t)e^{jk_z z_g}$ follows by a similar argument to that described in the previous section, the implicit dependence of $Q(\vec{k},t)$ on z_g has been dropped for notational convenience. Although the ionosphere changes in a continuous manner it does so very slowly compared with the propagation time between the surface and the ground (typically a few microseconds), or over the PRI for that matter (typically less than 0.1 second), so the reflected field generated at a particular instant t will propagate to the plane containing the array and remain more or less constant for a finite period of time. This allows the array to measure the field produced by a more or less frozen ionospheric structure before the field changes by an amount that is sufficiently large for the measuring instrument to detect.

The space-time Fourier transform $P(\vec{k},f_v)$ which describes the spatial and temporal variations of the field disturbance *at the phase screen* is given by,

$$P(\vec{k},f_v) = \int_{-\infty}^{\infty} P(\vec{k},t)e^{-j2\pi f_v t}dt \tag{3.7}$$

where f_v represents the different frequency components in the temporal fluctuations of the electric field disturbance at the screen. Similarly, the space-time Fourier transform of the field in the plane $z = z_g$ is given by $Q(\vec{k},f_v) = P(\vec{k},f_v)e^{jk_z z_g}$. The Weiner-Khintchine theorem states that the auto-correlation of a function is given by the inverse Fourier transform of its power spectrum. In this case we have a space-time power spectrum $|P(\vec{k},f)|^2$ for the field at the screen so the generalised auto-correlation function of the field at the screen $r(\vec{\Delta}d,\Delta t)$ is given by,

$$r(\vec{\Delta}d,\Delta t) = \frac{\int\int |P(\vec{k},f_v)|^2 e^{j\vec{k}\cdot\vec{\Delta}d}e^{j2\pi f_v\Delta t}d\vec{k}df_v}{\int\int |P(\vec{k},f_v)|^2 d\vec{k}df_v} \tag{3.8}$$

where Δt is the time interval and $\vec{\Delta}d = [\Delta x,\Delta y,0]^T$ is the vector displacement over the screen. At the plane $z = z_g$, the auto-correlation function is given by the same theorem,

$$r_z(\vec{\Delta}d,\Delta t) = \frac{\int\int |Q(\vec{k},f_v)|^2 e^{j\vec{k}\cdot\vec{\Delta}d}e^{j2\pi f_v\Delta t}d\vec{k}df_v}{\int\int |Q(\vec{k},f_v)|^2 d\vec{k}df_v} \tag{3.9}$$

but $|P(\vec{k},f_v)|^2 = |Q(\vec{k},f_v))|^2$ which implies that $r_z(\vec{\Delta}d,\Delta t) = r(\vec{\Delta}d,\Delta t)$. In words, the generalised space-time auto-correlation of the field distribution measured on a plane $z = z_g$ (i.e., that of the Fresnel diffraction pattern) is the same as that of the field distribution

at the screen which gives rise to it. This important result is a space-time generalisation of the one-dimensional spatial-only result reported by (Booker et al. 1950). Strictly, the equivalence is only for the generalised (normalised) auto-correlation function as the amplitude of the field diminishes according to the inverse square law as it propagates from the screen to the plane containing the array.

To calculate the generalised space-time auto-correlation function of the field received by the antenna array the time-varying field at the screen $\vec{E}_r(\vec{r}_{xy}, t)$ is introduced. This field is given by Eqn.(3.3) after replacing the "frozen" plasma-displacement function $f(\vec{r}_{xy}, \theta_i)$ by the time-varying function $f(\vec{r}_{xy}, \theta_i, t)$. Once this substitution is made, the space-time auto-correlation function of the field distribution at the screen is given by,

$$r(\vec{\Delta}d, \Delta t) = \frac{\int\int \vec{E}_r(\vec{r}_{xy}, t)\vec{E}_r^*(\vec{r}_{xy} + \vec{\Delta}d, t + \Delta t)d\vec{r}_{xy}dt}{\int\int |\vec{E}_r(\vec{r}_{xy}, t)|^2 d\vec{r}_{xy}dt} \tag{3.10}$$

and from the equivalence stated above it follows that $r(\vec{\Delta}d, \Delta t) = r_z(\vec{\Delta}d, \Delta t)$. By expanding Eqn.(3.10), the space-time auto-correlation function of the field measured by the array can be derived as,

$$r_z(\vec{\Delta}d, \Delta t) = \exp(-j\vec{k}_r \cdot \vec{\Delta}d) \int\int e^{j\frac{2\pi}{\lambda}[f(\vec{r}_{xy}+\vec{\Delta}d, t+\Delta t) - f(\vec{r}_{xy}, t)]} d\vec{r}_{xy}dt \tag{3.11}$$

where the carrier frequency dependent term $e^{-j\omega\Delta t}$ is neglected and the dependence of the function $f(\vec{r}_{xy}, t)$ on the angle of incidence θ_i has been dropped for notational convenience. The statistical properties of the ionosphere are known to be frequency dispersive, spatially inhomogeneous and nonstationary. However, if attention is restricted to narrowband signals (with bandwidths less than 20 kHz) and time intervals in the order of a few minutes the statistical properties of the reflecting surface in a localised region of ionosphere are more likely to be homogeneous and stationary. Homogeneity implies that the spatial variation of the plasma displacements have statistical properties which are independent of the spatial reference point over the surface, while stationarity implies that the ensemble statistics of these variations is independent of the time origin considered. It is then possible to associate a probability density function (PDF) $p[\delta(\vec{\Delta}d, \Delta t)]$ for the differential plasma displacement function $\delta(\vec{\Delta}d, \Delta t) = f(\vec{r}_{xy} + \vec{\Delta}d, t + \Delta t) - f(\vec{r}_{xy}, t)$ which is independent of the position $\vec{r}_{xy}$ and time t but is dependent on spatial separation $\vec{\Delta}d$ and time interval Δt. Once this description of the plasma is accepted, the ensemble statistics which are governed by the PDF are the same as those evaluated in for a particular space-time realisation of the plasma turbulence process in Eqn.(3.10).

$$r_z(\vec{\Delta}d, \Delta t) = \exp(-j\vec{k}_r \cdot \vec{\Delta}d) \int e^{j\frac{2\pi}{\lambda}\delta(\vec{\Delta}d, \Delta t)} p[\delta(\vec{\Delta}d, \Delta t)] d\delta(\vec{\Delta}d, \Delta t) \tag{3.12}$$

It can be seen from Eqn.(3.12) that for a statistically stationarity and spatially homoge-

neous plasma surface the generalised space-time auto-correlation function measured by an array on the ground is the *characteristic function* of the probability density which describes the space-time statistical properties of the relative plasma displacements at the radiating ionospheric surface. To derive models for the auto-correlation functions it is necessary to assume a model for the plasma turbulence process in terms of the joint (space-time) probability density function $p[\delta(\vec{\Delta}d, \Delta t)]$.

3.2.2.2 Models for the space-time auto-correlation function

There are many models which could be proposed for $p[\delta(\vec{\Delta}d, \Delta t)]$. For example, if there is a steady drift of "field-aligned" irregularities moving at a velocity $\vec{v}_p$ across the reflection region then the surface may be modelled as one of constant form but shifting in horizontal position over time. Such a model would result in an unchanging diffraction pattern which moves at a velocity $\vec{v}_p$ over the ground. In this case the temporal auto-correlation function for a time interval Δt is the same as the spatial auto-correlation function for a separation $\vec{\Delta}d = \vec{v}_p \Delta t$. Although such models have been considered by many researchers, there will in general be a random component which changes the structure of the surface over time in addition to the steady drift component. If no steady drift is present and there are only random fluctuations then such fluctuations may be more correlated in one direction than in another which implies that the spatial auto-correlation measured by the array depends on its orientation within the $z = z_g$ plane.

The simplest models occur when the spatial correlation of the surface fluctuations only depends on distance $|\vec{\Delta}d|$ (i.e., an isotropic surface) and the space-time PDF is separable which implies that $p[\delta(\vec{\Delta}d, \Delta t)] = p_s[\delta(|\vec{\Delta}d|)]p_t[\delta(\Delta t)]$ where $p_s[\delta(|\vec{\Delta}d|)]$ is the spatial PDF and $p_t[\delta(\Delta t)]$ is the temporal PDF. This type of model may be appropriate in the absence of large scale structures such as travelling ionospheric disturbances (TID's) which are expected to impose a dependence between the spatial and temporal PDF's. Hence, a separable model may not be appropriate in certain practical situations of interest but the evaluation of the one-dimensional correlation functions $r_s(|\vec{\Delta}d|)$ and $r_t(\Delta t)$ from the corresponding PDF's serves as a useful starting point. In accordance with Eqn.(3.12), a separable PDF model implies that the space-time auto-correlation function is given by the product of the spatial and temporal auto-correlation functions $r_z(\vec{\Delta}d, \Delta t) = r_s(|\vec{\Delta}d|)r_t(\Delta t)$.

Let us consider two limiting cases for which these correlation functions can be related analytically to the PDF of the plasma displacements. The first case corresponds to situations where the temporal interval Δt is *greater* than the time interval over which the velocity of the points in the surface remain constant. In this case it is assumed that the surface displacement probability $p_t[\delta(\Delta t)]$ is that of a random walk possibly around a

regular mean fluid motion v_z which is normal to the xy-plane.

$$p_t[\delta(\Delta t)] = \frac{1}{\sigma_t(\Delta t)\sqrt{2\pi}} \exp - \left\{ \frac{(\delta(\Delta t) - v_z \Delta t \cos\theta_i)^2}{2\sigma_t^2(\Delta t)} \right\} \tag{3.13}$$

The variance of the distribution $\sigma_t^2(\Delta t) = D_t|\Delta t| \cos\theta_i$ is assumed to vary linearly with temporal separation where the positive constant D_t is a measure of how quickly the surface changes. The dependence on $\cos\theta_i$ comes from the definition of $\delta(\Delta t) = f(\vec{r}_{xy}, \theta_i, t + \Delta t) - f(\vec{r}_{xy}, \theta_i, t)$ and the definition of $f(\vec{r}_{xy}, \theta_i, t) = z_s(x, y, t)\cos\theta_i$. The temporal auto-correlation function resulting from this probability density is given by,

$$r_t(\Delta t) = \int_{-\infty}^{\infty} e^{j\frac{2\pi}{\lambda}\delta(\Delta t)} p_t[\delta(\Delta t)] d\delta(\Delta t) = e^{j2\pi\Delta f_d \Delta t} e^{-|\vec{k}_s|^2 D_t \cos\theta_i |\Delta t|} \tag{3.14}$$

where $\Delta f_d = v_z \cos\theta_i/\lambda$ is the regular component of Doppler shift and $|\vec{k}_s|^2 = (\frac{2\pi}{\lambda})^2$. It can be seen from Eqn.(3.14) that the magnitude of $r_t(\Delta t)$ is a decaying exponential with a time constant that depends on D_t and $\cos\theta_i$. The phase of $r_t(\Delta t)$ is linear and depends on the mean component of Doppler shift Δf_d.

In the other limit, it is assumed the time interval Δt is shorter than the time interval over which the velocity of particles in the surface normal to the xy-plane is effectively constant. The fluid velocity probability distribution $p(v)$ is assumed to be Gaussian with mean velocity v_z and root mean square velocity σ_v.

$$p(v) = \frac{1}{\sigma_v\sqrt{2\pi}} \exp - \left\{ \frac{(v - v_z)^2}{2\sigma_v^2} \right\} \tag{3.15}$$

In this case, the plasma displacement probability distribution is related to the plasma velocity probability distribution through the relation $p_t[\delta(\Delta t)] = p(v\Delta t \cos\theta_i)$ and substitution of this relation into the integral in Eqn.(3.16) yields the following temporal auto-correlation function.

$$r_t(\Delta t) = \int_{-\infty}^{\infty} e^{j\frac{2\pi}{\lambda}\delta(\Delta t)} p_t[\delta(\Delta t)] d\delta(\Delta t) = e^{j2\pi\Delta f_d \Delta t} e^{-|\vec{k}_s|^2 \sigma_v^2 \cos\theta_i{}^2 \Delta t^2} \tag{3.16}$$

It can be seen from Eqn.(3.16) that the magnitude of $r_t(\Delta t)$ is a Gaussian envelope with a variance depending on σ_v^2 and $\cos\theta_i{}^2$ while the phase is linear and depends on the mean component of Doppler shift Δf_d.

The spatial auto-correlation function $r_s(|\vec{\Delta}d|)$ can be determined in a similar manner by defining the spatial probability distribution $p_s(|\vec{\Delta}d|)$ as that of a random walk about the mean horizontal plane at time t.

$$p_s[\delta(|\vec{\Delta}d|)] = \frac{1}{\sigma_s(|\vec{\Delta}d|)\sqrt{2\pi}} \exp - \left\{ \frac{\delta(\vec{\Delta}d)^2}{2\sigma_s^2(|\vec{\Delta}d|)} \right\} \tag{3.17}$$

The variance of the plasma displacements is assumed to be a linear function of distance $\sigma_s^2(|\vec{\Delta}d|) = D_s|\vec{\Delta}d|$ where the constant D_s is a measure of the roughness of the surface. In this case the spatial auto-correlation function is given by,

$$r_s(|\vec{\Delta}d|) = e^{-j\vec{k}_r\cdot\vec{\Delta}d}\int_{-\infty}^{\infty} e^{j\frac{2\pi}{\lambda}\delta(|\Delta d|)}p_s[\delta(|\vec{\Delta}d|)]d\delta(|\vec{\Delta}d|) = e^{-j\vec{k}_r\cdot\vec{\Delta}d}e^{-|\vec{k}_s|^2D_s|\vec{\Delta}d|} \qquad (3.18)$$

and has an amplitude which is an exponentially decaying function of distance $|\vec{\Delta}d|$ while its phase is linear for a uniform linear array with adjacent sensors displaced by $\vec{\Delta}d$. If the variance $\sigma_s^2(|\vec{\Delta}d|) = D_s'|\vec{\Delta}d|^2$ varies quadratically with separation then the amplitude of the spatial auto-correlation function will take on a Gaussian form.

$$r_s(|\vec{\Delta}d|) = e^{-j\vec{k}_r\cdot\vec{\Delta}d}\int_{-\infty}^{\infty} e^{j\frac{2\pi}{\lambda}\delta(|\Delta d|)}p_s[\delta(|\vec{\Delta}d|)]d\delta(|\vec{\Delta}d|) = e^{-j\vec{k}_r\cdot\vec{\Delta}d}e^{-|\vec{k}_s|^2D_s'|\vec{\Delta}d|^2} \qquad (3.19)$$

The power spectrum corresponding to a decaying exponential has a Lorentzian profile while a Gaussian shaped amplitude envelope in the auto-correlation function gives rise to a Gaussian shaped power spectrum (Kreyszig 1988). Correlation functions with amplitude envelopes that fall off rapidly with time or distance give rise to broad power spectrums and vice-versa. The linear phase shift in these functions simply shifts the centre of the power spectrum (whose shape is determined solely by the amplitude envelope of the auto-correlation function) to a position which corresponds to the mean Doppler shift or angle-of-arrival of the wave.

3.3 Validation method

Using a single reception channel (Watterson et al. 1970) experimentally verified a number of assumptions regarding the statistical properties of complex-valued random processes arising from narrowband HF signals reflected by a single layer in the ionosphere over a period of a few minutes. The data received from each propagation mode was described by a stationary complex Gaussian distributed random process that produces Rayleigh fading. The complex random processes received from different ionospheric modes were shown to be statistically independent and the parameters of the power spectrum which completely defines each process were confirmed to be those of a Gaussian function of frequency.

It is presently unclear how to extrapolate this model to describe the statistical properties of narrowband HF signals received by *antenna arrays* and this is partly due to the lack of measurements made on the spatial and spatio-temporal characteristics of the ionospheric.HF reflection channel with a very wide aperture array over periods of a few minutes. The aim of this section is to develop methods which can be used to validate or reject a number of hypothesised extrapolations of this model which are proposed to describe the statistical properties of narrowband ionospherically-propagated HF signals received

by *antenna arrays*. The Gaussian scattering assumption validated for the narrowband HF reflection channel by Watterson et al. (1970) is used as a foundation to construct hypothesis tests for the second order statistics (auto-correlation functions) which are assumed to statistically describe the spatial and spatio-temporal characteristics of quiet mid-latitude HF channels.

Section 3.3.1 develops a hypothesis test to determine whether the parameters of the model used to describe the second order statistics of the complex fading processes recorded by the antenna array for a particular propagation mode are spatially homogeneous (i.e., whether there is good reason to believe that the model parameters of the temporal auto-correlation function are invariant across receivers). Section 3.3.2 develops a hypothesis test which can be used to accept or reject a parametric model for the *spatial* auto-correlation function of the mode complex fading process. A method to determine whether the *space-time* auto-correlation function of such processes can be estimated with reasonable accuracy from a separate knowledge of the temporal and spatial auto-correlation function model parameters is proposed in section 3.3.2.

3.3.1 Temporal stationarity and spatial homogeneity

The temporal complex Gaussian distributed processes validated by (Watterson et al. 1970) are statistically characterised by a parametric model of the temporal second order statistics or auto-correlation function. In practice, these parameters are not known apriori and must be estimated from the available data. The estimated parameters define a hypothesised model for the "true" or expected auto-correlation function which is to be experimentally validated.

To validate the proposed model it is necessary to analyse the significance of any deviations between the assumed auto-correlation function and that estimated from the experimental data. If the probability distribution of these differences is known under the assumption that the model is correct, it is possible to determine whether the observed differences can be reasonably attributed to estimation errors arising due to finite sample effects or if there is good reason to reject the hypothesised model for the true auto-correlation function.

The first part of this section is concerned with estimating the parameters of the hypothesised temporal auto-correlation function model which best fits the sample auto-correlation sequence (ACS) obtained from the data. The second part of this section derives the probability density function for the magnitude and phase of the sample ACS under the assumption that the model is correct so as to develop a hypothesis test which can be used to accept or reject the validity of the temporal ACS model as well as to determine whether the parameters of this model are invariant across different receivers.

For digital or sampled random processes the auto-correlation function can only be evaluated at a number of discrete points which are temporally separated by a minimum

interval equal to the sampling interval. The term auto-correlation sequence (ACS) is adopted to describe the samples of the auto-correlation function (ACF) resulting at different temporal lags. The temporal ACS of the complex random process $x_k^{[n]}(t)$ recorded over the PRI $t = 1, 2, .., P$ in range cell k and receiver n is estimated as the *unbiased* sample ACS $\hat{r}_n(\tau)$ given by,

$$\hat{r}_n(\tau) = \frac{1}{P-\tau}\sum_{t=1}^{P-\tau} x_k^{[n]}(t)x_k^{[n]*}(t+\tau) = e^{\hat{P}_n(\tau)} \quad , \quad \begin{cases} \tau &= 0, 1, \cdots, Q-1 \leq P \\ n &= 0, 1, \cdots, N-1 \end{cases} \tag{3.20}$$

where the k-dependence of $\hat{r}_n(\tau)$ has been dropped as the processes in different range cells will be considered separately. The *mathematical model* of the *statistically expected* ACS $r_n(\tau)$ may be written in the following form,

$$r_n(\tau) = e^{P_n(\tau)} = e^{a\tau^2+b\tau+c_n} = e^{a\tau^2}e^{b\tau}e^{c_n} \tag{3.21}$$

where the scalar parameters a, b and c_n of the model are the coefficients of a quadratic polynomial $P_n(\tau)$ in lag index τ. As described later, the choice of a quadratic polynomial is consistent with the Gaussian and Lorentzian shaped auto-correlation functions derived from physical principles in section 3.2.2.2. The power of the signal $r_n(0)$ in the n^{th} receiver is modelled by the term e^{c_n} where c_n is a *real* scalar, the reason for the n-dependence of this term will be explained later. If the Doppler power spectrum model is a Gaussian function of frequency centred about a mean Doppler shift then the ACS model has a magnitude that is a Gaussian function of τ and a phase which is linear with a slope determined by the mean Doppler shift. In Eqn.(3.21), this corresponds to a purely real value of a and a purely imaginary value of b. If the Doppler power spectrum model is a Lorentzian function of frequency centred about a mean Doppler shift then the ACS model has a magnitude that is a decaying exponential function of τ and a linear phase with a slope determined by the mean Doppler shift. In Eqn.(3.21), this corresponds to $a = 0$ and a complex value of b.

The order of the polynomial $P_n(\tau)$ may be extended past two and the constraints on the parameters a and b can be relaxed to some extent when it is required to generate a wider variety of ACS models which may differ from the Gaussian or decaying exponential models. Despite this potential flexibility, only the above-mentioned two models are considered in this study for representing the second order statistics of the received signals. Models of higher complexity which would be able to fit the sample ACS more accurately could easily be proposed but the amount of statistical uncertainty often associated with estimating the ACS from experimental data will generally not warrant the search for extremely accurate models. Even if a large amount of temporally stationary data were available, one must bear in mind that a more complex model is more difficult to understand intuitively and such models usually lead to more complex signal processing implementations when it is required to simulate different realisations of the process.

It is noted that the two above-mentioned models have previously been used to represent the *temporal* ACS of HF signals which were obliquely *backscattered* by ionospheric irregularities, see (Villain, Andre, Hanuise and Gresillon 1996) and (Hanuise, Villain, Gresillon, Cabrit, Greenwald and Baker 1993). The authors concluded that it was preferable to interpret the statistical properties of the data in terms of ACS models rather than power spectrum models because the different features of the two above-mentioned models were more easily distinguished visually in the lag domain. As will be appreciated later, the ACS model interpretation has a further advantage in that it is more mathematically tractable than the frequency domain equivalent from both a parameter estimation and statistical validation point of view.

Before proceeding to describe the parameter estimation technique for the two ACS models in question, the receiver dependent power scaling term e^{c_n} in the mathematical model for the expected temporal ACS is explained. The power has been allowed to vary from one receiver to another for two reasons. Firstly, the potential existence of systematic instrumental errors, such as differences between the gain and phase response of the antenna sensors for example, will be absorbed by the receiver-dependent term e^{c_n} and not effect the shape of the ACS. Secondly, it is of interest to determine whether the shape of the ACS or power spectrum complies with some analytical model and whether the parameters of this model are the same for all receivers. The power or scaling which may be different from one receiver to another is of secondary importance as far as *temporal* signal processing at each receiver is concerned. This aspect may be of importance in *spatial* and *spatio-temporal* signal processing applications and will be covered later in section 3.3.2.

Since the sample ACS is unbiased it seems reasonable to estimate the parameters of the temporal ACS model according to the least squares principle. The following minimisation problem is formulated to estimate the model parameter vector $\mathbf{v} = [a\ b\ c_1 \cdots c_N]^T$ according to this principle,

$$\mathbf{v} = \text{argmin} \sum_{n=0}^{N-1} \sum_{\tau=0}^{Q-1} \| e^{\hat{P}_n(\tau)} - e^{P_n(\tau)} \|_F = \text{argmin} \sum_{n=0}^{N-1} \sum_{\tau=0}^{Q-1} \| e^{\hat{P}_n(\tau)} [1 - e^{P_n(\tau) - \hat{P}_n(\tau)}] \|_F \tag{3.22}$$

where $\| \cdot \|_F$ denotes the Frobenius or Euclidean squared norm and the minimisation is performed subject to the constraints on the elements of $\mathbf{v}$ associated with the ACS model $e^{P_n(\tau)}$ being considered. This is a non-linear optimisation problem which can only be solved by iterative methods. However, if at the minimum the model and sample ACS are quite similar, the value of $P_n(\tau) - \hat{P}_n(\tau)$ will be close to zero and $e^{P_n(\tau) - \hat{P}_n(\tau)}$ will be in the vicinity of one. In this case, the term $e^{P_n(\tau) - \hat{P}_n(\tau)}$ can be accurately approximated by a first order Taylor series expansion $1 + P_n(\tau) - \hat{P}_n(\tau)$. Substituting this truncated expansion into Eqn.(3.22) yields the following modified cost function which corresponds

to an approximate least squares criterion.

$$\tilde{\mathbf{v}} = \text{argmin} \sum_{n=0}^{N-1} \sum_{\tau=0}^{Q-1} \|e^{\hat{P}_n(\tau)}[P_n(\tau) - \hat{P}_n(\tau)]\|_F = \text{argmin} \sum_{n=0}^{N-1} \sum_{\tau=0}^{Q-1} \|e^{\hat{P}_n(\tau)}\|_F \|P_n(\tau) - \hat{P}_n(\tau)\|_F \tag{3.23}$$

The solution to this problem can be found analytically and depends on the constraints which are placed on the elements of the parameter vector $\mathbf{v}$. The *unconstrained* solution of the quadratic optimisation problem in Eqn.(3.23) is given by,

$$\tilde{\mathbf{v}} = (\mathbf{M}^H \mathbf{W} \mathbf{M})^{-1} \mathbf{M}^H \mathbf{W} \mathbf{p} \tag{3.24}$$

where the NQ-dimensional vector $\mathbf{p} = ln\{[\hat{\mathbf{r}}_1^T \cdots \hat{\mathbf{r}}_N^T]^T\}$ with $\hat{\mathbf{r}}_n = [\hat{r}_n(0) \cdots \hat{r}_n(Q-1)]^T$ and the matrices $\mathbf{M}$ and $\mathbf{W}$ are composed of the Q-dimensional column vectors $\mathbf{a}, \mathbf{b}, \mathbf{1}, \mathbf{0}$ and $\hat{\mathbf{w}}_n$ whose elements $\tau = 0, 1, .., Q-1$ are given by Eqn.(3.25).

$$\mathbf{M} = \begin{bmatrix} \mathbf{a} & \mathbf{b} & \mathbf{1} & \mathbf{0} & \cdots & \mathbf{0} \\ \mathbf{a} & \mathbf{b} & \mathbf{0} & \mathbf{1} & \cdots & \mathbf{0} \\ \vdots & \vdots & \vdots & \vdots & \vdots & \vdots \\ \mathbf{a} & \mathbf{b} & \mathbf{0} & \mathbf{0} & \cdots & \mathbf{1} \end{bmatrix}, \quad \mathbf{W} = \text{diag}[\hat{\mathbf{w}}_1^T \cdots \hat{\mathbf{w}}_N^T], \quad \begin{cases} \mathbf{a}^{[\tau]} &= \tau^2 \\ \mathbf{b}^{[\tau]} &= \tau \\ \hat{\mathbf{w}}_n^{[\tau]} &= |e^{\hat{P}_n(\tau)}|^2 \\ \mathbf{1}^{[\tau]} &= 1 \\ \mathbf{0}^{[\tau]} &= 0 \end{cases} \tag{3.25}$$

In the present case, it is of interest to constrain the values which certain parameters in the vector $\mathbf{v}$ can take so as to yield a valid model of the ACS in terms of a known function (i.e., the Gaussian or decaying exponential magnitude with linear phase). When one or more parameters in $\mathbf{v}$ are required to be either purely real or purely imaginary, as they are for both models of interest, it is better to treat the real and imaginary parts of the least squares optimisation problem separately. By substituting $P_n(\tau) = a\tau^2 + b\tau + c_n$ and $\hat{P}_n(\tau) = ln\{\hat{r}_n(\tau)\} = x_n(\tau) + jy_n(\tau)$ into Eqn.(3.23) it is possible to partition the problem into real and imaginary parts,

$$\begin{aligned} \tilde{\mathbf{v}}_{Gaussian} &= \text{argmin} \textstyle\sum_{n=0}^{N-1} \sum_{\tau=0}^{Q-1} \|e^{\hat{P}_n(\tau)}\|_F [(x_n(\tau) - a\tau^2 - c_n)^2 + (y_n(\tau) - b\tau)^2] \\ \tilde{\mathbf{v}}_{Lorentzian} &= \text{argmin} \textstyle\sum_{n=0}^{N-1} \sum_{\tau=0}^{Q-1} \|e^{\hat{P}_n(\tau)}\|_F [(x_n(\tau) - b_{re}\tau - c_n)^2 + (y_n(\tau) - b_{im}\tau)^2] \end{aligned} \tag{3.26}$$

where b_{re} and b_{im} are the real and imaginary parts of the polynomial coefficient of τ in $P_n(\tau)$ for the Lorentzian power spectrum model. It can be seen from Eqn.(3.26) that for each model there are two real-valued and *unconstrained* least squares problems which can be solved by tailoring the general solution for a complex-valued unconstrained case in Eqn.(3.24) to the specific problem arising for either the real or imaginary part in Eqn.(3.26). As an aside, it is noted that *linearly constrained* complex-valued least squares problems can be dealt with analytically using the theory described in (Kay 1987), but it

is not possible to constrain the real and imaginary parts of a complex variable separately using this approach so these standard results cannot be used to estimate the parameters required in this application.

After the parameters are estimated it is possible to generate a hypothesised model for the expected ACS and to assess the significance of any departures between the model ACS and the sample ACS. If these differences are small (i.e., small enough to be reasonably attributed to ACS estimation errors) then the HF channel which gives rise to the temporal processes measured in different receivers may be considered *spatially homogeneous* as no strong reason exists to reject the hypothesised temporal ACS model. Similarly, if the same statistical parameters can be used to describe the temporal ACS measured over different time intervals then there is no strong reason to reject the hypothesis that the *complex Gaussian distributed random process* is *temporally stationary.*

It is therefore important to quantify what is meant by a "significant" difference and to state the degree of confidence associated with the conclusion drawn about the temporal stationarity or spatial homogeneity of the measured HF channels. The distribution of the magnitude and phase of the sample ACS calculated in accordance with Eqn.(3.20) from the samples of a stationary complex Gaussian distributed random process that produces Rayleigh fading is derived in appendix A. The statistical properties of the sample ACS depends on the number of samples P used to form it and the expected ACS of the random process. Using the large sample distributions derived in appendix A for the magnitude and phase of the sample ACS, it is possible to derive bounds for the hypothesised ACS model (magnitude and phase) which are expected to contain (say) 90 percent of the estimates.

If either the magnitude or phase of a particular lag in the sample ACS lies beyond these bounds then such a departure is deemed to be significant and provides a strong reason for rejecting the hypothesised ACS model. If the entire ACS lies within these bounds then there is no strong reason to reject the proposed ACS model which may be accepted as valid with a significance level of (say) 90 percent. This criteria is used accept or reject the spatially homogeneous temporal ACS models proposed in this section, the actual distributions and associated error bars are quantified on a case by case basis in the experimental results section.

3.3.2 Spatial stationarity and space-time separability

As mentioned in chapter 2, the wavefront of a HF signal reflected by a single ionospheric region is often assumed to have a mean planar structure with some degree of time-varying amplitude and phase "crinkles" superimposed. The *mean* plane wavefront is assumed to have a direction-of-arrival that does not wander over a period of a few minutes and the time-varying "crinkles" can be viewed as spatial modulations imposed on the mean plane wave by the HF channel. These spatial modulations cause the angular spectrum of the received signal to spread about the mean direction-of-arrival much like the temporal

modulation causes the Doppler spectrum to spread about the mean Doppler shift.

The multiplicative complex-valued spatial modulations which the HF channel imposes on the mean plane wave are assumed to be described by a zero-mean complex Gaussian distributed process that produces Rayleigh fading in the spatial dimension. This description follows directly from the Gaussian scattering hypothesis validated by (Watterson et al. 1970). However, in the presence of array manifold errors the mean wavefront may not be planar and even in the absence of such errors it is conceivable that ionospheric phenomena may contribute to departures between the mean wavefront and the plane wavefront. For reasons mentioned below, it is considered important to determine the validity of the mean plane wavefront assumption as well as the validity of models which describe the second order statistics of the spatial modulations imposed on the mean wavefront.

The validity of the mean plane wavefront assumption is important in adaptive beamforming applications when the signal is considered as a *desired* signal which is to be detected by the system (i.e., protected from being cancelled by the adaptive beamformer). An aim of this section is to develop a statistical test which can be used to accept or reject the mean plane wavefront assumption with a known level of confidence. If the signal represents *interference* to the system the mean wavefront shape is of secondary importance in adaptive beamforming applications. Of primary importance is the magnitude of the *correlation coefficients* between different pairs of receiver outputs as the cancellation ratio achieved when the receiver outputs are weighted (each by a single complex weight) and combined is dependent on these coefficients which are not effected by the mean wavefront shape and hence array manifold errors. Another aim of this section is to develop a statistical test which can be used to accept or reject a model for the magnitude of the correlation coefficient between different pairs of receivers in the array with a known level of confidence. To see how the mean wavefront and the magnitude of the correlation coefficients are related to the spatial covariance matrix $\mathbf{R}_x$ of the process $\mathbf{x}_k(t)$ consider the following hypothesised model of $\mathbf{R}_x$ which appears in (Paulraj and Kailath 1988) and (Ringelstein, Gershman and Bohme 1999).

$$\mathbf{R}_x = E\{\mathbf{x}_k(t)\mathbf{x}_k^H(t)\} = \sigma_s^2[\mathbf{s}(\theta)\mathbf{s}^H(\theta)] \odot \mathbf{B} = [r_x^{[i,j]}]_{i,j=0}^{N-1} \tag{3.27}$$

In Eqn.(3.27) the symbol $\odot$ denotes Shur-Hadamard or element-wise product, σ_s^2 is the mean square value or power of the signal (assumed to be the same in all receivers), $\mathbf{s}(\theta)$ is the steering vector of a ULA for cone angle θ and $\mathbf{B}$ is an "angular spreading" matrix with its $(i,j)^{th}$ element equal to the magnitude of the correlation coefficient $\rho_{i,j} = |r_x^{[i,j]}|/\sqrt{r_x^{[i,i]}r_x^{[j,j]}}$ between the i^{th} and j^{th} receiver output. In the spatial covariance matrix model the phase of $r_x^{[i,j]}$ is determined by the mean plane wave just as the phase of the temporal ACS was determined by the mean Doppler shift. This is because the mean wavefront (or mean Doppler shift) is defined such that the real and imaginary parts of the spatial (or temporal) HF channel modulations are *independent* and only contribute

to the *magnitude* of the second order statistics. Stated another way, the magnitude of $r_x^{[i,j]}$ is determined by the second order statistics of the spatial HF channel modulations only, while the phase of $r_x^{[i,j]}$ is determined by the mean wavefront which is assumed to be planar in this case. The spatial covariance matrix model $\mathbf{R}_x$ can therefore be expressed in terms of the phase-only matrix $\mathbf{s}(\theta)\mathbf{s}^H(\theta)$ which determines the phase of all elements $r_x^{[i,j]}$ through the mean DOA parameter θ and the real-valued matrix $\mathbf{B}$ which determines the magnitude of all elements $r_x^{[i,j]}$ through other model parameters to be described later. Note that when the spatial HF channel modulations are normalised to have unit variance, the expected second order statistics or cross-correlation between the modulations on different receivers is given by the correlation coefficient $\rho_{i,j}$.

The plane wavefront $\mathbf{s}(\theta)$ is the hypothesised model for the mean wavefront, but in the presence of array manifold errors or other ionospheric effects, an arbitrary mean wavefront model denoted by $\mathbf{s}$ may be specified in Eqn.(3.27). Before proceeding to the validation stage it is first necessary to develop a model for correlation coefficients $\rho_{i,j}$ in the matrix $\mathbf{B}$. The combination of the mean wavefront and correlation coefficient models yields a model of the spatial covariance matrix for the array data, which for stationary Gaussian distributed processes, completely defines the spatial statistical properties of the process. As for the temporal ACS, the Gaussian and decaying exponential envelopes are considered as models for the real-valued correlation coefficients.

$$\rho_{i,j} = e^{P(|i-j|)} = e^{a|i-j|^2+b|i-j|} \begin{cases} a<0, \quad b=0 & \text{Gaussian} \\ a=0, \quad b<0 & \text{Decaying exponential} \end{cases} \tag{3.28}$$

In this model it is assumed that the second order statistics of the normalised spatial HF channel modulations only depend on the spacing between the receiver pair and not the location of the two receivers within the array. In other words, it is hypothesised that wavefront modulations imposed by the HF channel are spatially stationary and described by one of the two even functions (i.e., Gaussian or decaying exponential) which are parameterised by the real quantities a and b respectively. These parameters are usually not known apriori and must be estimated from the *unbiased* sample spatial covariance matrix $\hat{\mathbf{R}}_x$

$$\hat{\mathbf{R}}_x = \frac{1}{P}\sum_{t=0}^{P-1} \mathbf{x}_k(t)\mathbf{x}_k^H(t) = [\hat{r}_x^{[i,j]}]_{i,j=0}^{N-1} \tag{3.29}$$

This estimator coincides with the maximum likelihood estimator of the expected spatial covariance matrix $\mathbf{R}_x = E\{\mathbf{x}_k(t)\mathbf{x}_k^H(t)\}$ assuming the samples in each receiver are Gaussian distributed. By the *invariance property* of the maximum likelihood (ML) estimator, see (Kay 1993), it follows that the ML estimate of the magnitude of the complex correlation coefficient is given by $\hat{\rho}_{i,j} = |\hat{r}_x^{[i,j]}|/\sqrt{\hat{r}_x^{[i,i]}\hat{r}_x^{[j,j]}}$. Under the spatial stationarity assumption it is justifiable to estimate these coefficients by averaging estimates made on

different receiver pairs spaced by a common distance $d = |i - j|$.

$$\hat{\rho}(d) = e^{\hat{P}(d)} = \frac{1}{N-d-1} \sum_{i=0}^{N-d-1} |\hat{r}_x^{[i,i+d]}| / \sqrt{\hat{r}_x^{[i,i]} \hat{r}_x^{[i+d,i+d]}} \tag{3.30}$$

The parameters a or b which provide the best least squares fit between the estimated function $e^{\hat{P}(d)}$ and the model function $e^{P(d)}$ in Eqn.(3.28) can be calculated using the general unconstrained minimisation formula in Eqn.(3.24). It is then a matter of assessing the significance of the departure between the assumed model $\rho_{i,j} = \rho(d)$ and the estimates $\hat{\rho}_{i,j}$ in statistical terms so that a decision can be made with known confidence on whether to accept or reject the hypothesised model for these elements.

For multivariate complex Gaussian distributed processes, the sampling properties of the maximum likelihood estimate $\hat{\rho}^2$, also referred to as the magnitude squared coherence, have been found by (Goodman 1963). If n statistically independent samples are used estimate the true value of the magnitude squared coherence (denoted by ρ^2) between two receiver outputs then the distribution of $\hat{\rho}^2$ is given by,

$$p(\hat{\rho}^2) = (n-1)(1-\rho^2)^n (1-\hat{\rho}^2)^{n-2} F(n,n;1;\rho^2\hat{\rho}^2) \ , \quad F(x,y;w;z) = \sum_{k=0}^{\infty} \frac{(x)_k (y)_k}{(w)_k} \frac{z^k}{k!} \tag{3.31}$$

where $(x)_k = x(x+1)\cdots(x+k-1)$ and $F(\ ,\ ;\ ;\ )$ is the classical hypergeometric function or series which is guaranteed to converge if the argument of the function z has a modulus less than unity. In this case, $z = \rho^2\hat{\rho}^2 < 1$ so the function always converges. The density function $p(\hat{\rho}^2)$ was used by (Carter 1971) for coherence estimation in the frequency domain. In any case, this result may be used to derive confidence intervals for the value of the sample magnitude squared coherence which may then be used to accept or reject the assumed model for these quantities.

Since the P consecutive samples at the receiver outputs are not statistically independent it is necessary to determine the equivalent number of statistically independent observations or "degrees of freedom" (n) which must be substituted into Eqn.(3.31) to obtain the appropriate density function for hypothesis testing. For large values of P, Priestly (1981) describes a method for determining the equivalent number of statistically independent samples in a correlated Gaussian distributed random process. The first step is to compute the variance of the sample variance, for a complex process this is conveniently given by the following expression (Thierren 1992),

$$\sigma_r^2 = E\{[\hat{r}(0) - r(0)]^2\} = \frac{1}{P} \sum_{k=-(P-1)}^{P-1} (1 - \frac{|k|}{P}) |r(k)|^2 \tag{3.32}$$

where $r(k)$ is the expected correlation between data points spaced k samples apart in time

and $\hat{r}(0)$ is the sample variance of the random process. For n *statistically independent* samples the variance of this estimate is given by $r^2(0)/n$ as $n \to \infty$. Hence, the effective number of independent observations $P_{eff} \leq P$ is given by $P_{eff} = P(r^2(0)/\sigma_r^2)$. The calculated value of P_{eff} (to the nearest integer) may then be substituted for the number of independent samples n in Eqn.(3.31) to derive the appropriate (say 90 percent) confidence intervals. If the samples $\hat{\rho}_{i,j}$ fall within these bounds for all receiver pairs (i,j) then the model for the spatial correlation coefficients is accepted, otherwise it is rejected.

To verify the mean plane wavefront hypothesis it is first necessary to estimate the cone angle-of-arrival and power of the wave which best fits the assumed model for the spatial covariance matrix in Eqn.(3.27). By defining $\mathbf{s}^{[i]}$ as the i^{th} element of an arbitrary mean wavefront vector $\mathbf{s}$ in this model and expanding the $(i,j)^{th}$ element of the spatial covariance matrix in Eqn.(3.27) one obtains,

$$r_x^{[i,j]} = \sigma_s^2 \frac{\mathbf{s}^{[i]} |r_x^{[i,j]}| \mathbf{s}^{[j]*}}{\sqrt{r_x^{[i,i]}}\sqrt{r_x^{[j,j]}}} = \sigma_s^2 \mathbf{s}^{[i]} \rho_{i,j} \mathbf{s}^{[j]*} \tag{3.33}$$

since the $(i,j)^{th}$ element of $\mathbf{B}$ is $\rho_{i,j}$ by definition. As $\rho_{i,i} = 1$ for all $i = 1, 2, .., N$ it follows from Eqn.(3.33) that the amplitude of the i^{th} element in the mean wavefront is given by $|s^{[i]}| = \sigma_s \sqrt{r_x^{[i,i]}}$. By equating the phases of elements it follows that the phase of $r_x^{[i,j]}$, denoted by $\psi_{i,j}$, is equal to the phase of $\mathbf{s}^{[i]}$, denoted by ϕ_i, minus the phase of $\mathbf{s}^{[j]}$. The phases ϕ_i for $i = 1, 2, .., N$ can therefore be found by solving a set of linear equations $\psi_{i,j} = \phi_i - \phi_j$ for the elements of the spatial covariance matrix.

When only data samples are available, the expected lags $r_x^{[i,j]}$ in Eqn.(3.33) must be replaced by the sample lags $\hat{r}_x^{[i,j]}$ estimated from the data. Once the mean wavefront $\mathbf{s}$ is calculated the mean *plane wave* of best fit may be estimated as that which best fits $\mathbf{s}$ in a least squares sense. The amplitude A and cone angle θ of this wave are estimated according to the following optimisation problem,

$$\hat{A}, \hat{\theta} = \text{argmin} \|\mathbf{s} - As(\theta)\|_F \tag{3.34}$$

which may be solved by performing two one-dimensional searches, one for the magnitude and one for the phase. Once the plane wave of best fit is estimated it is then required to determine the significance of differences between this wave and the absolute amplitudes and relative phases of the sample spatial lags. The expected power of the random signal is reflected by the sample variance of the signal recorded in each receiver. To assess the significance of the difference between these sample variances and the expected power A^2 it is possible to evaluate confidence intervals and construct hypothesis tests using the distribution derived for the sample variances in appendix A. For the plane wavefront model to be accepted, all of the sample variances are required to lie within the 90 percent confidence interval calculated from this distribution.

Validation of the plane wavefront model also requires the distribution of the phase of the spatial auto-correlation function to be evaluated under the condition that the plane wavefront model is valid. The distribution of the phase of the temporal auto-correlation function derived in appendix A may also be used to evaluate the distribution of the phase of the spatial auto-correlation function which is expected to be linear and parameterised by θ under the mean plane wavefront model. This can be performed by replacing the statistical properties of correlation between spatial samples separated by a certain distance with those of temporal samples separated by an "equivalent" time interval.

In the previous statement, the term "equivalent" refers to the time interval or lag at which the phase distribution of the temporal auto-correlation function about its expected value is the same as that of the interrogated lag on the spatial auto-correlation function about its expected value. More specifically, the distribution of the phase of a sample spatial lag about its expected phase has the same shape as that of a sample temporal lag about its expected phase when the magnitudes of the expected correlations in the spatial and temporal domain are the same and the same number of samples are used to form them. Hence, the confidence intervals for the phase of the sample spatial lags may be obtained using the same formulas derived in appendix A for temporal lags at which the magnitude of the correlation falls to the same value as that which is expected for each spatial lag under the assumed model. For the plane wavefront model to be accepted, all of the sample spatial lag phases are required to lie within the 90 percent confidence interval calculated from this distribution.

If models for both the spatial and temporal correlation functions of the array data can be validated it is of interest to determine whether the space-time second order statistics can be deduced with reasonable accuracy from a knowledge of the spatial and temporal correlation functions. As mentioned previously, the space-time process is said to be separable if the space-time correlation function can be expressed as a product of the temporal-only and spatial-only correlation functions. Hypothesis tests may then be derived to accept or reject the space-time separability of the model by invoking the same argument as described in the previous paragraph and using the distributions in appendix A. A simpler measure of whether a separable model is accurate can be developed by quantifying the degree of fit between the expected separable model of the space-time correlation function, denoted by $r(\Delta d, \Delta t)$ and the sample space-time correlation function $\hat{r}(\Delta d, \Delta t)$ estimated from the data. In this instance, a separable model may be considered appropriate for describing the data if the fitting accuracy, defined by Eqn.(3.35), is greater than say 95 percent.

$$\text{Fitting Accuracy} = 1 - \frac{\sum_{\Delta d=0}^{N-1} \sum_{\Delta t=0}^{Q-1} |\hat{r}(\Delta d, \Delta t) - r(\Delta d, \Delta t)|^2}{\sum_{\Delta d=0}^{N-1} \sum_{\Delta t=0}^{Q-1} |\hat{r}(\Delta d, \Delta t)|^2} \tag{3.35}$$

3.4 Experimental results

After the accuracy of the theoretical distributions derived for the sample ACS in appendix A are checked by simulation, hypothesis tests based on these distributions are applied in section 3.4.1 to accept or reject the assumption that the temporal properties of the HF channel are spatially homogeneous across a very wide aperture antenna array. Section 3.4.2 analyses the sample spatial covariance matrix of the received signal modes to determine whether a stationary statistical model is suitable for representing the spatial properties of the HF channel over a period of a few minutes. This section also quantifies the degree to which the space-time second order statistics of the data can be deduced from models of the spatial-only and temporal-only auto-correlation functions.

3.4.1 Validation of ACS distributions and spatial homogeneity

The validity of the theoretical sample ACS distributions derived in appendix A can be ascertained by simulating many realisations of a complex Gaussian distributed random process with known second order statistics. The sample ACS is evaluated for each realisation so that for each component of the ACS it is possible to observe the statistical distribution of the sample by means of a histogram. The normalised histogram approaches the true probability density function of the sample ACS as the number of realisations tends to infinity, hence, for a large number of realisations the resulting histograms may be compared directly with the theoretically derived probability density functions.

A first order Gaussian distributed stationary auto-regressive (AR) process was simulated for the purpose of confirming the theoretically derived sample ACS distributions. The auto-correlation function of the AR(1) random process $z(t)$ coincides with the exponentially decaying model described in the previous section and realisations of $z(t)$ are relatively simple to generate by using the following recursive relation.

$$z(t) = \alpha z(t-1) + \sqrt{1-|\alpha|^2}\, n(t) \quad , \quad t = 0, 1, .., P-1 \tag{3.36}$$

In Eqn.(3.36), α is the AR(1) random process parameter which may be complex-valued and is such that $|\alpha| < 1$ to ensure the process is stable (i.e., with the pole inside the unit circle). The term $n(t)$ is a complex Gaussian distributed innovative white noise process with the following second order statistics.

$$E\{n(t)n^*(t+\tau)\} = \delta(\tau) \quad , \quad E\{n(t)n(t+\tau)\} = 0 \tag{3.37}$$

From Eqn.(3.36) and Eqn.(3.37) it can be shown that the statistically expected auto-correlation function of the process $z(t)$ is given by $r_z(\tau) = E\{z(t)z^*(t+\tau)\} = \alpha^\tau$ for $\tau = 0, 1, .., Q-1$. In the simulation study, a total of 10,000 realisations of this random process were generated with values of $P = 10,000$ and $\alpha = 0.99$. For each realisation the

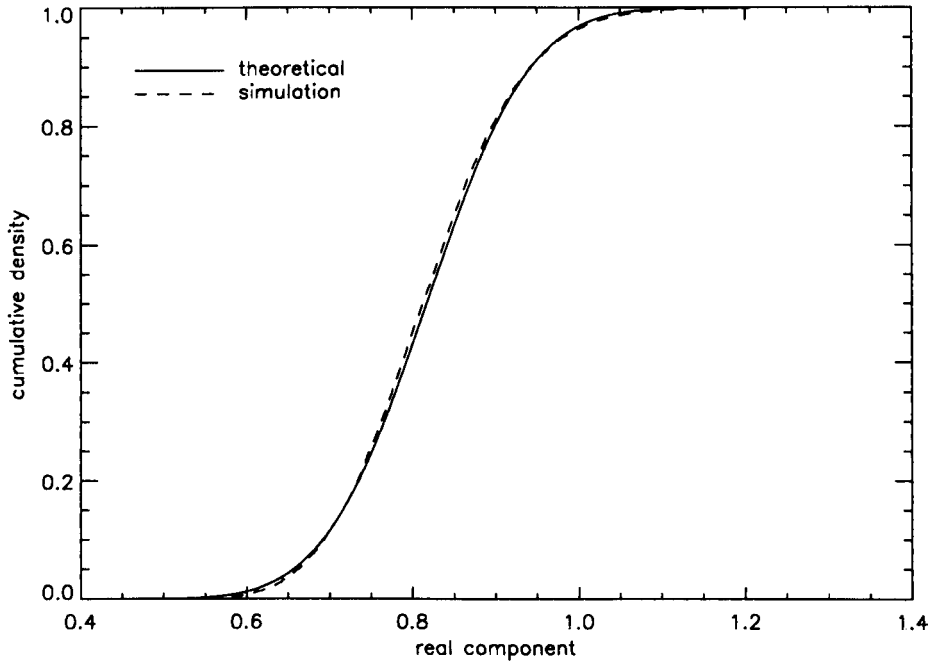

Figure 3.1: Cumulative densities for the real part of the sample ACS $\hat{r}_z(\tau)$ for an AR(1) process with $\alpha = 0.99$, $\tau = 20$ and $P = 10,000$

sample ACS, denoted by $\hat{r}_z(\tau)$, was evaluated in the manner described by appendix A at a number of lags $\tau = 0, 1, ..Q-1$ with $Q = 30$.

A value of $\tau = 20$ was arbitrarily chosen as an example component of the sample ACS to show a comparison between the cumulative density functions derived from theory and those computed from the simulations. At a lag interval of $\tau = 20$, the statistically expected value of the ACS is $r_z(20) = \alpha^{20} = 0.818$, and as the sample ACS $\hat{r}_z(\tau)$ is unbiased, this is equal to the mean value of the sample ACS $\hat{r}_z(20)$ when averaged over an infinite number of realisations. Due to finite sample effects, the interrogated component of the sample ACS $\hat{r}_z(20)$ will in general be complex-valued so the cumulative density may be presented either in terms of the real and imaginary parts or in terms of magnitude and phase. Figures 3.1 and 3.2 show the cumulative densities obtained for the real and imaginary parts of this component of the sample ACS. The theoretical curves in each figure correspond to normal probability density functions with means determined by the expected value of the ACS component and a variance given by the expressions derived in appendix A. It is evident that the theoretical curves accurately match those obtained by direct simulation. Figures 3.3 and 3.4 show analogous results for the magnitude and phase cumulative distributions.

The Gaussian model of the HF channel temporal auto-correlation function was experimentally confirmed by (Watterson et al. 1970) but it was not possible for the authors to determine whether the parameters of such a model could be assumed constant for all the receivers in a very wide aperture HF array. In this experiment the temporal auto-correlation function of each signal mode was computed in each of $N = 30$ receivers by

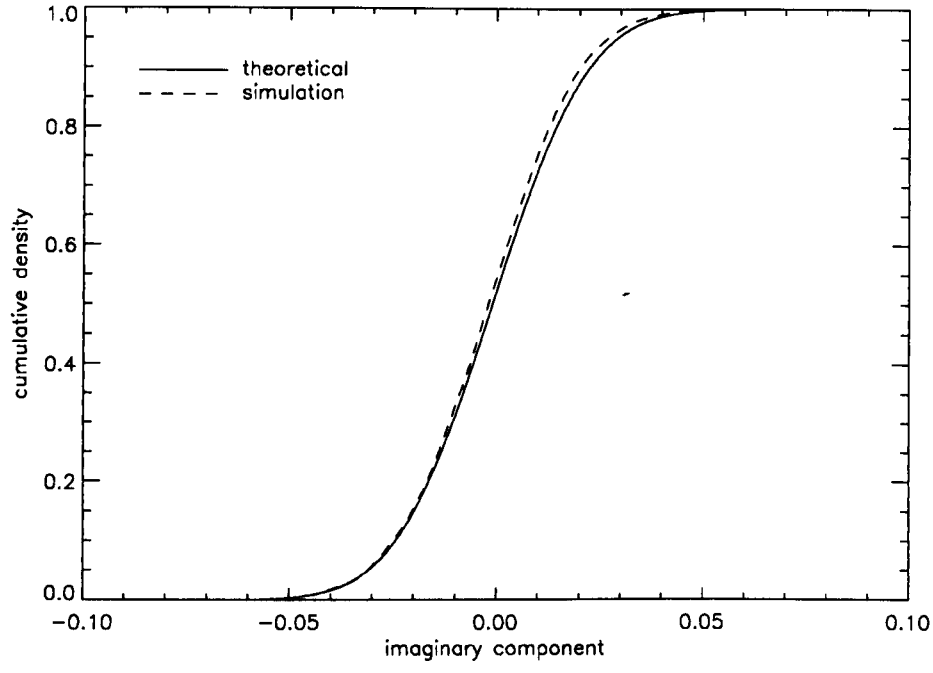

Figure 3.2: Cumulative densities for the imaginary part of the sample ACS $\hat{r}_z(\tau)$ for an AR(1) process with $\alpha = 0.99$, $\tau = 20$ and $P = 10,000$

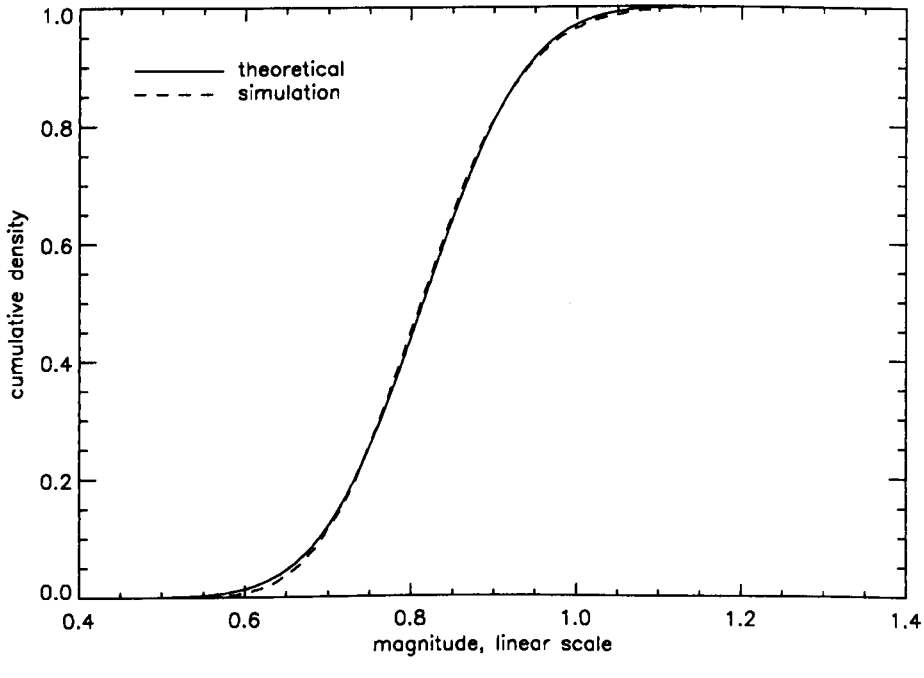

Figure 3.3: Cumulative densities for the magnitude of the sample ACS $\hat{r}_z(\tau)$ for an AR(1) process with $\alpha = 0.99$, $\tau = 20$ and $P = 10,000$

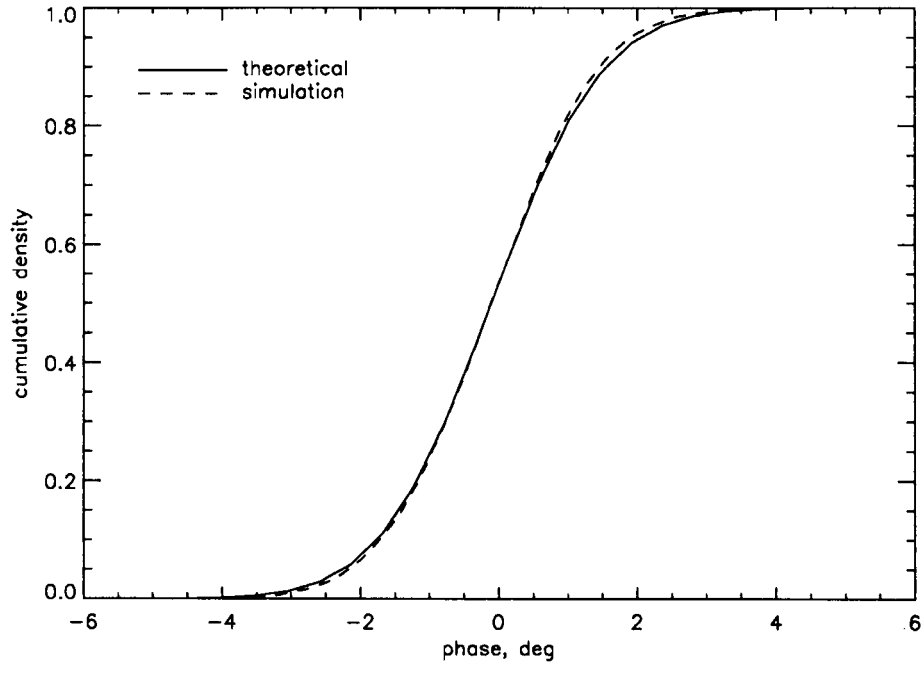

Figure 3.4: Cumulative densities for the phase of the sample ACS $\hat{r}_z(\tau)$ for an AR(1) process with $\alpha = 0.99$, $\tau = 20$ and $P = 10,000$

averaging a sum of lagged products in 47 dwells of data collected over a period of about 4 minutes (i.e., the number of time-series samples per receiver was $P = 47 \times 256 = 12,032$). A total of $Q = 30$ consecutive temporal sample lags were evaluated in each receiver at a lag spacing of 6 PRI (i.e., 0.1 seconds). Using all $N = 30$ sample ACS's, the Gaussian model parameters were estimated using the method described in section 3.3. The parameters which define the displacement and width of the Gaussian temporal auto-correlation functions that provide the best fit to the different modes are listed in Table 3.1. The power scaling factors associated with each of these models over different receivers will be considered later when the spatial properties of the HF channel are analysed. Under the null hypothesis of spatial homogeneity, the Gaussian temporal ACS model estimated for a particular mode is assumed to have the same form, apart from possibly a power scaling factor, across all $N = 30$ receivers.

Mode	a	b	B_t, Hz	Δf, Hz
$1E_s$	-2.09×10^{-4}	$j \times 0.268$	0.145	0.43
$1F_2$	-2.24×10^{-4}	$j \times 0.277$	0.149	0.44
$1F_2(o)$	-9.06×10^{-5}	$j \times 0.294$	0.095	0.47
$1F_2(x)$	-1.97×10^{-4}	$j \times 0.332$	0.140	0.53

Table 3.1: Gaussian temporal ACS model parameters estimated for the different propagation modes of the HF link.

The parameters B_t and Δf in Table 3.1 represent the Doppler bandwidth (the width of Gaussian power spectrum) and mean Doppler shift (the displacement of Gaussian power

spectrum) respectively. The mean Doppler shift is calculated as $\Delta f = \beta/2\pi\Delta t$ where the lag interval $\Delta t = 0.1$ since in the model β represents the change in phase per unit a lag interval. The Doppler bandwidth is calculated as the inverse of the time interval for which the magnitude of the Gaussian temporal auto-correlation function model drops by a factor of $1/e$, in mathematical terms $B_t = (\Delta t\sqrt{1/\alpha})^{-1}$. It is noted that the mean Doppler shifts estimated by this method are practically the same as those estimated for the same modes by conventional processing methods in chapter 2. The Doppler bandwidths indicated in Table 3.1 are of the same order as those measured in (Shepherd and Lomax 1967) and (Watterson et al. 1970) on mid-latitude ionospheric paths.

Assuming that each of the estimated models represents the true temporal ACS of the signal sampled in each receiver, it is possible to derive confidence bounds for each point on the sample ACS by using the theoretical results validated earlier in this section. For each point on the ACS, these confidence bounds specify the range of values which are expected to contain a certain percentage of the sample ACS values for a random process that is described by the assumed auto-correlation function model. Hence, if a particular component of the sample ACS has a value which lies outside (say) the 90 percent confidence bounds then there is strong reason to believe that the hypothesised model for the ACS does not coincide with that of the data. If the sample ACS lies within the confidence bounds then there is no strong reason to reject the hypothesised model which may then be accepted.

Figure 3.5 shows the real part of temporal ACS model estimated for the $1E_s$ mode (solid line) as well as the upper and lower deciles (dashed lines) of the sample ACS distribution associated with real component under this ACS model. A sample temporal ACS for this mode is estimated from *experimental data* recorded in each of the $N = 30$ receivers, these ACS's have been overplotted with a + symbol in Figure 3.5 after being normalised by the power scaling factor e^{c_n} estimated for each receiver $n = 1, 2, .., N$. Figure 3.6, in the same format as Figure 3.5, shows the results obtained for the imaginary part of the temporal ACS corresponding to the $1E_s$ reflection.

The oscillating behavior of the real and imaginary parts with respect to lag interval is due to the mean or steady component of Doppler shift, the higher the mean Doppler shift the higher the frequency of these oscillations. The rate of decay of the amplitude in both the real and imaginary parts is a consequence of Doppler spread, the higher the Doppler spread the faster the magnitude of the ACS falls with respect to lag interval. Figures 3.7 to 3.12 show the results for the other modes in analogous fashion. In all cases, the Gaussian temporal ACS model estimated for each mode agrees well with the sample ACS's derived for the corresponding mode in each of the $N = 30$ receivers.

On the basis of these results, it is evident that the there is no strong reason to reject a Gaussian shaped temporal ACS model for HF signals reflected by a quiet mid-latitude ionosphere. This is in agreement with the findings of (Watterson et al. 1970). Furthermore, the variability observed in the normalised sample ACS from one receiver to another

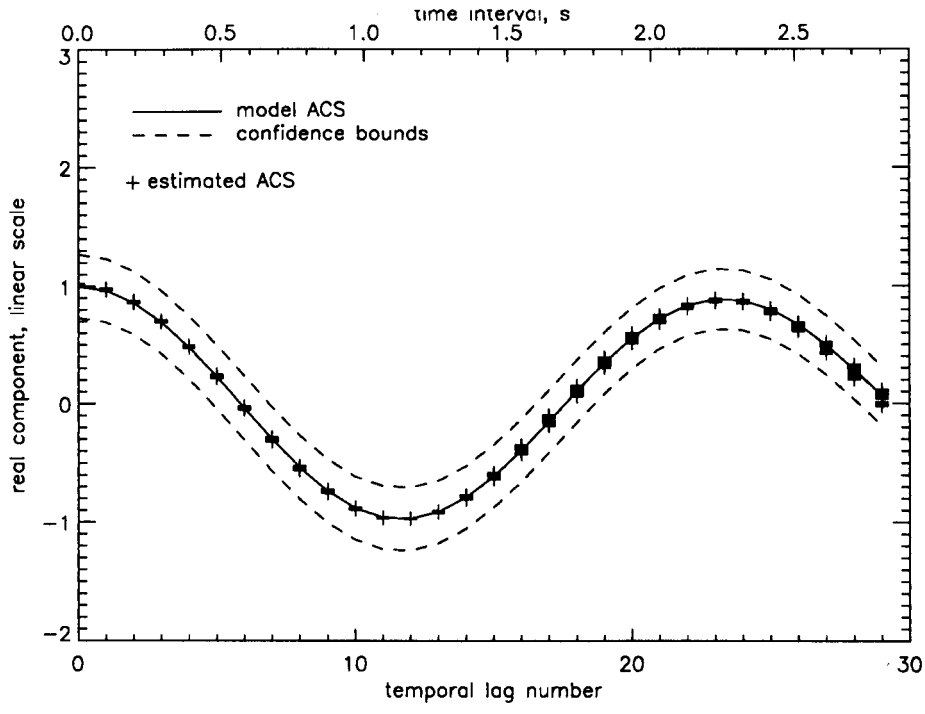

Figure 3.5: Temporal auto-correlation function for real component of $1E_s$ mode

is almost always contained within the confidence bounds calculated for the hypothesised Gaussian model. This observation, which could not be made by (Watterson et al. 1970), leads to the conclusion that there is no strong reason to reject the assumption of spatial homogeneity for the mid-latitude HF channel. In other words, for a very wide aperture antenna array spanning 2.7 km in length it has been demonstrated that the temporal ACS of a HF signal reflected by a single ionospheric layer and received at different points along the array can be described by a Gaussian model with the same mean Doppler shift and Doppler spread parameters. Apart from a possible power scaling factor these results suggest that the temporal second order statistics of the investigated mid-latitude HF channel are spatially homogeneous.

3.4.2 Spatial stationarity and space-time separability

The spatial properties of the HF channel are analysed by forming the sample spatial covariance matrix $\hat{\mathbf{R}}_x$ of the array data for each of the reflected signal modes. As described in section 3.3, it is of interest to study the behavior of the correlation coefficient as a function of both receiver spacing and absolute position over the array as well as the spatial structure of the mean wavefront arising for each propagation mode. A model for the correlation coefficients seen by a very wide aperture antenna array has not been rigorously verified by previous experimental data analysis. Similarly, the plane wave model often assumed for the *mean wavefront* of a HF signal reflected by a single ionospheric layer has not been experimentally confirmed by formal statistical tests.

Under the spatial stationarity assumption, the correlation coefficient between different

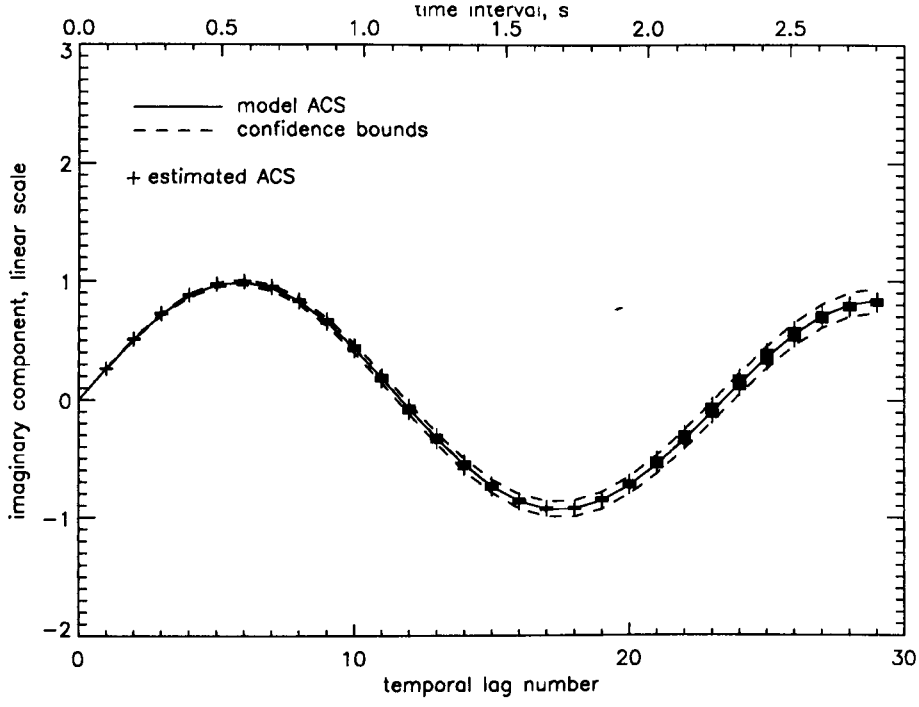

Figure 3.6: Temporal auto-correlation function for imaginary component of $1E_s$ mode

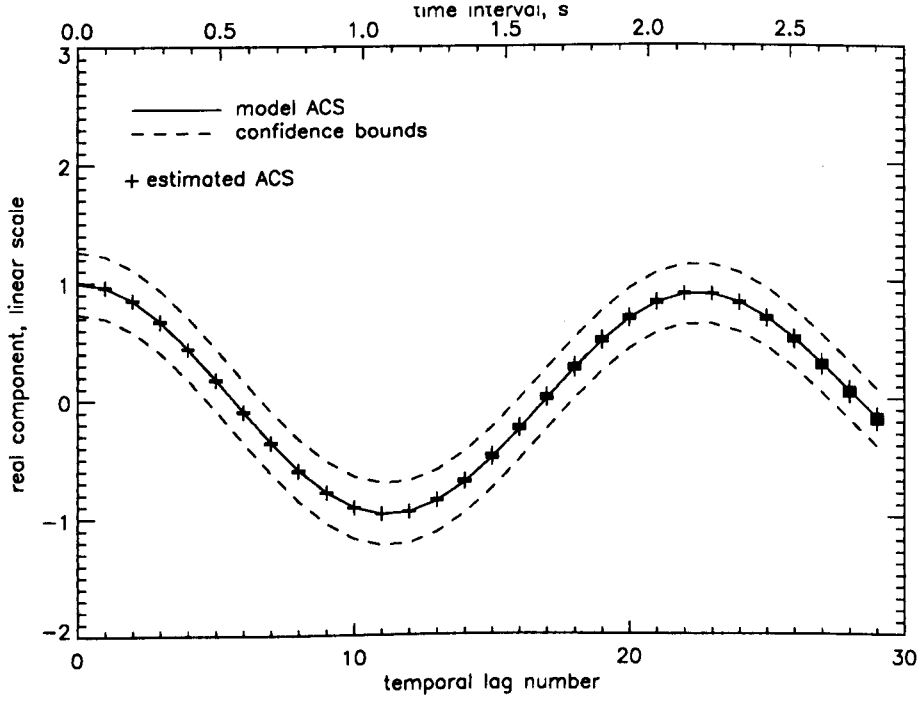

Figure 3.7: Temporal auto-correlation function for real component of $1F_2$ mode

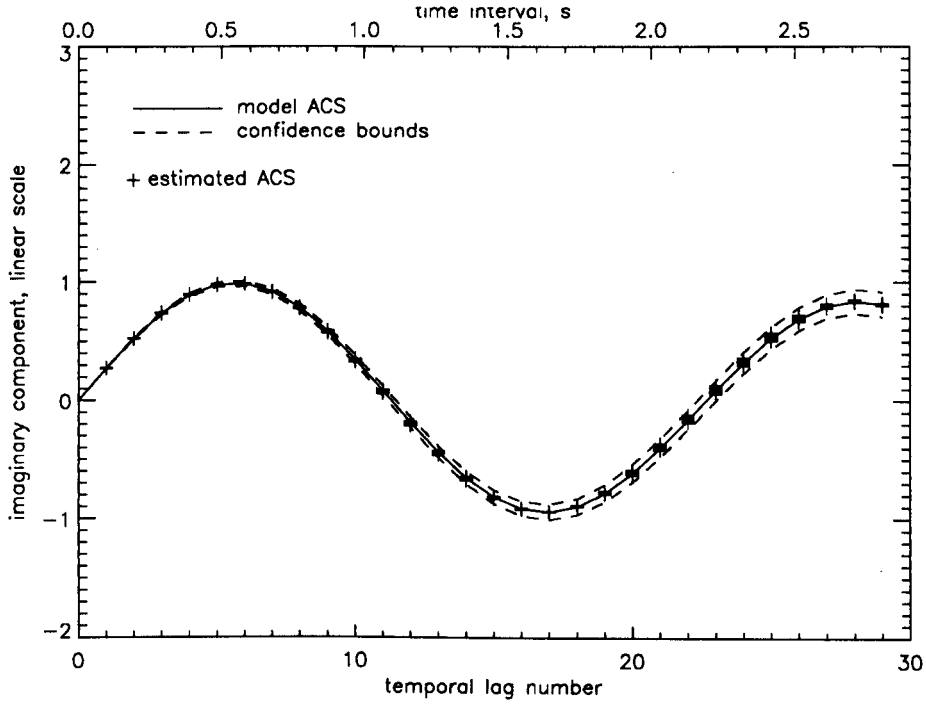

Figure 3.8: Temporal auto-correlation function for imaginary component of $1F_2$ mode

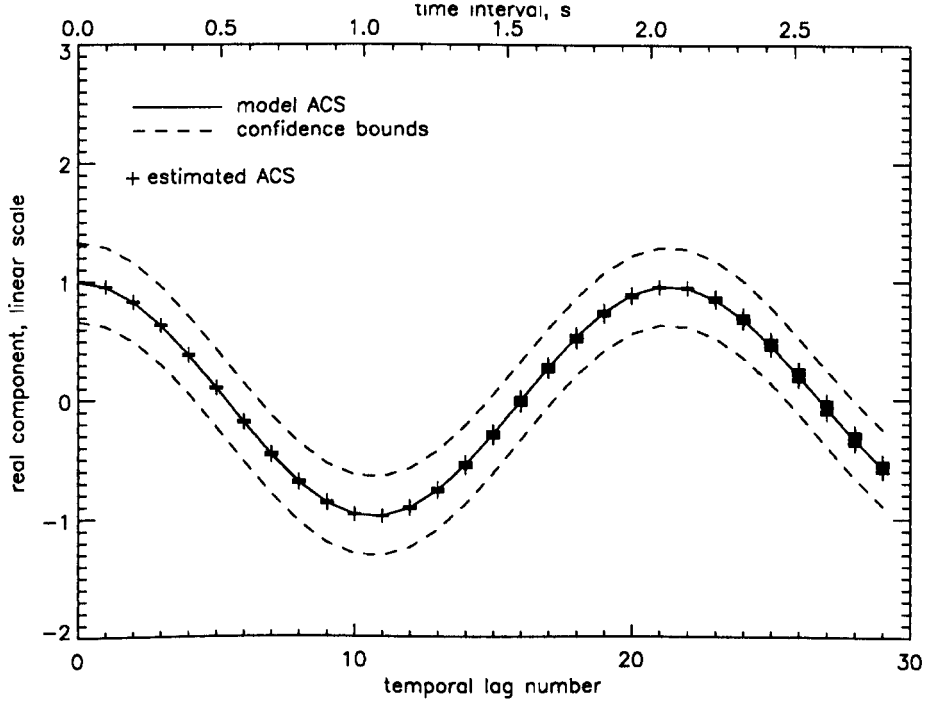

Figure 3.9: Temporal auto-correlation function for real component of $1F_2(o)$ mode

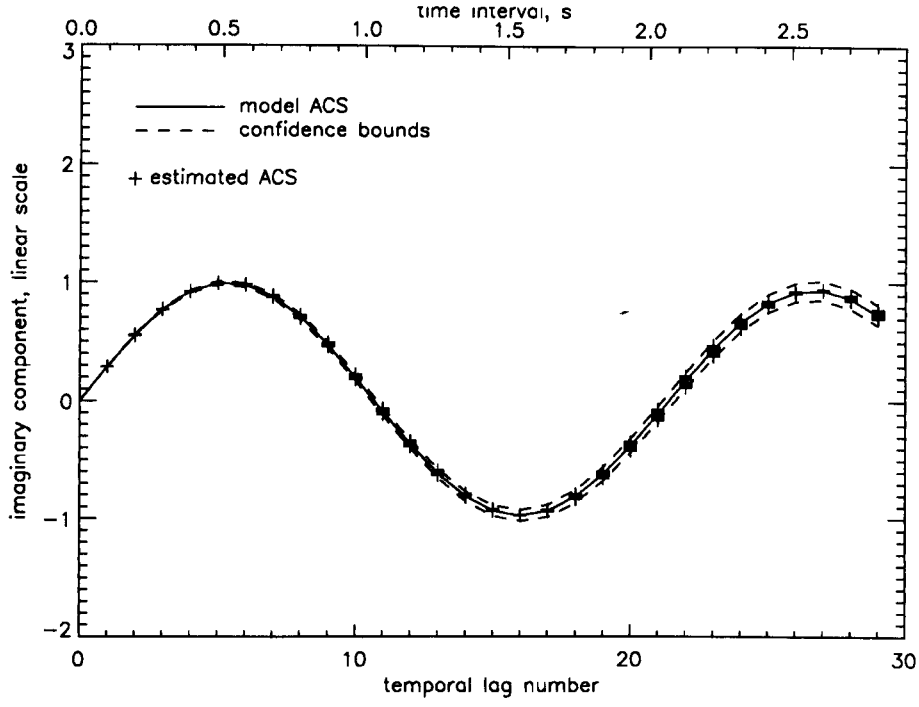

Figure 3.10: Temporal auto-correlation function for imaginary component of $1F_2(o)$ mode

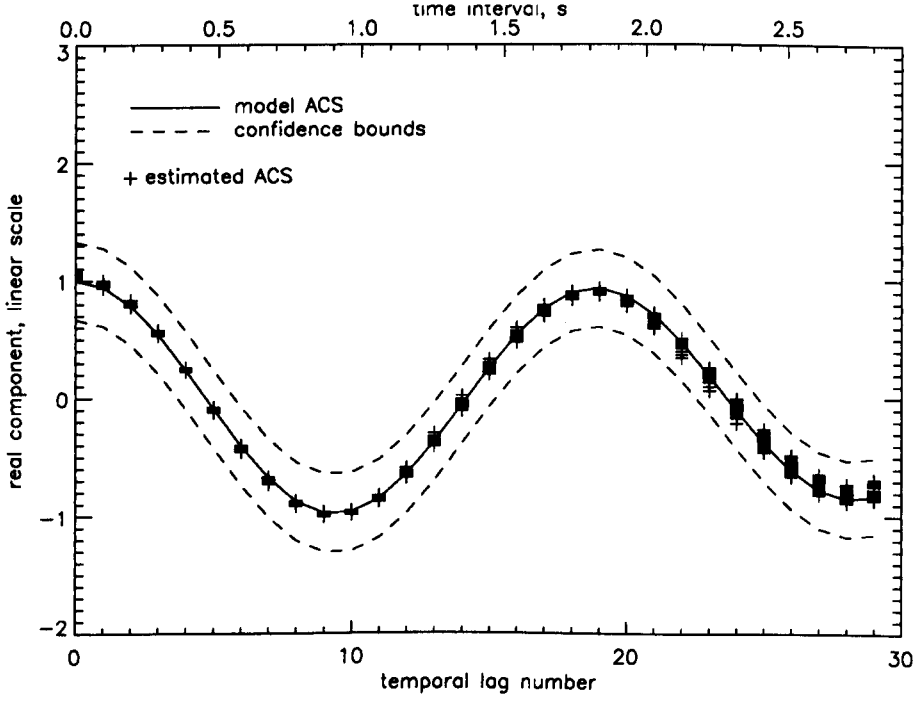

Figure 3.11: Temporal auto-correlation function for real component of $1F_2(x)$ mode

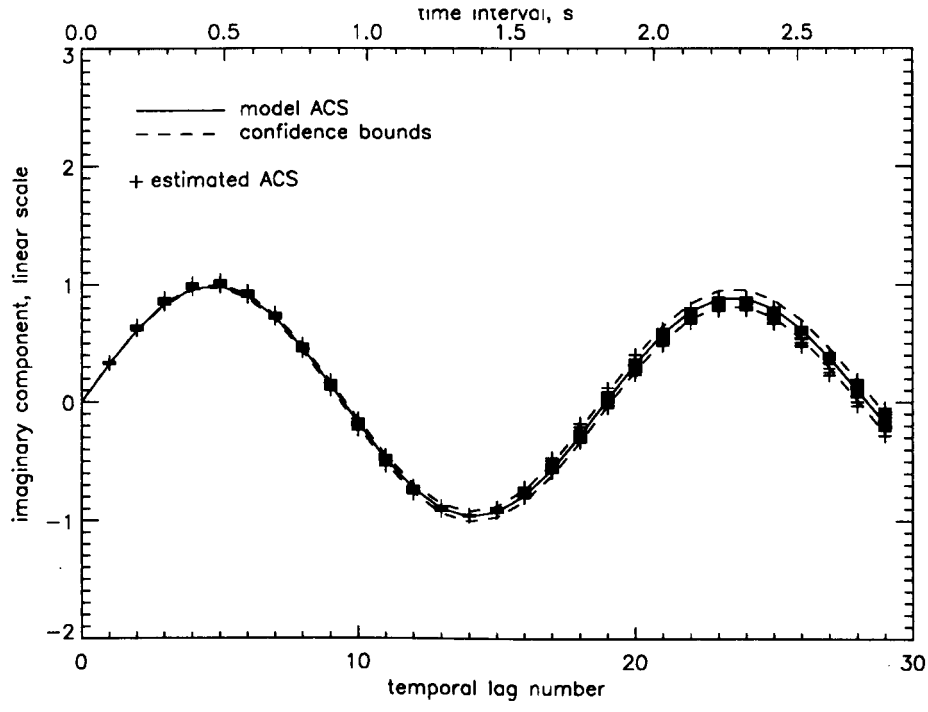

Figure 3.12: Temporal auto-correlation function for imaginary component of $1F_2(x)$ mode

receiver outputs only depends on receiver separation and not the absolute receiver positions within the array. If the HF channel is spatially stationary then the function which describes the behavior of the correlation coefficient with respect to receiver separation can be estimated using Eqn.(3.30). In accordance with the mathematical models derived from consideration of the physics in section 3.2, it is postulated that an exponentially decaying function of receiver separation describes the behavior of the correlation coefficient. The single parameter of this function is estimated for each mode as described in section 3.3 such that the analytic function provides a least squares fit to the measured data.

The $N \times N$ sample spatial covariance matrix $\hat{\mathbf{R}}_x$ used to compute the various correlation coefficients was estimated from the array data using Eqn.(3.29) with $N = 30$ receivers and $P = 12,032$ array snapshots recorded in 47 dwells over a period of approximately 4 minutes. For a separation of d receivers (equivalent to $d \times 84.0$ metres) there are $N - d$ correlation coefficients which can be formed using the $P = 12,032$ array snapshots. It should also be noted that the consecutive array snapshots used to form the sample spatial covariance matrix are correlated and hence *not* statistically independent.

Figures 3.13 to 3.16 show the models estimated for the HF signals reflected by different ionospheric layers along with the associated confidence bounds (i.e., upper and lower deciles) calculated from the expression in Eqn.(3.31). A method for calculating the number of *independent* observations or degrees freedom n in Eqn.(3.31) for a number of correlated observations was described in section 3.3. The actual estimates of the correlation coefficients resulting from the data have been overplotted with a + symbol in each of the figures. It is noted that there are more points marked with a + at smaller receiver separations because there are more pairs of receivers with such separations in

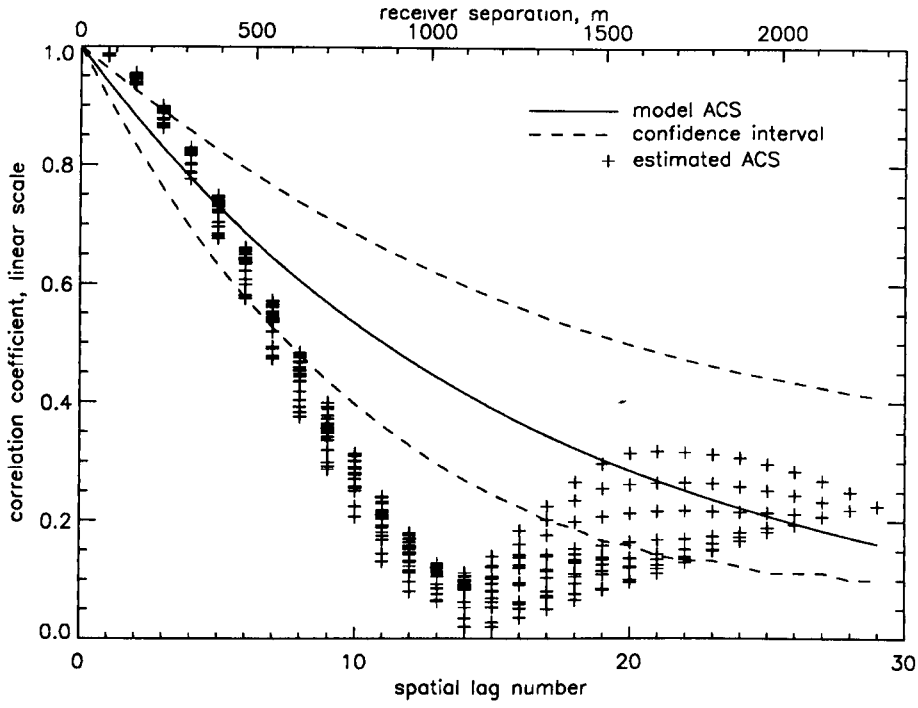

Figure 3.13: Spatial correlation coefficients for $1E_s$ mode

the array. This explains why there is only one point for the maximum spatial separation which occurs between the first and last receiver of the array.

It is evident from Figure 3.13 that correlation coefficients estimated for the $1E_s$ mode are not well described by the postulated exponentially decaying stationary model of the spatial ACS. This is not surprising because the array data processed in this case was shown in chapter 2 to result from two quite distinct sporadic-E reflections which have significantly different angles-of-arrival. The superposition of two different spatial frequencies is expected to produce regularly spaced nulls in the spatial ACS, the first (imperfect) null is evident at a receiver separation of approximately 1150 m and it appears that the correlation coefficient is falling towards a second null slightly past 2500 m. In contrast to the $1E_s$ mode, the remaining modes are in very good agreement with the postulated stationary model as the great majority of the measured points lie within the confidence bounds. Hence, for single modes there is no strong reason to reject the spatially stationary exponentially decaying model for the correlation coefficient.

The mean plane wavefront model assumes that the mean power of the signal is the same in all receivers. The estimated power or variance of the signal may vary from one receiver to another even if the model is valid due to either finite sample effects or instrumental errors such as mismatches between the gains of different reception channels in the array. Assuming the reception channels are well matched, the mean power of best fit to all reception channels can be calculated in accordance with Eqn.(3.34) and is given by the amplitude squared $\hat{A}^2$ of the plane wave of best fit. The results derived in appendix A can be used to calculate confidence bounds for the estimated power by using the temporal ACS model of the particular mode being analysed. The temporal ACS models used in

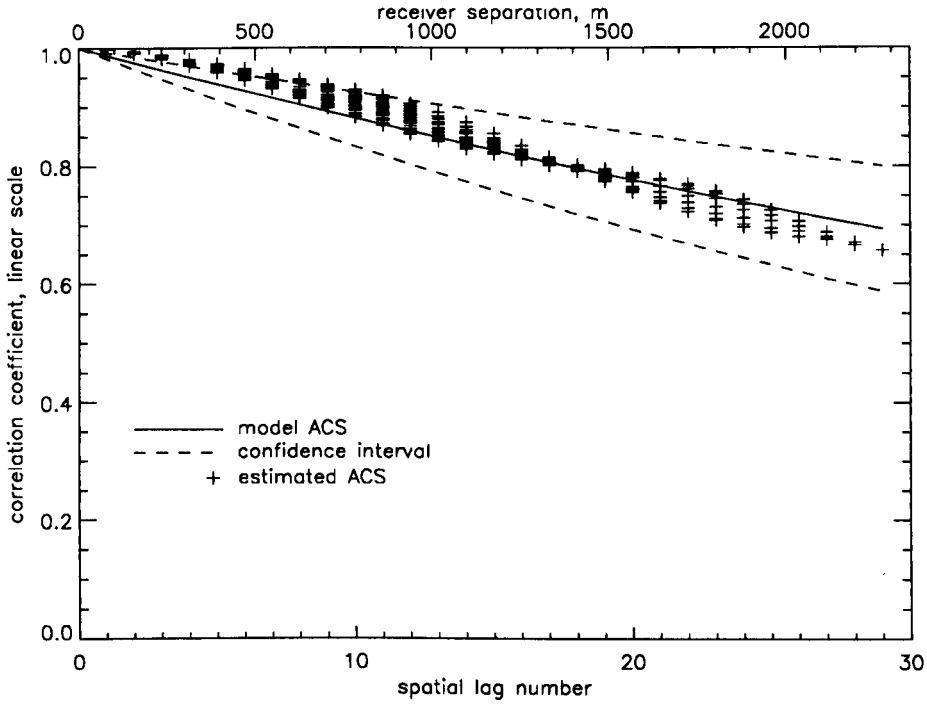

Figure 3.14: Spatial correlation coefficients for $1F_2$ mode

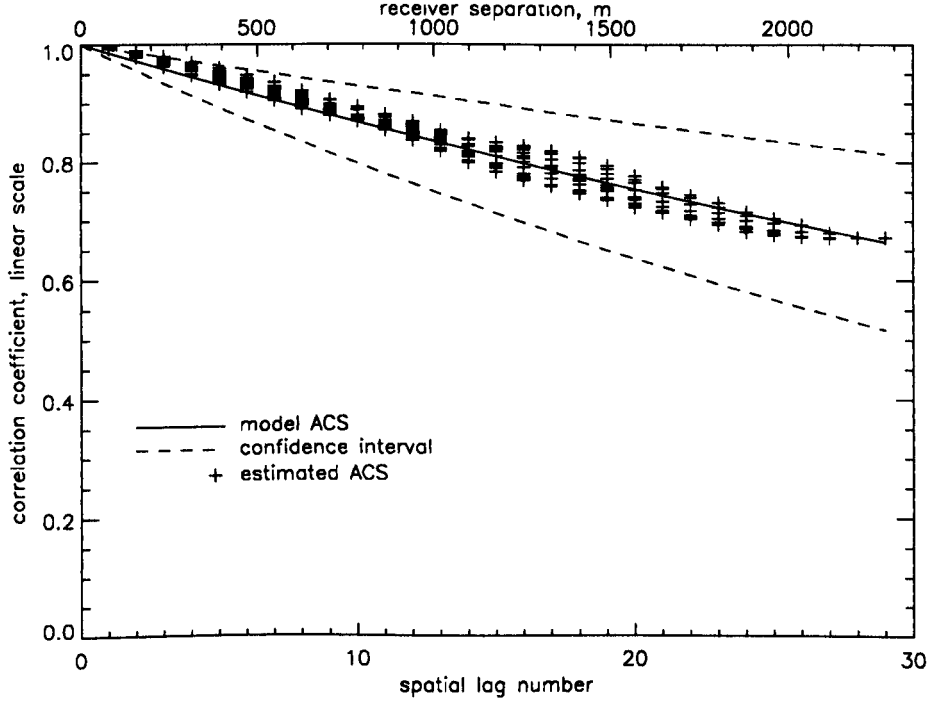

Figure 3.15: Spatial correlation coefficients for $1F_2(o)$ mode

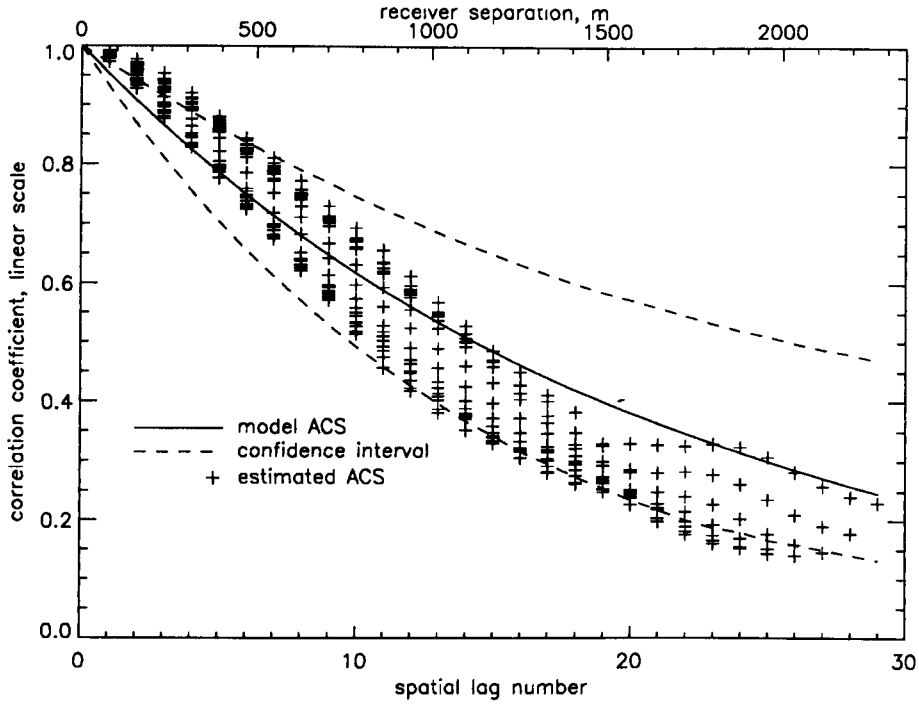

Figure 3.16: Spatial correlation coefficients for $1F_2(x)$ mode

this analysis are those which were previously validated for each mode in section 3.4.1.

Figures 3.17 to 3.20 show the mean power of best fit (solid line), confidence bounds (dashed lines) and the actual power estimated in different the receivers as "+" symbols for each HF signal reflection. The $1E_s$ and $1F_2(x)$ reflections have a significant number of measurements which lie outside the confidence bounds which suggests that the plane wavefront model is not representative of the mean wavefront for these signals. In the case of the $1E_s$ reflection this is understandable due to the two modes which are actually present, but for the $1F_2(x)$ mode this result is somewhat unexpected and indicates that the spatial structure of the ionosphere which propagates this single magneto-ionic component is relatively more disturbed than that which propagates the $1F_2$ and $1F_2(o)$ modes on this occasion. This is supported by the fact that the correlation coefficient measurements for this mode (Figure 3.16) are comparatively more spread than those of the $1F_2$ and $1F_2(o)$ modes. The latter two modes satisfy the constant power condition of the mean plane wavefront model; to validate this model it is also necessary to investigate the linearity of the phase across the aperture.

The expected linear phase component of the spatial ACS is calculated by estimating the mean direction of arrival θ in accordance with Eqn.(3.34). In the spatial covariance matrix, each column contains a spatial ACS with a different receiver chosen as the spatial reference point. Since the spatial covariance matrix is Hermitian it follows that all of the information is contained in the elements of either the upper or lower triangle of the matrix including the main diagonal. It is therefore required to check whether the phase progression exhibited by the elements in each column of either the upper or lower triangle of the sample spatial covariance matrix coincides within a reasonable tolerance with the

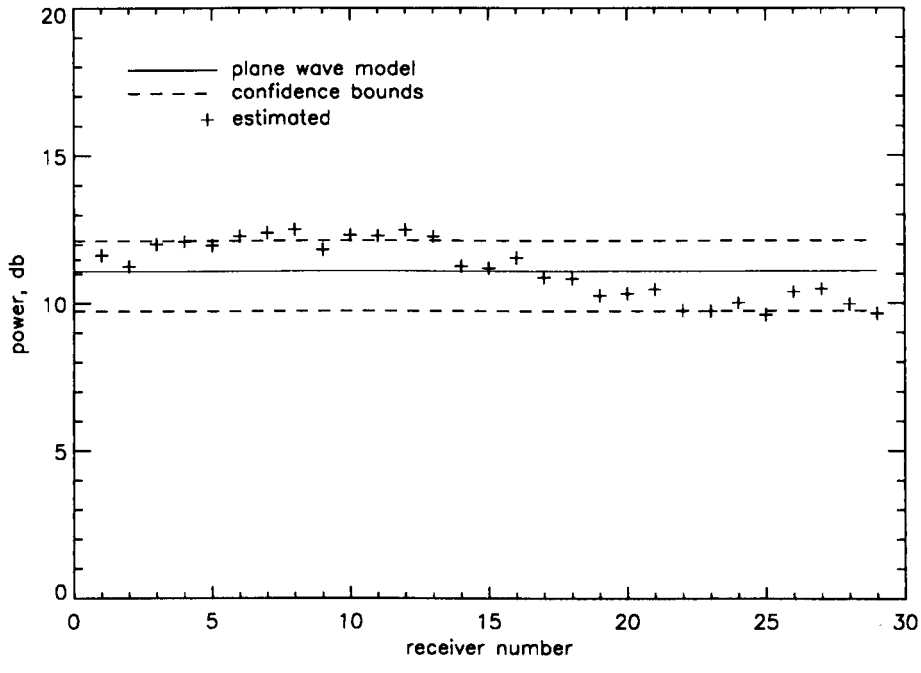

Figure 3.17: Power across aperture for $1E_s$ mode

linear phase front of best fit. A reasonable tolerance is defined by the confidence bounds chosen as upper and lower deciles of the phase distribution which can be calculated using the same theory developed for temporal random processes in appendix A, as described in section 3.3.

Figures 3.21 to 3.24 show the mean linear phase front (solid line), the confidence bounds (dashed lines) and the phases estimated at different spatial lags and reference receivers ("+" symbols) for each of the propagation modes. Unlike the power measurements, more than $N-1$ symbols appear in Figures 3.21 to 3.24 because each receiver in the array may be designated as the spatial reference. In all figures the right vertical axis shows the cone angle-of-arrival which depends on the slope of the linear phase-front, the cone angle for a particular propagation mode is indicated by the intersection of a straight line from the origin with the right vertical axis.

As for the power measurements, it should be kept in mind that phase measurements are also affected by instrumental errors such as phase mismatches in the response of different reception channels. Despite the potential existence of these mismatches it was assumed that the receivers were identical and no allowance was made to tolerate the potential influence of such errors by widening the confidence bounds. If the model is valid and such errors are present then more than the expected number of measurements will lie outside the confidence bounds calculated under the assumption of no errors. Hence, the presence of phase (and/or amplitude) mismatches between the responses of the reception channels will tend to favour the rejection of plane wavefront model.

It is clear from Figure 3.21 that the $1E_s$ mode is far from having a planar phase-front, this is expected due to there being two reflections with significantly different angles-of-

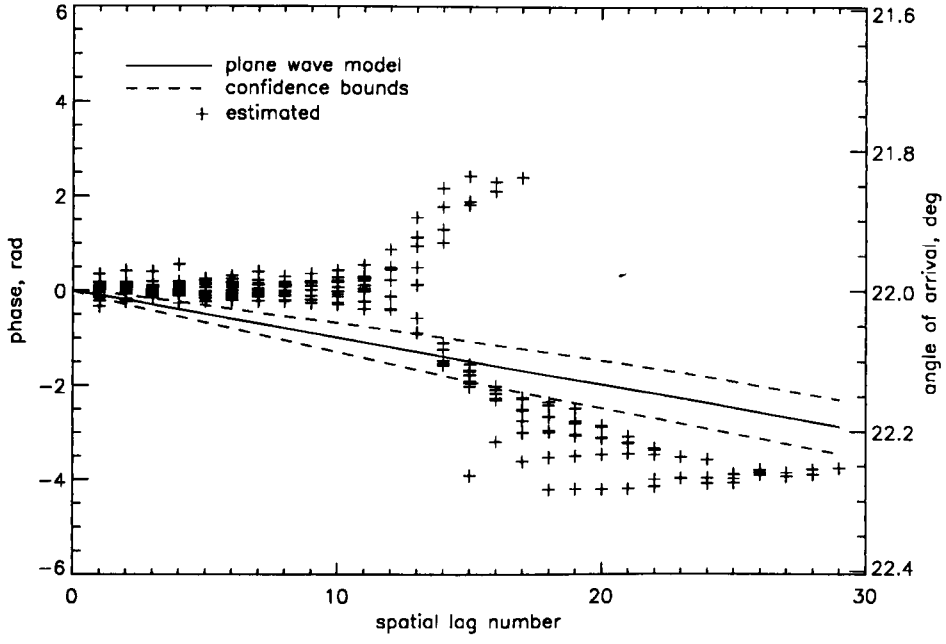

Figure 3.21: Phase measurements across the aperture for $1E_s$ mode with different receivers in the array used as the spatial reference

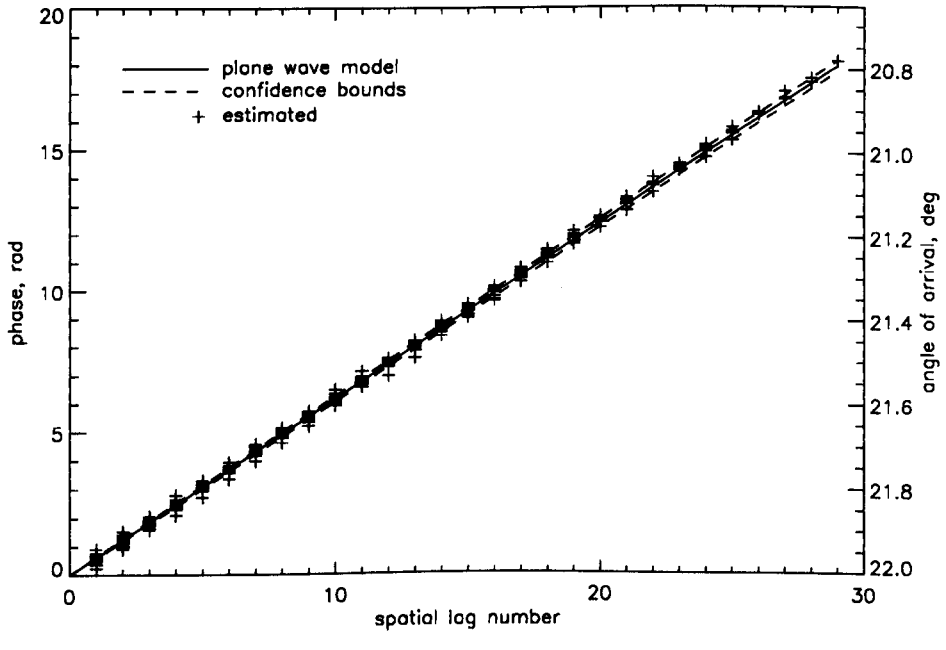

Figure 3.22: Phase measurements across the aperture for $1F_2$ mode with different receivers in the array used as the spatial reference

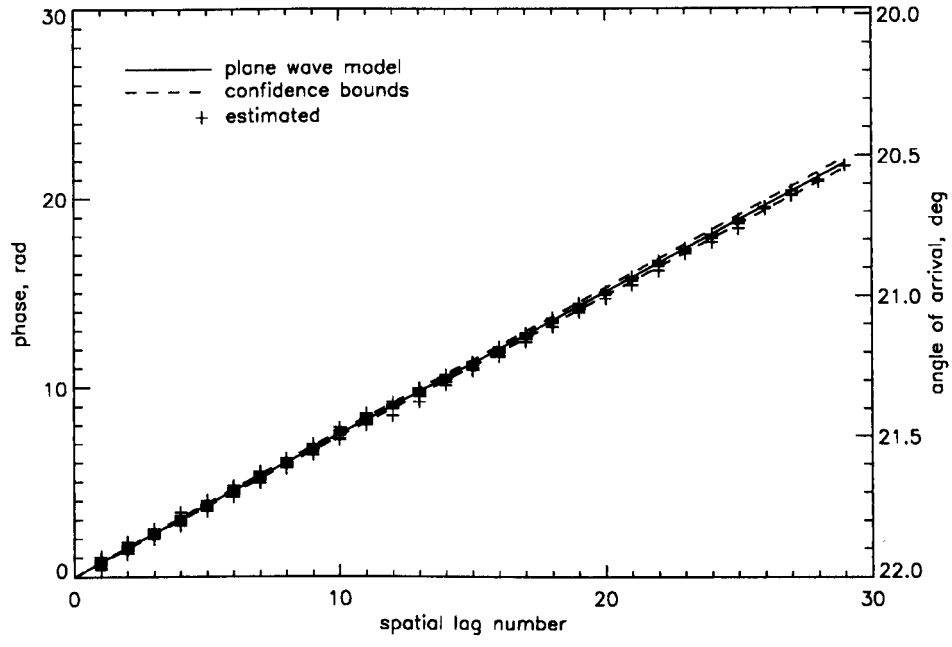

Figure 3.23: Phase measurements across the aperture for $1F_2(o)$ mode with different receivers in the array used as the spatial reference

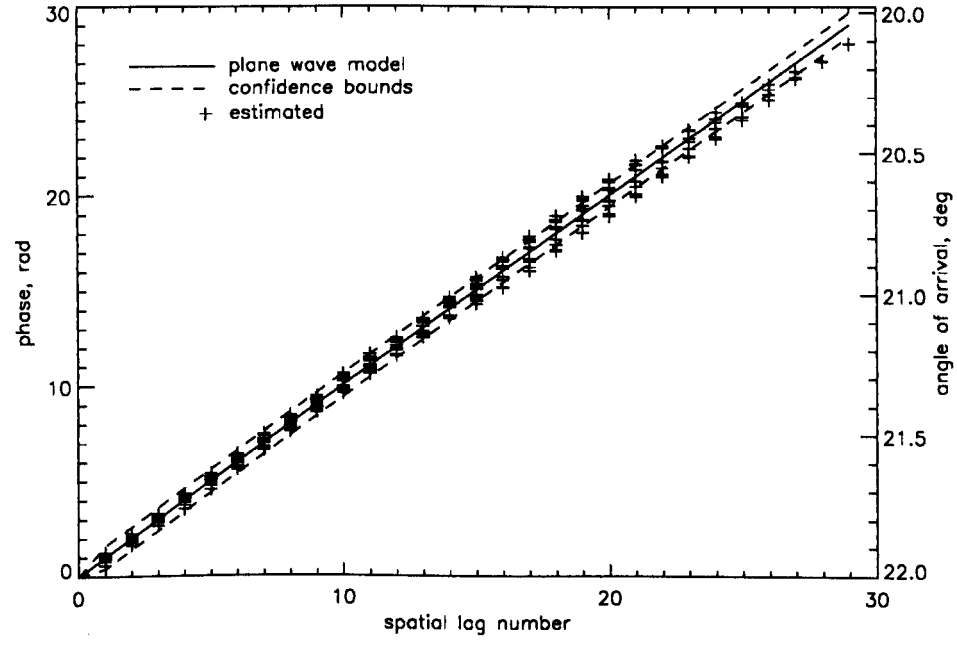

Figure 3.24: Phase measurements across the aperture for $1F_2(x)$ mode with different receivers in the array used as the spatial reference

Mode	b	B_s, deg	θ, deg	FA (%)
$1E_s$	−0.0628	1.58	22.20	24.0
$1F_2$	−0.0126	0.32	20.75	97.8
$1F_2(o)$	−0.0141	0.36	20.48	98.9
$1F_2(x)$	−0.0483	1.22	19.98	94.0

Table 3.2: Decaying exponential spatial ACS parameters estimated for the different propagation modes of the HF link along with the fitting accuracy achieved by the associated separable space-time ACS models

The separable model fitting accuracy measure represented by Eqn.(3.35) has been computed by synthesising a space-time ACS model of the data using the estimated Gaussian temporal ACS model and exponentially decaying spatial ACS model and assuming separability of the space-time ACS for each mode. The fitting accuracy (FA) measures resulting for the different propagation modes over 900 space-time lag points (i.e., 30 spatial lags by 30 temporal lags) are also listed in Table 3.2. As expected, the space-time ACS of the $1E_s$ mode is not well represented by this separable model since the spatial ACS model was previously rejected. The $1F_2$ and $1F_2(o)$ modes are very well represented by the synthesised model indicating that for these modes the space-time ACS can be deduced with good accuracy from a knowledge of the experimentally validated temporal-only and spatial-only ACS. The $1F_2(x)$ mode is well represented by the proposed separable model but not as well as the two latter modes. This may be due to the more disturbed nature of the $1F_2(x)$ mode on this occasion as well as the mean plane wavefront model being rejected for this mode.

Figures 3.25 to 3.32 graphically illustrate the matching between the model and sample space-time ACS in terms of the real and imaginary components for each mode. Although 900 space-time lags were used to compute the fitting accuracy only 100 space-time lags (10 spatial lags by 10 temporal lags) are shown in these figures to make the comparison more clearly visible. The 10 lags chosen in each domain correspond to every third lag such that the illustrated components are given by $\tilde{r}(i,j) = \hat{r}(3i\Delta t, 3j\Delta d)$ for $i,j = 0,1,...,9$. These lags have been stacked into a one-dimensional vector which is indexed by the space-time lag index $l = i \times 10 + j$. The almost exact representation of the sample space-time ACS derived from experimental data by the separable model space-time ACS in Figures 3.27 to 3.28 indicates that the second order statistics of single modes reflected by the mid-latitude ionosphere can be well represented by a separable space-time ACS model.

3.5 Chapter summary

Experimentally validated models which characterise the space-time statistical properties of HF signals reflected by the ionosphere are useful for the purpose of optimising the

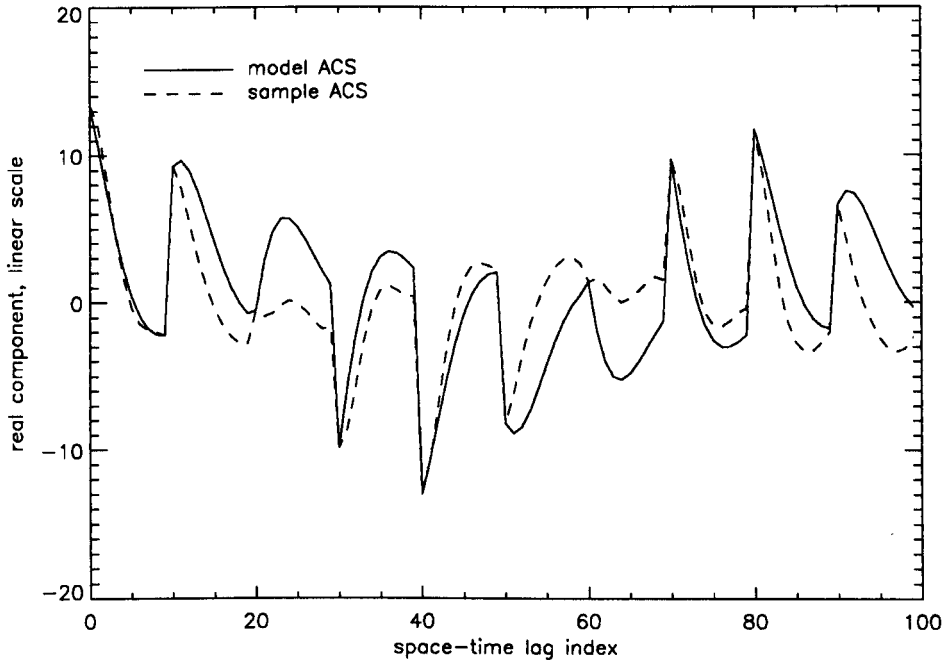

Figure 3.25: Real component of space-time ACS for $1E_s$ mode

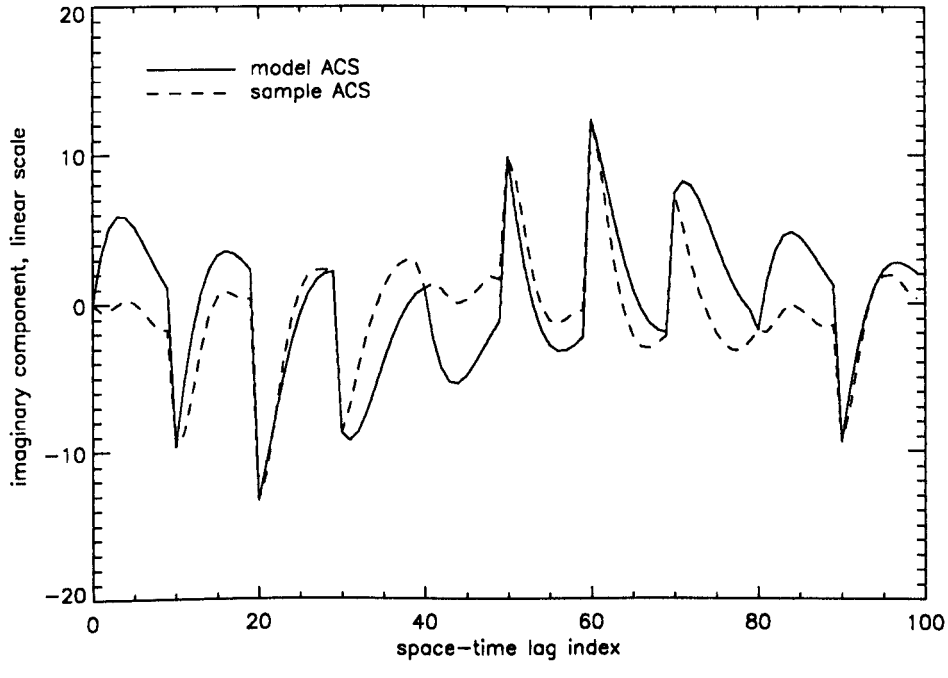

Figure 3.26: Imaginary component of space-time ACS for $1E_s$ mode

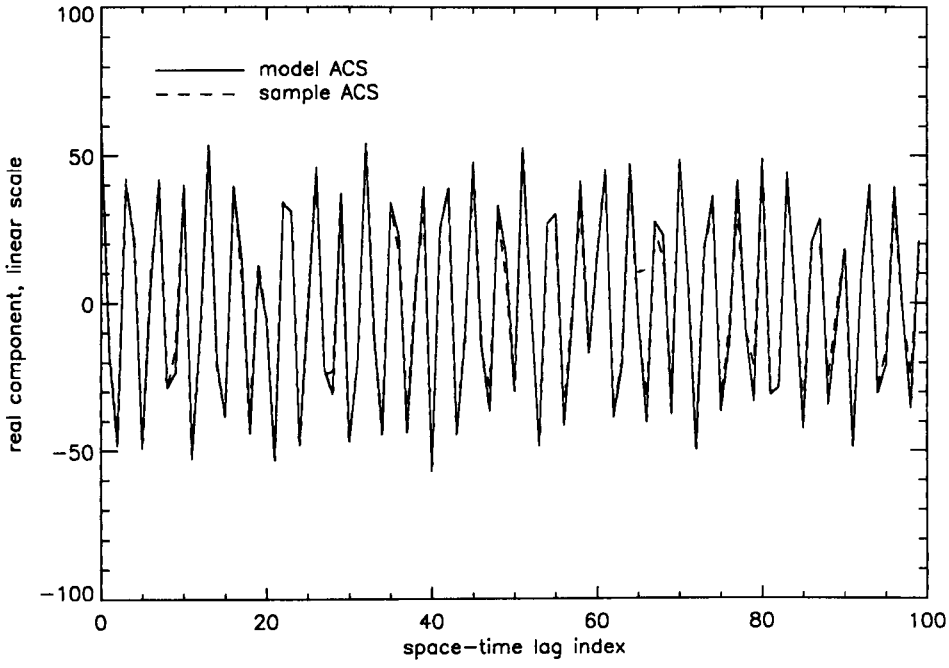

Figure 3.27: Real component of space-time ACS for $1F_2$ mode

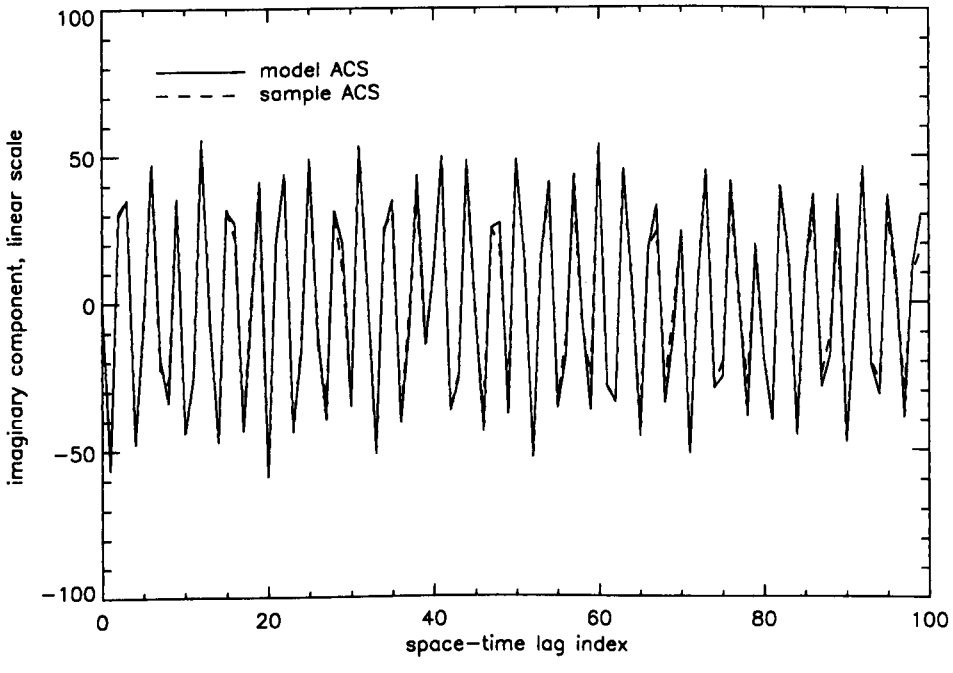

Figure 3.28: Imaginary component of space-time ACS for $1F_2$ mode

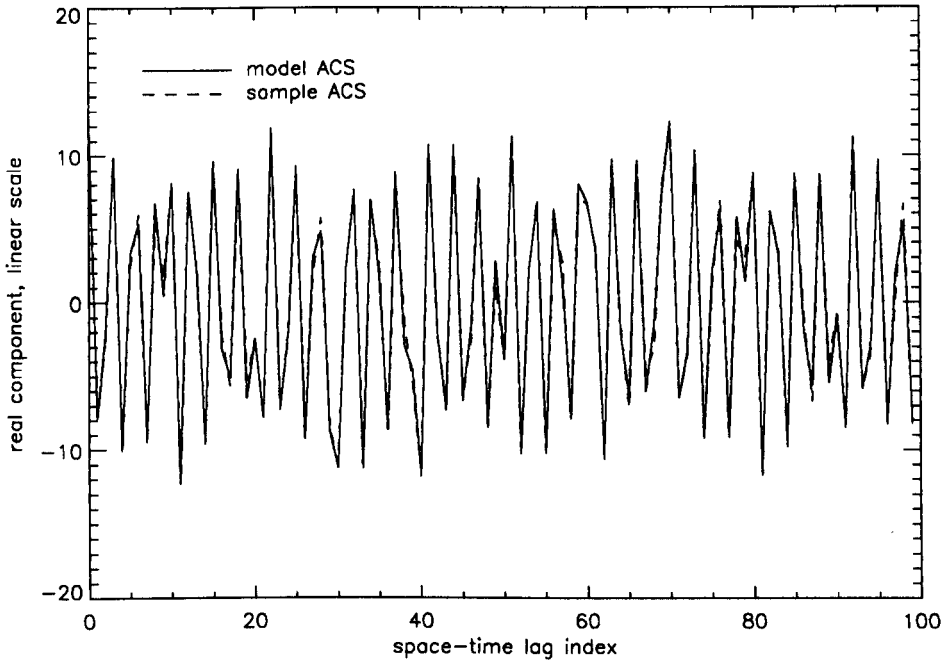

Figure 3.29: Real component of space-time ACS for $1F_2(o)$ mode

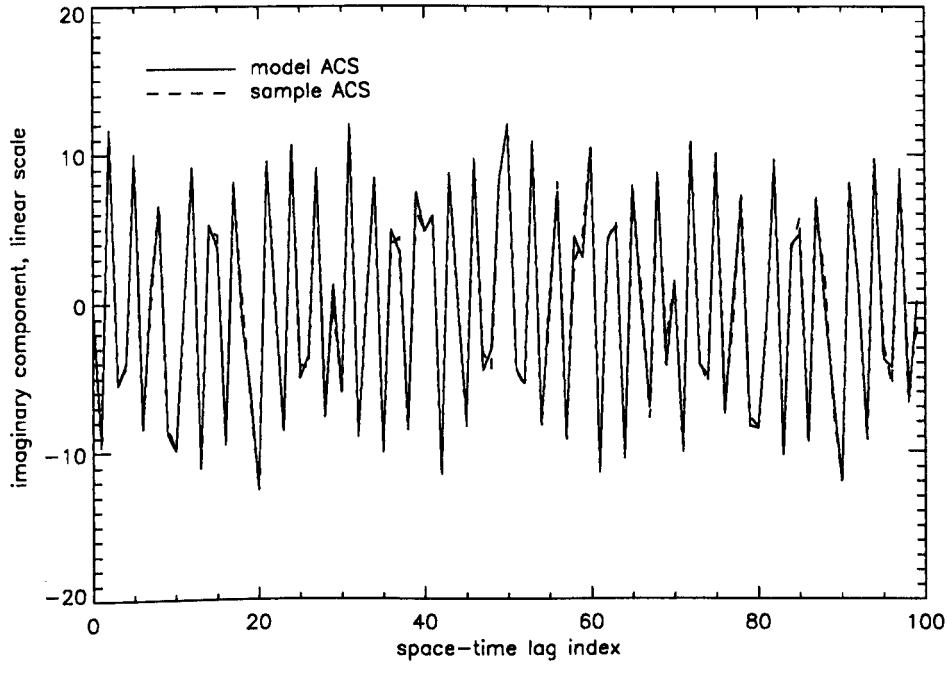

Figure 3.30: Imaginary component of space-time ACS for $1F_2(o)$ mode

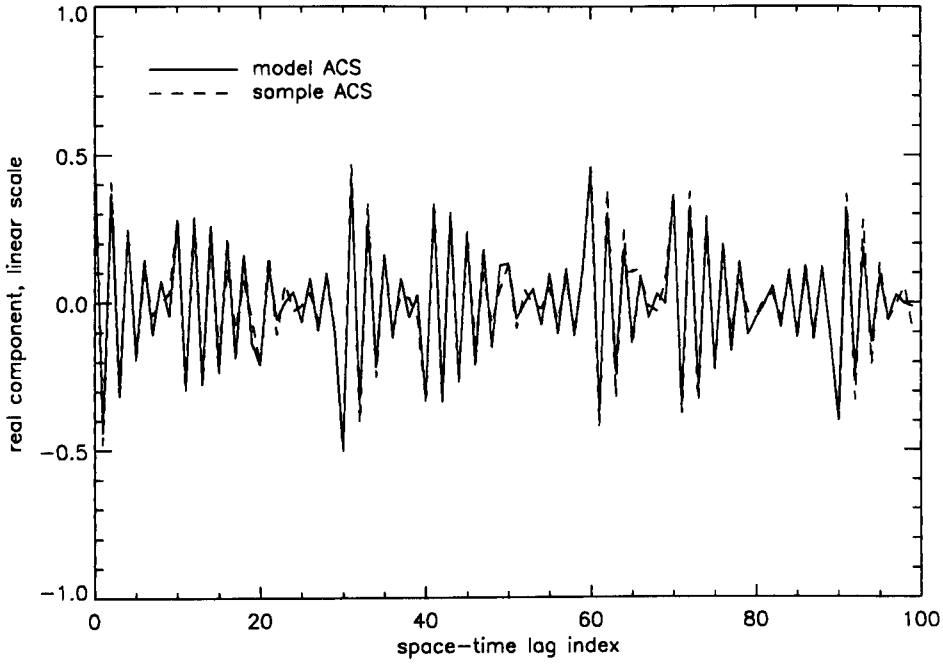

Figure 3.31: Real component of space-time ACS for $1F_2(x)$ mode

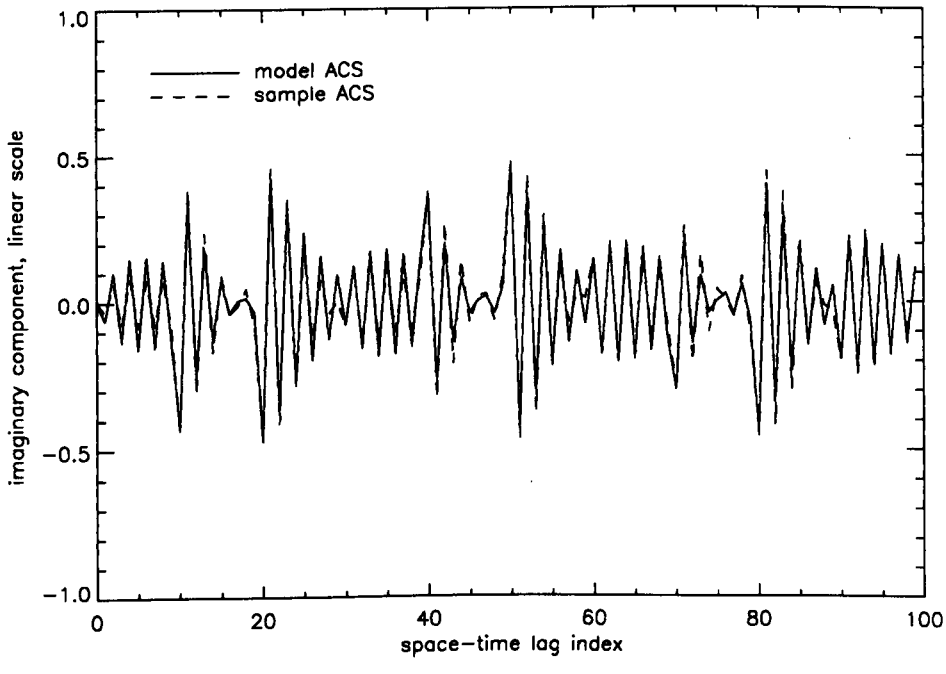

Figure 3.32: Imaginary component of space-time ACS for $1F_2(x)$ mode

choice of operating frequency and signal processing strategy in HF array systems such as OTH radar. A "good" signal model is one which can accurately represent the space-time characteristics of the received signal modes in a concise and intuitive manner which is directly applicable for the prediction of system performance.

Based on the theory which describes the reflection of high frequency radio waves from an interface between an ionospheric plasma and free space, this chapter has developed a physical model for the space-time second order statistics of signal modes reflected from a single localised region of an ionospheric layer. By treating the reflection region as a time-evolving and irregular diffraction grating for the incident HF signals, and by making certain assumptions regarding the statistical properties of the irregularities at this rough reflecting surface, it was possible to derive various analytical expressions for the space-time auto-correlation function of the scattered signal received by an array of antennas on the ground. Two auto-correlation function models were considered for experimental data analysis, the amplitude envelopes of these analytical models were described by Gaussian and exponentially decaying functions of spatial or temporal lag respectively while the phase progression for both models was assumed to be linear.

The model parameters corresponding to particular signal modes were then estimated from experimental temporal-only and spatial-only sample auto-correlation sequences. The distribution of the sample ACS was also derived and computed on a case by case basis to determine the significance of any departures between the estimated analytical model and the experimentally derived sample ACS in both domains. Using formal statistical tests, it was concluded that there is no strong reason to reject the validity of the Gaussian temporal auto-correlation function model for individual modes sampled in all receivers of a very wide aperture array. This suggested that the second order temporal statistics of the measured mid-latitude HF channel were spatially homogeneous over dimensions in the order of 2-3 km. It was also concluded that there is no strong reason to reject a stationary spatial ACS model with an exponentially decaying amplitude envelope and a linear phase corresponding to the mean plane wavefront angle-of-arrival when the received signal is reflected from a single localised region within an ionospheric layer. In addition, the space-time sample ACS corresponding to these propagation modes could be deduced with a high level of accuracy from the estimated temporal-only and spatial-only ACS models by assuming separability of the space-time ACS. The space-time statistical models experimentally validated in this chapter may be used for the purpose of assessing HF channel conditions as well as for simulating data for the design and evaluation of promising array signal processing techniques.

CHAPTER 4

Signal processing model

This chapter describes a signal processing model which represents the space-time characteristics of narrowband HF signals propagated by the ionosphere. The signal processing model may be used to generate space-time samples of the complex-valued wavefields produced by a superposition of multiple signal modes reflected by different ionospheric layers. The fine structure of each signal mode is simulated in accordance with either the wave interference model or as a realisation of a wide-sense stationary statistical model. The validity of the above-mentioned deterministic and statistical HF signal models was experimentally confirmed in chapters 2 and 3 for time intervals which do not exceed a few seconds and a few minutes respectively.

In practice it may required to estimate the model parameters from data which consists of a superposition of different propagation modes which cannot be resolved in range. The space-time MUSIC algorithm can be used to estimate the *wave interference model* parameters from the resultant wavefield. In the *stationary statistical model* each mode is represented by a "distributed" signal which is described by an angular and Doppler power density function. The simplest power density functions are analytically defined by a "mean" parameter which indicates the mean angle-of-arrival (or Doppler shift) of a mode and a "spread" parameter which reflects the level of angular spread (or Doppler spread) induced by the ionosphere. The joint space-time estimation of these density function parameters is not straightforward when the wavefield consists of two or more unresolved modes. A novel method which jointly estimates the mean and spread density function parameters from a convoluted mixture of space-time distributed modes is proposed.

The literature review in section 4.1 summarises previous models used to represent distributed signals in different fields and the parameter estimation techniques proposed for these models. The multi-sensor signal processing model used for the HF environment is described in section 4.2 and the space-time parameter estimation technique associated with this model is presented in section 4.3. The effectiveness of the proposed parameter estimation technique is demonstrated experimentally in section 4.4 using data which is known to consist of a superposition of unresolved space-time distributed signal modes.

4.1 Literature review

The background in section 4.1.1 explains the physical significance of coherently and incoherently distributed signal models and describes the conditions under which such models may be encountered in practice. The literature survey in section 4.1.2 describes previous work in the area of distributed signal models and parameter estimation, the latter is sometimes referred to as distributed source localisation. The specific research on distributed source localisation undertaken in this chapter is summarised and related to previous work in section 4.1.3.

4.1.1 Background

In many practical applications such as radar, sonar and mobile communications a distributed or diffuse source model may be more appropriate than a point source model for describing the spatial properties of the received signals. A distributed source can be thought of as possessing a spatial extent over some continuum of directions, the resultant signal can be expressed as a superposition of infinitely many plane waves with different angles-of-arrival spread over a continuous spatial distribution. This distribution is often modelled by a symmetric spatial density function which is typically defined by a mean angle-of-arrival parameter that corresponds to the centre of the distribution and a angular spread parameter which determines the spatial extent of the source about the mean angle-of-arrival. Once the analytical form of this function is decided upon, the source localisation problem reduces to one of parameter estimation where the angular spread parameter must be estimated in addition to the mean angle-of-arrival for each source.

The space-time properties of a distributed signal received by a sensor array are strongly dependent on the degree of correlation which exists between the complex amplitudes of the wave components incident from different angles-of-arrival. Depending upon the nature of the source and reflection medium, the wave components or rays received over an angular extent may exhibit varying degrees of correlation that ranges from fully correlated (coherent waves) to completely uncorrelated (incoherent waves). The former is termed a coherently distributed (CD) source and arises when there is no variation of the delay, attenuation and reflection coefficient(s) associated with each ray path. In other words, the properties of the reflection medium and source are static with respect to time. The latter is termed an incoherently distributed (ID) source and arises if either the reflective properties of the medium or the characteristics of the source changes in a random manner with time.

The parametric localisation of CD sources is simplified by the fact that each source produces a perfectly coherent (time-invariant) wavefront that contributes a rank one component to the spatial covariance matrix of the received array data. The wavefronts produced by such sources generally have a non-planar structure which do not bare any resemblance

to an array steering vector. Nevertheless, the shape of a CD source wavefront can be deduced from its spatial density function which is assumed to have a known parameterised form. Ideally, there is a one-to-one mapping between the spatial density function parameters and the corresponding CD source wavefront. The collection of distinct wavefronts or "spatial signatures" evaluated over the spatial density function parameter domain is analogous to an array manifold and can be used to uniquely localise CD sources. Providing the number of independent CD sources is less than the number of sensors, it follows that the spatial covariance matrix estimated from the received array data can be partitioned into signal and noise subspaces. By generating the collection of array response vectors in accordance with the adopted CD model, it is possible to use methods based on MUSIC to jointly estimate the mean angle-of-arrival and spread parameter for each CD source.

The parametric localisation of ID sources is relatively more difficult because random changes in the relative amplitude and phase of the different wave components produces wavefronts with a random spatial structure. An ID signal can alternatively be viewed as resulting from an infinite number of statistically independent sources incident on the array from a continuum of directions defined by the spatial density function. Unlike a CD source, one ID source occupies the full rank of the spatial covariance matrix which implies that the noise subspace becomes degenerate or equal to the zero vector. When the point source assumption is violated in this manner the application of MUSIC, and other direction-of-arrival estimators based on a subspace of an array covariance matrix, can lead to severe degradations in estimation performance. Moreover, existing subspace methods for direction-of-arrival estimation cannot be used to infer the angular spreads of superimposed ID sources.

In most practical applications the random motion of the propagation medium (e.g., reflection of radio signals by a changing ionosphere) or the relative motion between the source(s) and receiver array (e.g., airborne phased array radar) is prevalent so an ID source model is often more appropriate than a CD source model. Although the estimation of angular spread for ID sources is of paramount importance in many practical systems, little attention has been paid to the estimation of ID source parameters in the framework of subspace methods. Perhaps the major factor which has limited research in this area has been a pre-disposition to use the data covariance matrix as the starting point when its structure is not suited to the partitioning of (full rank) ID sources into signal and noise subspaces.

For the purpose of ID source localisation, this research steers away from the data covariance matrix and investigates the use of alternative matrix structures which contain all the estimated second order statistics of the array data. This chapter proposes alternative matrix structures for which the mean and spread parameters of an ID source collapse into a single subspace dimension. For a moderate number of ID sources the noise subspace of such matrices is of finite rank, unlike that of the covariance matrix which is degenerate. The existence of a noise subspace allows MUSIC-like parameter estimation

methods to be developed and applied to estimate *both the mean and spread parameters* of multiple ID sources. The proposed method may be extended to estimate the parameters of *space-time* ID sources, the effectiveness of this method is demonstrated by application to experimental space-time data records of ionospherically-propagated HF signals.

4.1.2 Distributed signal models and parameter estimation

Over the last two decades array signal processing research has strongly focused on the problem of estimating the direction-of-arrival of plane wave sources incident on an array of sensors in the presence of additive noise (Krim and Viberg 1996). Maximum likelihood (ML) estimators are generally considered optimal but the associated criterion function is non-linear and must be minimised over a multi-dimensional parameter space (Ottersten, Viberg, Stoica and Nehorai 1993). Although the ML estimator is expected to provide very accurate direction-of-arrival estimates when the presumed model is obeyed by the data, it requires the use of iterative search procedures which are computationally intensive. These iterative searches may not always converge, and even if they do, the parameter estimates are not guaranteed to reach their global optimum according to the ML criterion function.

The MUSIC algorithm proposed by (Schmidt 1979) is a spectral technique which is more attractive than the ML method from a computational point of view but solves for the signal parameters separately rather than jointly. When the sources are uncorrelated and the number of independent snapshots is large the performance of the MUSIC algorithm is comparable to that of the ML estimator (Stoica and Nehorai 1989). However, in the presence of correlated (or coherent) sources the computational advantage of the MUSIC algorithm is traded off against degradations in estimation performance with respect to the ML method. Thus, one of the main aims of research in this area has been to retain as closely as possible the estimation accuracy of the ML method using a procedure which is not as computationally intensive.

In the case of uniform linear arrays, a computationally attractive method for achieving similar performance to the ML estimator is known. The Iterative Quadratic Maximum Likelihood (IQML) method originated by (Besler and Macovski 1986) is based on a re-parameterisation of the orthogonal projection matrix in the ML criterion function which allows the minimisation to be performed as a series of quadratic optimisation problems. An improvement over IQML which exploits the weighted subspace fitting (WSF) algorithm of (Viberg and Ottersten 1991) was introduced by (Stoica and Sharman 1990) and is known as the Method of Direction Estimation (MODE). The idea is to replace the sample covariance matrix in the ML criterion function with an optimally weighted signal subspace and to apply IQML for minimisation. The important advantage of using the rank-truncated form of the sample covariance matrix is that the MODE (or root-WSF) algorithm is no longer an iterative procedure as it can be shown that after the second IQML pass the estimates have the asymptotic accuracy of the true optimum (Krim and

Viberg 1996). Simulations in (Stoica and Sharman 1990) suggest that MODE performs better than MUSIC and closely to the ML estimator, but unlike the latter, MODE is essentially in closed-form and is thus a strong candidate for the "best" method for ULA's.

All of the above-mentioned methods are based on the data covariance matrix and rely on the point source assumption which does not hold in many practical applications. As a result, none of these methods are directly applicable for the localisation of distributed sources in their strictly presented form. In the special case of CD sources, the MUSIC estimator was modified by (Valaee, Champagne and Kabal 1995) to estimate the mean angle-of-arrival and spread parameter of such sources. The main motivation for using MUSIC as a CD source localiser is that number of search dimensions equals the number of parameters used to describe the spatial density function of each source irrespective of the number of sources. For the corresponding ML localiser, the number of search dimensions is equal to this number of parameters multiplied by the number of sources so an exhaustive search can quickly become prohibitive. A polynomial rooting approach for the localisation of CD sources which avoids the calculation of a spectrum was proposed by (Goldberg and Messer 1998). This method uses a truncated Fourier series to *approximate* the collection of spatial signature vectors on the CD source "manifold" and relates the estimated parameters of this series to those of the assumed source spatial density function.

A Gaussian shaped spatial density function was assumed by (Trump and Ottersten 1996) to describe the angular spread of ID sources which arise in the field of mobile communication. The ML estimator for the mean and variance of the Gaussian envelopes was developed but it was found that the Newton-type search algorithm associated with this estimator required accurate initialisation and imposed a high computational load. An alternative estimator which performs an exhaustive search for the parameters of the model covariance matrix which yields the best least squares fit to the sample covariance matrix was also proposed but the search dimension for this algorithm grows as twice the number of sources. Another least squares spatial covariance matrix fitting approach was studied by (Gersham, Mecklenbrauker and Bohme 1997) where the "coherency loss" or angular spread in the spatial density function was assumed to be of identical form for all sources regardless of their mean angle-of-arrival. In the HF environment, and perhaps in other practical applications, this is an unrealistic assumption since the characteristics of the ionosphere are known to depend on the particular layer affording propagation as well as the geographical region of reflection. Another drawback of this approach is that computationally expensive genetic algorithms were needed to solve the highly non-linear parameter estimation problem.

More economical MUSIC-like estimators for ID source localisation were investigated by (Meng, Stoica and Wong 1996) and (Valaee et al. 1995). Both methods are based on the use of the array covariance matrix which does not strictly contain a noise-only subspace in the case of ID sources. Consequently, both methods require certain approximations and assumptions to hold in order to yield satisfactory parameter estimation performance.

The critical assumption is that the angular spread of all sources is small and that most of the signal power is concentrated into a small number of eigenvalues of the spatial covariance matrix. This is referred to as the effective dimension of the signal subspace and from it can be derived a "quasi-noise only" subspace. The main idea is to form a set of model spatial covariance matrices over a grid of mean and spread ID source model parameters, the quasi-noise subspace of the model matrices is then projected against the quasi-signal subspace of a sample covariance matrix and the result inverted so that the ID source parameters can be localised at points on the grid which correspond to the most prominent local peaks.

A class of statistical signal models which have received much attention in the field of time series analysis are so-called rational or pole-zero system models, these models have traditionally been used to parametrically describe the power spectral density of random temporal processes. The most general model of this class is known as the auto-regressive moving-average ARMA(p, q) model which contains p poles and q zeros, as described by (Marple 1987). Naturally, such a model can be also be used to represent the angular power spectrum of distributed sources received by antenna arrays. In fact, a first order auto-regressive (AR) model was proposed by (Abramovich et al. 1996) to represent spatial density function of ionospherically-propagated HF signals. When two or more independent sources with first order AR spatial density functions are present the resultant signal is statistically described by a more general ARMA model. More specifically, it can be shown that the superposition of M independent AR(1) sources produces a signal which is statistically described by an ARMA$(M, M-1)$ model where the M poles are given by the M complex AR(1) coefficients which parameterise the ID source spatial densities. It is apparent that in this case ID source localisation can be couched as an ARMA model identification problem.

Maximum likelihood parameter estimation techniques for ARMA model identification exist (Kay 1987), but even for one dimensional data these iterative procedures impose significant computational burdens and their convergence is not guaranteed. A computationally attractive ML estimator for the family of ARMA$(M, M-1)$ models is known (Kumaresan, Scharf and Shaw 1986), but this procedure is designed to operate on the deterministic *impulse response* of the process rather than a statistical realisation. The impulse response of the mechanisms which govern the time-evolution of the transmission medium (e.g., the ionospheric channel) is not available in practice, only statistical realisations of the process which cause angular spread can be measured by sensor arrays. Under these circumstances, it is most common to estimate the model parameters from the data sample auto-correlation sequence (ACS) (i.e., the estimated second order statistics).

Although a sample ACS vector of *finite length* is not a sufficient statistic for ARMA parameter estimation (Arato 1961), the popularity of sub-optimum approaches based on this form of data reduction stems from the relatively simple linear or quadratic equations which need to be solved to estimate the model parameters. It was found by (Bruzzone

and Kaveh 1984) that the statistical information preserved in the sample ACS, relative to that in the raw data, depends on the lags included and the characteristics of the ARMA process. The authors concluded that the sample ACS is best suited to the estimation of narrowband ARMA processes and that to obtain near optimum (maximum likelihood) performance they recommended the use of many lags as the increased statistical variability associated with extending the set of estimation equations is outweighed by the information gain accompanying the inclusion of later lags.

The extended Yule-Walker equations are the backbone of many ARMA parameter estimation techniques and make use of the recursive relation which the sample ACS is known to satisfy asymptotically under the assumed model. This recursive relation is completely defined by the AR parameters only so the over-determined Yule-Walker technique, examined by (Cadzow 1982) and (Porat and Friedlander 1985), uses the unbiased ACS estimates to estimate the AR parameters first. Once the AR parameters are estimated, the MA parameters can be estimated from a residual time series obtained by filtering the original data sequence with a filter whose transfer function is the inverse of the estimated AR transfer function, see (Marple 1987). This non-iterative least squares procedure adopted for ARMA model identification estimates the AR and MA parameters *separately* rather than *jointly* and is therefore sub-optimal even with respect to the sample ACS on which it is based.

To best utilise the statistical information preserved in the sample ACS it is necessary to simultaneously estimate the ARMA model parameters which provide the best (least-squares) fit to the unbiased sample lags. As found by (Beex and Scharf 1981), this approach leads to non-linear equations so the authors suggested a modified squared error criterion which was mathematically more tractable and allowed the parameter estimates to be derived analytically using a technique similar to Prony's method (de Prony 1795). However, a computationally attractive procedure which jointly solves for the ARMA model parameters that yield the exact least squares fit to the unbiased sample ACS is yet to be presented for either one or two dimensional data. This gap in current research is addressed for the special case of ARMA$(M, M-1)$ models in this chapter.

4.1.3 Significance of research relative to previous work

The distributed source model proposed by (Abramovich et al. 1996) is the preferred signal model for describing the second order statistics of ionospherically-propagated HF signals for a number of reasons. The parameters of this model can be chosen to select between CD and ID sources although in the HF environment ID source models are more relevant. For ID sources the adopted pole-zero modelling style is able to approximate a wide variety of power density functions, albeit at the expense of increasing the number of parameters. Other major advantages of such a model include the ease with which it can be used to generate realisations of the statistical processes on a digital computer and

the mathematical tractability associated with linear time-invariant systems. A potential disadvantage is that such a model does not take into account any information which may be contained in the higher order statistics of the data

The simplest ID source model involves one mean and spread parameter per source per dimension, in the spatial dimension this model represents the signal complex envelope across receivers as a first order auto-regressive process which corresponds to a Lorentzian shaped spatial density function. If M statistically independent signals with Lorentzian spatial distributions are present, the superposition of such signals received by a sensor array can be statistically described by a spatial ARMA$(M, M-1)$ model. In the HF environment these signals may correspond to M statistically independent propagation modes which originate from a single source. In addition, the generalised model is two-dimensional and can represent angular spread as well as Doppler spread imposed on individual propagation modes by the different ionospheric layers. Although such a model is quite versatile and may be appropriate in other fields of application no parameter estimation method was supplied in (Abramovich et al. 1996).

In this chapter an explicit connection is made between the problem of jointly estimating the ARMA$(M, M-1)$ parameters which yield the best least squares fit to an unbiased sample ACS and the problem of estimating the parameters of superimposed exponentially damped complex sinusoidal signals in additive noise. Although the problems are shown to be mathematically equivalent an important distinction exists between the two. In the latter, parameter estimation is performed on the raw data which is contaminated by additive noise, whereas in the former, the estimation is performed on the sample covariances of the data which do not equal the expected covariances as a result of statistical noise (i.e., finite sample effects). As an aside, both forms of "noise" can be treated as zero-mean and Gaussian distributed, this holds asymptotically for the sample lags by the central limit theorem and is an assumption often made for the raw data.

An exact least squares estimation procedure exists for superimposed exponential signals in noise, see (Besler and Macovski 1986), but this method has not previously been exploited for the purpose of jointly estimating the parameters of an ARMA$(M, M-1)$ model from one or more statistical realisations of the process. The cross-application of this mathematical technique leads to a computationally attractive method for optimally estimating the parameters of the family of ARMA$(M, M-1)$ processes from the unbiased sample ACS. In addition, the similarity between the two problems is traced further to arrive at a matrix structure which allows distributed sources arising from this model to be confined to a single subspace dimension. Providing the number of distributed sources is less than the number of lags, a noise subspace can be shown to exist for such a matrix and this in turn strictly permits the application of a generalised MUSIC spectral estimator which is introduced in this chapter as matched-field (MF)-MUSIC. The term matched-filed is used here because the manifold is parameterised by the the signal angle-of-arrival and Doppler shift as well as the statistical properties of the propagation channel(s).

The computationally attractive method used to solve the one dimensional ARMA($M, M-1$) parameter estimation problem is similar to MODE, the main distinction being that the the poles of the distributed signals are not constrained to lie on the unit circle as they are for discrete (plane wave) signals. For the case of two-dimensional (space-time) data, there is no direct generalisation of the MODE closed-form algorithm due to the lack of a fundamental theorem of algebra for polynomials in more than one variable. However, the MF-MUSIC algorithm can be extended to two dimensions to solve the space-time parameter estimation problem. Like the traditional MUSIC algorithm, this extension entails an increase of the search space dimension by a factor of two which for MF-MUSIC involves two mean and spread parameters per source. This four-dimensional manifold is not desirable from a computational standpoint and justifies the search for faster two-dimensional (2-D) parameter estimation algorithms based on prediction polynomials and the IQML idea.

The two-dimensional modal analysis problem was studied by (Clark and Scharf 1994); starting from the ML definition they solved the problem by using two polynomials referred to as the prediction polynomial and the interpolating polynomial. The modes in the first dimension were determined by finding the roots of the estimated prediction polynomial while the corresponding modes in the second dimension were determined by evaluating the estimated interpolating polynomial at each root estimated in the first dimension. This technique was motivated because when the 2-D problem is separated into two 1-D problems the roots have no particular ordering and the authors did "not know how to pair the modes between dimensions". Although their procedure avoids the pairing step, the existence of the interpolating polynomial requires that all of the modes in one of the dimensions are distinct and that this dimension is known apriori. If the modes become too closely spaced the magnitude of the derivate of the interpolating function may increase without bound and this can lead to numerical instability.

Other methods which decompose the inherently 2-D problem into 1-D problems have been developed, see (Sacchini, Steedly and Moses 1993) and (Hua 1992), but none of these estimators are minimisers of the 2-D least squares criterion function. This chapter proposes a novel method which splits the 2-D least squares problem into two 1-D least squares problems which can be solved using the computationally efficient IQML technique. In addition, a statistically consistent method for pairing the modes estimated in each dimension is described. The proposed method can be used to jointly estimate the 2-D ARMA($M, M-1$) model parameters in optimal (least squares) fashion from the sample space-time ACS or for the purpose of two-dimensional modal analysis based on maximum likelihood.

4.2 Space-time signal processing model

The purpose of this section is to describe the signal processing model for space-time distributed HF signals reflected by the ionosphere. Once this model has been described in mathematical detail in section 4.2.1 the second order statistics in the form of a space-time auto-correlation sequence (ACS) are derived in section 4.2.2 for commonly encountered cooperative and uncooperative HF signal sources.

4.2.1 Space-time distributed HF signal model

The narrowband HF channel model originally developed by (Watterson et al. 1970) for single receiver systems was extended in the work of (Abramovich et al. 1996) to model ionospherically-propagated HF signals received by antenna arrays. This multi-sensor model represents the composite N-dimensional antenna array snapshot vector $\mathbf{x}_k(t)$ recorded at the k^{th} range cell in the t^{th} PRI and as a superposition of M signal modes which propagate from source to receiver along different ionospheric paths and additive background noise. The contribution made by the m^{th} signal mode to the composite array snapshot is denoted by $\mathbf{s}_{k,m}(t)$ for $m = 1, 2, .., M$ while the additive noise component is represented by the term $\mathbf{n}_k(t)$. The range and PRI indices extend from $k = 0, 1, .., K-1$ and $t = 0, 2, .., P-1$ respectively for the data collected during one coherent processing interval (CPI).

$$\mathbf{x}_k(t) = \sum_{m=1}^{M} \mathbf{s}_{k,m}(t) + \mathbf{n}_k(t) = \sum_{m=1}^{M} A_m \mathbf{S}(\theta_m)\mathbf{c}_m(t)g_k(t,\tau_m)e^{j2\pi\Delta f_m t} + \mathbf{n}_k(t) \qquad (4.1)$$

The complex-valued scalar function $g_k(t, \tau_m)$ is the received source waveform which results after the transmitted signal is delayed by the m^{th} mode transit time τ_m, deramped, filtered, digitised and range processed at a reference receiver designated as the first receiver ($n = 0$) in this case. This waveform is normalised to have unit variance as the root mean square (RMS) amplitude of the m^{th} mode is denoted by A_m and hence the power of the m^{th} mode is A_m^2. Note that A_m includes the attenuation incurred due to path distance loss (i.e., the inverse square law), ionospheric absorption as well as polarisation mismatch between the incident wave and receiving antenna.

As the time delay τ_m associated with each propagation mode varies with time due to ionospheric movements, the value of τ_m is defined as the time delay associated with the path taken by the m^{th} signal mode between transmitter and reference receiver at the beginning of the CPI ($t = 0$). The *linear* component of time-delay variation of a mode during the CPI is taken into account by the constant Doppler shift term $e^{j2\pi\Delta f_m t}$ while random time-delay variations about this component are modelled by a Doppler spread term $\mathbf{c}_m(t)$ to be described later.

The characteristics of the received source waveform $g_k(t, \tau_m)$ depend on the interaction

between the transmitted waveform and the method of reception which involves FMCW deramping, filtering, digitisation and range processing. The space-time distortions imposed by the ionosphere on a signal mode are taken into account by various other terms in Eqn.(4.1), hence the form of $g_k(t,\tau_m)$ is independent of any propagation effects. In essence, $g_k(t,\tau_m)$ is the normalised (unit power) waveform which is received if each ionospheric layer were considered as a perfect and time-invariant mirror to the incident HF signal.

When the transmitted waveform is a synchronised replica of the deramping FMCW waveform the relationship between the transmitted waveform and the reception process is identical (excluding propagation effects) from one PRI to another. In this case, $g_k(t,\tau_m)$ is a deterministic function of range $k = 0, 1, .., K-1$ which is independent of slow-time (t) and given by,

$$g_k(t,\tau_m) = W(f_p[k - \tau_m f_b]) \tag{4.2}$$

where $W(f)$ is the normalised Fourier Transform of the range processing window function, f_b is the FMCW signal bandwidth and f_p is the linear FM pulse repetition frequency. Note that a time-delay τ_m on a synchronised FMCW waveform produces a frequency of $f_p\tau_m f_b$ after deramping and that range index k corresponds to an actual frequency of $f_p k$ Hertz.

When the transmitted waveform originates from an uncooperative source there is no fixed or predictable relationship between the emitted interference and the deramping waveform so $g_k(t,\tau_m)$ is modelled as a statistical process with respect to both range cell k and slow-time t. If the transmitted waveform is *broadband* interference of bandwidth greater than the deramping signal bandwidth f_b, the received waveform $g_k(t,\tau_m)$ can be modelled as white noise with the following correlation properties.

$$E\{g_k(t,\tau_m)g^*_{k'}(t',\tau_{m'})\} = \mathrm{sinc}(f_b[\tau_m - \tau_{m'}])\delta(k-k')\delta(t-t') \tag{4.3}$$

The sinc function $(\frac{\sin x}{\pi x})$ used to describe the inter-mode correlation coefficient implicitly assumes that the power spectral density of the interference is flat over the receiver bandwidth. The correlation between neighbouring ranges k introduced as a result of the range processing window function has also been ignored.

The terms Δf_m and θ_m in Eqn.(4.1) denote the mean Doppler shift and cone angle-of-arrival of the m^{th} mode respectively. Note that the mean Doppler shift manifests itself as a regular phase progression $e^{j2\pi\Delta f_m t}$ across PRI, in accordance with the results of chapter 3 this progression is assumed to be the same in all receivers for a particular mode. The spatial properties of the m^{th} signal mode are partly modelled by the $N \times N$ diagonal matrix $\mathbf{S}(\theta_m)$ which represents the mean wavefront. For far-field sources and a narrowband uniform linear array the mean wavefront is modelled as the plane wavefront so this matrix contains the steering vector elements corresponding to the mean cone

angle-of-arrival θ_m along its main diagonal.

$$\mathbf{S}(\theta_m) = diag[e^{j2\pi\frac{n\Delta d}{\lambda}\sin\theta_m}]_{n=0}^{N-1} \tag{4.4}$$

In Eqn.(4.4), Δd is the distance between adjacent antenna sensors (i.e., the separation between sub-array centres) and $\lambda = c/f_c$ is the carrier wavelength. If the mean wavefront cannot be defined as the plane wavefront, as in the case of a non-linear array or when array manifold errors are present, it is possible to define a more general mean wavefront as $\mathbf{S}_m = \Gamma_m \mathbf{S}(\theta_m)$ where Γ_m is an $N \times N$ diagonal matrix which modifies the ULA steering vector for the m^{th} mode accordingly.

The statistical characteristics of the ionospheric channel are modelled by the complex N-dimensional vector $\mathbf{c}_m(t)$ for each mode $m = 1, 2, .., M$. Variation of the individual elements in $\mathbf{c}_m(t)$ with respect to slow-time (t) represents the temporal gain and phase modulation sequence induced on the m^{th} mode by the ionosphere to produce Doppler spread in the different receivers. Changes in the gain and phase relationship between the elements of $\mathbf{c}_m(t)$ with respect to slow-time (t) represents the time evolution of the spatial modulations imparted by the ionosphere to produce angular spread on the m^{th} mode.

The two-dimensional (space-time) model proposed by (Abramovich et al. 1996) adopts a multi-variate scalar type auto-regressive (AR) process to generate the random vector $\mathbf{c}_m(t)$.

$$\mathbf{c}_m(t) = \sum_{i=1}^{I} \alpha_{m,i}(\Delta t)\mathbf{c}_m(t - i\Delta t) + \mu_m \xi_m(t) \tag{4.5}$$

The scalar AR coefficients $\alpha_{m,i}(\Delta t)$ for $i = 1, 2, .., I$ and the normalising constant μ_m define the Doppler spectrum characteristics of the m^{th} mode for a sampling interval of $\Delta t/f_p$ seconds. The slow-time (t) dependent random vector $\mathbf{c}_m(t)$ is assumed to be invariant over the PRI which is justifiable in cases when the pulse repetition frequency f_p is much greater than the Doppler bandwidth $B_t(m)$ induced by the ionosphere on all the $m = 1, 2, .., M$ signal modes. For typical mid-latitude ionospheric propagation channels, the coefficients $\alpha_{m,1}(\Delta t) \to 1$ and $\alpha_{m,i} \to 0 \ \ \forall i = 2, 3, ..I$ when $\Delta t/f_p < 0.1$ seconds (Abramovich et al. 1996). If the bandwidth parameter $B_t(m)$ is defined as the inverse of the time interval which it takes for the temporal ACS of the m^{th} mode to drop by a factor of $1/e$ then for a first order (I=1) AR model representation it follows that $\alpha_{m,1}(\Delta t) = e^{-B_t(m)\Delta t/f_p}$.

Similarly, spatial fluctuations of the channel causing angular spread may be described by the simplest (first order) AR process;

$$\xi_m^{[n]}(t) = \beta_m(\Delta d)\xi_m^{[n-1]}(t) + \nu_m \gamma_{m,n}(t) \tag{4.6}$$

where $\xi_m^{[n]}(t)$ denotes the n^{th} element of the vector $\xi_m(t)$ and $\nu_m = \sqrt{1 - |\beta_m(\Delta d)|^2}$ is the scaling term associated with a *first order* AR process of unit power. The unit power

assumption is in accordance with the previous definition of A_m which for an AR(1) temporal process also requires that $\mu_m = \sqrt{1 - |\alpha_m(\Delta t)|^2}$ where $\alpha_{m,1}(\Delta t)$ has been replaced by $\alpha_m(\Delta t)$ for notational convenience.

The spatial correlation coefficient defined as $\beta_m(\Delta d)$ depends on the inter-sensor spacing Δd, the angular bandwidth induced by the ionosphere on the m^{th} mode $B_s(m)$ as well as the mean cone angle-of-arrival θ_m, although only the Δd dependence is explicitly shown. More specifically, $\beta_m(\Delta d) = e^{-B_s(m)|1-\sin\theta_m|\Delta d}$ where $B_s(m)$ is defined in analogous manner to $B_t(m)$ for a boresight arrival ($\theta_m = 0$). Note that as the mean cone angle-of-arrival tends to endfire ($\theta_m \rightarrow 0$) the perceived angular spread is reduced by a factor of $|1 - \sin\theta_m| \rightarrow 0$ as at endfire only temporal fluctuations of the wavefront can be observed (Abramovich et al. 1996).

The driving noise process $\gamma_{m,n}(t)$ is a zero-mean complex Gaussian process having independent identically distributed (i.i.d.) real and imaginary parts and the following correlation properties.

$$E\left\{\gamma_{m_1,n_1}(t_1)\gamma^*_{m_2,n_2}(t_2)\right\} = \delta(m_1 - m_2)\delta(n_1 - n_2)\delta(t_1 - t_2) \tag{4.7}$$

This description of the driving white noise process is in accordance with the assumptions of Rayleigh fading and mutually independent modes, as experimentally verified by (Watterson et al. 1970). The additive noise term $\mathbf{n}_k(t)$ is due to a combination of internal receiver noise and background noise in the HF environment, this term is in no way related to the driving white noise $\gamma_{m,n}(t)$ used to generate the complex space-time HF channel distortions embodied in the vector $\mathbf{c}_m(t)$. The additive noise is assumed to be uncorrelated with the received mode waveforms $g_k(t, \tau_m)$ and complex Gaussian distributed with the following second order statistics.

$$E\{\mathbf{n}_k^{[n]}(t)\mathbf{n}_{k'}^{[n']*}(t')\} = \sigma_n^2\delta(k - k')\delta(t - t')\delta(n - n') \tag{4.8}$$

A difference between the simplest (first order AR) version of this model and the Watterson model is that in the time domain the amplitude envelope of the auto-correlation function is a decaying exponential rather than Gaussian shaped. Nevertheless, the order of temporal AR process used to describe the Doppler power spectrum of different propagation modes can be extended so as approximate a Gaussian function of frequency, or alternative spectral density functions, to the desired level of accuracy. The spatial homogeneity, stationarity and space-time separability of the above-mentioned model (to be derived later) are in agreement with the previous experimental measurements made in chapter 3. This includes the amplitude envelope of the spatial auto-correlation function which was shown to be consistent with exponentially decaying function of distance.

4.2.2 Space-time second order statistics

The *scalar-type* multi-dimensional AR process used to model the random HF channel distortions implies that in each receiver the time series of distortions is generated with the *same time-invariant* AR coefficients. The time-invariance of these coefficients means that the resulting process is temporally stationary while the same AR coefficients in each receiver implies that the second order statistics are spatially homogeneous or independent of receiver location. Similarly, the spatial AR coefficients used to model the angular spread of each propagation mode are time-invariant which gives rise to a time-sequence of spatially stationary array snapshots. The space-time separability and hence space-time stationarity of this model will be derived later.

The space-time auto-correlation sequence (ACS) of the statistically stationary composite snapshots $\mathbf{x}_k(t)$ generated by the multi-sensor HF channel model in Eqn.(4.1) is given by,

$$r_k(i\Delta t, j\Delta d) = E\{\mathbf{x}_k^{[n]}(t)\mathbf{x}_k^{[n-j]*}(t-i)\} \quad \begin{cases} i = 0,..,L_t-1 \\ j = 0,..,L_s-1 \end{cases} \tag{4.9}$$

where $r_k(i\Delta t, j\Delta d)$ is the expected correlation between samples of the received signal taken $i\Delta t/f_p$ seconds apart in the k^{th} frequency bin (range cell) at receivers spaced by $j\Delta d$ metres. From Eqn.(4.1) the space-time ACS $r_k(i\Delta t, j\Delta d)$ can equivalently be written as,

$$r_k(i\Delta t, j\Delta d) = \sum_{m=1}^{M} E\{\mathbf{s}_{k,m}^{[n]}(t)\mathbf{s}_{k,m}^{[n-j]*}(t-i)\} + \sigma_n^2\delta(i)\delta(j) \tag{4.10}$$

since the different signal modes $\mathbf{s}_{k,m}^{[n]}(t)$ are statistically independent and the uncorrelated additive noise $\mathbf{n}_k^{[n]}(t)$ is both spatially and temporally white. For each signal mode, the space-time ACS $r_{k,m}(i\Delta t, j\Delta d) = E\{\mathbf{s}_{k,m}^{[n]}(t)\mathbf{s}_{k,m}^{[n-j]*}(t-i)\}$ can be expanded further using Eqn.(4.1),

$$r_{k,m}(i\Delta t, j\Delta d) = A_m^2 z_m^i w_m^j \; E\{g_k(t,\tau_m)g_k^*(t-i,\tau_m)\} \; E\{\mathbf{c}_m^{[n]}(t)\mathbf{c}_m^{[n-j]*}(t-i)\} \tag{4.11}$$

where $z_m = e^{j2\pi\Delta f_m}$ and $w_m = e^{j2\pi\frac{\Delta d}{\lambda}\sin\theta_m}$. The separability of the expectation in Eqn.(4.11) follows from the statistical independence of the random HF channel modulation sequence $\mathbf{c}_m^{[n]}(t)$ and the transmitted waveform $g_k(t,\tau_m)$.

The term $E\{g_k(t,\tau_m)g_k^*(t+i,\tau_m)\}$ depends on the type of waveform emitted by the source. When the transmitted waveform is a synchronised FMCW it follows from Eqn.(4.2) that $E\{g_k(t,\tau_m)g_k^*(t-i,\tau_m)\} = |W(f_p[k-\tau_m f_b])|^2$. If the emitted waveform is broadband interference then $E\{g_k(t,\tau_m)g_k^*(t-i,\tau_m)\} = \delta(i)$ can be derived from Eqn.(4.3).

In the FMCW case this term is a constant with respect to temporal lag (i) so the space-time ACS of the received mode $r_{k,m}(i\Delta t, j\Delta d)$ is directly related to the space-

time ACS of the fluctuations imposed by the ionospheric layer which propagates it (i.e., $E\{\mathbf{c}_m^{[n]}(t)\mathbf{c}_m^{[n-j]*}(t-i)\}$). Due to the relatively discrete nature of $|W(f_p[k-\tau_m f_b])|^2$ in the range domain k, the space-time ACS corresponding to different propagation modes can often be isolated into different range cells and analysed separately.

A non-cooperative broadband interference source only allows the spatial characteristics of the HF channel to be observed since the space-time ACS has an expected value of zero for all temporal lags greater than zero. Although non-cooperative broadband interference waveforms do not allow individual modes to be separated in range and studied individually, they are often present in large numbers and allow certain statistical properties of many different ionospheric circuits to be investigated.

When first order AR processes are used to generate the samples of $\mathbf{c}_m^{[n]}(t)$ according to Eqn.(4.5) and Eqn.(4.6), it is shown in appendix B that the space-time ACS of the random fluctuations is separable and given by the following product,

$$E\{\mathbf{c}_m^{[n]}(t)\mathbf{c}_m^{[n-j]*}(t-i)\} = \alpha_m^i(\Delta t)\beta_m^j(\Delta d) \tag{4.12}$$

where $\alpha_m(\Delta t) = e^{-B_t(m)\Delta t/f_p}$ and $\beta_m(\Delta d) = e^{-B_s(m)|1-\sin\theta_m|\Delta d}$ are the coefficients of the temporal and spatial AR(1) processes respectively. In summary, the space-time ACS of the received data which may consist of multiple modes can be represented by the following analytical model,

$$r_k(i\Delta t, j\Delta d) = \sum_{m=1}^{M} E\{g_k(t,\tau_m)g_k^*(t-i,\tau_m)\}h_m z_m^i w_m^j \tag{4.13}$$

where $h_m = A_m^2$ is the power of the m^{th} mode, $z_m = \alpha(\Delta t)e^{j2\pi\Delta f_m}$ is the temporal pole incorporating the regular component of Doppler shift and $w_m = \beta(\Delta d)e^{j2\pi\frac{\Delta d}{\lambda}\sin\theta_m}$ is the spatial pole incorporating the mean DOA θ_m.

In the discussion so far it has been assumed that each mode reflected from a certain ionospheric layer corresponds to a particular value of $m = 1, 2, .., M$. However, there is no reason why a single mode cannot be modelled by more than one component or value of m. For example, two or more components may represent different rays in the wave interference model providing the spatial and temporal poles of the AR(1) processes used to generate each ray are on the unit circle (i.e., monochromatic plane waves are produced by the model when $|z_m| = |w_m| = 1$ since the AR(1) driving noise normalisation factors $\mu_m = \nu_m = 0$ under this condition and this effectively blocks the introduction of statistical variations).

Another physical interpretation arises if the spatial and temporal poles of the components which model a single ionospheric mode are not on the unit circle. This scenario might occur when the angular and Doppler power density functions of a distributed mode differ significantly from the Lorentzian shape. In this case, multiple components may be required to accurately model the features of the observed power densities such as Gaus-

sian shaped functions for instance. In signal processing terms, the value of M may be regarded as the number of terms in the modal decomposition of the observed space-time ACS without regard to the physical interpretation. When the individual modes cannot be resolved in range and analysed separately it therefore becomes relatively more difficult to attribute certain values of m and the associated parameters to particular signal modes.

4.3 Parameter estimation

This section introduces spectral and parametric methods for estimating the modal pairs (z_m, w_m) with the associated residues h_m from the sample space-time ACS $\hat{r}_k(i\Delta t, j\Delta d)$. When synchronised FMCW signals are used to probe a particular HF channel, such estimates provide valuable information regarding the level of Doppler spread and angular spread imposed by different ionospheric layers on the corresponding signal modes.

Section 4.3.1 mathematically discusses the application of existing methods for estimating the parameters of distributed signals from the sample space-time ACS. The modal structure of the statistically expected ACS derived in the previous section is exploited in section 4.3.2 to derive a novel subspace parameter estimation technique referred to as matched-field (MF) MUSIC. A computationally attractive closed-form parameter estimation technique which makes use of the MF-MUSIC principle but is based on the least squares criterion is introduced in section 4.3.3.

4.3.1 Comments on the application of standard techniques

Subspace techniques based on the data covariance matrix, such as the MUSIC algorithm for example, cannot be used to estimate the poles (z_m, w_m) and the residues h_m for $m = 1, 2, .., M$. To see this, consider the following expression for the $N \times N$ spatial covariance matrix $\mathbf{R}_x(k)$ which results for the assumed data model.

$$\mathbf{R}_x(k) = E\{\mathbf{x}_k(t)\mathbf{x}_k^H(t)\} = \sum_{m=1}^{M} A_m^2[\mathbf{s}(\theta_m)\mathbf{s}^H(\theta_m)] \odot \mathbf{B}_m + \sigma_n^2\mathbf{I} \tag{4.14}$$

The symbol $\odot$ denotes element-wise product and the N-dimensional vector $\mathbf{s}(\theta_m)$ is the array steering vector corresponding to the mean cone angle-of-arrival θ_m. The $N \times N$ matrix $\mathbf{B}_m$ may be referred to as an angular "spreading" matrix whose $(i,j)^{th}$ component is expressed as,

$$\mathbf{B}_m^{[i,j]} = e^{-B_s(m)|1-\sin\theta_m||i-j|\Delta d} \tag{4.15}$$

where $B_s(m)$ is the spatial bandwidth of the ionospheric channel which propagates the m^{th} mode. Note that the spatial covariance matrix in Eqn.(4.14) is Toeplitz and its $(i,j)^{th}$ element on the diagonal defined by $n = (i-j)_{i,j=0}^{N-1}$ is consistent with the spatial-only

version of the ACS model $r_k(n\Delta d)$ derived in section 4.2.2 for a sum of M independent AR(1) processes, as shown in Eqn.(4.16).

$$r_k(n\Delta d) = \sum_{m=1}^{M} h_m w_m^n \ , \quad h_m = A_m^2 \ , \quad w_m = e^{-B_s(m)|1-\sin\theta_m|\Delta d} e^{j2\pi\frac{\Delta d}{\lambda}\sin\theta_m} \tag{4.16}$$

If the spatial bandwidth $B_s(m) = 0$ for all modes $m = 1, 2, .., M < N$ then $\mathbf{B}_m^{[i,j]} = 1$ and $\mathbf{R}_x(k) = \sum_{m=1}^{M} A_m^2 \mathbf{s}(\theta_m)\mathbf{s}^H(\theta_m) + \sigma_n^2\mathbf{I}$. In this special case, MUSIC and other subspace DOA estimation methods can be used to estimate the cone angles-of-arrival θ_m since $\mathbf{R}_x(k)$ can be partitioned into two vector subspaces, an M-dimensional signal subspace and an $(N-M)$-dimensional noise subspace. However, when one or more of the modes exhibits angular spread (i.e., $B_s(m) > 0$) the spatial covariance matrix corresponding to such a mode takes the form $A_m^2[\mathbf{s}(\theta_m)\mathbf{s}^H(\theta_m)] \odot \mathbf{B}_m$ which has full rank so there is, strictly speaking, no noise-only subspace from which to compute the MUSIC spectra.

In appendix C it is shown that an ARMA$(M, M-1)$ model gives rise to an ACS which has the same form as $r_k(n\Delta d)$ in Eqn.(4.16). As described by (Marple 1987), the non-iterative least squares procedure adopted for ARMA model identification estimates the AR and MA parameters separately, rather than jointly, as required for optimal parameter estimation. More importantly, the above-mentioned procedure does not exploit the modal structure of the ACS corresponding to the ARMA$(M, M-1)$ family of random processes. This structure is exploited in the following section to derive a novel subspace method which estimates both the mean and spread parameters of all signal modes jointly from the sample ACS in one or two dimensions.

4.3.2 Subspace method for parameter estimation

To describe the novel two-dimensional (space-time) parameter estimation technique an $(L_s - P_s + 1) \times P_s$ matrix $\mathbf{C}(i)$ and the related $(L_t - P_t + 1)(L_s - P_s + 1) \times P_t P_s$ block matrix $\mathbf{D}$ are defined as;

$$\mathbf{C}(i) = \begin{bmatrix} \bar{r}(i, P_s - 1) & \cdots & \bar{r}(i,1)\bar{r}(i,0) \\ \bar{r}(i, P_s) & \cdots & \bar{r}(i,2)\bar{r}(i,1) \\ \vdots & & \\ \bar{r}(i, L_s - 1) & & \end{bmatrix} \quad \mathbf{D} = \begin{bmatrix} \mathbf{C}(P_t - 1) & \cdots & \mathbf{C}(1)\mathbf{C}(0) \\ \mathbf{C}(P_t) & \cdots & \mathbf{C}(2)\mathbf{C}(1) \\ \vdots & & \\ \mathbf{C}(L_t - 1) & & \end{bmatrix} \tag{4.17}$$

where $M < P_t < L_t$ and $M < P_s < L_s$. The sample ACS $\bar{r}(i\Delta t, j\Delta d)$ is computed by first averaging the sum of lagged products within each dwell to form $\hat{r}(i\Delta t, j\Delta d)$,

$$\hat{r}_k(i\Delta t, j\Delta d) = \frac{1}{N_t N_s} \sum_{t=1}^{N_t} \sum_{d=1}^{N_s} \mathbf{x}_k^{[d]}(t)\mathbf{x}_k^{[d+j]*}(t+i) \quad \begin{cases} i = 0, .., L_t - 1 \\ j = 0, .., L_s - 1 \end{cases} \tag{4.18}$$

where $N_t = P - i\Delta t + 1$, $N_s = N - j\Delta d + 1$ and then averaging these lags *over different dwells or CPI* to form the mean ACS $\bar{r}(i\Delta t/f_p, j\Delta d)$ over the period of data collection. As attention is being confined to a single range cell, the associated subscript k has been dropped for notational convenience in the term $\bar{r}(i\Delta t/f_p, j\Delta d)$ as well as in the definitions of $\mathbf{C}(i)$ and $\mathbf{D}(i)$.

In the absence of estimation errors and additive noise $\bar{r}(i,j) = \sum_{m=1}^{M} h_m z_m^i w_m^j$ under the assumed model, and the matrix $\mathbf{D}$ may be factorised as $\mathbf{D} = \mathbf{FG}$ where the $(L_t - P_t + 1)(L_s - P_s + 1) \times M$ matrix $\mathbf{F}$ and the $M \times P_t P_s$ matrix $\mathbf{G}$ are respectively defined by Eqn.(4.19) and Eqn.(4.20);

$$\mathbf{F} = [h_1 \mathbf{z}_1' \otimes \mathbf{w}_1' \cdots h_m \mathbf{z}_M' \otimes \mathbf{w}_M'] \quad \left\{ \begin{array}{lcl} \mathbf{z}_m' & = & [z_m^{P_t-1}\ z_m^{P_t} \cdots z_m^{L_t-1}]^T \\ \mathbf{w}_m' & = & [w_m^{P_s-1}\ w_m^{P_s} \cdots w_m^{L_s-1}]^T \end{array} \right. \tag{4.19}$$

the symbol $\otimes$ represents a Kronecker product between the indicated vector pairs for both matrices.

$$\mathbf{G} = [\mathbf{z}_1'' \otimes \mathbf{w}_1'' \cdots \mathbf{z}_M'' \otimes \mathbf{w}_M'']^H \quad \left\{ \begin{array}{lcl} \mathbf{z}_m'' & = & [z_m^0\ z_m^{-1} \cdots z_m^{-(P_t-1)}]^H \\ \mathbf{w}_m'' & = & [w_m^0\ w_m^{-1} \cdots w_m^{-(P_s-1)}]^H \end{array} \right. \tag{4.20}$$

Since the vectors $\mathbf{z}_m' \otimes \mathbf{w}_m'$ and $\mathbf{z}_m'' \otimes \mathbf{w}_m''$ have a Vandermonde structure and the parameter pairs (z_m, w_m) for $m = 1, 2, .., M$ are assumed to be distinct it follows that both matrices $\mathbf{F}$ and $\mathbf{G}$ have full rank M. As a result, the $M \times M$ Hermitian matrix $\mathbf{F}^H\mathbf{FGG}^H$ is positive definite with M eigenvalues $\lambda_m > 0$ and eigenvectors denoted by $\mathbf{u}_m$.

$$(\mathbf{F}^H\mathbf{FGG}^H)\mathbf{u}_m = \lambda_m \mathbf{u}_m \ , \quad m = 0, 1, .., M \tag{4.21}$$

Pre-multiplication of the left and right hand side of Eqn.(4.21) by $\mathbf{G}^H$ and noting that $\mathbf{D}^H\mathbf{D} = \mathbf{G}^H\mathbf{F}^H\mathbf{FG}$ one obtains,

$$(\mathbf{G}^H\mathbf{F}^H\mathbf{FG})\mathbf{G}^H\mathbf{u}_m = (\mathbf{D}^H\mathbf{D})\mathbf{G}^H\mathbf{u}_m = (\mathbf{D}^H\mathbf{D})\mathbf{q}_m = \lambda_m \mathbf{q}_m \tag{4.22}$$

where $\mathbf{q}_m = \mathbf{G}^H\mathbf{u}_m$ is an eigenvector of $\mathbf{D}^H\mathbf{D}$ with corresponding eigenvalue λ_m. In other words, the $(P_tP_s) \times (P_tP_s)$ Hermitian matrix $\mathbf{D}^H\mathbf{D}$ is of rank M with the M non-zero eigenvalues equal to λ_m for $m = 1, 2, ., M$ and the remaining $(P_t \times P_s) - M$ eigenvalues equal to zero. Moreover, the M principle eigenvectors $\mathbf{q}_m$ of the matrix $\mathbf{D}^H\mathbf{D}$ are formed as a linear combination of the columns in $\mathbf{G}^H$ which are composed of the M space-time signal vectors $\mathbf{z}_m'' \otimes \mathbf{w}_m''$. In the presence of lag estimation errors and additive noise, these properties are not exactly true but they tend to be approximately true. Naturally, the accuracy of this description is dependent on the number of statistically independent observations used for estimation and the power of the additive noise relative to that of the received signal modes.

To estimate the parameter pairs (z_m, w_m) the sample lags $\bar{r}(i,j)$ are used to form the

matrix $\mathbf{D}$ as in Eqn.(4.17) and the Hermitian matrix $\mathbf{D}^H\mathbf{D}$ is represented in terms of its eigen-decomposition into signal and noise subspaces.

$$\mathbf{D}^H\mathbf{D} = \mathbf{Q}_s\Lambda_s\mathbf{Q}_s^H + \mathbf{Q}_n\Lambda_n\mathbf{Q}_n^H \tag{4.23}$$

In Eqn.(4.23), the $P_tP_s \times M$ matrix $\mathbf{Q}_s$ contains the M signal subspace eigenvectors as its coloumns and the $M \times M$ diagonal matrix Λ_s contains the M corresponding eigenvalues. The $P_tP_s \times (P_tP_s - M)$ matrix $\mathbf{Q}_n$ and $(P_tP_s - M) \times (P_tP_s - M)$ diagonal matrix Λ_n are defined in analogous fashion and contain the noise subspace eigenvectors and eigenvalues respectively. The existence of non-zero noise subspace eigenvalues indicates the presence of a combination of estimation errors, additive noise and, potentially, model mismatches.

The approximate orthogonality between the signal vectors $\mathbf{v}(\phi) = \mathbf{z}''(\alpha(\Delta t), \Delta f) \otimes \mathbf{w}''(\beta(\Delta d), \theta)$ and the noise subspace spanned by the columns of $\mathbf{Q}_n$ is exploited to form a MUSIC-like cost function $p(\phi)$ defined in Eqn.(4.24).

$$p(\phi) = \{\mathbf{v}^H(\phi)\mathbf{Q}_n\mathbf{Q}_n^H\mathbf{v}(\phi)\}^{-1} \tag{4.24}$$

where parameter vector $\phi = [\alpha(\Delta t), \beta(\Delta d), \theta, \Delta f]^T$. An exhaustive search for the peaks of the MUSIC-like cost function $p(\phi)$ over a four dimensional manifold defined by the parameter vector ϕ yields estimates of both the complex pole locations (z_m, w_m) and the pairing at the same time. Once these parameters have been estimated the corresponding residues h_m can be estimated by a least squares fit to the sample ACS.

The residues h_m for $m = 1, 2, .., M$ are constrained to be real when the ARMA$(M, M-1)$ process is to be generated as a sum of M independent AR(1) processes. This follows from the fact that the power of the m^{th} AR(1) process is given by $h_m = A_m^2$. To estimate the residues a stacked vector $\tilde{\mathbf{r}}$ is defined to contain the space-time sample ACS.

$$\tilde{\mathbf{r}} = [r(0,0)\cdots r(0,L_s-1)\vdots r(1,0)\cdots r(1,L_s-1)\vdots\cdots\vdots r(L_t-1,L_s-1)]^T \tag{4.25}$$

Similarly, a matrix $\tilde{\mathbf{V}}$ is defined in Eqn.(4.26) to contain the space-time signal vectors estimated for the m^{th} mode.

$$\tilde{\mathbf{V}} = [\mathbf{z}_1 \otimes \mathbf{w}_1 \cdots \mathbf{z}_M \otimes \mathbf{w}_M] \quad \begin{cases} \mathbf{z}_m &= [z_m^0\ z_m^1 \cdots z_m^{(L_t-1)}]^T \\ \mathbf{w}_m &= [w_m^0\ w_m^1 \cdots w_m^{(L_s-1)}]^T \end{cases} \tag{4.26}$$

The vector of residues $\mathbf{h} = [h_1\ h_2 \cdots h_M]^T$ is estimated such that it minimises the difference between the model and sample ACS in a least squares sense;

$$\hat{\mathbf{h}} = \text{argmin}\ \|\mathbf{r} - \mathbf{V}\mathbf{h}\|_F\ ,\quad \mathbf{r} = \begin{bmatrix} \Re\{\tilde{\mathbf{r}}\} \\ \Im\{\tilde{\mathbf{r}}\} \end{bmatrix}\ ,\quad \mathbf{V} = \begin{bmatrix} \Re\{\tilde{\mathbf{V}}\} \\ \Im\{\tilde{\mathbf{V}}\} \end{bmatrix} \tag{4.27}$$

where the *real* vector $\mathbf{r}$ and matrix $\mathbf{V}$ are constructed from the real $\Re\{\cdot\}$ and imaginary

$\Im\{\cdot\}$ parts of $\tilde{\mathbf{r}}$ and $\tilde{\mathbf{V}}$ respectively. The minimising argument $\hat{\mathbf{h}}$ in Eqn.(4.27) is given by;

$$\hat{\mathbf{h}} = [\mathbf{V}^H\mathbf{V}]^{-1}\mathbf{V}^H\mathbf{r} = \mathbf{V}^+\mathbf{r} \tag{4.28}$$

where $\mathbf{V}^+ = [\mathbf{V}^H\mathbf{V}]^{-1}\mathbf{V}^H$ is the Moore-Penrose pseudo inverse of $\mathbf{V}$. Once all the model parameters have been estimated, it is required to assess the accuracy with which the model ACS fits the sample ACS calculated from the received data. The modelling performance may in the first instance be quantified by a fitting ăccuracy (FA) measure defined in Eqn.(4.29).

$$\text{FA} = 1 - \frac{\|\tilde{\mathbf{r}} - \tilde{\mathbf{V}}\hat{\mathbf{h}}\|_F}{\|\tilde{\mathbf{r}}\|_F} \tag{4.29}$$

The ACS model estimated from the data may be extended to an infinite number of space-time lags and Fourier transformed in order to estimate the power spectral density of the channel fluctuations in the angle-Doppler domain. The resulting two-dimensional spectra provides a quantitative measure of the angle-Doppler bandwidth occupied by a particular ionospheric channel.

Since the manifold is parameterised by the statistical properties of the channel model $[\alpha(\Delta t), \beta(\Delta d)]$ as well as the regular (deterministic) components $[\theta, \Delta f]$, this technique may be regarded as a "matched field" (MF) version of MUSIC. The presented technique can also be applied to estimate the parameters of two-dimensional exponentially damped sinusoidal signals in noise. An important distinction between these two applications is that in the former case the matrix $\mathbf{D}$ contains the covariances or lags estimated from the data of a statistical process while in the latter case it contains the actual data samples in which the signals are corrupted by additive noise. In both cases, the computational complexity of evaluating the cost function over four-dimensional manifold may be prohibitive in some applications. In this situation an alternative closed form procedure based on the least squares criterion would be desirable, such a procedure is introduced in the next section.

4.3.3 Closed-form least squares method

To introduce the two-dimensional least squares method an $L_t \times L_s$ matrix $\mathbf{T}$ is defined such that its $(i,j)^{th}$ entry equals $r(i\Delta t, j\Delta d)$.

$$\mathbf{T} = \begin{bmatrix} r(0,0) & r(0,1) & \cdots & r(0,L_s-1) \\ r(1,0) & r(1,1) & \cdots & r(1,L_s-1) \\ \vdots & & \ddots & \vdots \\ r(L_t-1,0) & \cdots & \cdots & r(L_t-1,L_s-1) \end{bmatrix} \tag{4.30}$$

Using the modal decomposition of $r(i\Delta t, j\Delta d)$ in Eqn.(4.13) it is possible to factorise the matrix $\mathbf{T}$ in the following way;

$$\mathbf{T} = \sum_{m=1}^{M} h_m \mathbf{z}_m \mathbf{w}_m^H = \mathbf{Z}\mathbf{H}\mathbf{W}^H \tag{4.31}$$

by defining the vectors $\mathbf{z}_m = [z_m^0 \; z_m^1 \cdots z_m^{L_t-1}]^T$, $\mathbf{w}_m = [w_m^0 \; w_m^1 \cdots w_m^{L_s-1}]^H$ the $L_t \times M$ matrix $\mathbf{Z} = [\mathbf{z}_1 \; \mathbf{z}_2 \cdots \mathbf{z}_M]$, the $L_s \times M$ matrix $\mathbf{W} = [\mathbf{w}_1 \; \mathbf{w}_M \cdots \mathbf{w}_M]$ and the $M \times M$ diagonal matrix $\mathbf{H} = diag[h_1 \; h_2 \cdots h_M]$.

In practice, we have an estimate $\hat{\mathbf{T}}$ containing the sample spatio-temporal lags. Even in the absence of modelling errors and additive noise, the matrix $\hat{\mathbf{T}}$ will generally be of full rank despite $L_t > M$ and $L_s > M$ due to the presence of estimation errors in the sample lags. In an analogous manner to (Cadzow 1983), we can attempt to reduce the influence of estimation uncertainty on the parameter estimates by taking the reduced rank-M approximation of $\hat{\mathbf{T}}$ using a truncated singular value decomposition (SVD).

$$\tilde{\mathbf{T}} = \sum_{m=1}^{M} \sigma_m \mathbf{u}_m \mathbf{v}_m^H = \mathbf{U}_s \Sigma_s \mathbf{V}_s^H \tag{4.32}$$

In Eqn.(4.32), σ_m are the principal singular values of $\hat{\mathbf{T}}$, $\mathbf{u}_m$ are the L_t-dimensional left singular vectors and $\mathbf{v}_m$ are the L_s-dimensional right singular vectors. The matrices $\mathbf{U}_s = [\mathbf{u}_1 \cdots \mathbf{u}_M]$ and $\mathbf{V}_s = [\mathbf{v}_1 \cdots \mathbf{v}_M]$ contain the left and right singular vectors as their coloumns respectively while the $M \times M$ diagonal matrix $\Sigma_s = diag[\sigma_1, \cdots, \sigma_M]$ contains the singular values.

The proposed parameter estimation method is based on finding the model parameters $h_m, z_m, w_m \; \forall m = 1, 2, .., M$ which provides the best least-squares fit to $\tilde{\mathbf{T}}$ by minimising the Frobenius norm $\|\cdot\|_F$ in the following criterion function.

$$f_{cr}(\mathbf{Z}, \mathbf{H}, \mathbf{W}) = \|\tilde{\mathbf{T}} - \mathbf{Z}\mathbf{H}\mathbf{W}^H\|_F \tag{4.33}$$

This multidimensional optimisation problem is separable and for a given matrix $\mathbf{Z}$ it can be shown that the arguments $\mathbf{H}$ and $\mathbf{W}$ which minimise the criterion function satisfy,

$$\mathbf{H}\mathbf{W}^H = (\mathbf{Z}^H\mathbf{Z})^{-1}\mathbf{Z}^H\hat{\mathbf{T}}_s = \mathbf{Z}^+\tilde{\mathbf{T}} \tag{4.34}$$

where $\mathbf{Z}^+ = (\mathbf{Z}^H\mathbf{Z})^{-1}\mathbf{Z}^H$ is the Moore-Penrose pseudo inverse of $\mathbf{Z}$. Substitution of Eqn.(4.34) into Eqn.(4.33) yields the following criterion function in terms of the matrix $\mathbf{Z}$.

$$\hat{\mathbf{Z}} = \text{argmin} \; \|(\mathbf{I} - \mathbf{Z}\mathbf{Z}^+)\tilde{\mathbf{T}}\|_F = \text{argmin} \; \|\mathbf{P}_z\tilde{\mathbf{T}}\|_F \tag{4.35}$$

where $\mathbf{P}_z = (\mathbf{I} - \mathbf{Z}\mathbf{Z}^+)$ is the orthogonal projector onto the null space of $\mathbf{Z}^H$. Using the

fact that $\|Q\|_F = \mathrm{Tr}\{QQ^H\}$, where $\mathrm{Tr}\{\cdot\}$ denotes the trace operator, it is possible to re-write Eqn.(4.35) as,

$$\hat{\mathbf{Z}} = \text{argmin } \mathrm{Tr}\{\mathbf{P}_z\tilde{\mathbf{T}}\tilde{\mathbf{T}}^H\mathbf{P}_z^H\} = \text{argmin } \mathrm{Tr}\{\mathbf{P}_z^H\mathbf{P}_z\hat{\mathbf{T}}_s\hat{\mathbf{T}}_s^H\} \tag{4.36}$$

since a cyclic rotation of the elements in the $\mathrm{Tr}\{\cdot\}$ operator does not effect the value of the trace. The projection matrix is symmetric ($\mathbf{P}_z = \mathbf{P}_z^H$) and idempotent ($\mathbf{P}_z^2 = \mathbf{P}_z$) so Eqn.(4.36) may be simplified to the following concentrated expression.

$$\hat{\mathbf{Z}} = \text{argmin } \mathrm{Tr}\{\mathbf{P}_z\tilde{\mathbf{T}}\tilde{\mathbf{T}}^H\} \tag{4.37}$$

Assuming the number of modes M is known or can be estimated by a suitable method beforehand, solving for $\mathbf{Z}$ is more tractable (Stoica and Sharman 1990) when the projection matrix is re-parameterised in terms of an $L_t \times (L_t - M)$ Toeplitz matrix $\mathbf{A}$ defined by,

$$\mathbf{A} = \begin{bmatrix} a_M & a_{M-1} & \cdots & a_0 & \cdots & 0 \\ & \ddots & \ddots & & \ddots & \\ 0 & & a_M & a_{M-1} & \cdots & a_0 \end{bmatrix}^H \tag{4.38}$$

such that its elements $a_0, a_1, .., a_M$ are the coefficients of the following characteristic polynomial.

$$p(z) = a_0 z^M + a_1 z^{M-1} + \cdots + a_M = \prod_{m=1}^{M}(z - z_m) \tag{4.39}$$

Since the matrix $\mathbf{A}$ has full rank $(L_t - M)$ and by construction it is apparent that $\mathbf{A}^H\mathbf{Z} = \mathbf{0}$ it follows that the coloumns of $\mathbf{A}$ do in fact form a basis for the null space of $\mathbf{Z}^H$. As a result, the projection matrix can be re-parameterised as $\mathbf{P}_z = \mathbf{A}(\mathbf{A}^H\mathbf{A})^{-1}\mathbf{A}^H$ which leads to a criterion function in terms of the polynomial coefficient vector $\mathbf{a} = [a_0, a_1, .., a_M]^T$.

$$\hat{\mathbf{a}} = \text{argmin } \mathrm{Tr}\{\mathbf{A}(\mathbf{A}^H\mathbf{A})^{-1}\mathbf{A}^H\tilde{\mathbf{T}}\tilde{\mathbf{T}}^H\} \tag{4.40}$$

As pointed out in (Krim and Viberg 1996), the coefficient vector $\mathbf{a} = [a_0 \cdots a_M]^T$ which minimises Eqn.(4.40) may be estimated analytically by sequentially solving two quadratic optimisation problems;

$$\begin{aligned} &1) \quad \hat{\mathbf{a}} = \text{argmin } \mathrm{Tr}\{\mathbf{A}\mathbf{A}^H\tilde{\mathbf{T}}\tilde{\mathbf{T}}^H\} \\ &2) \quad \hat{\mathbf{a}} = \text{argmin } \mathrm{Tr}\{\mathbf{A}(\hat{\mathbf{A}}^H\hat{\mathbf{A}})^{-1}\mathbf{A}^H\tilde{\mathbf{T}}\tilde{\mathbf{T}}^H\} \end{aligned} \tag{4.41}$$

subject to the linear constraint $\hat{\mathbf{a}}^H\mathbf{e} = 1$ where $\mathbf{e} = [1, 0, \cdots, 0]^T$ ensures a non-trivial solution. Note that the elements of the vector $\hat{\mathbf{a}}$ which solves the first quadratic problem in Eqn.(4.41) is used to form the matrix $\hat{\mathbf{A}}$ in the second quadratic problem according to

its definition in Eqn.(4.38). The matrix $(\hat{\mathbf{A}}^H\hat{\mathbf{A}})^{-1}$ is a data-dependent weighting matrix in the second quadratic problem.

A more complex set of constraints can be applied in certain situations to ensure that the roots corresponding to the estimated polynomial coefficients $\hat{\mathbf{a}}$ lie on the unit circle. These constraints are useful for the direction-of-arrival estimation problem treated by (Stoica and Sharman 1990) where the received signals are assumed to be discrete in angle-of-arrival (i.e., plane waves). Such constraints should not be applied in this instance because the received signals are assumed to be distributed over angle and Doppler space, the width of the distribution for the m^{th} mode is indicated by the distance between the root $\hat{z}_m$ (derived from the estimated polynomial $\hat{p}(z)$) and the unit circle. In other words, the modulus of $\hat{z}_m$ constitutes an estimate of the mode Doppler spread while the argument of $\hat{z}_m$ constitutes an estimate of the mean Doppler shift.

As shown in (Besler and Macovski 1986), both quadratic problems in Eqn.(4.41) may be solved using the same technique as that for deriving linear prediction coefficients by the covariance method. The solution of the first problem in Eqn.(4.41) is given by,

$$\hat{\mathbf{a}} = \frac{[\sum_{j=0}^{L_s-1}\mathbf{Y}^H(j)\mathbf{Y}(j)]^{-1}\mathbf{e}}{\mathbf{e}^T[\sum_{j=0}^{L_s-1}\mathbf{Y}^H(j)\mathbf{Y}(j)]^{-1}\mathbf{e}}, \quad \mathbf{Y}(j) = \begin{bmatrix} \hat{r}(M,j) & \cdots & \hat{r}(1,j)\hat{r}(0,j) \\ \hat{r}(M+1,j) & \cdots & \hat{r}(2,j)\hat{r}(1,j) \\ \vdots & & \\ \hat{r}(L_t-1,j) & & \end{bmatrix} \tag{4.42}$$

and the estimated coefficients $\hat{\mathbf{a}} = [\hat{a}_0 \cdots \hat{a}_M]^T$ are used to form the matrix $\hat{\mathbf{A}}$ according to Eqn.(4.38). The second quadratic problem in Eqn.(4.41) can then be solved in similar fashion to the first, as shown in Eqn.(4.43)

$$\hat{\mathbf{a}} = \frac{[\sum_{j=0}^{L_s-1}\mathbf{Y}^H(j)(\hat{\mathbf{A}}^H\hat{\mathbf{A}})^{-1}\mathbf{Y}(j)]^{-1}\mathbf{e}}{\mathbf{e}^T[\sum_{j=0}^{L_s-1}\mathbf{Y}^H(j)(\hat{\mathbf{A}}^H\hat{\mathbf{A}})^{-1}\mathbf{Y}(j)]^{-1}\mathbf{e}} \tag{4.43}$$

The least squares estimates of the temporal poles $\hat{z}_m$ for $m = 1, 2, .., M$ are then given by the roots of the estimated characteristic polynomial $\hat{p}(z)$. The polynomial roots can be found using the algorithm in (Aurand 1987) for example which is guaranteed to converge.

In analogous manner, the argument $\mathbf{W}$ minimising the criterion function $f_{cr}(\cdot)$ is estimated as, Eqn.(4.44).

$$\hat{\mathbf{W}} = \text{argmin Tr}\{\mathbf{P}_w\tilde{\mathbf{T}}^H\tilde{\mathbf{T}}\} \tag{4.44}$$

where $\mathbf{P}_w = (\mathbf{I} - \mathbf{W}\mathbf{W}^+)$ is the orthogonal projector onto the null space of $\mathbf{W}^H$ and $\mathbf{W}^+ = (\mathbf{W}^H\mathbf{W})^{-1}\mathbf{W}^H$ is the Moore-Penrose pseudo inverse of $\mathbf{W}$. In this case the

projection matrix is re-parameterised as $\mathbf{P}_w = \mathbf{B}(\mathbf{B}^H\mathbf{B})^{-1}\mathbf{B}^H$ where the matrix

$$\mathbf{B} = \begin{bmatrix} b_M & b_{M-1} & \cdots & b_0 & \cdots & 0 \\ & \ddots & \ddots & & \ddots & \\ 0 & & b_M & b_{M-1} & \cdots & b_0 \end{bmatrix}^H \tag{4.45}$$

is constructed from the coefficients of the following characteristic polynomial.

$$q(w) = b_0 w^M + b_1 w^{M-1} + \cdots + b_M = \prod_{m=1}^{M} (w - w_m) \tag{4.46}$$

As before, the polynomial coefficients are estimated by sequentially solving two quadratic optimisation problems,

$$\begin{aligned} &1) \quad \hat{\mathbf{b}} = \text{argmin Tr}\{\mathbf{B}\mathbf{B}^H\tilde{\mathbf{T}}^H\tilde{\mathbf{T}}\} \\ &2) \quad \hat{\mathbf{b}} = \text{argmin Tr}\{\mathbf{B}(\hat{\mathbf{B}}^H\hat{\mathbf{B}})^{-1}\mathbf{B}^H\tilde{\mathbf{T}}^H\tilde{\mathbf{T}}\} \end{aligned} \tag{4.47}$$

subject to the linear constraint $\hat{\mathbf{b}}^H\mathbf{e} = 1$. The vector $\hat{\mathbf{b}}$ that solves problem 1) in Eqn.(4.47) is given by,

$$\tilde{\mathbf{b}} = \frac{[\sum_{i=0}^{L_t-1} \mathbf{X}^H(i)\mathbf{X}(i)]^{-1}\mathbf{e}}{\mathbf{e}^H[\sum_{i=0}^{L_t-1} \mathbf{X}^H(i)\mathbf{X}(i)]^{-1}\mathbf{e}}, \quad \mathbf{X}(i) = \begin{bmatrix} \hat{r}(i,M) & \cdots & \hat{r}(i,1)\hat{r}(i,0) \\ \hat{r}(i,M+1) & \cdots & \hat{r}(i,2)\hat{r}(i,1) \\ \vdots & & \\ \hat{r}(i,L_s-1) & & \end{bmatrix} \tag{4.48}$$

this estimate is used to form the matrix $\hat{\mathbf{B}}$ according to Eqn.(4.45) for problem 2) in Eqn.(4.47). The polynomial coefficient vector $\hat{\mathbf{b}}$ is then estimated as,

$$\hat{\mathbf{b}} = \frac{[\sum_{i=0}^{L_t-1} \mathbf{X}^H(i)(\hat{\mathbf{B}}^H\hat{\mathbf{B}})^{-1}\mathbf{X}(i)]^{-1}\mathbf{e}}{\mathbf{e}^H[\sum_{i=0}^{L_t-1} \mathbf{X}^H(i)(\hat{\mathbf{B}}^H\hat{\mathbf{B}})^{-1}\mathbf{X}(i)]^{-1}\mathbf{e}} \tag{4.49}$$

from which the polynomial $\hat{q}(w)$ is constructed. The spatial poles $\hat{w}_m$ are then estimated by finding the roots of the polynomial $\hat{q}(w)$.

Note that aside from the initial SVD and final polynomial rooting, this algorithm estimates the temporal poles z_m and spatial poles w_m of the M modes from the sample spatio-temporal lags in closed form. Once the poles have been estimated, it is then necessary to correctly pair the temporal and spatial poles associated with each mode before estimating the residues h_m. A brute force method for pairing the temporal poles z_m and spatial poles w_m is to try all possible combinations and choose the one which leads to the smallest modelling error. For M modes the number of combinations to be tried equals $M!/2(M-2)!$ which becomes quite large for M greater than five. An alternative way of pairing the poles exploits the approximate orthogonality noted in section 4.3.2

between the signal vectors $\mathbf{z}''_m \otimes \mathbf{w}''_m$ and the noise subspace spanned by the columns of $\mathbf{Q}_n$. In other words, the spatial pole w_m paired to a reference temporal pole z_{m_r} is the one which minimises the cost $c(m)$.

$$c(m) = (\mathbf{z}''_{m_r} \otimes \mathbf{w}''_m)^H \mathbf{Q}_n \mathbf{Q}_n^H (\mathbf{z}''_{m_r} \otimes \mathbf{w}''_m) \tag{4.50}$$

4.4 Experimental results

In order to demonstrate the performance of the two-dimensional (space-time) parameter estimation techniques presented in section 4.3 it is necessary to process a data set which allows the space-time characteristics of the ionospheric channel to be observed over a time scale of a few minutes. The experiment described in section 2.2.2 makes use of an FMCW signal to measure the delay, angle and Doppler characteristics of different signal modes propagated via a mid-latitude ionospheric path over an interval of approximately 4 minutes. This data allows the two-dimensional spectral and parametric techniques described in the previous section to estimate the angular and Doppler spread imposed by different ionospheric layers on the signal modes even when the individual modes cannot be resolved in time-delay or range.

The estimation of these space-time model parameters when only one propagation mode is present within a particular range cell is relatively straightforward and does not warrant the use of the sophisticated parameter estimation techniques presented in section 4.3. Although most of the propagation modes were resolved in delay, this particular data set contains a valuable example where two sporadic-E modes were known to propagate by inspection of the oblique incidence ionogram but could not be resolved in delay or group range by the main array which has a comparatively lower range resolution. Since the modes are likely to have closely spaced angular and Doppler power spectral densities, the estimation of the individual mode parameters from the signal mixture is no longer straightforward and requires the use of more sophisticated parameter estimation techniques, such as those presented in section 4.3.

Section 4.4.1 applies the two-dimensional constrained least squares technique developed in section 4.3.3 to estimate the mean angle-of-arrival and Doppler frequency of two sporadic-E modes in a particular range cell as well as the temporal and spatial dampening factors which cause Doppler and angular spread in each mode respectively. The application of the matched-field MUSIC technique is illustrated for the same two mode mixture in section 4.4.1, the parameters estimated by both techniques are expected to be the same in the absence of modelling errors, estimation uncertainty and additive noise. However, when two different techniques are applied to an experimental data sample ACS the parameter estimates are not expected to be exactly the same. A comparison between the parameters estimated by the two methods and a measurement of the accuracy with which the model ACS represents the sample ACS provides useful information regarding

Mode	Δf_m, Hz	$\alpha(\Delta t)$	θ_m, deg	$\beta(\Delta d)$	h_m	$m=1$, dB	$m=2$, dB
$m_r=1$	0.46	0.998	22.2	0.920	9.46	-56.1	-39.3
$m_r=2$	0.39	0.997	21.7	0.963	5.23	-40.3	-62.7

Table 4.1: Distributed signal model parameters estimated from the sample ACS $\bar{r}_k(i\Delta t, j\Delta d)$ derived from data which is known to consist of a superposition of two sporadic-E modes.

the validity of the assumed distributed signal model and the robustness of the proposed parameter estimation techniques.

4.4.1 Least squares

The sample ACS $\bar{r}_k(i\Delta t, j\Delta d)$ used for parameter estimation is computed by first averaging the sum of lagged products within each dwell to form $\hat{r}(i\Delta t, j\Delta d)$,

$$\hat{r}_k(i\Delta t, j\Delta d) = \frac{1}{N_t N_s} \sum_{t=1}^{N_t} \sum_{d=1}^{N_s} \mathbf{x}_k^{[d]}(t) \mathbf{x}_k^{[d+j\Delta d]*}(t+i\Delta t) \quad \begin{cases} i = 0,..,L_t-1 \\ j = 0,..,L_s-1 \end{cases} \tag{4.51}$$

where $N_t = P - i\Delta t + 1$, $N_s = N - j\Delta d + 1$ and then averaging these lags over different dwells to form the mean ACS, denoted by $\bar{r}_k(i\Delta t, j\Delta d)$, over the period of data collection. In this experiment, the interval between adjacent temporal lags was 0.1 seconds ($\Delta t =$ 6 PRI with $f_p = 60$ Hz) and the spacing between adjacent spatial lags was 84 metres which is equivalent to $\Delta d = 1$ sub-array spacing. The number of lags calculated was $L_t = L_s = 30$ using $P = 256$ PRI per dwell and $N = 30$ sub-array receivers. The lags $\hat{r}_k(i\Delta t, j\Delta d)$ were estimated according to Eqn.(4.51) in range cell $k = 16$ (containing the sporadic-E modes) for each dwell and then averaged over a total of 47 dwells to form the sample ACS $\bar{r}_k(i\Delta t, j\Delta d)$ used in further processing.

Table 4.1 lists the parameters estimated by the *closed-form least squares technique* assuming $M = 2$ modes. The pairing of temporal and spatial poles for each mode was performed by evaluating the function $c(m)$ in Eqn.(4.50) for different combinations of temporal pole z_{m_r} and spatial pole w_m for $m_r, m = 1, 2$. This pairing step is necessary because the roots of the estimated polynomials $\hat{p}(z)$ and $\hat{q}(w)$ have no ordering. This pairing was performed by choosing $P_s = P_t = M + 1$ to guarantee the existence of a noise-only subspace in the absence of modelling errors.

For each reference temporal pole $m_r = 1, 2$ Table 4.1 shows the value of the function $c(m)$ for the spatial poles indexed by m=1,2. The poles are paired as the combinations which yield the lowest values of this function. In other words, the first temporal pole ($m_r = 1$) is paired to the first spatial pole ($m = 1$), and as expected, the poles indexed by ($m_r, m = 2$) gives rise to a minimum to form the other pair.

Note that the mean cone angle-of-arrival θ_m and Doppler shift Δf_m estimated for each

mode in Table 4.1 are very similar to those estimated by the space-time MUSIC algorithm in Figure 2.32. Unlike space-time MUSIC, the least squares technique additionally estimates the temporal and spatial ACS dampening coefficients denoted by $\alpha(\Delta t)$ and $\beta(\Delta d)$ respectively. These coefficients represent a parametric fit of the angular and Doppler power density of the channel fluctuations to a class of power density functions known as Lorentzian functions.

Using Eqn.(C.7) it is possible to plot the spatial and spectral power densities corresponding to the distributed signal model parameters estimated for the two sporadic-E modes in Table 4.1; these are shown in Figure 4.1. It can be seen from curve 1 that the Doppler spread on both modes, defined here as the half power bandwidth, is in the order of 0.1 Hz. Previous results for the Doppler spread of sporadic-E modes on oblique mid-latitude paths are difficult to find, although it is noted that the above-mentioned result is similar to the Doppler spread measurements of 0.18, 0.07 and 0.16 Hz published by Shepherd and Lomax (1967) for clean single-mode signals propagated by the F-region on a 4100 km mid-latitude path. The angular spread is approximately 0.2 degrees which agrees well with measurements in the order of 0.4 degrees made for single-hop E and F-region modes by Balser and Smith (1962) on a 1566 km mid-latitude path with a very wide aperture array (2000 ft). Larger directional dispersions of 1-2 degrees were observed for sporadic-E modes by (Sherill and Smith 1977) although these measurements were made on a much smaller array aperture (350 m).

The estimated model ACS resulted in a fitting accuracy of 97 percent when compared to the experimentally derived sample ACS, this high modelling accuracy was obtained using the two step quadratic minimisation procedure described by Eqn.(4.41) and Eqn.(4.47). It is possible to repeat this procedure more then twice by using an updated estimate of the polynomial coefficients to form the weighting matrix at each iteration. Figure 4.2 shows the value of the criterion function to be minimised at different iterations for both the spatial and temporal parameter estimation problem. It is evident that only two iterations (steps one and two in Eqn.(4.41) and Eqn.(4.47)) are required to reach the minimum value in each case. In fact, the improvement between the first and second iteration corresponds to the extra reduction in the least squares criterion function achieved by the described method relative to Prony's method which is traditionally used to estimate the parameters of damped sinusoidal signals in noise.

Figures 4.3 and 4.4 are examples comparing the real and imaginary parts respectively of the space-time ACS predicted by the model with those of the sample ACS. The $L_t L_s = 900$ space-time ACS samples are stacked as described for the vector $\tilde{\mathbf{r}}$ in section 4.3.2. As expected for a fitting accuracy of 97 percent, the model ACS closely tracks the 900 point ACS estimated from real data using only $M = 2$ modes. This experimental example serves to illustrate the application of the least-squares parameter estimation technique to jointly determine the Doppler and angular statistical characteristics of multiple ionospheric reflected modes.

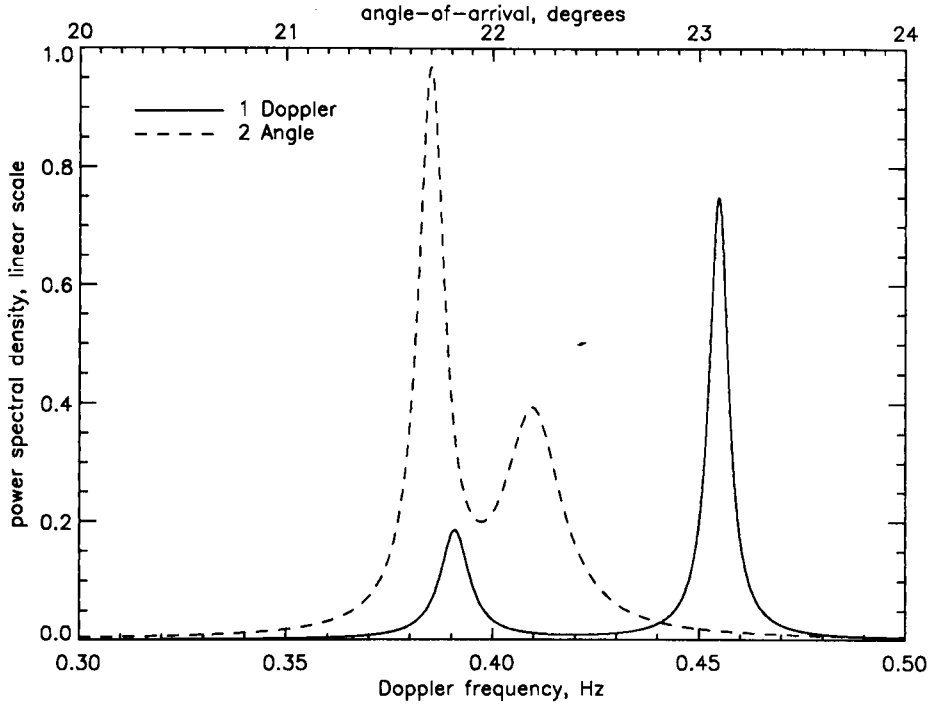

Figure 4.1: The spatial and temporal power densities of the two mode mixture in range cell $k = 16$. These densities were calculated by extending the parameterised model ACS where the parameters were estimated from a finite length experimental data sample ACS. Note that the linear scale on the vertical axis is arbitrary for both spectra since the power of the received signal in Watts is not known.

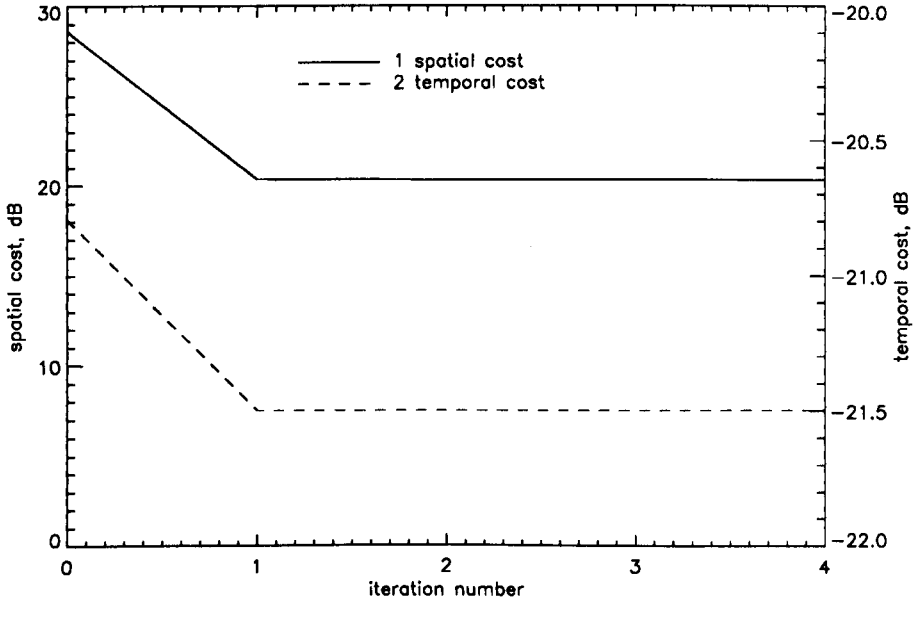

Figure 4.2: The spatial cost $\mathrm{Tr}\{\mathbf{P}_w \hat{\mathbf{T}}_s^H \hat{\mathbf{T}}_s\}$ and temporal cost $\mathrm{Tr}\{\mathbf{P}_z \hat{\mathbf{T}}_s \hat{\mathbf{T}}_s^H\}$ as a function of iteration number for the proposed closed-form distributed signal parameter estimation technique.

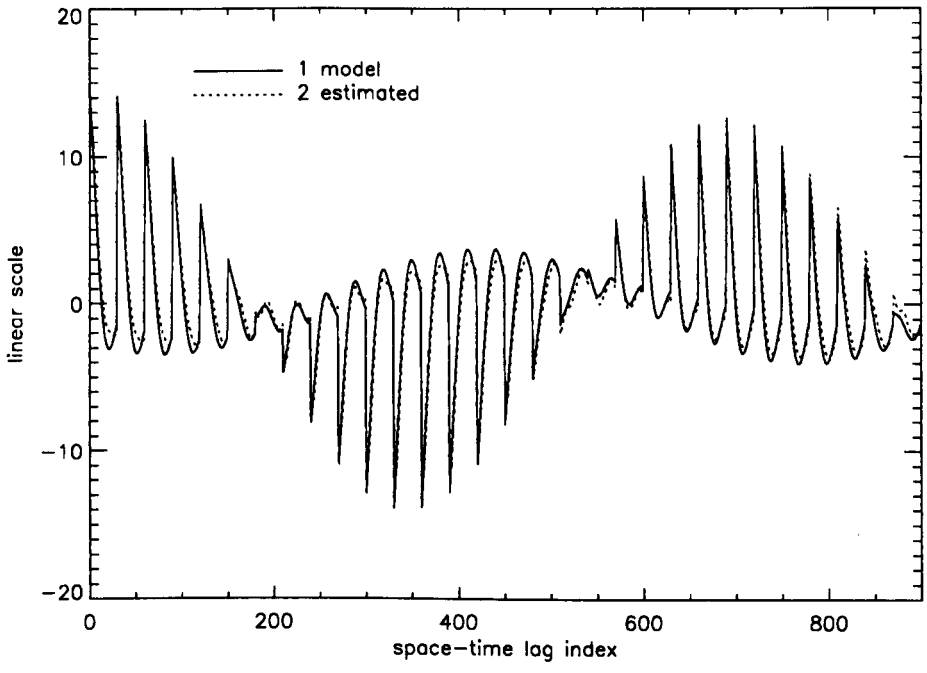

Figure 4.3: Real component of the space-time ACS predicted by the model compared with the real component of the space-time ACS estimated from experimental data.

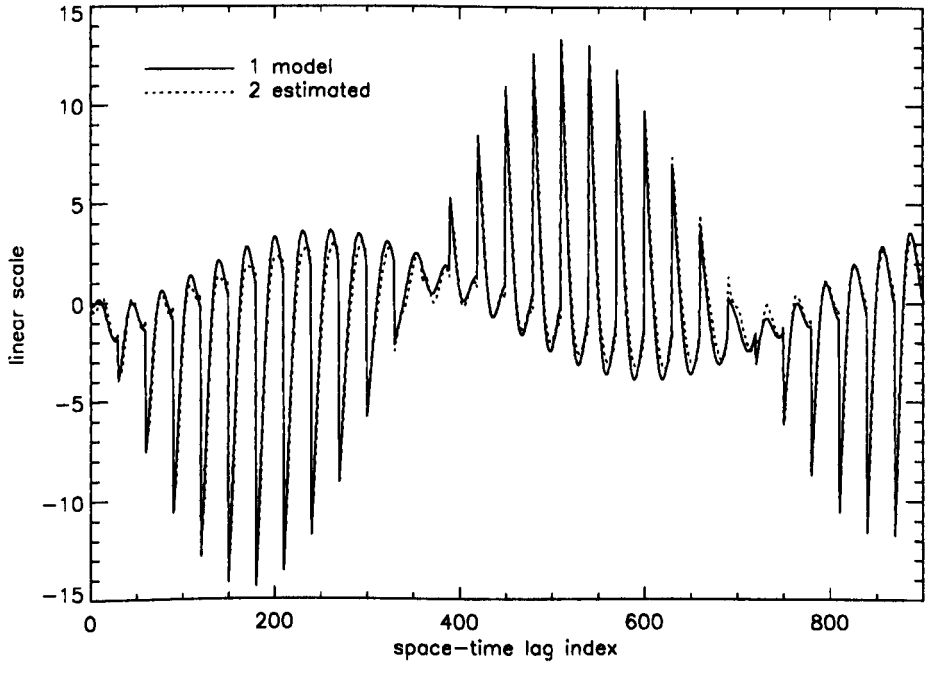

Figure 4.4: Imaginary component of the space-time ACS predicted by the model compared with the imaginary component of the space-time ACS estimated from experimental data.

4.4.2 MF-MUSIC

In order to generate MF-MUSIC spectra it is necessary to specify the spatial dimension P_s and temporal dimension P_t which determine the size of the data matrix $\mathbf{D}$ in Eqn.(4.17). As for the MUSIC algorithm, large values of P_s and P_t increase (in theory) the ability of the estimator to resolve closely spaced modes. However, in practice this results in fewer "snapshots" which in turn leads to increased variance of the parameter estimates. In this section, the dimensions $P_s = P_t = 6$ were chosen to represent a compromise between resolution and variance of the estimator.

Figures 4.5 and 4.6 show the MF-MUSIC spectra $p(\phi)$ plotted in the Angle-Doppler $(\theta, \Delta f)$ domain according to Eqn.(4.24) with parameter vectors $\phi = [\alpha(\Delta t), \beta(\Delta d), \theta, \Delta f]^T$ that have dampening terms $[\alpha(\Delta t), \beta(\Delta d)]$ set to the values estimated for modes one and two respectively in Table 4.1. The coordinates of the peaks in both spectra are the same and closely match the the mean Doppler frequency and angle-of-arrival of the two modes estimated using the least squares technique. On the other hand, the amplitude of each peaks is dependent on values of the damping factors $[\alpha(\Delta t), \beta(\Delta d)]$ set in the parameter vector ϕ as the manifold is partly determined by these terms.

Note that when the dampening factors take the values corresponding to the first mode (i.e., by setting $[\alpha, \beta] = [0.998, 0.920]$ in Figure 4.5) the amplitude of the peak occurring at the angle-Doppler coordinates of this mode is relatively higher (40.5 dB) than that of the other mode (33.1 dB) which is not as well matched to the resulting "steering" vectors $\mathbf{v}(\phi)$ defined in section 4.3.2. When the manifold is focussed in the second mode (i.e., by setting $[\alpha, \beta] = [0.997, 0.963]$ in Figure 4.5) the amplitude of the peak occurring at the angle-Doppler coordinates of this mode increases from 33.1 dB to 38.5 dB while that of the first mode drops from 40.5 dB to 31.3 dB. The substantial changes in the peak amplitudes with respect to the choice of dampening coefficients is an additional indication that these coefficients have been accurately estimated.

An alternative way to evaluate the MF-MUSIC spectrum is to keep the mean Doppler shift and angle parameters $[\Delta f, \theta]$ constant and to evaluate $p(\phi)$ over a manifold in that changes as a function of the Doppler and angular spread parameters $[\alpha, \beta]$. Figures 4.7 and 4.8 illustrate the spectra resulting in the dampening coefficient domain when $[\Delta f, \theta]$ is set to [0.46, 22.2] and [0.39, 21.7] which are the values estimated for modes one and two respectively in Table 4.1.

The physical interpretation is that such spectra attempts to resolve modes which have similar mean Doppler shift and cone angle-of-arrival but are reflected from distinct ionospheric regions that impose different levels of angular and Doppler spread on the modes. This situation may occur in practice due to the presence of altitude-dependent ionospheric tilts and the elevation-azimuth ambiguity associated with the use of linear arrays. In this case the two sporadic-E modes have sufficiently different Doppler shifts and angles-of-arrival so only a single peak is observed in each of the spectra plotted in

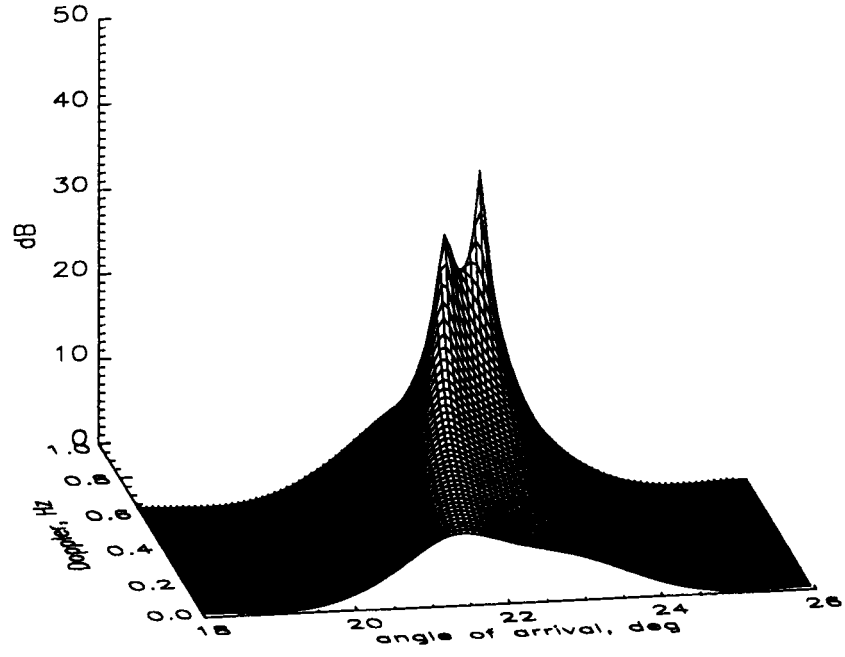

Figure 4.5: MF-MUSIC spectrum evaluated over the angle-Doppler domain for $[\alpha, \beta] = [0.998, 0.920]$ (i.e., dampening parameters matched to $m = 1$). The larger peak (40.5 dB) has coordinates $[\Delta f, \theta] = [0.46, 22.2]$ while the smaller peak (33.1 dB) has coordinates $[\Delta f, \theta] = [0.39, 21.7]$.

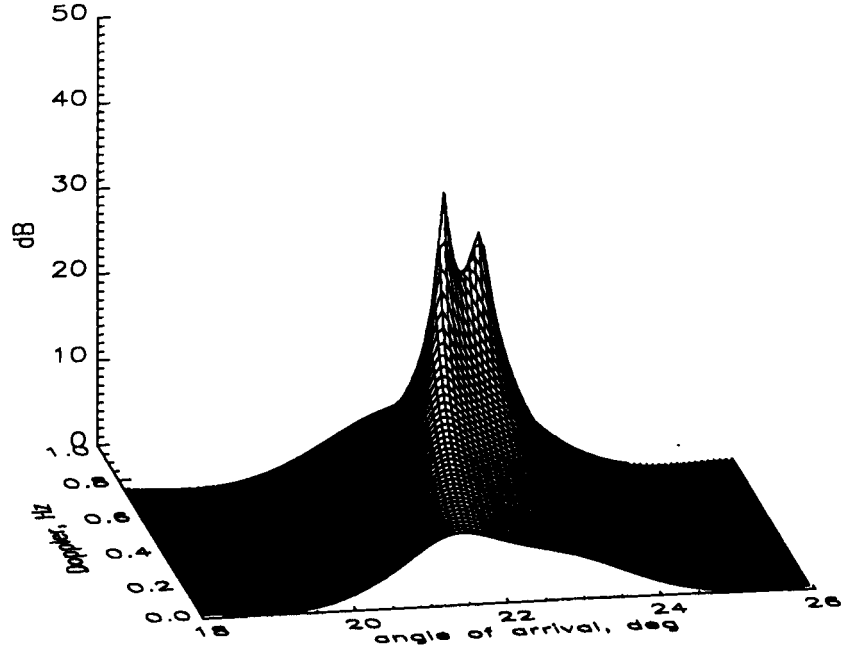

Figure 4.6: MF-MUSIC spectrum evaluated over the angle-Doppler domain for $[\alpha, \beta] = [0.998, 0.920]$ (i.e., dampening parameters matched to $m = 2$). The coordinates of both peaks are the same as those quoted for Figure 4.5 but the amplitudes of the peaks have changed to 31.3 dB and 38.5 dB respectively.

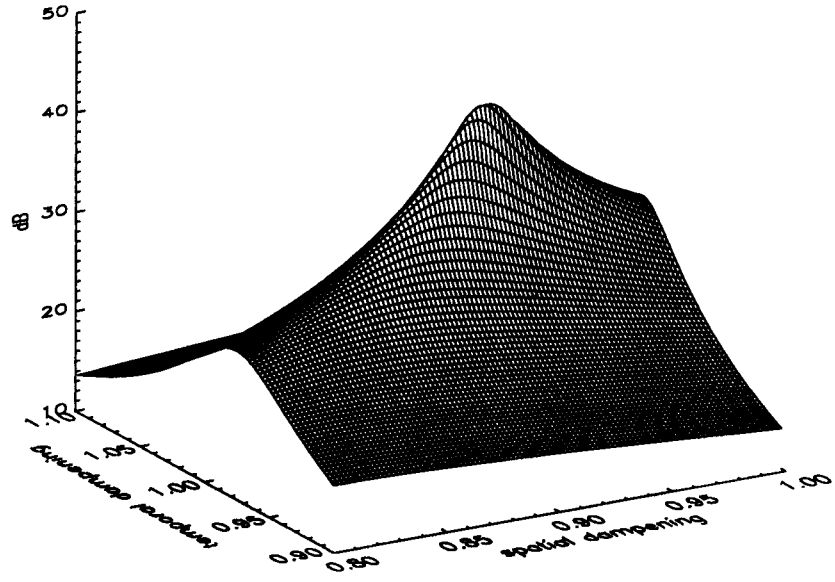

Figure 4.7: MF-MUSIC spectrum evaluated for different space-time dampening factors at angle-Doppler coordinates $[\Delta f, \theta] = [0.46, 22.2]$. The peak (43.3 dB) occurs at $[\alpha, \beta] = [0.996, 0.922]$.

Figures 4.7 and 4.8.

The location of the peak in Figures 4.7 and 4.8 are quoted in the captions and closely match those estimated by the least squares method for each mode in Table 4.1. This indicates that both methods may be used to estimate the distributed signal model parameters from the sample ACS, the closeness of the estimates in angle-Doppler and dampening coefficient domains reflects the robustness of these techniques to modelling errors, estimation uncertainty and additive noise in this experiment.

4.5 Chapter summary

A space-time mathematical model was described in this chapter to parametrically describe the statistical characteristics of ionospherically propagated HF signals received by antenna arrays. The rational or pole-zero framework adopted by this model permits distributed signals to be represent by a wide variety of power density functions in both the angular and Doppler dimensions. It also enables statistical realisations of the received multi-sensor random data processes to be generated with relative ease on a digital computer. Although the model was originally intended for the HF environment, it is envisaged that such a model may be useful in representing distributed signals which arise in other practical applications.

When the array data consists of a superposition of M statistically independent modes with Lorentzian shaped angular and Doppler power densities the composite random pro-

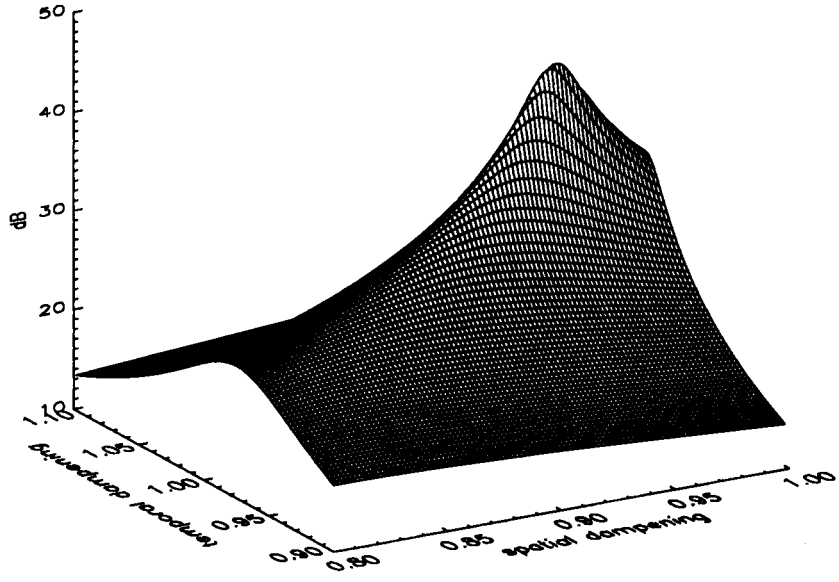

Figure 4.8: MF-MUSIC spectrum evaluated for different space-time dampening factors at angle-Doppler coordinates $[\Delta f, \theta] = [0.39, 21.7]$. The peak (45.3 dB) occurs at $[\alpha, \beta] = [0.998, 0.952]$.

cess can be represented in a spectral sense by an ARMA$(M, M-1)$ model. This chapter proposed a novel closed-form parameter estimation technique for such a model which jointly estimates the parameter pairs (mean and spread parameter of the power density function) for each mode which provides the best least squares fit to the sample space-time ACS. This computationally attractive technique enables the Doppler and angular occupancy of different ionospheric channels to be quantified from the received array data and is valuable for the purpose of real-time frequency management or passive channel evaluation (i.e., optimising the selection of carrier frequency based on the spatial and temporal bandwidth occupied by the co-channel signals).

Special experiments were conducted to validate the space-time model and the proposed two-dimensional parameter estimation techniques. The array data was collected using a cooperative transmitter beyond the line-of-sight of the array, the signal emitted allowed the time-delay, Doppler and angular characteristics of the ionospheric channel to be observed. After range processing, it was found that two ionospheric modes propagated by the sporadic-E layer could not be resolved in time-delay by the main array although their presence was certified by oblique incidence ionogram records. Assuming the presence of two modes, the proposed 2-D parameter estimation techniques were applied and yielded estimates which accurately matched the space-time sample ACS of the convoluted mode mixture. The parameter estimates were consistent with previous quantitative measurements of Doppler and angular spread of HF signals propagated over mid-latitude ionospheric paths.

CHAPTER 5

Adaptive beamforming

Data-dependent or adaptive beamforming is an alternative to data-independent or conventional beamforming which may be used to improve the signal detection and signal parameter estimation performance of a sensor array in the presence of co-channel interference. An adaptive beamformer tailors the directional response of the array to the prevailing signal and interference environment so that it can, in principle, filter out desired signals masked by strong directional interference more effectively than a conventional beamformer. In practice, the higher computational cost associated with adaptive beamforming can only be justified when a significant improvement in system performance results and this improvement is often measured in terms of output signal-to-interference plus noise ratio (SINR). In the HF environment where interference-free conditions seldom occur, relatively few studies have actually quantified the capabilities and limitations of adaptive beamformers, especially for very wide aperture antenna arrays used by OTH radar and for multipath interference reflected by the ionosphere. The purpose of this chapter is to describe adaptive beamforming algorithms suitable for OTH radar systems and to quantify the performance of these algorithms experimentally on a very wide aperture HF antenna array.

The literature review in section 5.1 summarises the key developments in the field of adaptive beamforming and points out the small number of relevant experimental investigations reported for the HF environment. Section 5.2 mathematically describes adaptive beamforming schemes suitable for OTH radar systems and establishes criteria for assessing the performance of these schemes against the conventional beamformer. More advanced adaptive beamforming algorithms designed to enhance performance in certain operational situations of interest are discussed in section 5.3. Various adaptive beamforming schemes are applied to cancel ionospherically-propagated HF interference recorded by a very wide aperture antenna array in section 5.4, the scope of this section is to experimentally evaluate the interference cancellation performance achieved in the HF environment and to assess the accuracy with which the previously validated HF channel models can predict the observed improvement over conventional beamforming.

5.1 Literature review

The background contained in section 5.1.1 qualitatively explains the concept of adaptive beamforming and describes the motivation for conducting research on the use of adaptive beamforming in narrowband very wide aperture HF arrays. The literature survey which follows in section 5.1.2 overviews the advances which have taken place in the area of adaptive beamforming from both a theoretical and practical perspective. A vast quantity of documentation exists on this subject and it is beyond the scope of the literature review to provide a comprehensive list of references, although many of them can be found in the text books by (Monzingo and Miller 1980), (Hudson 1981) and (Compton 1988a) and the tutorial papers by (Van Veen and Buckley 1988) and (Steinhardt and Van Veen 1989). The specific research addressed by this chapter is summarised in section 5.1.3 and related to previous work in the field.

5.1.1 Background

An adaptive beamformer is a processor of multi-channel data that forms a scalar output time series by weighting and summing the sensor outputs. The task of the processor is to isolate and recover a desired signal from a superposition of unwanted signals or interferers which occupy the same spectral band but originate from sources that are spatially separate. In essence, the signal processing problem is to find the optimal data-dependent set of weights, often referred the *array weight vector*, which maximises the output SINR. When the noise-field is spatially white and uncorrelated with the desired signal the optimal weight vector coincides with the conventional beamformer, but in practice, the high degree of user congestion in the HF band frequently gives rise to highly directional noise-fields. In such circumstances the conventional beamformer is sub-optimal and may lead to significant degradations in output SINR with respect to that attained by the optimum weight vector. For this reason, as well as the growing availability of high-speed computational resources, the field of adaptive array signal processing is presently in a state of intense research.

Most of the research in this area has been devoted to the theoretical development of different adaptive beamforming algorithms and the evaluation of performance by either analytical methods or by computer simulation. Each invented algorithm is shown to have certain desirable advantages over previously proposed methods, whether it be increased resolution, greater robustness to signal and interference model mismatches, lower computational complexity, faster convergence rate or mathematical tractability. In the large majority of works such improvements have been claimed solely on the basis of theoretical analysis and/or computer simulation, where to a large extent, the characteristics of the signal environment and the properties of the hypothesised sensor array are controlled by making certain assumptions. Although these studies provide valuable information for dis-

cerning between the potential usefulness of different adaptive beamformers in a particular practical application, the actual performance improvements should be interpreted with caution as they may not be typical of those encountered in practice.

In many simulation studies the desired signal and interference(s) received by a narrowband ULA are assumed to have a plane wave spatial structure with a fixed angle of arrival over the observation interval. In chapters 2 and 3 it was demonstrated that the spatial structure of HF signals reflected by the ionosphere is generally non-planar and time-varying over time scales of interest in OTH radar. Apart from the violation of the fixed plane wave model assumption, it is noted that experimental sensor arrays are subject to operational constraints which influence adaptive beamformer design and inevitably contain instrumental imperfections which may also contribute to differences between actual adaptive beamformer performance and that predicted by theory or simulation.

A significant number of non-experimental investigations have analysed the effect of practical issues, such as multipath propagation, finite sample sizes and receiver mismatch on adaptive beamformer performance. Typically, such investigations evaluate and compare the advantages of different approaches for a specific practical issue or at best a subset of the physical, operational and instrumental factors which can limit adaptive beamformer performance in a real system. Although such investigations provide useful quantitative information, the results may not reflect the actual improvements in output SINR gained by adaptive beamforming over conventional beamforming on a very wide aperture HF antenna array. A more direct method of quantifying the output SINR improvement involves processing experimental data acquired by these systems.

There is currently a paucity of *experimental results* published in the open literature to indicate the interference cancellation performance of modern adaptive beamforming algorithms in very wide aperture HF antenna arrays. Moreover, insufficient attention has been paid to the effect of time-varying spatial distortions imposed on interference signals by the ionosphere on the quality of interference cancellation achieved by these algorithms. This chapter experimentally quantifies the output SINR improvement gained by various adaptive beamforming schemes relative to the classical beamformer for different CIT lengths and beam steer directions. In addition, the previously validated space-time HF channel model is revisited in order to determine the accuracy with which it can predict the experimentally observed relative improvement in output SINR.

5.1.2 Studies on adaptive beamforming

The reason for expecting the performance of adaptive beamformers to exceed that of conventional beamformers may be described in terms of the *array beampattern* which is defined as the magnitude of the spatial transfer function presented to a far-field source by a weighted sum of the sensor outputs. A plane wavefront incident on the array from a far-field source gives rise to a spatial frequency at the sensor outputs which is a function of

the direction-of-arrival and the sensor spacing in wavelengths. Conventional beamformers have beampatterns which are independent of data received from the sources, for a *narrowband* ULA the simplest beampattern results when the sensor outputs are weighted by the coefficients of the discrete Fourier transform (DFT). In this case the array beampattern is electronically steered by matching the set of DFT coefficients to the spatial frequency of a plane wave incident from the direction of interest.

The conventional DFT beamformer is optimum in terms of output SNR when the noise-field is spatially white. In many practical applications including OTH radar, the noise-field is generally not spatially white as the background noise tends to possess some degree of anisotropicy and directional interference from other users is often present. The sub-optimality of the DFT-based beamformer is most noticeable when powerful interference leaks through the sidelobes of the conventional beampattern and contaminates the beam estimate. Spectral leakage of interference through the beampattern sidelobes has the potential to mask a weak signal incident from the steer direction and hence degrade target detection performance.

The use of window functions to taper or shade the sensor outputs prior to DFT beamforming lowers the sidelobes of the beampattern at the expense of increasing the main lobe width and reducing the main lobe maxima. A wide selection of window functions may be used, see (Harris 1978), the specific choice depends on the tradeoff between sidelobe level and main lobe width which is considered to yield the best signal detection performance under the expected interference and noise conditions. The shaded DFT beamformer is generally preferred over the unshaded version because it is more immune to interference in the sidelobe region and the wider main lobe is more robust to slight errors between the steer direction and the DOA of the desired signal. The price often paid for the computational advantages of conventional beamforming is the sub-optimality in output SINR, when powerful and persistent interference is present the sub-optimality in output SINR can reach intolerable levels and cause system outage.

In such situations, adaptive beamforming can be used to remove interference more effectively than conventional beamforming while simultaneously allowing for the transparent reception of desired signals. In simple terms, adaptive beamformers improve the output SINR by steering beampattern nulls in the direction(s) of strong interference while maintaining the unity gain response of the beampattern in the look direction. The weight vector producing the beampattern which optimises the output SINR is usually synthesised from the information contained in the interference-plus-noise spatial covariance matrix. Before proceeding to describe some commonly used methods for calculating the optimal weight vector, it is noted that use of the spatial covariance matrix for representing the second order statistics of the interference-plus-noise data carries with it the assumption of wide-sense spatial stationarity. Some of the references to be discussed also assume that the array data is Gaussian distributed and hence fully characterised by the second order statistics contained in the spatial covariance matrix.

The multiple sidelobe canceller (MSC) described by (Applebaum 1976) was one of the earliest adaptive array systems. In this system, the array is usually composed of one highly directional sensor, referred to as the *main* channel, and a set of omni-directional sensors referred to as the *auxiliary* channels. The main channel is pointed in the direction of the desired signal and receives the signal as well as uncorrelated interference through the sensor sidelobes. The auxiliary channels are assumed to receive the interference only. The aim of the MSC is to cancel the interference in the main channel by weighting the auxiliary channel outputs and adding them to the main channel. The weight vector which maximises the SINR at the MSC output is a function of the inverse of the interference-plus-noise spatial covariance matrix (Applebaum 1976). In practice it is often not possible to completely isolate the desired signal from the auxiliary channels and if the desired signal is present in these channels it may be partially cancelled from the MSC output causing serious performance degradations. The assumption of no signal in the auxiliary channels correlated with the desired signal in the main channel may be violated in OTH radar applications, and moreover, the interference may fade or be absent (i.e., switched off) from time to time which potentially leaves the MSC with spare adaptive degrees of freedom that may inadvertently be used to cancel the signal of interest.

A popular adaptive beamforming algorithm which avoids this limitation of the MSC is known as the minimum variance distortionless response (MVDR) technique (Capon 1969) in which all of the array channels are adaptively weighted. The MVDR beamformer calculates the optimal weight vector which minimises the output power subject to a linear constraint which ensures that signals incident from the direction of interest are passed with unity gain. A generalisation of the MVDR beamformer which incorporates additional linear constraints is known as the linearly constrained minimum variance (LCMV) beamformer (Frost 1972). Additional linear constraints can, for example, be applied to steer nulls in directions where interferences are known to be present apriori, or to flatten the shape of the main lobe which increases robustness to slight mismatches between the theoretically expected steering vector and the received spatial structure of the desired signal. An analytic solution for the weight vector which optimises the output SINR exists for both the MVDR and LCMV approaches in terms of the inverse of the interference-plus-noise spatial covariance matrix and the imposed linear constraints. The LCMV approach is versatile in the sense that it offers a designer extensive control over the adapted beampattern, from this point of view this generalised approach represents an attractive foundation for the development of operational OTH radar routines.

The LCMV approach may be generalised further to the case of space-time adaptive processing (STAP) which may be used in both broadband and narrowband arrays. In narrowband arrays, a tap delay line may be inserted at the output of every channel to mitigate correlated multipath interference as well as to perform joint angle-Doppler processing of the data. STAP processors are expected to provide exceptional performance in theory, but in practice the increased dimensionality of STAP processors brings with it

two significant limitations. Firstly, the computational complexity increases with the cube of the weight vector dimension (in the worst case) which can quickly become prohibitive for STAP in real-time applications. Secondly, and perhaps more importantly, the space-time covariance matrix of the data required for calculating the optimum STAP weight vector is not usually known apriori and must be estimated from the available data. If the number of data samples with homogeneous space-time second order statistics is limited by either instrumental or physical factors then the optimum weight vector cannot be estimated accurately and processor performance may become very poor. For the above-mentioned reasons, the number of adaptive degrees of freedom in the processor should be minimised and limited to the amount which is required to effectively cancel the interference.

Once it is decided to use the LCMV adaptive beamforming algorithm, two fundamental issues must be addressed in order to fully realise the benefits of either spatial or space-time adaptive processing in a practical system. The first issue is the allocation of adaptive degrees of freedom. If the dimensionality of the adaptive weight vector is too small the interference cannot be rejected to the thermal noise-floor even with perfect knowledge of the data second order statistics. On the other hand, if it is too high the amount of available data may not be sufficient to estimate the weight vector accurately and this also leads to poor performance. Methods of optimal allocation of adaptive degrees of freedom have been suggested by (Steinhardt and Van Veen 1989). An alternative way to proceed is to select the adaptive weight vector dimensionality such that the losses arising due to finite sample effects are maintained at some reasonable level irrespective of the interference-plus-noise environment. A simple rule of thumb to ensure less than 3 dB average losses in output SINR was derived for complex Gaussian distributed data by (Reed et al. 1974), it states that the weight vector dimension needs to be less than half the number of independent interference-plus-noise snapshots available for estimating the covariance matrix.

The second issue is the choice of adaptive algorithm to calculate the optimum weight vector in cases when the statistically expected covariance matrix is unknown. The least mean square (LMS) algorithm developed by (Widrow, Mantey, Griffiths and Goode 1967) is a well-known iterative technique which does not require matrix inversion but may require a relatively long time or large amount of data to converge when powerful interference is present. Slow convergence can be a major disadvantage when the characteristics of the interference-plus-noise field change rapidly enough to preclude the LMS algorithm from reaching the optimal weight vector solution for any segment of data. The sample matrix inverse (SMI) technique proposed by (Reed et al. 1974) is based on the direct substitution of the data sample spatial covariance matrix for the true covariance matrix in the analytical MVDR or LCMV expressions for the optimum weight vector. This technique has a rapid convergence rate compared with the LMS algorithm and this advantage is often significant enough to outweigh the relatively higher computational cost incurred due to the matrix inversion.

It can be shown that the LCMV weight vector estimated by the SMI technique coincides with the maximum likelihood (ML) estimate providing the interference-plus-noise snapshots used to form the sample covariance matrix over a particular data segment are from a stationary multi-variate Gaussian distributed random process. When the desired signal is present in the training data the weight vector estimated according to the SMI technique no longer coincides with the (ML) estimate which then becomes rather complex to evaluate (Steinhardt and Van Veen 1989). Consequently, it is often sought to estimate the adaptive beamforming weight vector using data snapshots which are free of the desired signal, if the desired signal is present more data is generally required to yield the the same output SINR performance.

The effect of HF signal spatial distortions on the performance of a very wide aperture array was quantified by (Sweeney 1970) for applications where the signal is considered a *signal of interest.* However, there is an important distinction between the effect of spatial distortions on the *reception* performance and the *rejection* performance of a HF array. In the former case, the effect of spatial distortions imposed by the ionosphere on *desired* signals is observed in the main lobe of the beampattern whereas in the latter case the spatial distortions imposed on *interference* signals are observed close to the relatively steep nulls of an adaptive beampattern where the directional response of the array is much more sensitive to variations in spatial structure.

Another aspect worth noting is that in OTH radar applications the desired signal and interference typically propagate via different ionospheric paths which may have quite different characteristics. While the operating frequency is usually chosen to ensure a stable ionospheric environment for the desired signal, the RFI sources are arbitrarily located with respect to the surveillance region and may be propagated by highly perturbed ionospheric layers. In these circumstances, the temporal variability in the spatial characteristics of interference signals may be substantially more pronounced than those exhibited by HF signals propagated over a relatively quiet mid-latitude path. Hence, analysis of adaptive beamformer performance based on a fixed plane wavefront interference model are likely to be unreliable indicators of practical performance, and due to the unique peculiarities of the HF environment, the remaining portion of this review focuses on the application of adaptive beamformers in HF arrays.

An on-line adaptive beamforming capability for HF backscatter radar was developed by (Washburn and Sweeney 1976) using a 2.5 km long ULA composed of eight 32-element sub-arrays each connected to a digital receiver. In this experiment, the desired signals were aircraft target's and a fixed ground-based repeater simulating a moving target. The unwanted signals were interferences from other users in the HF band as well as a signals from a separate ground based radar repeater. The performance of a recursive time-domain adaptive beamforming technique which converges towards the optimum MVDR solution was compared against a conventional beamformer with a -25 dB Dolph taper. The authors stated that the rejection of unwanted signals with the adaptive beamformer

was variable but side-by-side comparisons showed that adaptive beamforming can reject off-azimuth signals up to 20 dB better than the conventional beamformer. However, important quantities such as the mean improvement in output SINR and the distribution of its variability over different data sets, CIT lengths and beam steer directions were not reported in (Washburn and Sweeney 1976).

Separate training samples containing interference only could not be obtained in this study so the adaptive beamformer was applied to data which additionally contained backscattered clutter and the desired signals. It was found that slight mismatches between the target's spatial structure and the plane wavefront expected from the beam steer direction caused the adaptive beamformer to try and cancel the signal of interest. Although losses in desired signal gain were also observed for the conventional beamformer and partly attributed to beam pointing errors, the losses were more significant in the adaptive case (especially for high SNR targets) as slight mismatches cause the adaptive beamformer to view the desired signal as an interferer. One possible solution offered by (Washburn and Sweeney 1976) to reduce the effect of this problem is to steer a higher number of more closely spaced beams in order to increase the chances of the target signal being well matched to one of them.

The adaptive beamformer was found to reject substantial amounts of clutter, but perhaps of greater importance, was the observation that the adaptive beamformer cancelled off-azimuth interference more effectively when a temporal filter was applied to remove the clutter prior to adaptation. This is not surprising since the rejection of clutter consumes spatial degrees of freedom which are are better spent on the interference as in most cases standard Doppler processing is sufficient to separate the clutter from the target echoes. After filtering out the clutter, the weight adaptations were performed in the *time domain* in order to track temporal variations in the interference spatial characteristics. The resulting time-sequence of adaptive weight vectors was stored and then used to re-process the original (i.e., unfiltered) data containing clutter and target signals. It was found that the subsequent application of the time-varying beamforming weights to the original data resulted in significant Doppler broadening of the clutter and targets on some occasions. This broadening is a potentially serious consequence of time-domain adaptation as it can impair the detection of targets located near the clutter ridge or prevent the resolution of targets closely spaced in Doppler frequency.

To prevent this broadening, Washburn and Sweeney (1976) decided to form the adaptive beam using a fixed weight vector which resulted at the end of the 2.1 second coherent integration time. Although this eliminated the spreading of clutter and target signals after Doppler processing, it was noted that disallowing the weights to vary over the CIT lead to poorer level of interference suppression. This problem was also cited by (Games, Townes and Williams 1991) where it was concluded that variations in the HF signal environment over time intervals in the order of seconds can significantly impact on the rejection performance of adaptive beamforming algorithms.

Another investigation, conducted with the same experimental facility at nearly the same time by (Griffiths 1976), actually plotted the time variation of weight values adapted over the radar CIT. The author found that the time scale of the variation was in the order of 1 second or less in the HF environment, and that the ability of the adaptive algorithm to track such variations led to interference and noise levels as much as 20 dB lower than that of conventional beamforming methods. However, the time domain weight fluctuations required to achieve this level of interference suppression is associated with a time-varying beampattern that induces a temporal modulation on any signal which is passed by any unconstrained point on the beampattern. The backscattered clutter is spatially broadband and is received over the entire beampattern. Hence, one of the main problems in the HF environment is to solve the paradox of allowing the weights to fluctuate over the CIT in order to effectively reject HF interference but to prevent these fluctuations from broadening the Doppler spectrum of clutter and other signals which are passed through the unconstrained portions of the time-varying adaptive beampatterns.

The first studies which directly addressed this problem were the ones carried out by (Abramovich 1993) and (Abramovich, Gorokhov, Mikhaylyuvov and Malyavin 1994). The authors adopted a scalar-type auto-regressive model for the clutter process and incorporated so-called *stochastic constraints* on the time-varying adaptive weight vectors in order to preserve the Doppler spectrum properties of the clutter and other backscattered signals at the beamformer output. This approach, to be described in mathematical detail later, is based on the SMI/LCMV adaptive beamformer and has been extended to the case of space-time adaptive processing in (Anderson, Abramovich and Fabrizio 1997) and (Abramovich, Spencer and Anderson 1998). Alternative methods based on the use of soft constraints (or penalty functions) have been proposed by (Van Veen 1991) and (Hughes and McWhirter 1996) to control the departure of the adaptive beampattern from a quiescent tapered array or conventional beampattern that has proven advantages in the absence of strong interference. The coefficient which controls the cost or penalty associated with a given departure is selected depending on the stringency required for quasi-fixed beampatterns that do not greatly distort the clutter Doppler spectrum and the leniency required for time-varying beampatterns that effectively reject interferers with changing spatial characteristics. A technique for the data-dependent selection of this coefficient was proposed by (Turley 1999) and makes use of the eigen-values of the interference-plus-noise spatial covariance matrix.

To determine when time-varying weight solutions are necessary for interference rejection in the HF environment, (Fabrizio, Abramovich, Gray, Anderson and Turley 1998) quantified the improvement in output SINR achieved by the SMI/MVDR adaptive beamforming algorithm as a function of time-interval for which the adaptive beamformer was held fixed. Experimental results were derived on a 1.4 km ULA containing 16 digital receivers for two different ionospherically-propagated interference sources, one source was known to propagate over a one-hop mid-latitude path while the other involved multi-hop

propagation via the typically disturbed equatorial ionosphere. At small integration times (less than 0.1 seconds) the performance of the adaptive beamformer was being limited by finite sample effects (i.e., estimation errors) to roughly 3-4 dB below the highest mean relative SINR improvement (of approximately 22-24 dB) achieved for both sources at a CIT of about 0.2 seconds. Increasing the CIT for the source propagated via a single-hop quiet mid-latitude ionosphere hardly effected rejection performance. On the other hand, when identical processing was applied to the second source which propagated via the equatorial ionosphere, it was found that degradations in the order of 4-5 dB relative to the highest SINR improvement occurred within a matter of 3-4 seconds.

5.1.3 Significance of research relative to previous work

Existing theoretical analysis and computer simulation studies of adaptive beamformer performance provide valuable information and are useful in guiding the user to the most promising adaptive beamforming methodology for the application at hand. The unique spatial and temporal characteristics of multipath HF signals reflected by the ionosphere requires that the performance of promising algorithms be evaluated experimentally so as to quantify the actual improvements in output SNR which can be obtained in practice over conventional processing. From the literature review, it is evident that there is very limited information available which quantifies the relative improvement in output SINR which can be realised on a very wide aperture HF antenna array. This information would be valuable for the purpose of justifying the use of adaptive beamformers in operational HF systems such as OTH radar.

The first aim of this chapter is to describe suitable adaptive beamforming schemes for OTH radar to quantify the benefits in interference rejection which these schemes offer relative to conventional spatial processing. The second aim is to determine the accuracy with which the previously validated models of the HF channel can predict the experimental performance of these adaptive beamformers. In severe interference conditions, intra-CIT variations of the adaptive beampattern may be necessary to yield satisfactory output SINR levels and the previously mentioned side-effects of such processing (i.e., backscattered clutter smearing) must be addressed. The final aim of this chapter is to illustrate the performance of the stochastic constraints approach using real interference data superimposed with simulated clutter and target signals.

5.2 Interference rejection analysis

The purpose of this section is to describe the procedure used to quantify the signal-to-interference and noise ratio (SINR) improvement which is gained by adaptive beamforming relative to conventional beamforming in the HF environment. In this analysis the SINR improvement in the beam estimates is determined by comparing the level of *interference*

rejection achieved by the adaptive and conventional beamformers with both beamformers having the same (unity) gain response to ideal target signals. The interference cancellation performance is studied by operating the radar system in passive mode (i.e., with the transmitter switched off) so that the antenna array samples co-channel HF interference and noise only. This passive mode analysis indicates the maximum potential for SINR improvement in OTH radar systems as the presence of clutter and non-ideal target signals is likely to reduce the performance of an adaptive beamformer more than that of a conventional beamformer. Section 5.2.1 describes the basic theoretical aspects of the adaptive beamforming algorithm used for HF interference rejection in this analysis and the reasons for its selection. The practical application of this adaptive beamforming algorithm to the recorded ionospherically-propagated HF interference data is discussed in section 5.2.2 which also defines the output SINR improvement factor used to quantify the potential benefits of adaptive beamforming.

5.2.1 Adaptive beamforming algorithms

The criteria most often used to determine the optimal adaptive beamforming weight vector $\mathbf{w}_{opt}$ is that of maximising the SINR at the output of the beamformer. Let $\mathbf{x}_k(t)$ be the array snapshot vector received at the k^{th} fast-time sample in the t^{th} PRI and assume that this vector contains a desired signal component $\mathbf{s}_k(t)$ superimposed with uncorrelated interference and noise lumped into the term $\mathbf{n}_k(t)$.

$$\mathbf{x}_k(t) = \mathbf{s}_k(t) + \mathbf{n}_k(t) = g_k(t)\mathbf{s}(\theta) + \mathbf{n}_k(t) \tag{5.1}$$

In Eqn.(5.2), $g_k(t)$ is the desired signal waveform to be estimated at the output of the beamformer and $\mathbf{s}(\theta)$ is the narrowband ULA response vector associated with an ideal (plane wave) signal incident from the cone angle of interest θ. The scalar beamformed output $y_k(t)$ is given by the inner product of the beamforming weight vector $\mathbf{w}_{opt}$ and the array data snapshot vector $\mathbf{x}_k(t)$.

$$y_k(t) = \mathbf{w}_{opt}^H \mathbf{x}_k(t) = g_k(t)\mathbf{w}_{opt}^H \mathbf{s}(\theta) + \mathbf{w}_{opt}^H \mathbf{n}_k(t) \tag{5.2}$$

Based on the assumption that the interference and noise processes are uncorrelated with the desired signal and that all signals are wide-sense spatially stationary, the optimum weight vector $\mathbf{w}_{opt}$ is derived by minimising the output power $E\{|y_k(t)|^2\}$ subject to a linear constraint which ensures that the desired signal is passed with unity gain (i.e., $\mathbf{w}_{opt}^H \mathbf{s}(\theta) = 1$). Since the desired signal is uncorrelated with the interference and noise it follows from Eqn.(5.2) that an arbitrary weight vector $\mathbf{w}$ which satisfies this linear constraint will produce an output power given by,

$$E\{|y_k(t)|^2\} = \sigma_g^2 + \mathbf{w}^H E\{\mathbf{n}_k(t)\mathbf{n}_k^H(t)\}\mathbf{w} = \sigma_g^2 + \mathbf{w}^H \mathbf{R}_n \mathbf{w} \tag{5.3}$$

where $\sigma_g^2 = E\{|g_k(t)|^2\}$ is the desired signal power at the beamformer output and $\mathbf{R}_n$ represents the interference-plus-noise spatial covariance matrix. The term $\mathbf{w}^H\mathbf{R}_n\mathbf{w}$ is the residual interference and noise power which must be minimised in order to maximise the output SINR. In mathematical terms, the minimum variance distortionless response (MVDR) criterion finds the optimum weight vector $\mathbf{w}_{opt}$ as the solution to the following multi-dimensional quadratic minimisation problem.

$$\mathbf{w}_{opt} = \text{argmin } \mathbf{w}^H\mathbf{R}_n\mathbf{w} \quad \text{subject to :} \quad \mathbf{w}^H\mathbf{s}(\theta) = 1 \tag{5.4}$$

Using the method of Lagrangian multipliers it can be shown that the solution which maximises the output SINR under the above-mentioned assumptions is given by the analytical expression in Eqn.(5.5) which is sometimes referred to as the Wiener-Hopf solution.

$$\mathbf{w}_{opt} = \frac{\mathbf{R}_n^{-1}\mathbf{s}(\theta)}{\mathbf{s}^H(\theta)\mathbf{R}_n^{-1}\mathbf{s}(\theta)} \tag{5.5}$$

More than a single linear constraint (i.e., the unity gain constraint) may be required in certain applications. For example, apriori information may be available regarding the direction of intermittent interference sources which may not always be present at the time of spatial covariance matrix estimation, it is then desirable to force "anticipatory" nulls in the adaptive beampattern explicitly in these directions (Griffiths and Buckley 1987). If such an interference source is expected to have a plane wave structure and be incident from direction θ_i then the linear constraint $\mathbf{w}^H\mathbf{s}(\theta_i) = 0$ can be added to the optimisation problem in Eqn.(5.4) to ensure that such a source is always cancelled. The derivative constraint $\mathbf{w}^H\partial\mathbf{s}(\theta)/\partial\theta = 0$ is sometimes used to flatten the shape of the main lobe near the array look direction so as to increase the robustness of the adaptive beamformer to differences between the expected and received desired signal wavefronts. Such mismatches can arise due to propagation effects as well as instrumental errors which produce uncertainties in the array manifold. For M arbitrary linear constraints $\mathbf{w}^H\mathbf{c}_m = f_m$ where $m = 1, 2, .., M \leq N$, the linearly constrained minimum variance (LCMV) adaptive beamforming algorithm can be mathematically formulated as,

$$\mathbf{w}_{opt} = \text{argmin } \mathbf{w}^H\mathbf{R}_n\mathbf{w} \quad \text{subject to :} \quad \mathbf{C}^H\mathbf{w} = \mathbf{f} \tag{5.6}$$

where the $N \times M$ matrix $\mathbf{C}$ contains the M vectors $\mathbf{c}_m$ as its columns and the M-variate column vector $\mathbf{f}$ contains the f_m^*. The solution $\mathbf{w}_{opt}$ to this more general optimisation problem is expressed in closed form by Eqn.(5.7).

$$\mathbf{w}_{opt} = \mathbf{R}_n^{-1}\mathbf{C}(\mathbf{C}^H\mathbf{R}_n^{-1}\mathbf{C})^{-1}\mathbf{f} \tag{5.7}$$

In practice, the spatial covariance matrix of the interference and noise is unknown and must be estimated from the array data. A well known algorithm for estimating the

optimum weight vector $\hat{\mathbf{w}}_{opt}$ is known as the sample matrix inverse (SMI) technique where the sample covariance matrix $\hat{\mathbf{R}}_n$ is directly substituted for the statistically expected covariance matrix $\mathbf{R}_n$ in either Eqn.(5.5) or Eqn.(5.7). Although this may appear to be a somewhat ad-hoc approach, it has a number of very important advantages over the less computationally expensive estimation methods, such as the LMS algorithm for example, which iteratively converges towards the estimate $\hat{\mathbf{w}}_{opt}$ without performing matrix inversion.

The first major advantage of the SMI technique is that for a finite number of available array snapshots $\mathbf{n}_k(t)$ the SMI method converges much more rapidly to the optimum weight vector (i.e., $\hat{\mathbf{w}}_{opt} \rightarrow \mathbf{w}_{opt}$) than the LMS technique, especially when the spatial covariance matrix $\mathbf{R}_n$ is ill-conditioned or has a high eigenvalue spread due to the presence of powerful interference. Moreover, for stationary zero-mean complex Gaussian distributed interference and noise processes (i.e., $\mathbf{n}_k(t)$ distributed as $N(0, \mathbf{R}_n)$) the sample covariance matrix is the maximum likelihood (ML) estimate of the true covariance matrix and by the invariance principle $\hat{\mathbf{w}}_{opt}$ is the ML estimate of $\mathbf{w}_{opt}$. For the MVDR beamformer, it is known that $2N$ statistically independent snapshots $\mathbf{n}_k(t)$ are required to limit the average loss in output SINR to about 3 dB relative to the true optimum as a result of estimation errors. These losses are maintained irrespective of the form of the interference-plus-noise spatial covariance matrix. Perhaps less known are the results of (Cheremisin 1982) which show that by appropriate diagonal loading of the sample covariance matrix the number of independent snapshots required for 3 dB average losses in output SINR can be reduced to $2P$ where P is the number of interference sources. Another point worth noting is that the addition of linear constraints effectively removes adaptive degrees of freedom from the processor but it also reduces the number of snapshots required to achieve the same average SINR loss with respect to the optimum SINR under the given constraints.

5.2.2 Adaptive beamforming schemes

To quantify the HF interference cancellation performance for the class of adaptive beamformers described above in a meaningful way it is necessary to consider the operational constraints imposed by a real system and how they affect the manner in which the adaptive beamforming theory is applied in practice. The main point to consider for OTH radar systems is that during normal operation such systems cannot receive desired signals without simultaneously receiving clutter. The presence of desired signals and clutter in the array snapshots significantly complicates the estimation of the optimum weight vector according to the MVDR or LCMV criterion which ideally requires the best possible estimate of the interference-plus-noise spatial covariance matrix $\mathbf{R}_n$. A well known approach to circumvent this problem in active radar systems is to turn the transmitters off for a brief period prior to each coherent integration time (CIT) and to estimate the matrix $\mathbf{R}_n$ from interference-plus-noise snapshots received over this interval. The "optimal" weight vector

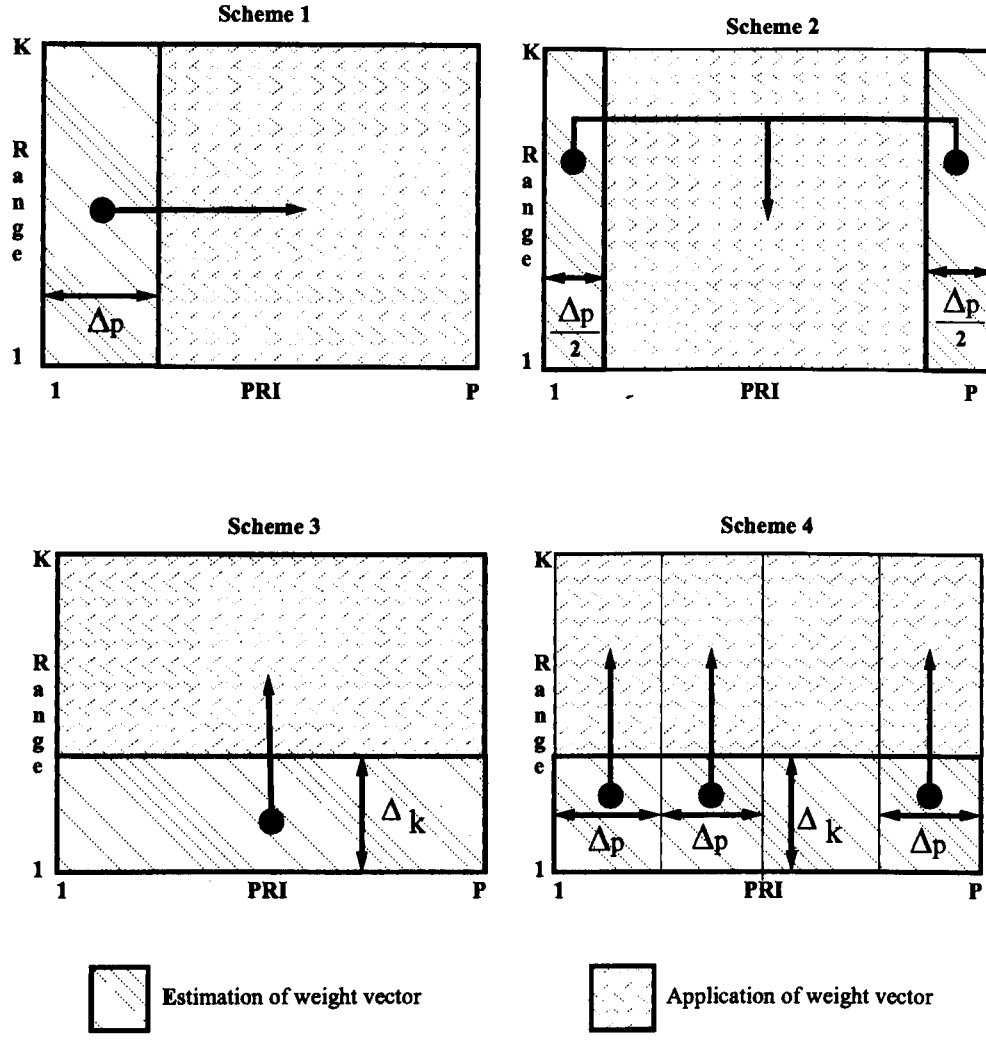

Figure 5.1: Diagrammatic illustration of the four adaptive beamforming schemes. Each diagram shows the dwell regions in which the recorded array snapshots are used for estimation of the adaptive weight vector and those where this weight vector is applied to beamform the data.

may then be formed using the SMI technique and frozen to process the entire CIT of data which immediately follows the interference-plus-noise sample train. The same procedure is invoked once again to process the next CIT and so on. Updating the weight vector from one CIT to another is advisable, especially in the HF environment, to compensate for temporal fluctuations in the spatial properties of the external interference-plus-noise field.

The above-mentioned methodology is referred to as adaptive beamforming scheme 1, this scheme is illustrated in the upper left diagram of Figure 5.1 and the MVDR implementation is now described in mathematical detail. Since the interference-plus-noise snapshot $\mathbf{n}_k(t)$ is uncorrelated with the deramping FMCW waveform at each receiver, the interference-plus-noise energy is spread over all range samples (k). Assuming the statistical properties of $\mathbf{n}_k(t)$ are invariant over the waveform PRI the snapshots received at different range cells $k = 1, 2, .., K$ may be considered as different realisations of the multi-channel interference-plus-noise process. These realisations will be statistically in-

dependent when the interference is broadband (of bandwidth larger than or equal to the radar bandwidth) and sampled at the Nyquist rate at the receiver outputs. The degree of independence between these realisations is in general dependent on the interference-plus-noise waveform characteristics and the use of range processing window functions which tend to correlate neighboring FFT outputs. In any case, the sample spatial covariance matrix $\hat{\mathbf{R}}_n$ is usually formed using all available realisations (i.e., range cells $k = 1, 2, .., K$) which are recorded during a passive mode time interval of Δ_p PRI between the end of one CIT and the commencement of another. Note that Δ_p is an integer which represents the number of PRI of *passive* mode data used to estimate the *interference-plus-noise* only sample spatial covariance matrix $\hat{\mathbf{R}}_n$ in the manner described by Eqn.(5.8). The remaining PRI in the dwell (indexed by $t = \Delta_p + 1, \Delta_p + 2, .., P$) additionally contain clutter and desired signals under normal operating conditions but for this study only passive mode data were recorded.

$$\hat{\mathbf{w}}_1 = \frac{\hat{\mathbf{R}}_n^{-1}\mathbf{s}(\theta)}{\mathbf{s}^H(\theta)\hat{\mathbf{R}}_n^{-1}\mathbf{s}(\theta)} \quad , \quad \hat{\mathbf{R}}_n = \frac{1}{K\Delta_p}\sum_{k=1}^{K}\sum_{t=1}^{\Delta_p}\mathbf{n}_k(t)\mathbf{n}_k^H(t) \tag{5.8}$$

When the number of available snapshots $K\Delta_p$ is limited, the performance of this method may be improved by diagonal loading of the covariance matrix $\tilde{\mathbf{R}}_n = \hat{\mathbf{R}}_n + \sigma^2\mathbf{I}$ and substituting $\tilde{\mathbf{R}}_n$ for $\hat{\mathbf{R}}_n$ in Eqn.(5.8). The optimal choice of σ^2 is non-trivial and data-dependent, typically low levels of loading (in the vicinity of the additive noise power) are used to improve performance when the number of samples is limited (Carlson 1988). Another modification which may improve performance is to average the covariance matrices resulting at both ends of a particular CIT since any variation in the interference-plus-noise field over the CIT will be better captured. This method is referred to as adaptive scheme 2 in Figure 5.1 and denoted by the weight vector $\hat{\mathbf{w}}_2$. The scalar beamformed outputs $y_k(t)$, $y_k^1(t)$ and $y_k^2(t)$ corresponding to the conventional beamformer and adaptive weight vectors $\hat{\mathbf{w}}_1$ and $\hat{\mathbf{w}}_2$ respectively can be derived by processing the data $\mathbf{x}_k(t)$ recorded during the CIT;

$$y_k(t) = \frac{\mathbf{s}(\theta)^H\mathbf{T}\mathbf{x}_k(t)}{\mathbf{s}(\theta)^H\mathbf{T}\mathbf{s}(\theta)} \quad , \quad y_k^1(t) = \hat{\mathbf{w}}_1^H\mathbf{x}_k(t) \quad , \quad y_k^2(t) = \hat{\mathbf{w}}_2^H\mathbf{x}_k(t) \tag{5.9}$$

where $k = 1, 2, ..K$, $t = 1, 2, .., P$ for $y_k(t)$, $t = \Delta_p + 1, \Delta_p + 2, .., P$ for $y_k^1(t)$ and $t = \Delta_p/2 + 1, \Delta_p + 2, .., P - \Delta_p/2$ for $y_k^2(t)$. The conventional beamformer may include a taper represented by the diagonal matrix $\mathbf{T}$ to reduce sidelobes, the normalisation term $\mathbf{s}(\theta)^H\mathbf{T}\mathbf{s}(\theta)$ ensures that the response to a desired signal is the same (unity) as that of the adaptive beamformers $\hat{\mathbf{w}}_1$ and $\hat{\mathbf{w}}_2$. Using the *passive mode* data $\mathbf{x}_k(t)$, the improvement in output SINR gained by adaptive beamforming relative to conventional beamforming can be estimated (for an ideal desired signal) as the interference cancellation ratio $\hat{q}_1$ or

$\hat{q}_2$ given by Eqn.(5.10).

$$\hat{q}_1 = \frac{\sum_{k=1}^{K}\sum_{t=\Delta_p+1}^{P}|y_k(t)|^2}{\sum_{k=1}^{K}\sum_{t=\Delta_p+1}^{P}|y_k^1(t)|^2} \;,\quad \hat{q}_2 = \frac{\sum_{k=1}^{K}\sum_{t=\Delta_p/2+1}^{P-\Delta_p/2}|y_k(t)|^2}{\sum_{k=1}^{K}\sum_{t=\Delta_p/2+1}^{P-\Delta_p/2}|y_k^2(t)|^2} \;, \tag{5.10}$$

An alternative approach is based on the observation that while HF interference and noise appear in all range cells, the clutter and desired signals often appear over a range extent beyond the so-called skip zone. At distances between the receiver and the skip-zone boundary the propagation of HF signals is not well supported by the ionosphere so the signal received in the skip-zone range cells (say $k = 1, 2, .., \Delta_k < K$) is dominated by the interference component. This natural phenomenon can be exploited to estimate the interference-plus-noise spatial covariance matrix *within the CIT* rather than at its extremities. This alternative scheme is referred to as adaptive beamforming scheme 3 in Figure 5.1 and the MVDR implementation is described by Eqn.(5.11).

$$\hat{\mathbf{w}}_3 = \frac{\hat{\mathbf{R}}_n^{-1}\mathbf{s}(\theta)}{\mathbf{s}^H(\theta)\hat{\mathbf{R}}_n^{-1}\mathbf{s}(\theta)} \;,\quad \hat{\mathbf{R}}_n = \frac{1}{P\Delta_k}\sum_{k=1}^{\Delta_k}\sum_{t=1}^{P}\mathbf{n}_k(t)\mathbf{n}_k^H(t) \tag{5.11}$$

As described by Eqn.(5.12), the adaptive and conventional beamformed outputs $y_k^3(t)$ and $y_k(t)$ are calculated by processing the CIT data $\mathbf{x}_k(t)$ recorded in the range cells beyond the skip-zone since these cells potentially contain desired signals. The estimate of SINR improvement factor for this scheme is denoted by $\hat{q}_3$ and given by Eqn.(5.12). The advantage of this scheme is that the adaptive beamformer is tuned with an estimate of the spatial properties of the interference-plus-noise integrated *within the CIT* of data to be processed. However, the range coverage is reduced due to the need for skip-zone cells and it is noted that at low frequencies where the ionosphere is more likely to permit vertical incidence propagation these cells may not be available at all. The adaptive beamformer output $y_k^3(t)$ for this scheme is given by Eqn.(5.12) along with the associated improvement factor $\hat{q}_3$.

$$y_k^3(t) = \hat{\mathbf{w}}_3^H\mathbf{x}_k(t) \;,\quad \hat{q}_3 = \frac{\sum_{k=\Delta_k+1}^{K}\sum_{t=1}^{P}|y_k(t)|^2}{\sum_{k=\Delta_k+1}^{K}\sum_{t=1}^{P}|y_k^3(t)|^2} \left\{ \begin{array}{rcl} k & = & \Delta_k+1, \Delta_k+2, ..K \\ t & = & 1, 2, .., P \end{array} \right. \tag{5.12}$$

The interference rejection analysis is concerned with experimentally evaluating the quantities $\hat{q}_{1,2,3}$ to gain a numerical appreciation for the potential SINR improvement offered by the different adaptive beamforming schemes. Of particular interest is to quantify the distribution describing the variation of these quantities with respect to the CIT length in seconds, the mean and deciles of these distributions will be illustrated in the experimental results section.

5.3 Advanced adaptive weight control

It was shown in chapter 2 that the spatial structure of HF signals reflected by the ionosphere varies significantly over time scales much smaller than the duration of typical OTH radar CIT. Moreover, these variations in wavefront shape are highly correlated from one PRI to another and the wavefronts are seen to evolve in a smooth fashion when observed at a temporal resolution of less than one tenth of a second. Due to this high correlation, a HF signal reflected by a particular ionospheric region (i.e., a single mode) has almost *unit spatial rank* or is characterised by a fixed spatial structure when view over the quasi-instantaneous PRI employed in OTH radar applications. Note that even though the quasi-instantaneous spatial covariance matrix is of unit rank in this case, for a stationary angularly spread signal mode, the *statistically expected* spatial covariance matrix has full rank. It is then evident that forming the interference-plus-noise sample covariance matrix over short time segments (equal to the PRI for example) is an effective means for reducing the dimension of the interference subspace. A reduction in the subspace dimension occupied by such sources increases the capacity of adaptive beamformers with a finite number of degrees of freedom to cancel interference.

This observation leads to the conclusion that re-adapting the beampattern over short time segments within the CIT allows the beamformer greater scope to reject the HF interference completely. The most difficult practical situation arises when the number of interference sources is high, the spatial properties of these sources are changing quickly, the CIT is long and the number of adaptive degrees of freedom is limited. In such situations, re-adaptation of the beampattern within the CIT reduces the consumption of adaptive degrees of freedom and may be essential for the effective removal of interference. An apparently reasonable way of re-adapting the beampattern within the CIT is to form the slow-time varying interference-plus-noise sample covariance matrix $\hat{\mathbf{R}}_n(t)$ from the skip-zone range cells in successive data frames of Δ_p PRI duration within the CIT and to calculate the fluctuating weight vector $\hat{\mathbf{w}}_4(t)$ in accordance with the well known rule.

$$\hat{\mathbf{w}}_4(t) = \frac{\hat{\mathbf{R}}_n^{-1}(t)\mathbf{s}(\theta)}{\mathbf{s}^H(\theta)\hat{\mathbf{R}}_n^{-1}(t)\mathbf{s}(\theta)}\ , \quad \hat{\mathbf{R}}_n(t) = \frac{1}{\Delta_k \Delta_p}\sum_{k=1}^{\Delta_k}\sum_{t'=t}^{t+\Delta_p-1}\mathbf{n}_k(t')\mathbf{n}_k^H(t') \tag{5.13}$$

As depicted by Figure 5.1, the slow-time varying weight vector $\hat{\mathbf{w}}_4(t)$ corresponding to adaptive scheme 4 is then used to beamform the data $\mathbf{x}_k(t)$ recorded in the range cells beyond the skip-zone $k = \Delta_k{+}1, \Delta_k{+}2, .., K$ over the current set of PRI $t, t{+}1, .., t{+}\Delta_p{-}1$. Once the entire CIT of data has been beamformed by the sequence of different adaptive weight vectors the scalar output must then be Doppler processed to separate the desired signal from the strong clutter returns.

While the interference is expected to be rejected effectively by this approach a potentially serious problem can arise from the interaction between the intra-CIT varying

adaptive beampatterns and the unrejected clutter returns. The clutter is spatially broadband and enters the beamformed output through the main lobe and sidelobes of the adaptive beampatterns which fluctuate throughout the CIT. Fluctuations in the directional response of the array impose a temporal modulation on the beamformed clutter signal that causes it to spread across the velocity search space after Doppler processing. While $(N-1)$ additional linear constraints can be applied to fix the response of the beampattern at certain points, such a method cannot protect the clutter from spreading as it is received over a continuum of points along the beampattern. Hence, the problem faced is to allow beampattern re-adaptations in order to increase interference rejection but to simultaneously control these re-adaptations in a way that preserves the temporal correlation properties of the spatially broadband clutter. An approach which addresses this problem is described in the following section.

5.3.1 Stochastic constraints algorithm

The stochastic constraints (SC) algorithm was originally developed by (Abramovich et al. 1994) for spatial-only adaptive filtering and has more recently been generalised for the case of space-time adaptive processing (STAP) in (Anderson et al. 1997) and (Abramovich et al. 1998). Only the underlying principles and essential mathematical features of the stochastic constraints algorithm are described here, the reader is referred to the above-mentioned citations for a more in-depth description of the algorithm and its operational implementation.

The SC algorithm relies on a p^{th} order scalar-type auto-regressive (AR) modelisation of the random multi-channel clutter process where the AR order $p \ll N$ and the AR parameters determine the Doppler characteristics of the received clutter process. These temporal second order statistics of the clutter process are preserved at the beamformed output by imposing p data-dependent or stochastic linear constraints on the re-adapted weight vector. These constraints are designed to control the beampattern fluctuations such that the output clutter process is statistically described by a uni-variate AR process with the same scalar parameters. To demonstrate the essential features of this algorithm, let $\mathbf{c}_k(t)$ be the clutter snapshot having temporal properties described by the following AR recursive relation.

$$\mathbf{c}_k(t) + \sum_{i=1}^{p} \alpha_i \mathbf{c}_k(t-i) = \eta_k(t) \tag{5.14}$$

In Eqn.(5.14), the α_i for $i = 1, 2, .., p$ are the scalar AR process parameters and $\eta_k(t)$ is a zero mean complex innovative white noise vector such that $E\{\eta_k(t)\eta_k^H(t-i)\} = \mathbf{R}_c(k)\delta(i)$ where $\mathbf{R}_c(k)$ is the spatial covariance matrix of the clutter at range cell k. The SC algorithm estimates a range-dependent beamforming weight vector $\hat{\mathbf{w}}_k^{(sc)}(t)$ according to Eqn.(5.7) after substitution of $\mathbf{R}_n$ with $\hat{\mathbf{R}}_n(t)$ by incorporating a linear deterministic

constraint (i.e., the unity gain constraint) along with the following additional set of p range-dependent stochastic constraints;

$$\mathbf{C}_k(t) = [\mathbf{s}(\theta)\ \mathbf{c}_k(t-1)\cdots\mathbf{c}_k(t-p)]\ ,\ \mathbf{f}_k(t) = [1\ \mathbf{w}_0^H\mathbf{c}_k(t-1)\cdots\mathbf{w}_0^H\mathbf{c}_k(t-p)]^H \quad (5.15)$$

where $\mathbf{C}_k(t)$ and $\mathbf{f}_k(t)$ are substituted for $\mathbf{C}$ and $\mathbf{f}$ respectively in Eqn.(5.7). As explained in (Abramovich et al. 1994), the first weight vector in the sequence $\mathbf{w}_0$ is the reference weight vector which is derived using the first segment of data comprising the PRI $t = 1, 2, .., \Delta_p = p$ *without* the use of stochastic constraints.

From the AR relation in Eqn.(5.14), the current clutter snapshot $\mathbf{c}_k(t)$ to be processed by $\hat{\mathbf{w}}_k^{(sc)}(t)$ is a linear function of the past p clutter snapshots so the imposed constraints ensure that the current beamformed clutter output $\hat{\mathbf{w}}_k^{(sc)H}(t)\mathbf{c}_k(t)$ is also a linear function of the past p beamformed clutter outputs. Moreover, it can be shown that the coefficients of this linear function coincides with the scalar AR coefficients α_i of the original multi-channel clutter process in Eqn.(5.14). As the scalar output process is statistically described by the same AR coefficients it follows that such constraints do in fact preserve the spectral characteristics of the beamformed clutter process whilst allowing the adaptive weight vector to change during the CIT. Note that it is not necessary to estimate the AR clutter process parameters α_i in Eqn.(5.14) to ensure this.

Naturally, the clutter-only snapshots are not available in practice to form the stochastic constraints in Eqn.(5.15). An operational procedure for obtaining close approximations to these constraints is described in (Abramovich et al. 1998) when clutter free array snapshots are available (supervised training) and in (Abramovich, Anderson and Spencer 2000) when clutter free array snapshots are not available (unsupervised training). The performance of an operational stochastic constraints procedure with supervised training will be illustrated in the following section.

A potential disadvantage of the stochastic constraints approach is that it cannot be used to preserve the clutter Doppler spectrum when the clutter spatial snapshots do not accurately obey the AR model in Eqn.(5.14). Even if such a model were accurate the order of the model needs to be estimated and if p approaches N then a significant amount of adaptive degrees of freedom are consumed only to protect the clutter, leaving relatively little scope for the beamformer to cancel the interference effectively. Another disadvantage of the SC algorithm, and many other adaptive beamformers in their strictly presented form, is that the sidelobes of the adapted beampatterns do not necessarily have the desirable characteristic of falling off in magnitude with increasing separation from the main lobe. This aspect has the potential to cause false alarms because target signals are not present in the training data and may therefore be received on large sidelobes of the beampattern well away from the main lobe.

5.4 Experimental results

The experimental data used for this study involves the passive reception of a co-operative HF interference source transmitting a "white noise" signal from a known location. The procedure for data collection is described in section 5.4.1 while the results of the interference rejection analysis are presented in sections 5.4.2 and 5.6. The benefits of applying more sophisticated adaptive weight control algorithms is illustrated in section 5.4.5 to motivate further research.

5.4.1 Data collection

In this experiment a vertically polarised omni-directional (whip) antenna was utilised to transmit a strong radio frequency interference (RFI) signal over a single-hop mid-latitude ionospheric path. The cooperative RFI source was positioned in the far-field of the Jindalee array, near Darwin, which is approximately 1265 km from the receiver site and offset +22 degrees from the array boresight. A clear frequency channel of 3 kHz bandwidth at a carrier frequency of 16.050 MHz was exclusively alloted for the purposes of this experiment which was conducted on 1 April 1998 between 06:22 UT and 06:32 UT. Note that the HF propagation data analysed in the previous chapters were recorded for the same mid-latitude ionospheric circuit immediately prior to this experiment (06:17-06:21 UT) on a nearby frequency channel (16.110 MHz).

The JFAS frequency management system (FMS) described in (Earl and Ward 1986) simultaneously monitored the prevailing ionospheric conditions on this mid-latitude path. In particular, ionograms from an oblique sounder also situated in the Darwin region were collected to determine the ionospheric mode content of the RFI signal. As predicted by the FMS system, the source frequency of 16.050 MHz coincided with near optimum single-hop ionospheric propagation conditions over the mid-latitude path which linked the interference source to the receiving antenna array at the time of recording.

All 32 subarrays of the Jindalee uniform linear array were steered towards the Darwin region and tuned to the designated frequency channel to passively receive the ionospherically-reflected RFI signal after FMCW deramping. The received "white noise" interference signal was seen to spread across the entire range-Doppler search space in a significant number of beams after conventional (FFT-based) processing was performed on the data received during each coherent integration time (CIT).

Each CIT of data contains 256 PRI's with 42 range cells retained for every PRI in all of the 32 receivers. The actual CIT lengths in seconds were therefore set by choice of the FMCW waveform repetition frequency (PRF) in Hertz. A low PRF of say 1 Hz permits the study of interference rejection over long CIT lengths (up to 256 seconds) but limits the minimum time interval over which the interference properties can be integrated to the PRI which equals 1 second in this case. Using a high PRF (of say 50 Hz) allows

one to observe interference rejection over very small time intervals but leads to short CIT lengths. In the experiment a PRF of 5 Hz was used to record interference data over CIT lengths of approximately 50 seconds, this value was chosen because the ionospheric channel propagating the interference is not expected to vary significantly over PRI shorter than 0.2 seconds.

The RFI source was switched off momentarily during the recording period in order to collect background noise only on the same clear frequency channel. The background noise-field was also sampled at a 5 Hz PRF and the same receiver configuration was maintained for all data recording. This data serves a reference point or benchmark which can be used to determine whether the adaptive beamformer has been able to completely mitigate the interference. If complete mitigation is not achieved, a comparison between the residual interference-plus-noise power and the noise-only power levels allows one to establish limits on the interference cancellation performance of the adaptive beamformer.

5.4.2 Intra-CIT analysis of adaptive beamformer performance

The purpose of this section is to experimentally demonstrate the improvement in HF interference cancellation gained by the adaptive beamforming schemes described in section 5.2 relative to the conventional beamformer as a function of sweep number throughout the CIT. As the spatial structure of the interference modes is not expected to change significantly over the "quasi-instantaneous" PRI, the relative improvement observed from one PRI to another within the CIT serves to quantify the effect of intra-CIT spatial structure variations on adaptive beamformer performance.

To illustrate the impact of interference spatial structure variations during the CIT on the performance of adaptive beamforming scheme 1 the quasi-instantaneous SINR improvement estimate $\hat{q}^{(1)}_{inst}(t)$ was calculated as,

$$\hat{q}^{(1)}_{inst}(t) = \frac{\mathbf{s}^H(\theta)\mathbf{T}\hat{\mathbf{R}}_n(t)\mathbf{T}\mathbf{s}(\theta)}{\hat{\mathbf{w}}_1^H\hat{\mathbf{R}}_n(t)\hat{\mathbf{w}}_1 \;\; \mathbf{s}^H(\theta)\mathbf{T}\mathbf{s}(\theta)}\,, \quad \hat{\mathbf{R}}_n(t) = \frac{1}{K'}\sum_{k=\Delta_k+1}^{\Delta_k+K'} \mathbf{n}_k(t)\mathbf{n}_k^H(t) \tag{5.16}$$

where $\Delta_k = 16$, $K' = 16$, $t = \Delta_p + 1, \Delta_p + 2, ..., P = 256$. Note that the adaptive spatial filter $\hat{\mathbf{w}}_1$ was formed according to Eqn.(5.8) using $K = 32$ and $\Delta_p = 6$, the reason for calculating the rejection over K' instead of all range cells will become apparent later when the performance of the different adaptive schemes are compared. The cone angle θ corresponds to the steer direction of the adaptive and conventional beams, both of which have a unity gain response to ideal target signals incident from this direction. A Hamming window function was used in the diagonal taper matrix $\mathbf{T}$ to reduce the sidelobes of the conventional beampattern.

Curve 1 in Figure 5.2 shows the relative improvement $\hat{q}^{(1)}_{inst}(t)$ as a function of slow-time t over a 50 second CIT of data. The average interference-to-noise ratio (INR) measured

at the receiver output was 54.3 dB for this CIT. To calculate the average INR, a CIT of background noise data (recorded on the same frequency channel immediately after switching off the interferer) was compared to the interference-plus-noise CIT to evaluate the INR at each receiver and these values were averaged across different receivers to yield the average INR. In OTH radar applications a set of mutually orthogonal beams is usually formed such that $\mathbf{s}^H(\theta_i)\mathbf{s}(\theta_j) = 0$ for $i \neq j$ where the integers $i, j = 1, 2, ..N$ are the referred to as the beam numbers. In this example, a cone angle of $\theta = 21.6^o$ (beam number 12) was chosen and corresponds to the beam steer direction in which the classical beamformer received the most interference-plus-noise power.

It is evident from Curve 1 in Figure 5.2 that the adaptive beamformer $\hat{\mathbf{w}}_1$ trained on a sample of $K \times \Delta_p = 192$ spatial interference-plus-noise snapshots has an initial effectiveness which is superior to the conventional beamformer by 30 dB. However, this initial improvement in interference suppression fades quickly to almost 0 dB (i.e., equivalent cancellation performance with the conventional beamformer) in a matter of 2 seconds. After about 20 seconds the adaptive beamformer $\hat{\mathbf{w}}_1$ "ages" to the point that conventional beamforming provides superior interference cancellation performance. Another point worth noting is that the small amplitude noise-like variations in the relative improvement (possibly caused by finite sample effects) are superimposed on an underlying larger-scale variation which varies relatively smoothly and exhibits a wave-like nature between 20-50 seconds. These fluctuations of over 30 dB can only be attributed to temporal changes in the spatial structure of the interference modes induced by the ionospheric reflection process during the CIT. Based on this result, it appears that in the HF environment adaptive scheme 1 is quite inappropriate for the purpose of ionospherically-propagated HF interference cancellation when CIT lengths greater than one second are required.

Curve 2 in Figure 5.2 shows the relative improvement $\hat{q}^{(2)}_{inst}(t)$ calculated for adaptive scheme 2. In this case the spatial filter $\hat{\mathbf{w}}_2$ is calculated using the interference-plus-noise snapshots received in $\Delta_p/2 = 3$ PRI immediately before and after the CIT of data to be processed.

$$\hat{\mathbf{w}}_2 = \frac{\hat{\mathbf{R}}_n^{-1}\mathbf{s}(\theta)}{\mathbf{s}^H(\theta)\hat{\mathbf{R}}_n^{-1}\mathbf{s}(\theta)}\ , \quad \hat{\mathbf{R}}_n = \frac{\sum_{k=1}^{K}\sum_{t=1}^{\Delta_p/2}\mathbf{n}_k(t)\mathbf{n}_k^H(t) + \sum_{k=1}^{K}\sum_{t=P-\Delta_p/2+1}^{P}\mathbf{n}_k(t)\mathbf{n}_k^H(t)}{K\Delta_p} \tag{5.17}$$

As for scheme 1, the quasi-instantaneous relative improvement $\hat{q}^{(2)}_{inst}(t)$ is computed by substituting $\hat{\mathbf{w}}_1$ for $\hat{\mathbf{w}}_2$ in Eqn.(5.16) for $t = \Delta_p/2 + 1, \Delta_p/2 + 2, ..., P - \Delta_p/2$. Note that the same number of training samples are used to estimate $\hat{\mathbf{w}}_1$ and $\hat{\mathbf{w}}_2$ while the range cells processed within the CIT by these two spatial filters are also the same so $\hat{q}^{(1)}_{inst}(t)$ and $\hat{q}^{(2)}_{inst}(t)$ can be meaningfully compared.

It can be seen from Curves 1 and 2 in Figure 5.2 that the relative improvement of scheme 2 is superior to that of scheme 1 over practically all of the CIT. In particular, the

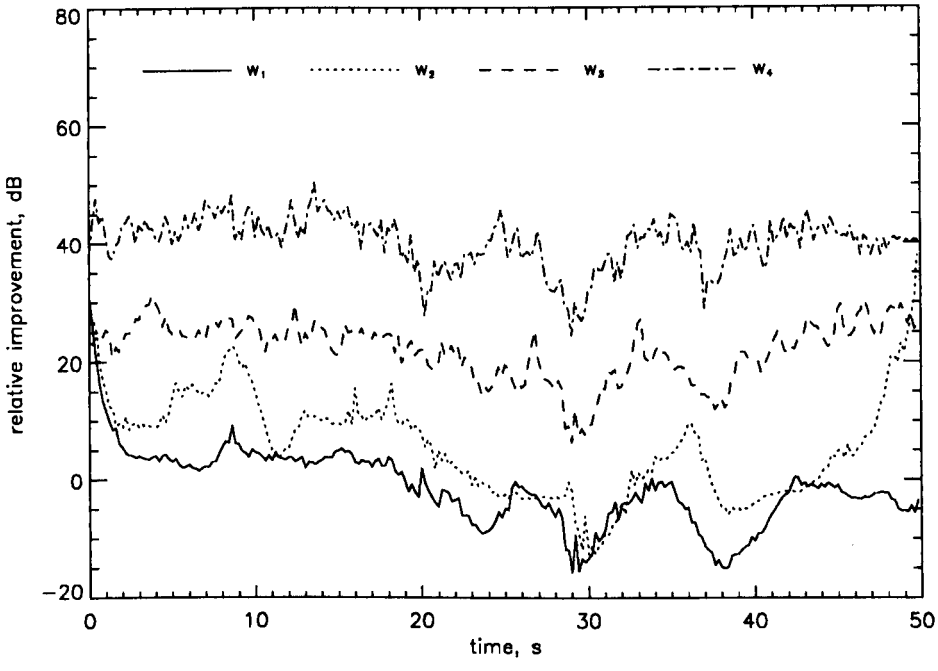

Figure 5.2: Quasi-instantaneous relative improvement in interference rejection performance obtained by four adaptive beamforming schemes as a function of PRI number over the CIT

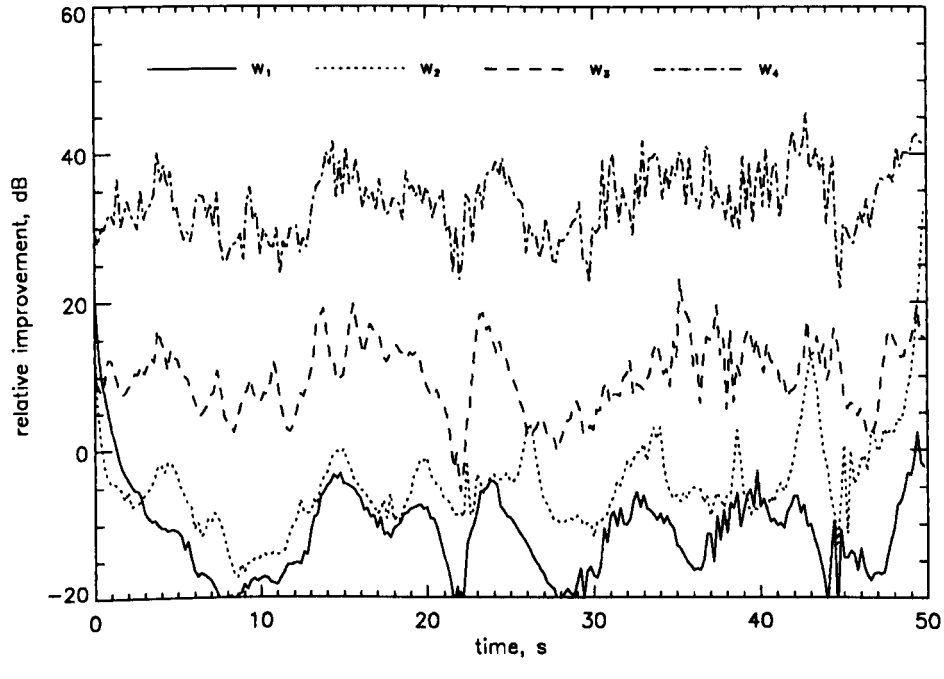

Figure 5.3: Quasi-instantaneous relative improvement in interference rejection performance obtained by the same adaptive beamforming schemes for a different CIT and beam steer direction

relative improvement of scheme 2 is 20-30 dB better than that of scheme 1 in the final second of the CIT. This is expected because adaptive scheme 2 operates on an estimate of the interference spatial properties which exist near the beginning and end of the CIT whereas adaptive scheme 1 operates only on an estimate at the beginning of the CIT. The relative improvement of scheme 2 in the middle stages of CIT is degraded by about 20 dB relative to that near the extremities of the CIT. This is also expected because adaptive scheme 2 has no "knowledge" of the intermediate variations in the interference spatial structure. In general, this information cannot be deduced from the interference spatial properties at the beginning and end of the CIT.

Nevertheless, averaging the spatial properties estimated at the extremities of the CIT seems to give a better estimate of those occurring within the CIT, as evidenced by the 10 dB performance improvement of adaptive scheme 2 relative to scheme 1 in the middle stages of the CIT. However, it is apparent from this analysis that scheme 2 is also unsuitable for ionospherically-propagated HF interference rejection in applications where the CIT exceeds one or two seconds. This motivates the need for adaptive schemes which operate on estimates of the interference spatial covariance matrix *within the CIT*, such as adaptive scheme 3 for instance.

Curve 3 in Figure 5.2 shows the relative improvement $\hat{q}^{(3)}_{inst}(t)$ calculated for the adaptive weight vector $\hat{\mathbf{w}}_3$. This weight vector is estimated according to Eqn.(5.11) using $\Delta_k = 16$ ranges and then held fixed to process the range cells $k = \Delta_k + 1, .., \Delta_k + K'$ in each PRI ($K' = 16$ as before). Unlike the previous schemes, adaptive scheme 3 uses an estimate of the interference spatial structure which is averaged over the *whole CIT* of data to be processed. The relative improvement gained by adopting this approach is 15-20 dB better than that observed for scheme 2 over the great majority of the CIT. If more enhanced cancellation is required the only remaining alternative is to re-adapt the weight vector within the CIT in order to track temporal variations in the interference spatial structure.

Curve 4 in Figure 5.2 shows the relative improvement $\hat{q}^{(4)}_{inst}(t)$ corresponding to the slow-time varying adaptive weight vector $\hat{\mathbf{w}}_4(t)$. This weight vector has been calculated by forming the slow-time varying covariance matrix $\hat{\mathbf{R}}_n(t)$ in Eqn.(5.13) with $\Delta_p = 4$, $\Delta_k = 16$ and deriving the associated MVDR solution using Eqn.(5.5). As described in section 5.3, the resulting weight vector is applied to range cells $k = \Delta_k + 1, .., \Delta_k + K'$ in the same Δ_p PRI to obtain the estimate of the relative improvement $\hat{q}^{(4)}_{inst}(t)$ as a function of slow time t.

A relative improvement in the order of 40 dB is evident in Curve 4 of Figure 5.2 and this indicates that re-adaptations of the beampattern within the CIT leads to substantial gains in interference cancellation performance. More specifically, a comparison between the fixed weight vector (Curve 3) and the re-adapted weight vector (Curve 4) demonstrates that allowing the weight vector to change during the CIT provides an extra $15-20$ dB in interference cancellation. Later in this section it will be seen that such dramatic increase

could potentially have been even greater if it were not limited by the underlying noisefloor.

The reason for the enhanced performance of the time-varying beamformer $\hat{\mathbf{w}}_4(t)$ relative to the fixed beamformer $\hat{\mathbf{w}}_3$ may be explained in terms of the dimensionality of the interference subspace in the spatial covariance matrix relative to the available number adaptive degrees of freedom. Both processors have the same number of adaptive degrees of freedom available for interference cancellation but the amount consumed by the dimension of the interference subspace *grows* as the time-interval over which the spatial covariance matrix is integrated increases. This growth with integration time is primarily caused by the time-varying spatial distortions induced by the ionospheric reflection process on the interference signals. Since these distortions evolve in a correlated manner with respect to time it follows that limiting the integration time reduces the effective dimension of the interference subspace and this in turn allows an MVDR beamformer with finite degrees of freedom to cancel more of the interference.

Figure 5.3, in the same format as Figure 5.2, shows the results for the subsequent CIT of interference-plus-noise data in which the average INR was computed as 57.9 dB. In this example, the cone angle $\theta = 20.8^o$ (beam number 10) was chosen. This beam steer direction is slightly further away from the direction in which the maximum interference power was received by the classical beamformer (beam number 12). Although the basic characteristics of the four curves in Figure 5.3 are similar to those of Figure 5.2, the absolute values are seen to be different from one CIT to another and will depend on the beam steer direction. This illustrates the need for further data processing to quantify the variability in the performance of the various adaptive schemes over both beam steer direction and the particular CIT of data. In this way a more reliable estimate of the average or expected performance of the different schemes can be obtained as a function of the CIT length for a given interference scenario.

5.4.3 Statistical analysis of adaptive beamformer performance

For CIT's of a given duration the relative improvement in interference cancellation varies as a function of beam steer direction and the particular CIT of data processed. It is therefore of interest to quantify the *distribution* of the relative improvements observed for each of the adaptive beamforming schemes in the same interference scenario.

Figure 5.4 shows the mean and deciles of the distribution for the relative improvement gained by adaptive scheme 1 over different CIT lengths. For a given CIT length, a total of 10 mutually orthogonal beams were processed in each of 40 different CIT so that the distribution obtained for each CIT length comprises 400 samples. Each sample in the distribution is calculated as the relative interference cancellation improvement averaged over the CIT for a particular beam steer direction.

It is noted from Figure 5.4 that the mean relative improvement drops markedly from above 30 dB to below 0 dB as the CIT is increased from a fraction of a second to 40 seconds.

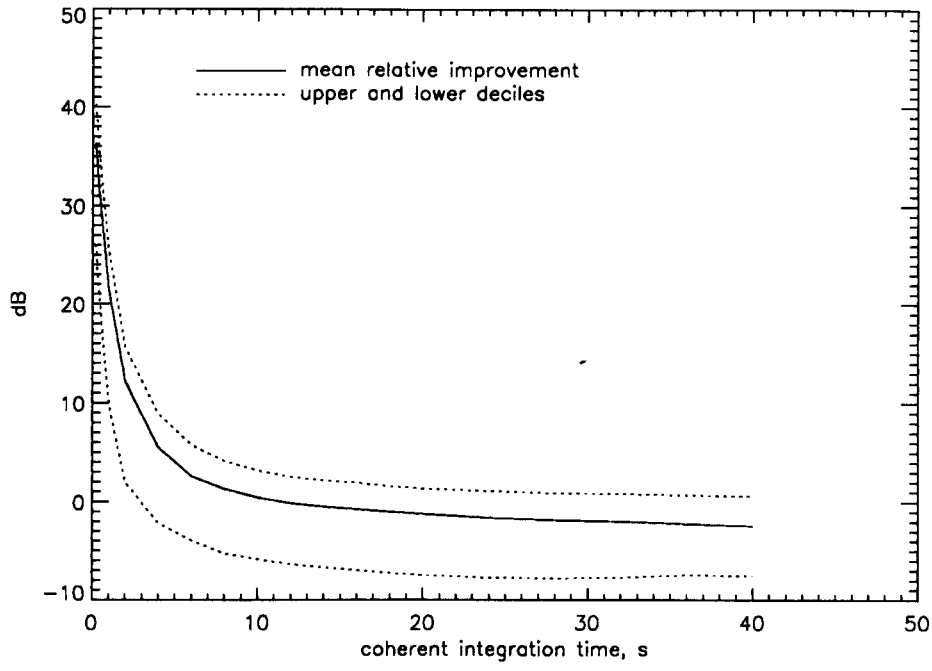

Figure 5.4: Mean and deciles of the improvement in interference rejection performance achieved by adaptive scheme 1 ($\hat{q}_1$) over the conventional beamformer as a function of CIT length.

Moreover, this degradation is very rapid in the sense that over 20 dB of interference cancellation gain is lost in less than 2 seconds which is typically the lower limit of typical OTH radar CIT. The extra computational (and operational) complexity associated with adaptive scheme 1 relative to conventional beamforming is therefore not warranted for such CIT lengths according to these experimental results.

Figure 5.5, in the same format as Figure 5.4, shows the results derived for adaptive scheme 2. The mean relative improvement of this scheme is above 40 dB for very small CIT lengths but decays to 25 dB after two seconds and to approximately 0 dB by the time the CIT reaches 30 seconds. Although the interference cancellation gain decays less rapidly for this scheme than it does for scheme 1 the significant drop in performance for CIT lengths exceeding 2 seconds may not be tolerable when a powerful interferer is present. Based on these experimental results, it is evident that this scheme may not perform well enough compared to the conventional beamformer to justify its operational implementation.

Figure 5.6 illustrates the mean and deciles of the relative improvement distributions resulting for adaptive scheme 3. The maximum mean relative improvement gained by this scheme is about 43 dB and occurs for a CIT length slightly over 1 second. A degradation of up to 8 dB is observed for smaller CIT lengths and this is caused by the finite number of samples available for spatial covariance matrix estimation in this scheme when the CIT is reduced. For CIT lengths longer than 1 second the degradation is caused by the increased consumption of adaptive degrees of freedom due to temporal variations in the interference

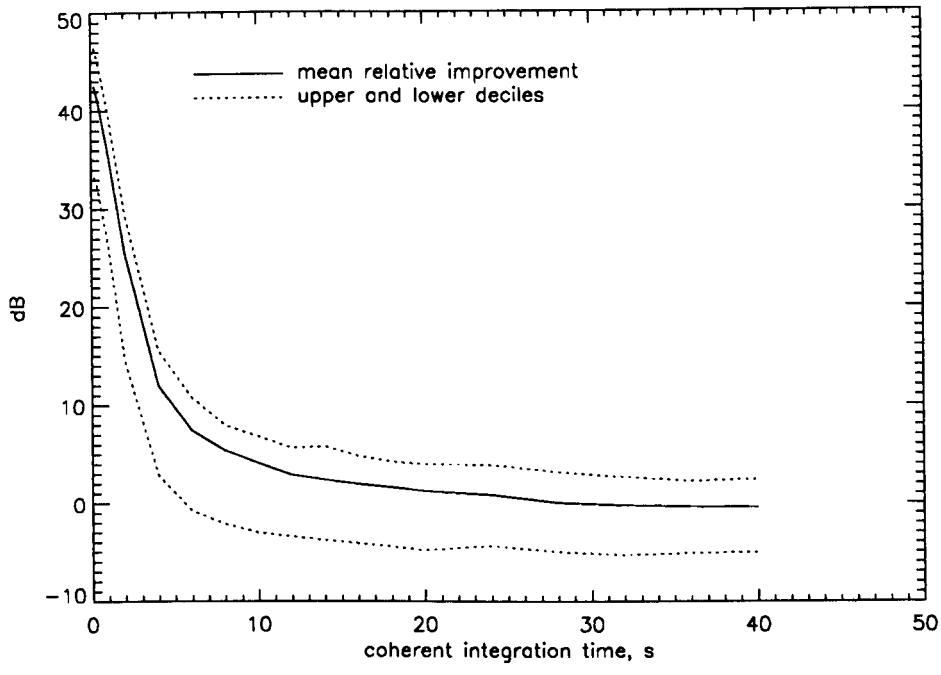

Figure 5.5: Mean and deciles of the improvement in interference rejection performance achieved by adaptive scheme 2 ($\hat{q}_2$) over the conventional beamformer as a function of CIT length.

spatial structure.

Using this scheme leads to an interference cancellation gain of over 30 dB for CIT lengths smaller than 5 seconds and this may be sufficient is some applications to maintain satisfactory target detection performance. Diagonal loading can be employed to improve the performance at very small CIT lengths if required, as illustrated by Figure 5.7 where a loading factor of -20 dB is applied (i.e., $0.01 \times \mathbf{I}$ is added to the sample spatial covariance matrix used to form the MVDR weight vector). This relatively simple operation improves the relative cancellation performance from 35 dB to 45 dB at very small CIT lengths, a remarkable 10 dB increase.

The performance degradation of over 25 dB experienced as the CIT is increased towards 50 seconds may pose a problem in certain OTH radar applications and the 10 dB drop as the CIT increases from 1 second to 8 seconds can make a significant difference to the performance of systems requiring intermediate CIT lengths. For this reason it is of interest to determine the potential effectiveness of re-adapting the beampattern within the CIT (scheme 4). The effectiveness of adaptive scheme 4 is also quantified by Figure 5.6 since every segment of data over which the beampattern is re-adapted may be considered as a sub-CIT of the total CIT. In other words, if the adaptive weight vector were re-computed every second, which coincides with a mean relative improvement of about 43 dB in Figure 5.6, then such an improvement can be realised for any CIT length by the re-adapting the MVDR weight vector every second.

Before investigating the use of adaptive scheme 4, it is of interest to compare the

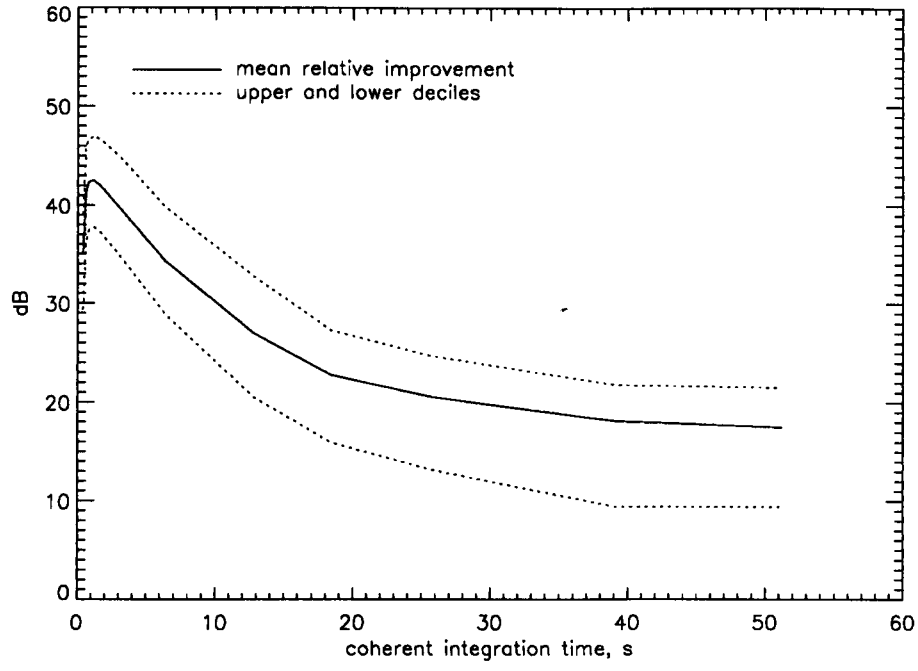

Figure 5.6: Mean and deciles of the improvement in interference rejection performance achieved by adaptive scheme 3 ($\hat{q}_3$) over the conventional beamformer as a function of CIT length.

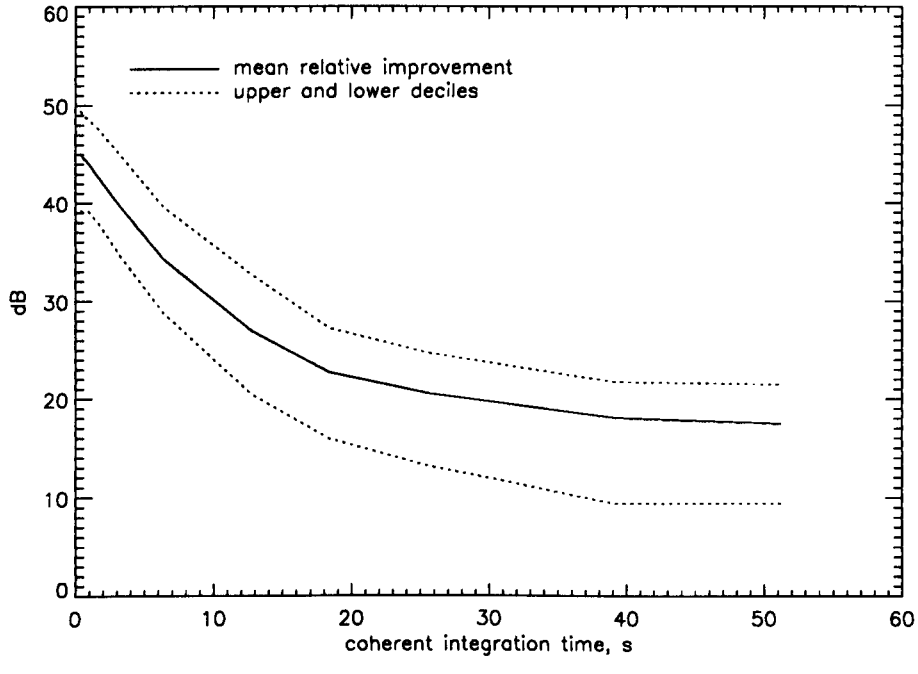

Figure 5.7: Mean and deciles of the improvement in interference rejection performance achieved by adaptive scheme 3 *after diagonal loading* relative to the conventional beamformer as a function of CIT length.

statistical interference cancellation performance predicted by the HF channel model with the experimentally observed distributions. Such a comparison allows one to determine the fidelity with which the previously validated HF channel model can predict the relative SINR gain under ideal target signal conditions.

5.4.4 Statistical analysis with simulated interference

As mentioned in chapter 4, the space-time signal processing model of the HF channel can be used to simulate the statistical characteristics of the complex-valued digital samples received by an array of sensors due to an interference source propagated by the ionosphere. The space-time parameters of the HF channel model described in the previous chapter cannot be estimated directly from the received interference because the incoherent nature of this signal with respect to the FMCW mixing waveform does not allow the temporal or Doppler properties of the channel to be observed. Nevertheless, the interference has been received at a similar time and frequency to the channel scattering function (CSF) data analysed and modelled in the previous chapters. The CSF data was received between $06:17-06:21$ UT on 1 April 1998 at a frequency of 16.110 MHz while the interference was received between $06:22-06:32$ UT on the same day at a frequency of 16.050 MHz.

Although the channel parameters may vary over this time and frequency interval it is of interest to compute the interference cancellation distributions using the model parameters estimated from the CSF data. The model parameters used for the simulation are listed in Table 5.1. The relative power ratio of the different interference modes are assumed to be the same as those measured for the CSF data, but the absolute power of each interference mode has been scaled such that the total power of the modelled signal equals the estimated power of the received interference. The power of the received interference was estimated by evaluating the variance of the data recorded in each receiver throughout the data collection period and then averaging these variances across receivers. The average variance of the received interference was 30.2 dB.

Note that the mode powers given in Table 5.1 are not the mode INR's, for this data set the noise level is at approximately -27 dB when measured in receiver space *prior* to Doppler processing. The INR's can be calculated by adding 27 dB to the powers listed in Table 5.1 and it is noted that the average INR over the data collection period is approximately 30.2 dB + 27 dB = 57.2 dB. The noise added to the simulated interference is real background noise recorded on the same frequency band in the absence of the RFI signal.

Another point which needs to be considered in the simulation is the nature of the interference waveform $g_k(t-\tau_m)$ and the effect of the relative mode time-delays τ_m for each mode $m = 1, 2, .., M = 5$. The interference signal is of $f_b = 3$ kHz bandwidth and its spectral density is expected to be approximately flat over this passband because

Mode	power, dB	temporal pole, α	spatial pole, β
$1E_s(a)$	20.5	$0.998\ e^{jk_1 0.46}$	$0.920\ e^{jk_2 \sin(22.2-\theta_s)}$
$1E_s(b)$	17.9	$0.997\ e^{jk_1 0.39}$	$0.963\ e^{jk_2 \sin(21.7-\theta_s)}$
$1F_2$	28.6	$0.994\ e^{jk_1 0.44}$	$0.988\ e^{jk_2 \sin(20.7-\theta_s)}$
$1F_2(o)$	21.8	$0.997\ e^{jk_1 0.47}$	$0.986\ e^{jk_2 \sin(20.5-\theta_s)}$
$1F_2(x)$	7.9	$0.994\ e^{jk_1 0.53}$	$0.953\ e^{jk_2 \sin(19.9-\theta_s)}$

Table 5.1: Interference simulation parameters assuming five propagation modes and the HF channel model estimated from the channel scattering function data. The constants are $k_1 = 2\pi/f_p$ where $f_p = 5\ Hz$ and $k_2 = 2\pi\Delta d/\lambda$ where $\Delta d = 84\ m$, $\lambda = c/f_c = 18.7\ m$ and the subarray steer direction $\theta_s = 22.0$ degrees.

the emitted signal is derived by filtering a broadband (greater than 3 kHz) source of "white noise". Assuming the spectral density is constant over the band, the temporal autocorrelation function of the transmitted interference signal is given by the sinc function with the first null at a time delay $\tau = 1/f_b$ (i.e., 0.33 ms in this case).

The differential time delay between modes can be estimated from the oblique incidence ionogram recorded for the CSF data analysis in chapter 2. For each pair of modes, the differential time-of-arrival can be calculated from the ionogram and expressed in terms of an inter-mode correlation coefficient by evaluating the sinc auto-correlation function of the interference waveform at this differential time delay. Once the correlation coefficients $\rho_{i,j}$ are calculated in this manner for all pairs of modes $i, j = 1, 2, .., M = 5$ they can be entered into the so-called source covariance matrix $\mathbf{R}_s$.

$$\mathbf{R}_s = E\{\mathbf{g}_k \mathbf{g}_k^H\} = [\rho_{i,j}]_{i,j=1}^{M}\ ,\ \ \mathbf{g}_k = [g_k(t-\tau_1) \cdots g_k(t-\tau_M)]^T \tag{5.18}$$

Note that the diagonal elements of $\mathbf{R}_s$ are unity by definition as the mode waveforms $g_k(t-\tau_M)$ are normalised to have unit variance in the model. Once the source covariance matrix has been evaluated the interference mode waveforms can be generated as,

$$\mathbf{g}_k(t) = \mathbf{R}_s^{1/2} \mathbf{n}_k(t)\ ,\ \ E\{\mathbf{n}_{k_1}(t_1)\mathbf{n}_{k_2}^H(t_2)\} = \delta(k_1-k_2)\delta(t_1-t_2)\mathbf{I} \tag{5.19}$$

where $\mathbf{R}_s^{1/2}$ is the Hermitian square root of the source covariance matrix $\mathbf{R}_s$. The independence of the zero-mean complex-Gaussian vectors $\mathbf{n}_k(t)$ over range k and slow-time t implies that the interference samples are white and hence independent over both these data dimensions.

Figure 5.8 shows the relative interference cancellation improvement distribution which results when the interference modes are simulated with *no spatial distortions* and processed by adaptive scheme 3 in identical manner to that of Figure 5.7. No spatial distortions refers to spatial poles on the unit circle, this has been simulated by setting the magnitude of the spatial pole estimated for each mode in Table 5.1 to unity. In other words, the interference modes are modelled as plane waves with Doppler shifted and Doppler spread waveforms. Since the spatial structure of the interference is invariant over

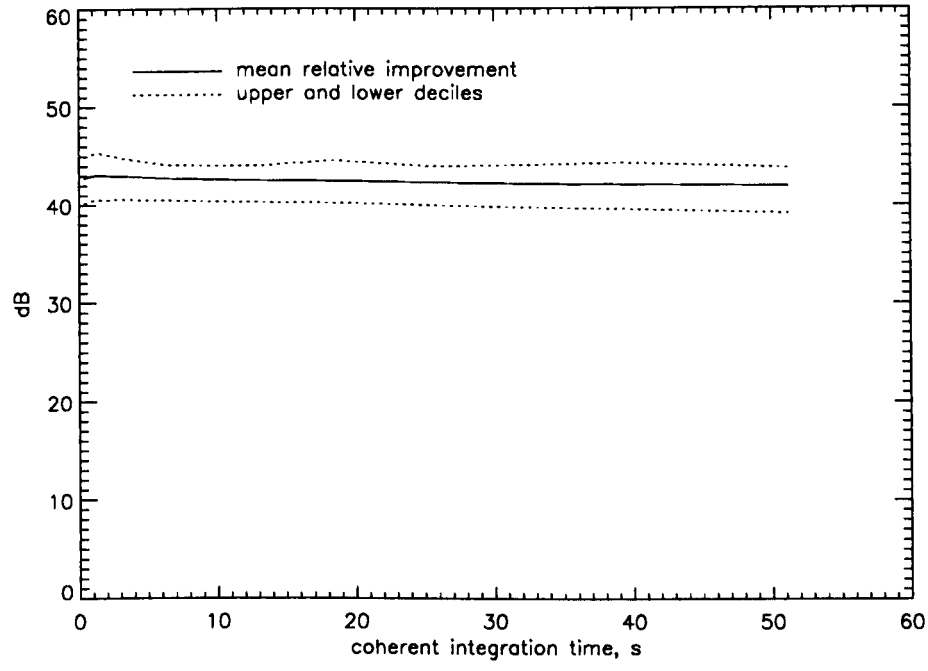

Figure 5.8: Relative improvement achieved by adaptive scheme 3 (after diagonal loading) for simulated HF interference with temporal distortions but in the *absence* of spatial distortions.

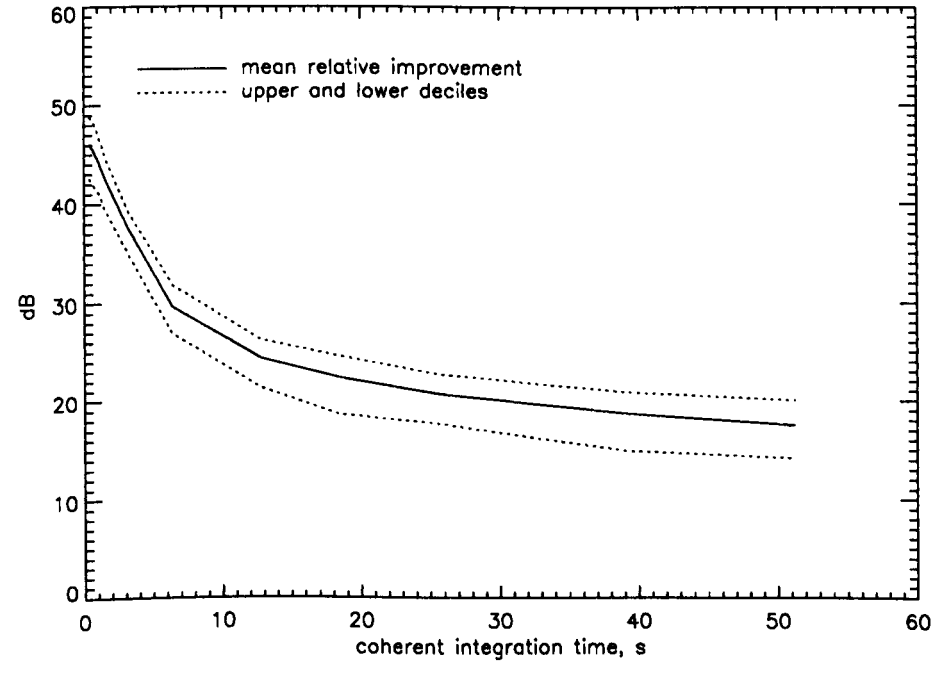

Figure 5.9: Relative improvement achieved by adaptive scheme 3 (after diagonal loading) for simulated HF interference with the inclusion of space-time distortions.

the CIT the dimension of the interference subspace does not increase past $M = 5$ as the CIT is increased. This explains the uniformity of the relative interference cancellation improvement distributions with respect to CIT length. Obviously, the traditional plane wave interference model does not provide an accurate representation of the distributions derived by experimental data processing in Figure 5.7. The substantial difference between Figure 5.7 and Figure 5.8 illustrates the need to interpret results obtained from such a model with caution.

Figure 5.9 shows the relative interference cancellation improvement distribution which results when the spatial distortions described by the first order AR model parameters in Table 5.1 are introduced. The mean relative improvement ranges from 46 dB at small CIT lengths (less than one second) to 18 dB at CIT lengths of about 50 seconds. This compares favourably with the experimentally observed reduction from 45 dB to 17 dB over the same CIT range. The precise shapes of the curves in Figure 5.7 are not identical to those in Figure 5.9 but the estimated model parameters provide a fairly accurate representation of adaptive beamformer performance in the HF environment. A similar experiment that favourably compares the simulated and experimental performance of another adaptive beamforming scheme (scheme 1) with a different set of CSF and interference data can be found in (Fabrizio, Abramovich, Gray, Anderson and Turley 1998).

5.4.5 Constrained intra-CIT beampattern re-adaptations

It was stated earlier that re-adapting the beampattern over small time intervals within the CIT can be used to enhance interference cancellation performance. The problem encountered in practice is that such re-adaptations destroy the temporal correlation properties of the clutter which spreads over the search space after Doppler processing and potentially obscures the presence of useful signals. The stochastic constraints approach proposed by (Abramovich et al. 1994) attempts to prevent this Doppler smearing and has been tested on real clutter returns for beampatterns which re-adapted to simulated interference (Abramovich et al. 1998). In this section the performance of this algorithm is demonstrated for *experimentally recorded* HF interference and simulated clutter signals, the latter being described by a second order AR model. The main purpose is to illustrate the advantages and shortcomings of this approach as well as to motivate further research in this area.

The temporal poles of the scalar-type AR(2) model have been placed at $p_t^{(1)} = 0.99e^{j\pi/90}$ and $p_t^{(2)} = 0.98e^{j\pi/180}$ to generate a clutter process that is narrowband in Doppler. The spatial pole was placed at $p_s = 0.5$ to produce a spatially broadband clutter process that is received through the main lobe and sidelobes of the beampattern. A synthetic target signal which is discrete in the angle-Doppler domains was simulated to illustrate the SINR gain achieved by the intra-CIT adaptive beamforming re-adaptations. This synthetic target has a normalised Doppler frequency of 0.5 and is incident from the

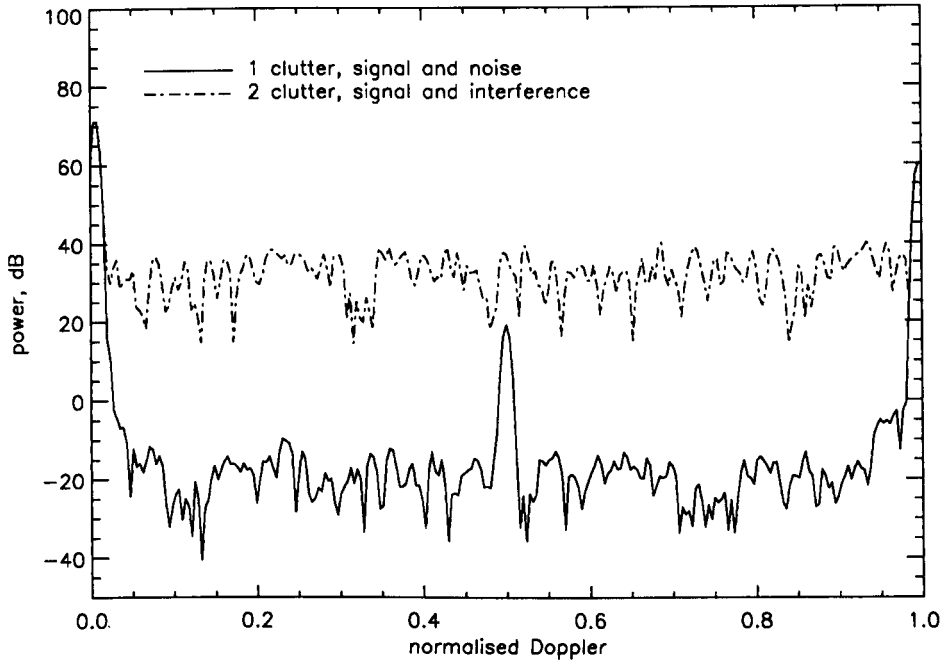

Figure 5.10: Conventional Doppler spectra for simulated clutter and target signals with and without the presence of experimentally recorded HF interference

same steer direction as beam number 10 which is the beam to be processed.

Figure 5.10 shows the Doppler spectrum resulting after conventional beamforming for the range-azimuth cell containing the desired signal at 0.5 normalised Doppler frequency. The solid curve shows the case when clutter, signal and additive background noise are present. The additive background noise was experimentally recorded on the same frequency channel in the absence of the interference and has been superimposed on the simulated clutter and desired signal. The dashed curve shows the case where interference is also present. In this beam the residual interference power at the conventional beamformer output is powerful enough to completely mask the desired signal.

The first question to be addressed is whether adaptive beamforming with intra-CIT beampattern re-adaptations can be used to reject the interference to the background noise level. To answer this question the simulated clutter is momentarily removed from the data to observe the effect of adaptive beamforming on the interference-plus-noise only. Curves 1 and 3 in Figure 5.11 show the Doppler spectra resulting for the conventional beamformer when the interference is present and absent respectively. By comparing Curve 2 in Figure 5.10 with Curve 3 in Figure 5.11 it is evident that in Doppler regions away from the clutter (i.e., 0.1-0.9 normalised Doppler frequency) the signal in Figure 5.10 is being detected against additive noise and not against the clutter sidelobes in Doppler.

Curve 2 in Figure 5.11 shows the Doppler spectrum resulting at the output of the adaptive beamformer *when the interference is present.* In this case the adaptive weight vector was updated from one PRI to another throughout the CIT; the sample spatial covariance matrix was formed in each PRI using 32 interference-plus-noise snapshots and

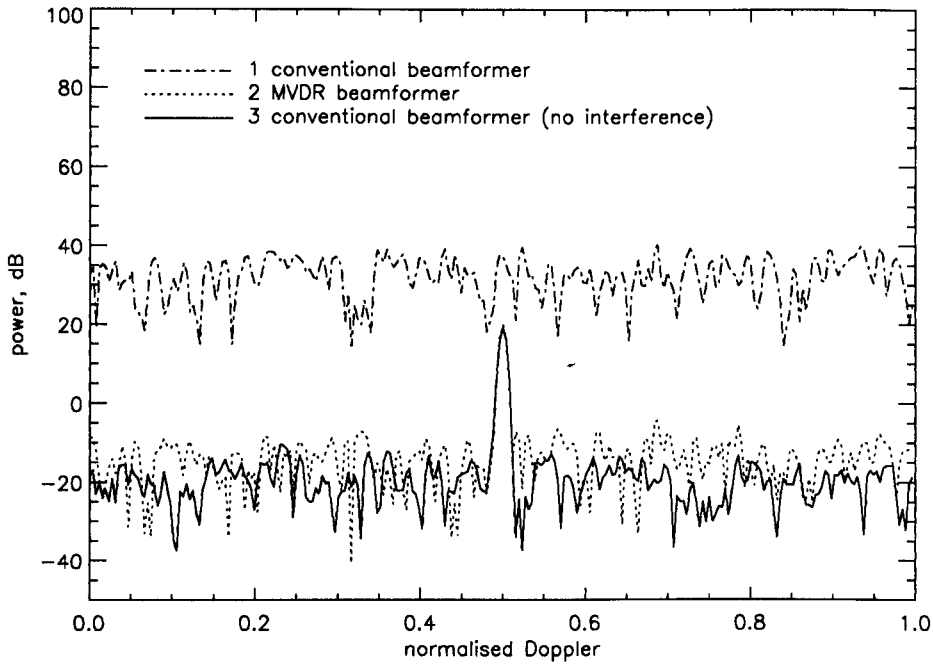

Figure 5.11: Conventional Doppler spectra for a simulated target signal in real HF interference (Curve 1) and real background noise (Curve 3). Curve 2 shows the Doppler spectra resulting for the simulated target signal in real HF interference when the MVDR adaptive beamformer is re-adapted in every PRI of the CIT

-20 dB diagonal loading. The slow-time dependent MVDR weight vectors calculated from these matrices were then applied to beamform the test range cell which was not included in the training data. A comparison of Curve 2 and Curve 3 in Figure 5.11 demonstrates that re-adaptations of the beampatterns from one PRI to another can be used to remove an additional 45 dB of interference relative to the conventional beamformer and restore the SINR practically to the same level obtained by the conventional beamformer in the *absence* of interference. Hence from an interference rejection point of view the performance of this scheme could not be much better since the residual non-signal power coincides more or less with the noisefloor.

The second question which arises relates to the application of these slow-time varying adaptive beamforming weights to a CIT of data which also contains clutter. Curve 1 in Figure 5.12 illustrates the answer to this question. Although the interference is almost perfectly rejected by the time-sequence of MVDR weight solutions, it is quite evident that re-adapting the beampattern in an uncontrolled manner (i.e., with no regard to the clutter) within the CIT can grossly distort the clutter spectrum properties. The spreading of the clutter signal across Doppler space is so drastic that the 45 dB gain in interference rejection is completely negated by the loss in sub-clutter visibility.

Curve 2 and Curve 3 in Figure 5.12 illustrates the Doppler spectrum which results when the beampattern re-adaptation is controlled by means of one and two stochastic constraints respectively. Note that clutter, signal and interference are present in all of

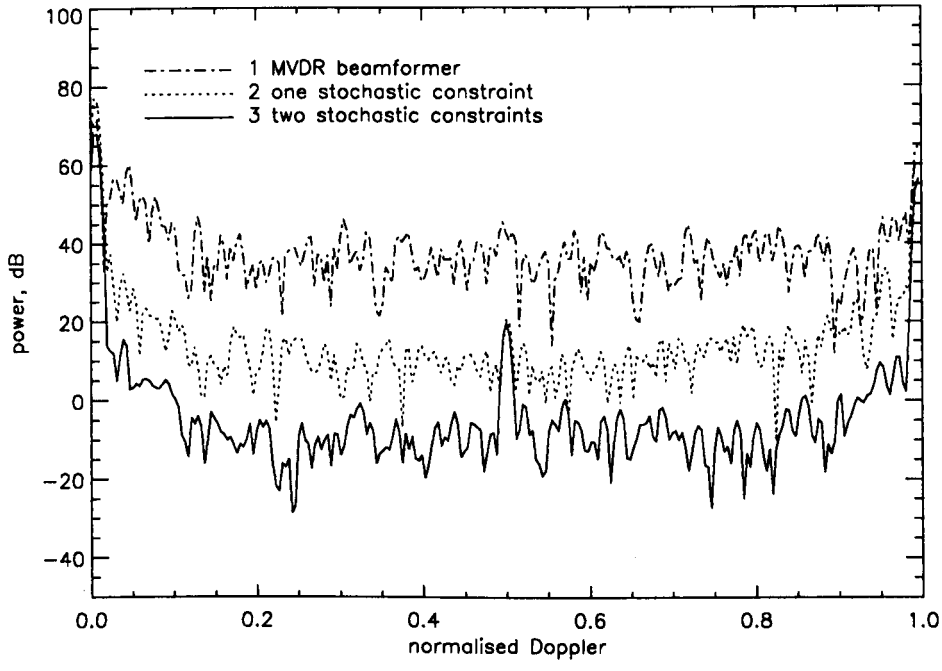

Figure 5.12: Doppler spectra resulting for the simulated clutter and target signal in real HF interference when the MVDR adaptive beamformer is re-adapted at every PRI in the CIT with no (Curve 1), one (Curve 2) and two (Curve 3) stochastic constraints

the spectra in Figure 5.12. The use of a single stochastic constraint leads to a 25 dB clutter power reduction over most of the Doppler search space but this improvement is insufficient to detect the relatively weak signal at 0.5 normalised Doppler frequency. The use of two stochastic constraints (equal to the order of the clutter model) reduces the output clutter power over the search space by a further 20 dB which subsequently allows desired signal detection. A comparison between Curve 2 in Figure 5.10 and Curve 3 in Figure 5.12 highlights the benefits of slow-time dependent adaptive beamforming with stochastic constraints over conventional beamforming.

However, the SINR in Curve 3 of Figure 5.12 is not quite as good as that obtained by conventional beamforming in the absence of interference (Curve 1 in Figure 5.10). These losses arise partly due to the inclusion of further constraints which consume adaptive degrees of freedom otherwise used for interference cancellation as well as the unavailability of clutter-only snapshots which implies that the stochastic constraints must be estimated using the method described in (Abramovich et al. 1994). In this example, these factors cause a 10 dB loss in the potentially achievable output SINR. Further losses are to be expected if the real clutter obeys a much higher order AR model. These remaining issues provide motivation for further research in this area.

5.5 Chapter summary

This chapter has experimentally quantified the gains in interference cancellation performance which can be realised by various adaptive beamforming schemes on a very wide aperture antenna array in the HF environment. It was found that the space-time distortions imposed on HF interference modes by the ionospheric reflection process has the potential to cause dramatic degradations in adaptive beamformer performance. For some adaptive schemes, ionospherically-induced variations in the spatial structure of interference modes with respect to time resulted in cancellation performances inferior to that of the conventional beamformer.

These results illustrate that while spatial distortions over a mid-latitude one-hop ionospheric path may not impact greatly on systems which receive the signal in the main beam (i.e., a desired signal), they can seriously effect performance of systems in which the signal is considered as interference and cancelled by means of adaptive beamforming. The reason for this is that interfering signals are received close to the relatively steep nulls of an adaptive beampattern where the array response is significantly more sensitive to the time-varying spatial distortions.

It was also demonstrated that the previously validated HF channel model could be used to simulate ionospherically-propagated interference signals to accurately predict the statistical performance of the MVDR adaptive beamformer as a function of CIT length. By freezing the spatial structure of the interference modes in the simulation it was explicitly shown that degradations in the adaptive beamformer performance are essentially caused by the time-varying spatial distortions induced by the ionosphere rather than finite sample effects or the temporal distortions only. The statistical distributions obtained by experiment and by simulation indicate that for long CIT lengths (e.g., 50 seconds) a performance enhancement of over 20 dB can be realised with respect to the fixed MVDR weight solution by diagonal loading of the sample spatial covariance and re-adapting the MVDR weight vector at every PRI within the CIT. In operational systems, these intra-CIT beampattern re-adaptations unfortunately smear the clutter signals across the Doppler search space and can prevent target detection.

The stochastic constraints method for controlling these re-adaptations was described and relies on a scalar-type AR modelisation of the backscattered clutter returns. The performance of the method was illustrated using real HF interference and simulated clutter and target signals. Although this method enabled the detection of a relatively weak target in a powerful interference and clutter background, the output SINR was below that potentially achievable and this observation serves to motivate further research in this area.

CHAPTER 6

Receiver mismatch

The performance of an adaptive array is not always limited by the capabilities of the adaptive processor or the complexity of the interference scenario; in many practical applications significant performance degradations may be encountered as a result of instrumental uncertainties. A hardware imperfection which can severely limit the interference nulling capability of an adaptive array is the non-identical transfer functions of the different receivers. In narrowband arrays, mismatches between the receiver transfer functions cause the signals received on various antenna sensors to differ from one another by some manner other than a complex multiplicative constant and this prevents an adaptive spatial processor from nulling the interfering signal perfectly.

This chapter is concerned with estimating digital compensation for non-identical receiver transfer functions in HF antenna arrays using interference sources of opportunity. Background information and a literature review on this topic is contained in Section 6.1 to introduce and motivate this research as well as to explain its significance relative to previous work. Suitable interference sources of opportunity are identified for the HF band in section 6.2 and a mathematical model is developed to represent such sources as sampled by an antenna array with non-identical reception channels. This mathematical model is used in section 6.3 to derive a signal processing algorithm which estimates digital compensation for non-identical receiver transfer functions. Section 6.4 describes the experimental procedure used to collect data for this study and includes a description of the Jindalee array calibration system which is used to provide "ground truth" measurements of the receiver transfer functions.

The proposed compensation algorithm is tested using an interference source of opportunity in section 6.5 where digital corrections are estimated for actual imperfections in the Jindalee receivers. The performance of the algorithm is compared against a commonly used adaptive receiver equalisation method and measurements made by the Jindalee calibration system. Section 6.5 also demonstrates the improvement in interference cancellation which results at the output of an adaptive sidelobe canceller after receiver frequency response correction.

6.1 Literature Review

The meaning of the terms "receiver mismatch" and "array manifold errors" is explained in section 6.1.1 in order to underline the distinction between these two forms of hardware imperfection. Section 6.1.1 also discusses the instrumental origin of both forms of hardware imperfection as well as their potential influence on adaptive spatial processing performance. Existing methods for receiver mismatch compensation are reviewed in section 6.1.2 while section 6.1.3 describes the research undertaken in this chapter relative to previous work in the field.

6.1.1 Background

Instrumental imperfections can be classified into two categories; those which occur at the antenna sensor level and in the signal paths up to but not including the receivers (i.e., in the "front end" of each reception channel), and those which occur within the receivers themselves. The antenna sensors, cables and amplifiers in the front end are so-called "broadband" components as they are designed for operation over the HF band, while the various filters in the receivers are "narrowband" components designed only to pass signals within a relatively narrow bandwidth of interest.

At the antenna sensor level, imperfections which can limit adaptive spatial processing performance mainly arise due to uncertainties in the relative sensor positions, radiation patterns and the effects of mutual coupling. Differences in the characteristics of the amplifiers and cables from one reception channel to another can also limit performance and superimpose on the above-mentioned antenna sensor imperfections. In narrowband arrays, the influence of these uncertainties on the received signals is expected to be a function of carrier frequency due to variations in the response of the broadband components, but may be regarded as fixed over the relatively narrow passband of interest.

These fixed or passband-independent errors are often referred to as array manifold errors (Ng, Er and Kot 1994) or array steering vector errors (Compton 1982) and cause the perceived signal wavefronts to differ from the incident ones by a multiplicative complex scalar at each reception channel. Array manifold errors may depend on the signal direction-of-arrival and are corrected by applying a single complex digital correction per reception channel. The field of signal processing concerned with estimating this compensation is commonly known as the field of "array calibration".

Uncertainties in the array manifold can degrade the reception of desired signals in adaptive beamforming applications because they represent errors in the mathematically defined array steering vector (Kelly 1989). However, array manifold errors do not effect the interference cancellation performance of adaptive beamformers or sidelobe cancellers because the adaptive algorithm automatically compensates for fixed amplitude and phase distortions to the interference wavefront (Farina 1992). In sidelobe cancellation applica-

tions the desired signal is assumed to be absent from the auxiliary channels and in this case array manifold errors are not expected to degrade signal reception or interference cancellation.

Now let us turn our attention to imperfections arising in the narrowband receivers of the array. The transfer functions of the analog filters in each receiver can deviate or mistune from their nominal frequency response due to the non-ideal nature of the hardware components. Unlike array manifold errors, the deviations in gain and phase from the nominal receiver frequency response are independent of carrier frequency but usually vary over the passband of interest. Importantly, the variation of these errors across the passband is generally not identical from one receiver to another and the resulting differences in frequency response is often referred to as receiver mismatch.

Receiver mismatch can severely limit the interference nulling capability of adaptive *spatial* processors used for either beamforming or sidelobe cancellation, note that in such processors a single complex weight per channel is used to spatially combine the signals. The effect of receiver mismatch is to reduce the correlation coefficient between the signals received on different array channels and hence to degrade the maximum achievable cancellation ratio after a single complex weight per channel is used to spatially combine the signals. Typically, receiver mismatch is compensated by inserting an adaptively tuned digital transversal filter (tap delay-line), or its frequency domain equivalent, at the output of each reception channel (Monzingo and Miller 1980).

Ideally, compensation is required for array manifold errors as well as receiver mismatch in order to equalise the global transfer function of the reception channels. In the context of HF antenna arrays, there is currently great interest in using external sources of opportunity to estimate digital compensation for array manifold errors and receiver mismatch. The use of such sources for HF array calibration allows modern OTH surface wave radars to be more cost effective and rapidly deployable with a reduced need for site preparation (Solomon, Gray, Abramovich and Anderson 1998). Another motivation for using sources of opportunity is to provide measurements which are independent of those made by other array calibration methods, these measurements become particularly valuable at times when standard calibration procedures malfunction (Bourdillon and Delloue 1994). So far, it has only been possible to calibrate the manifold of HF arrays using external sources of opportunity (Solomon 1998). The complimentary problem of correcting for receiver mismatch using *HF sources of opportunity* has, to the authors knowledge, not yet been addressed and is the subject of the current chapter.

6.1.2 Studies on receiver mismatch

A two channel model of a tap-delay line compensated adaptive processor is shown in Figure 6.1, the reference and auxiliary channel transfer functions are denoted by $H_R(f)$ and $H_A(f)$ respectively. Traditionally, a powerful source of wideband noise is injected at

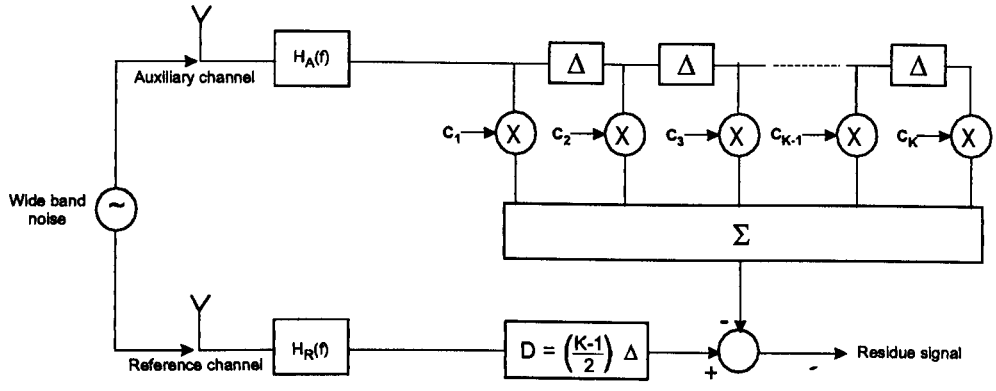

Figure 6.1: A two channel compensated adaptive processor in self-cancellation mode

the channel inputs and the complex valued transversal filter coefficients are adjusted so that the power of the output difference signal (i.e., the residue signal) is minimised.

Closed form solutions for the optimal filter coefficients are traditionally derived in accordance with the unconstrained least squares criterion, as in (Monzingo and Miller 1980), (Lewis, Kretschmer and Shelton 1986) and (Farina 1992). The effectiveness of the compensation is measured in terms of the cancellation ratio, which is the ratio of the input wideband noise power to the output residue power. A good compensator yields a high cancellation ratio while a poor compensator yields a low cancellation ratio. The achievable cancellation ratio depends on the characteristics of the frequency mismatch, the dimensionality of the compensator (the number of taps K) and the product between the tap delay (Δ) and the analog filter bandwidth.

Based on filters of the Butterworth type, a pole-zero error model of the channel transfer functions was used by (Lewis et al. 1986) to derive analytical expressions for the maximum achievable cancellation ratio as a function of the adaptive canceller system parameters. The author used these results to propose a procedure for "optimising" the design of an adaptive canceller with respect to both system parameters and constraints. The relationship between cancellation ratio and adaptive canceller system parameters was also analysed for sinusoidal amplitude and phase mismatches by (Monzingo and Miller 1980) and for triangular amplitude and linear phase mismatch by (Farina 1992). In all cases, the transversal filter coefficients were adjusted using the least squares principle.

The practical importance of digital channel equalisation was experimentally demonstrated by (Johnson, Fenn, Aumann and Willwerth 1991). A four channel L-band adaptive nulling system with a frequency range of 1.25 to 1.35 GHz was used in conjunction with a 16 tap equaliser to cancel a powerful wideband jammer injected into the receiver inputs. A cancellation ratio of approximately 50 dB was achieved by the four channel system after equalisation. Moreover, the inclusion of digital equalisers in the auxiliary channels was found to improve the cancellation ratio by approximately 20 dB and 10 dB when one and three auxiliary channels were used respectively. These results demonstrate that the degradation in cancellation ratio caused by receiver mismatch can be reduced by in-

creasing the number of such receivers in the array. Naturally, it is preferable to avoid degradations in cancellation ratio by adaptively correcting the existing receivers.

An experimental adaptive array radar system was used by (Teitelbaum 1991) to investigate the effectiveness of 31 tap transversal digital filters for channel equalisation. For a two channel system, measurements of the transfer functions over a 600 kHz bandwidth revealed amplitude and phase mismatches within plus or minus 2 dB and 30 degrees respectively. Such mismatches were found to limit the cancellation ratio to approximately 20 dB, this ratio was restored to approximately 65 dB after equalisation. These results demonstrate that the receiver mismatch does not need to be very large for the cancellation ratio to drop by as much as 45 dB, such a large degradation due to instrumental errors can impact greatly on system performance when powerful interference is present.

Compensation for receiver mismatch can also be applied in the frequency domain by performing an FFT on segments of data taken at the output of the reference and auxiliary reception channels (Abramovich, Kachur and Struchev 1984). In this case, compensation is applied via a direct weighting of the FFT outputs in the auxiliary channel(s) over the frequency range of interest. The complex valued weights are also estimated according to the least squares principle, the optimum weighting at a particular point in the passband is determined by the ratio of the reference to auxiliary channel response at the particular frequency. The statistical variability of the estimated corrections due to finite sample effects was quantified for the frequency domain in (Abramovich and Kachur 1987). It has been shown by (Compton 1988b) that identical compensation can be provided by an equivalent tap-delay line which has the same number of taps as the number of time samples in the FFT with a tap spacing equal to the delay between samples in the FFT. The equivalent tap-delay line filter coefficients are given by the inverse FFT of the frequency domain compensation weights.

6.1.3 Significance of research relative to previous work

HF sources of opportunity are normally received via the ionosphere, and in this medium, propagation is most often by multipath components or signal modes whose temporal and spatial characteristics are affected by the random and dynamic nature of the ionospheric reflection process. As a result of uncertain propagation effects, the precise temporal and spatial structure of the signal mode(s) received by an antenna array are generally unknown and time-varying, such effects were quantitatively demonstrated in chapters 2 and 3. Standard least squares techniques commonly used to equalise multi-channel digital receivers, such as those described in (Farina 1992, Monzingo and Miller 1980, Johnson et al. 1991, Abramovich et al. 1984, Lewis et al. 1986), rely on specific assumptions regarding signal structure, particularly the spatial structure, and as a consequence they fail to provide effective corrections in the multipath HF environment.

An alternative approach is to use space-time adaptive processing (STAP) which can,

in principle, mitigate co-channel interference and compensate for the effects of channel mismatch at the same time. However, in practice the interference environment typically changes much faster than do the passband characteristics of the reception channels. Under these conditions, compensation for receiver mismatch can be applied separately and updated at a much slower rate than the adaptive processor used to cancel interference. This approach is justifiable because compensation for receiver mismatch relates only to the properties of the receiving system and hence remains effective regardless of changes in the interference environment.

The degradation in cancellation ratio caused by receiver mismatch in a STAP processor of fixed dimensions was simulated by (Fante and Vacarro 1998), while the application of digital channel equalisers to pre-process the output of each auxiliary channel before STAP was investigated by (Shunjun and Yingjun 1995). The main advantage of providing separate and prior compensation for receiver mismatch is that it reduces the dimensionality or number of degrees of freedom needed by the adaptive processor to effectively cancel the external interference(s). A reduction in processor dimensionality has two significant advantages in real-time applications. Firstly, adaptive algorithms converge more rapidly when the weight vector estimated from a finite sample size has a lower dimensionality (Reed et al. 1974), and secondly, the computational load which is typically proportional to the cube of the weight vector dimension is drastically reduced.

This chapter is concerned with the problem of estimating separate compensation for receiver mismatch in HF antenna arrays using passive sources of opportunity (interference). This complements the work of (Solomon 1998) which addressed the problem of correcting for array manifold errors using active sources of opportunity (meteor echoes). Complete equalisation of the reception channels in a HF antenna array can, in theory, be achieved through the sequential application of receiver mismatch compensation and array manifold corrections.

6.2 Interference Model

The most suitable HF sources of opportunity for receiver mismatch compensation have been identified as amplitude modulated (AM) radio broadcasts. These sources are present in large numbers and are widely dispersed in both geography and frequency over the HF band. Particular sources can be readily identified and selected by consulting broadcasting schedules (Sennitt and Kuperus 1997). A space-time model for AM sources of opportunity received by narrowband antenna arrays is first developed for the case of perfectly calibrated receivers, a frequency domain version of this model is then developed to include the effects of receiver mismatch.

6.2.1 Space-time model for perfectly calibrated receivers

Let $\mathbf{x}_l(t)$ denote the complex N-dimensional snapshot vector received by a narrowband antenna array with perfectly calibrated receivers at l^{th} fast-time sample in the t^{th} pulse repetition interval (PRI). The parameters of the Jindalee receiving system used to perform the experiment (to be described in section 6.4) were $N = 32$ digital receivers, $L = 2500$ fast-time samples and $P = 256$ PRI in each coherent processing interval (CPI). The output of the n^{th} receiving element is expressed as,

$$\mathbf{x}_l^{[n]}(t) = \mathbf{i}_l^{[n]}(t) + \mathbf{n}_l^{[n]}(t) \begin{cases} n &= 1,2,..,N = 32 \text{ digital receivers} \\ t &= 1,2,..,P = 256 \text{ linear FM PRI} \\ l &= 1,2,..,L = 2500 \text{ fast-time samples} \end{cases} \tag{6.1}$$

where $\mathbf{i}_l^{[n]}(t)$ is the interference signal and $\mathbf{n}_l^{[n]}(t)$ is uncorrelated receiver noise. For M ionospherically-propagated interference modes we adopt the following space-time model for the received interference signal.

$$\mathbf{i}_l^{[n]}(t) = \sum_{m=1}^{M} \Psi_n(f_c, \alpha_m, \beta_m)\Phi_n(f_c)A_{m,n}(t)g(t/f_p + lT_s - \tau_m)e^{j2\pi\frac{\Delta f_m}{f_p}t}e^{j2\pi n\frac{\Delta d}{\lambda}\sin\alpha_m\cos\beta_m} \tag{6.2}$$

Before describing the various terms in Eqn.(6.2) it is worthwhile to explain how this model relates to the wave interference and stationary statistical models previously considered in chapters 2 and 3 respectively. The main point to note is that these models are special cases of the current model in Eqn.(6.2). The current model is more general than the previously considered models in the sense that it makes no assumptions regarding the *statistical properties* of the propagation channel. For this reason, such a model may be relevant for the purpose of receiver mismatch compensation using sources of opportunity which are propagated by channels different from the HF channel.

The terms Δf_m, α_m and β_m for $m = 1,2,..,M$ are the mode Doppler shifts, azimuth angles of arrival and elevation angles of arrival respectively, τ_m is the time delay taken by the m^{th} mode to travel from the emitter to the first receiver of the array, Δd is the distance between adjacent antenna sensors, λ is the carrier wavelength and $T_s = 1/(Lf_p)$ is the fast-time sampling period.

The complex scalar $\Psi_n(f_c, \alpha_m, \beta_m)$ represents the directional gain and phase response of the n^{th} antenna sensor to the m^{th} interference mode, while the complex scalar $\Phi_n(f_c)$ represents the gain and phase response of the amplifiers and cables which connect the n^{th} antenna sensor to the n^{th} receiving module. The terms $\Psi_n(f_c, \alpha_m, \beta_m)$ and $\Phi_n(f_c)$ vary with carrier frequency f_c but are assumed constant over the passband of narrowband HF arrays which typically is in the order of a few kilohertz. These two terms represent the passband-independent array manifold errors.

The complex scalar $A_{m,n}(t)$ represents the random temporal and spatial distortions imposed by the movement of irregularities in the ionosphere on the m^{th} mode, these ionospherically induced amplitude and phase modulations give rise to Doppler spread and angular spread on each mode (Fabrizio, Gray, Turley and Anderson 1998). This term also accounts for attenuations in signal amplitude due to path loss (inverse square law) and polarisation mismatch between the incident wave and the receiving antennas. With reference to the previous statistical model, the term $A_{m,n}(t)$ plays an analogous role to the n^{th} element of the vector $c_m(t)$. However, unlike the vector $c_m(t)$ which was described by a two-dimensional (space-time) stationary auto-regressive model, the term $A_{m,n}(t)$ is not required to conform to a specific model and may even be a non-stationary process with respect to slow-time (t) and receiver (n). Note that $A_{m,n}(t)$ is independent of fast-time (l), this assumes that the pulse repetition interval is relatively short compared with the time scale of ionospheric fluctuations. The assumption of a "frozen" ionosphere over the PRI is later shown to be quite reasonable for PRI's with a duration of less than one tenth of a second. The passband-independence of $A_{m,n}(t)$ implicitly assumes a dispersionless ionospheric propagation channel, this assumption is justifiable for receiver passbands in the order of a few kilohertz (Watterson et al. 1970).

The scalar function $g(t/f_p + lT_s - \tau_m)$ represents the complex envelope of the transmitted signal waveform, after it is mixed with the local oscillator, filtered by the perfectly calibrated receivers and evaluated at the differential time delay τ_m. Most of the power in *AM radio broadcasts* is transmitted over a small effective bandwidth B_{eff} which is centered around the strong carrier frequency component. The mode waveforms are highly correlated with one another if the condition $B_{eff}\delta_m \ll 1$ is satisfied $\forall m = 1, 2, .., M$, where $\delta_m = \tau_m - \tau_{m_{ref}}$ is the time-of-arrival of mode m relative to a reference mode m_{ref}. As this is typically the case for AM signals, each mode waveform can be related to the reference mode waveform by the corresponding phase shift $e^{j2\pi f_c \delta_m}$. By substituting $g(t/f_p + lT_s - \tau_m) = e^{j2\pi f_c \delta_m} g(t/f_p + lT_s - \tau_{m_{ref}})$ into Eqn.(6.2) the interference signal can be written more compactly as,

$$\mathrm{i}_l^{[n]}(t) = \Gamma_n(t) g(t/f_p + lT_s - \tau_{m_{ref}}) \tag{6.3}$$

where the complex scalar $\Gamma^{[n]}(t)$ is given by Eqn.(6.4). Note that this expression may not be valid if the received signal comes from a broadband source and the relative time-delays existing between different propagation modes are sufficiently high to effectively de-correlate the modes.

$$\Gamma_n(t) = \sum_{m=1}^{M} \Psi_n(f_c, \theta_m, \phi_m) \Phi_n(f_c) A_{m,n}(t) e^{j2\pi f_c \delta_m} e^{j2\pi \frac{f_m}{f_p} t} e^{j2\pi n \frac{d}{\lambda} \sin\theta_m \cos\phi_m} \tag{6.4}$$

Although $\Gamma_n(t)$ is a random process causing some uncertainty in the signal structure, we note that this term is independent of fast-time (l). In other words, the interference

snapshots $\mathbf{i}_l^{[n]}(t)$ recorded during a particular PRI are expected to have the same (but unknown) spatial structure in the *absence* of receiver mismatch.

6.2.2 Frequency domain model with receiver mismatch

Range processing is performed by taking a windowed Fast Fourier Transform (FFT) of the fast-time samples $\mathbf{x}_l^{[n]}(t)$ recorded in each PRI. The FFT outputs denoted by $\mathbf{x}_k^{[n]}(t)$ are often termed range samples; the frequency domain samples retained are indexed according to the frequency bin $k = 1, 2, .., K$ over the receiver passband (K=42). Mixing the continuous waveform (CW) carrier component of the AM signal with a linear FM waveform yields an output that is also linear FM. Obviously, the instantaneous frequency of the down converted AM signal is not linearly dependent on the group range of the emitter. In general, the *output* linear FM signal corresponding to the received CW component has a frequency content that spreads across receiver passband so that all frequency bins $k = 1, 2, .., K$ are "interrogated" by the signal of opportunity.

By defining $h_{n,k}$ as the complex frequency response of the n^{th} (non-ideal) receiver at the k^{th} frequency bin, we can introduce receiver mismatch by writing the range processed outputs $\tilde{\mathbf{x}}_k^{[n]}(t)$ in the following way,

$$\tilde{\mathbf{x}}_k^{[n]}(t) = h_{n,k}\mathbf{x}_k^{[n]}(t) = h_{n,k}\Gamma_n(t)g_k(t) + \tilde{\mathbf{n}}_k^{[n]}(t) \tag{6.5}$$

since, as discussed above, $\Gamma_n(t)$ is independent of fast-time. In Eqn.(6.5), the complex scalar $g_k(t)$ is the k^{th} FFT output calculated from the L fast-time samples of the reference mode waveform $g(t/f_p + lT_s - \tau_{m_{ref}})$ and $\tilde{\mathbf{n}}_k^{[n]}(t)$ is the k^{th} FFT output arising due to additive noise.

The model described by Eqn.(6.5) has quite general statistical properties and may therefore be relevant in other adaptive array applications where multipath signals with time-varying spatial and Doppler signatures arise due to other physical phenomena. For example, a mathematically equivalent slow-time model was used in (Hayward 1997) to represent line-of-sight interference received by adaptive sensor arrays mounted on rapidly moving platforms. Another operational situation of interest in the area of airborne antenna arrays results when a stand-off jammer (SOJ) deliberately directs the jamming beam towards the ground to produce a reflected jammer that is highly correlated with the direct path jammer (Farina 1992). In this case, the relative motion between the transmitting source and the receiving platform can lead to significant variation in spatial and temporal structure of the incident signal modes over the coherent processing interval(CPI). If the signal scenario can be assumed "frozen" over a short pulse repetition interval (PRI) and the narrowband assumption is valid then such a model seems appropriate for representing the received interference.

6.3 Compensation algorithm

Existing techniques used for receiver frequency response equalisation are overviewed in this section and reasons are given for the inapplicability of such techniques to the multipath HF environment. Based on the interference model developed in the previous section, a different estimator is proposed for receiver mismatch compensation and its significance is explained in relation to existing techniques.

6.3.1 Existing techniques

Let $\mathbf{c} = [c_1 c_2 \cdots c_K]^T$ be the complex digital frequency response corrections required to match the transfer function of an auxiliary channel "a" with respect to a reference channel "r" at K discrete and equally spaced frequencies within the passband. The reference channel is usually chosen arbitrarily when all the reception channels in the array have the same nominal characteristics, in some applications the array contains one more highly directional sensor which forms a natural choice for the reference channel.

In the frequency domain, weighting the k^{th} FFT output of the auxiliary channel by the k^{th} element of the correction vector $\mathbf{c}$ achieves the equalisation objective. In the time domain, the inverse FFT of the elements in $\mathbf{c}$ yields the transversal filter coefficients of an equivalent equaliser based on a K-tap delay line. As the receivers only operate on down converted signals the compensation for receiver mismatch remains effective at different carrier frequencies, this point is illustrated in the results section.

To estimate the equaliser $\mathbf{c}$, a signal source must be used to "probe" the passbands of the reference and auxiliary receivers and a noise source with a bandwidth greater than the receiver passbands is often used for this purpose. Indirect equalisation techniques (Farina 1992) estimate the compensation by injecting a wideband noise source at the reference and auxiliary receiver inputs (after the antennas), in (Lewis et al. 1986) this mode of operation is referred to as the self-cancellation mode. The disadvantage of indirect methods is that they cannot account for array manifold errors in the antenna sensors and they generally require an extra calibration of the distribution network which is used to carry the signals from the noise source to each receiver input.

Direct equalisation techniques estimate the compensation by using an antenna to transmit a wideband signal which is received directly (line-of-sight) by the antennas of the receiving array. The signal source is most conveniently placed at broadside for linear arrays so that planar or perfectly coherent wavefronts are incident at the antenna sensors. Although direct methods can additionally compensate for array manifold errors and there is no distribution network to speak of, there may be unwanted multipath and for very large HF arrays such sources cannot be placed in the far-field and in the line-of-sight at the same time.

For both direct and indirect equalisation techniques, the least squares criterion is the

mathematical foundation for estimating the frequency response corrections $\mathbf{c}$. In our application, the estimate of $\mathbf{c}$ is optimised according to this criterion by finding,

$$\hat{\mathbf{c}} = \arg\min \sum_{t=1}^{P} \|\mathbf{z}(t) - \mathbf{Y}(t)\mathbf{c}\|_F \tag{6.6}$$

where the column vector $\mathbf{z}(t) = [\mathbf{x}_1^{[r]}(t)\mathbf{x}_2^{[r]}(t)\cdots\mathbf{x}_K^{[r]}(t)]^T$, the $K \times K$ diagonal matrix $\mathbf{Y}(t) = diag[\mathbf{x}_1^{[a]}(t)\mathbf{x}_2^{[a]}(t)\cdots\mathbf{x}_K^{[a]}(t)]^T$ and $\|\cdot\|_F$ denotes the Frobenius or squared Euclidean norm. It can be shown that the vector $\hat{\mathbf{c}}$ is given by,

$$\hat{\mathbf{c}} = [\sum_{t=1}^{P} \mathbf{Y}^H(t)\mathbf{Y}(t)\,]^{-1} \sum_{t=1}^{P} \mathbf{Y}^H(t)\mathbf{z}(t) \tag{6.7}$$

where H denotes the conjugate transpose or Hermitian operator.

The unconstrained least squares estimator described above is not suitable for application to HF interference signals of opportunity described by the multipath model in the previous section. To see this, consider a time-varying complex correction vector $\mathbf{c}(t)$ which perfectly cancels the *interference component* of the partial error $\|\mathbf{z}(t) - \mathbf{Y}(t)\mathbf{c}(t)\|_F$ at time t. Using Eqn.(6.5), it can be shown that the vector providing perfect cancellation of the *interference component* is given by $\mathbf{c}(t) = \Gamma_r(t)/\Gamma_a(t)\mathbf{c}$, where $\mathbf{c}$ represents the true or required equalisation vector.

Since ionospherically-propagated multipath interference generally does not satisfy the condition $\Gamma_r(t) = \Gamma_a(t)$, the vector $\mathbf{c}(t)$ may not be equal to the required equalisation vector $\mathbf{c}$ at any time $t = 1, 2, .., P$ during the averaging interval. As a result, the vector $\hat{\mathbf{c}}$ estimated by Eqn.(6.6) is additionally (and perhaps mostly) determined by the interference characteristics rather than those of the receiver passbands. It is for this reason that corrections which effectively compensate for receiver mismatch cannot be derived in the multipath HF environment using the standard (unconstrained) least squares criterion.

The same interference model can be used to interpret the self-cancellation mode described earlier. In the self-cancellation mode the same signal, denoted by $g_k(t)$, enters both receivers and this is equivalent to setting $\Gamma_r(t) = \Gamma_a(t) = 1$ in Eqn.(6.5). Under this condition, the vector $\mathbf{c}(t) = \Gamma_r(t)/\Gamma_a(t)\mathbf{c}$ becomes time (t)-invariant and equals the true or required equalisation vector $\mathbf{c}$ over the whole averaging interval. Minimising the sum of partial errors over $t = 1, 2, .., P$ is performed to improve the estimate of $\mathbf{c}$ in the presence of uncorrelated receiver noise.

6.3.2 Proposed algorithm

The following linearly constrained and weighted least squares estimator is proposed for HF sources of opportunity,

$$\hat{\mathbf{c}}_a = \arg\min \sum_{t=1}^{P} \mathbf{z}^H(t)\mathbf{z}(t)\, \|\alpha(t)\mathbf{z}(t) - \mathbf{Y}(t)\mathbf{c}_a\|_F \quad \text{subject to : } \mathbf{c}_a^H\mathbf{e} = 1 \tag{6.8}$$

where $\alpha(t)$ is a complex scalar, $\mathbf{c}_a$ is an alternative frequency domain compensation vector and $\mathbf{e} = [0\ \cdots\ 0\ 1\ 0 \cdots 0]^T$ is a K-dimensional constraint vector with a one in position k_{ref} and zeros elsewhere. This estimator differs from that in Eqn.(6.6) due to the inclusion of a linear constraint and the two data-dependent weighting terms $\mathbf{z}^H(t)\mathbf{z}(t)$ and $\alpha(t)$.

Let us first consider the effect of including the complex scalar $\alpha(t)$ and the linear constraint $\mathbf{c}_a^H\mathbf{e} = 1$. The complex scalar $\alpha(t)$ is unconstrained and its value is found as part of the optimisation problem, in appendix D the value of $\alpha(t)$ is calculated so that it minimises the partial error term $\|\alpha(t)\mathbf{z}(t) - \mathbf{Y}(t)\mathbf{c}_a\|_F$ at time t for any arbitrary (non-zero) vector $\mathbf{c}_a$. The linear constraint is incorporated to ensure that a *fixed* vector $\mathbf{c}_a$, to be discussed below, perfectly cancels the *interference component* of all the partial error terms being averaged $t = 1, 2, .., P$. To explain the relationship between the corrections $\mathbf{c}_a$ and $\mathbf{c}$, consider the time-varying vector $\mathbf{c}_a(t)$ which perfectly cancels the interference component of the partial error $\|\alpha(t)\mathbf{z}(t) - \mathbf{Y}(t)\mathbf{c}_a(t)\|_F$ at time t. Using Eqn.(6.5), it can be shown that the vector providing perfect cancellation is given by $\mathbf{c}_a(t) = \alpha(t)\Gamma_r(t)/\Gamma_a(t)\mathbf{c}$, where $\mathbf{c}$ represents the equalisation vector as before. If the k_{ref} element of $\mathbf{c}_a(t)$ is fixed to unity by the constraint then perfect (interference) cancellation occurs when $\alpha(t) = \Gamma_a(t)/\Gamma_r(t)\mathbf{c}^{[k_{ref}]}$ and $\mathbf{c}_a(t) = \mathbf{c}/\mathbf{c}^{[k_{ref}]}$.

In other words, the time (t)-invariant vector $\mathbf{c}_a = \mathbf{c}/\mathbf{c}^{[k_{ref}]}$ estimated as $\hat{\mathbf{c}}_a$ in Eqn.(6.8) is the equalising vector $\mathbf{c}$ normalised by the k_{ref} element of this vector. The aim of the estimated corrections $\hat{\mathbf{c}}_a$ is not to strictly equalise the channels but rather to relate the auxiliary and reference channel transfer functions by *a complex scalar* $\mathbf{c}^{[k_{ref}]}$. This passband-independent difference between the channel transfer functions constitutes an array manifold error which can be compensated (if necessary) with other sources of opportunity using the calibration techniques developed and tested in (Solomon 1998). When no prior information is available regarding the channel passbands, the reference frequency bin k_{ref} can be chosen arbitrarily. Some systems make use of a CW signal to equalise the channel frequency responses at a discrete frequency within the passband (Farina 1992), k_{ref} should then be selected as the equalised frequency bin so that $\mathbf{c}^{[k_{ref}]} = 1$ and the corrections $\hat{\mathbf{c}}_a$ aim to strictly equalise the channels.

The effect of additive noise on the estimate $\hat{\mathbf{c}}_a$ is reduced by the weighting term $\mathbf{z}^H(t)\mathbf{z}(t)$ and the statistical average over $t = 1, 2, .., P$. The influence of additive noise is most pronounced when the source of opportunity exhibits a deep fade at the reference antenna sensor *at the same time* as a comparatively high signal level at the auxiliary

antenna sensor. This situation corresponds to a low value of $\Gamma_r(t)$ and a comparatively high value of $\Gamma_a(t)$. The scalar $\alpha(t)$ has a large magnitude at such instants which effectively amplifies the noisy reference signal $\mathbf{z}(t)$ in Eqn.(6.8). The weighting term $\mathbf{z}^H(t)\mathbf{z}(t)$ reduces the effect of this unwanted amplification on the estimate of $\mathbf{c}_a$ by *weighting down* the contribution of the partial error $\|\alpha(t)\mathbf{z}(t) - \mathbf{Y}(t)\mathbf{c}_a\|_F$ arising at such instants.

In appendix D it is shown that the solution of Eqn.(6.8) can be expressed in closed form and is given by,

$$\hat{\mathbf{c}}_a = \frac{\mathbf{Q}^{-1}\mathbf{e}}{\mathbf{e}^T\mathbf{Q}^{-1}\mathbf{e}} \tag{6.9}$$

where $\mathbf{Q} = \sum_{t=1}^{P}\{\mathbf{z}^H(t)\mathbf{z}(t)\mathbf{Y}^H(t)\mathbf{Y}(t) - \mathbf{Y}^H(t)\mathbf{z}(t)\mathbf{z}^H(t)\mathbf{Y}(t)\}$.

6.4 Data collection and array calibration

Three experiments were conducted to collect data for this study. Section 6.4.1 describes these experiments which involve the recording of a source of opportunity, a broadband interference and the receiver frequency response measurements from the Jindalee array calibration system. The essential features of the Jindalee array calibration system are qualitatively described in section 6.4.2, further information is available in (Solomon 1998).

6.4.1 Data collection

In experiment A, the Jindalee OTH radar receiving array described in section 2.2 was tuned to receive an AM radio broadcast of opportunity at a carrier frequency of 13.830 MHz. This data was received on 4 April 1998 at 05:59 UT using an FMCW pulse repetition frequency of 10 Hz, a sweep bandwidth of 8 kHz and a CPI of 25.6 seconds. The AM source of opportunity is used to estimate digital frequency response corrections for real mismatches in the 32 receivers of the Jindalee array.

In experiment B, the Jindalee OTH radar receiving array was tuned to a carrier frequency of 12.877 MHz to receive broadband interference, this experiment was conducted on 4 April 1998 at 05:47 UT (12 minutes prior to experiment A). The broadband interference was received using identical system parameters as experiment A (only the carrier frequency was changed), this signal is particularly severe because it masks the entire range-Doppler search space and is incident from a number of directions. Hence, from the point of view of Doppler processing, the mitigation of this broadband interference is a spatial filtering problem.

The Jindalee array calibration system described below was used to measure the receiver transfer functions immediately prior to the collection of the two data sets. The gain and phase measurements made by this system are normally used to calibrate the Jindalee array and may be considered as "ground truth" measurements of the receiver transfer

functions when it comes to evaluating compensation estimated by alternative methods which use sources of opportunity.

6.4.2 Array calibration

Jindalee performs calibration by injecting a CW signal at a calibration port located immediately behind the hardware beamformer corresponding to each subarray, as indicated in Figure 2.1. The linear FM signal which results at the output of the mixer probes the passbands of the IF and baseband filters in each reception channel before being digitised by the A/D converter.

The FFT of the digital samples resulting at the output of each reception channel is then compared with that theoretically expected for receivers with a constant amplitude and linear phase response expected over the frequency range of interest. Calibration weights are then computed so that multiplication of the FFT outputs by these weights reconciles the measured frequency domain samples with those expected for ideal receivers. The inverse of these weights represents a normalised measurement of the receiver transfer function in each reception channel. Under normal operating conditions, the calibration weight estimates are very accurate due to the high SNR of the calibration signal and the stability of the oscillators and waveform generator.

All hardware components upstream from the calibration port are unobservable so the calibration system does not attempt to measure the directional characteristics of the antenna sensors. However, it does measure the carrier frequency dependent responses of cables and amplifiers, and importantly, the frequency responses of all the receiver passbands. Calibration is performed regularly under normal operational conditions since gain and phase errors in the reception channels also depend on environmental factors such as external temperature which changes over time.

The array manifold errors contributed by the non-identical amplifier and cables are dependent on carrier frequency so the calibration weights need to be updated when the carrier frequency is changed. On the other hand, the gain and phase errors due to receiver filter mistuning do not depend on carrier frequency but need to be updated when the pulse repetition frequency or bandwidth of the mixing waveform changes because the FFT outputs sample different points of the analog receiver passbands.

6.5 Experimental results

The experimental results which demonstrate the performance of the proposed receiver mismatch compensation algorithm are presented in three sections. Section 6.5.1 plots measurements of two Jindalee receiver transfer functions to show the real receiver mismatch to be compensated. This section also shows the receiver transfer functions which result after applying the compensation estimated from the source of opportunity . The

impact of receiver mismatch on the spatial dynamic range of the Jindalee array is demonstrated for all 32 receivers using the source of opportunity in section 6.5.2. This section also compares the effectiveness of the compensation estimated by the Jindalee calibration system, the proposed algorithm and the standard least squares estimator. In section 6.5.3, the compensation estimated by these three methods is applied to a situation where adaptive spatial processing was required to cancel strong broadband interference and Doppler processing was required to detect a weak target-like signal.

6.5.1 Estimating compensation for receiver mismatch

Curves 1 and 2 in Figure 6.2 show the amplitude response of a reference and auxiliary channel transfer function respectively as measured by the Jindalee array calibration system. Curve 3 in Figure 6.2 shows the ratio of the reference amplitude to the auxiliary amplitude, the *variation* exhibited by Curve 3 over the passband is a consequence of receiver mismatch. The vertical axis on the left hand side of Figure 6.3 relates only to Curves 1 and 2 which show the phase response of the reference and auxiliary channels respectively. The absolute difference in phase of approximately 170 degrees is due to the unequal length cables which carry the signals from the antenna sensors to the receivers in these two channels. A longer cable is associated with a greater time delay and hence a larger phase shift. Curve 3 in Figure 6.3 relates to the right vertical axis and shows the difference in phase between the reference and auxiliary channel over the receiver passband of interest. The *variation* exhibited by Curve 3 in Figure 6.3 over the passband is a result of receiver mismatch.

Figures 6.4 and 6.5, in the same format as Figures 6.2 and 6.3, demonstrate the effect of applying the digital corrections estimated by Eqn.(6.8) to the auxiliary receiver transfer function. The flatness of Curve 3 in both these figures indicates that the amplitude and phase relationship between the two receiver transfer functions is approximately constant over the passband. A fixed relationship between the receiver transfer functions over the passband indicates that receiver mismatch has been compensated for and is no longer present. This example demonstrates that HF sources of opportunity can be used to estimate effective compensation for receiver mismatch.

The constant offset between the receiver transfer functions arises from the linear constraint used in Eqn.(6.8), but as noted in (Farina 1992), such offsets are compensated by adaptive sidelobe cancellation algorithms and do not affect interference cancellation performance. The offset between the receiver transfer functions constitutes an array manifold error which can degrade the output signal-to-interference and noise ratio (SINR) in adaptive beamforming applications. These degradations can be avoided by calibrating the array manifold errors with other HF sources of opportunity using the calibration techniques developed and tested by (Solomon 1998).

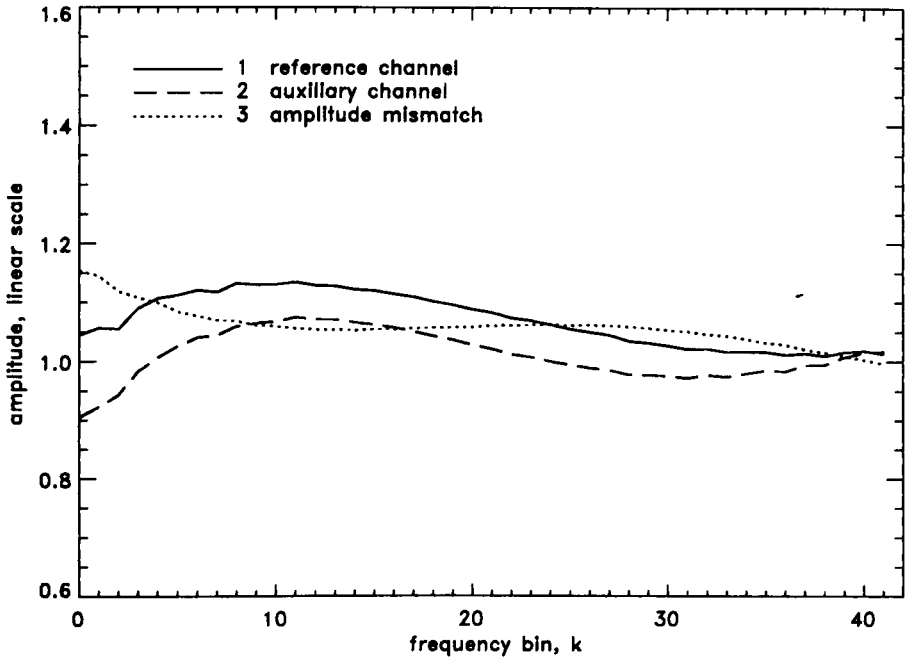

Figure 6.2: Amplitude of reference channel transfer function (curve 1) and auxiliary channel transfer function (curve 2). Curve 3 shows the amplitude mismatch as the ratio of the reference to the auxiliary channel amplitude over the passband of interest.

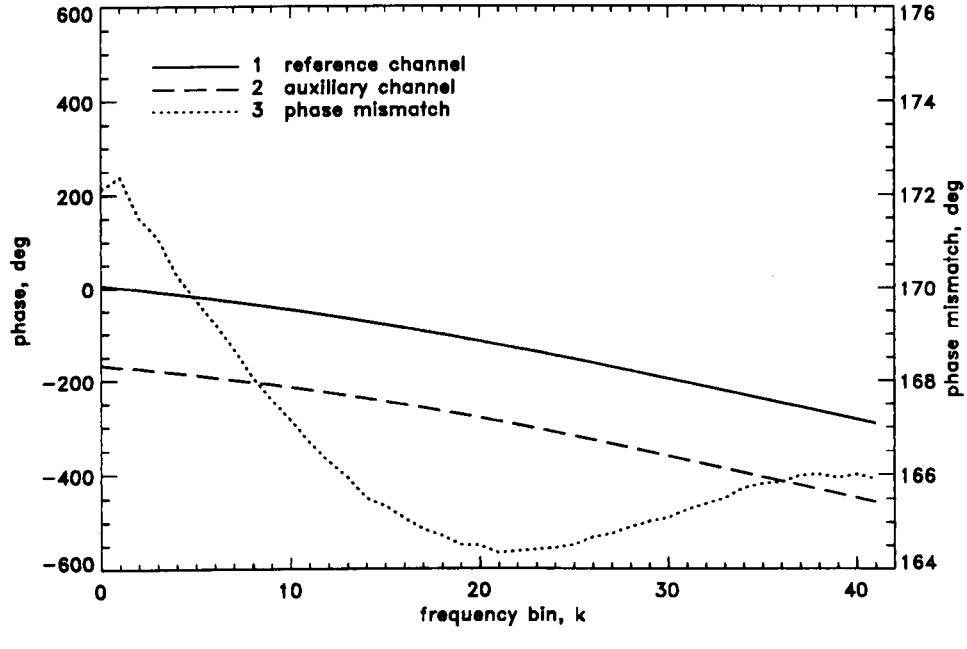

Figure 6.3: The left hand vertical axis shows the phase of the reference (curve 1) and auxiliary (curve 2) channel transfer functions. Curve 3 relates to the right hand vertical axis and shows the difference between the reference and auxiliary channel phases over the passband of interest.

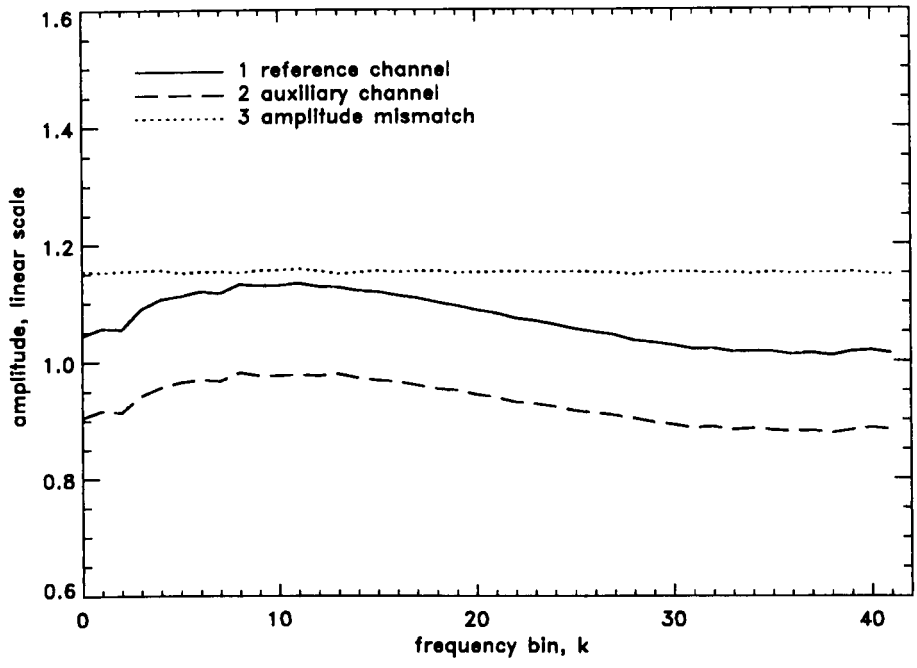

Figure 6.4: Curve 1 shows the amplitude of the reference channel transfer function. Curve 2 shows the amplitude of the auxiliary channel transfer function after the estimated compensation for channel mismatch is applied. Curve 3 shows the amplitude mismatch between the reference and auxiliary channels over the passband of interest.

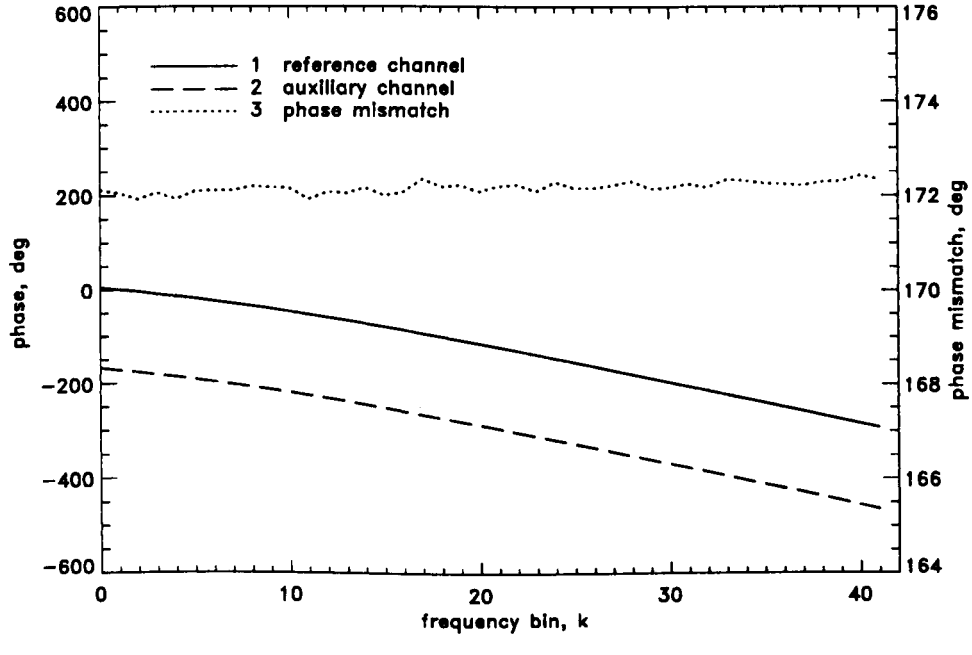

Figure 6.5: The left hand vertical axis shows the phase of the reference (curve 1) and compensated auxiliary (curve 2) channel transfer functions. Curve 3 relates to the right hand vertical axis an shows the phase difference between the two channels after compensation is applied to the auxiliary channel.

6.5.2 Effect of receiver mismatch on spatial dynamic range

The deleterious effects of receiver mismatch over all $N = 32$ reception channels can be appreciated by observing the eigenvalues of the sample spatial covariance matrices $\mathbf{R}(t)$ averaged over $K = 42$ retained range cells.

$$\mathbf{R}(t) = \frac{1}{K}\sum_{k=1}^{K}\mathbf{x}_k(t)\mathbf{x}_k^H(t) = \sum_{i=1}^{N}\lambda_i(t)\mathbf{q}_i(t)\mathbf{q}_i^H(t) \tag{6.10}$$

In Eqn.(6.10), $\mathbf{x}_k(t)$ represents the range processed array snapshots recorded from the *AM source of opportunity* after calibration with the Jindalee system, $\lambda_1(t) > \lambda_2(t) > \ldots > \lambda_N(t)$ are the eigenvalues of $\mathbf{R}(t)$ and $\mathbf{q}_1(t), \mathbf{q}_2(t), \ldots, \mathbf{q}_N(t)$ are the corresponding eigenvectors. According to the model developed in Eqn.(6.5), the interference component of $\mathbf{x}_k(t)$ is expected to have the same (but unknown) spatial structure for $k = 1, 2, .., K$ in the *absence* of receiver mismatch. As a consequence, the rank of the *interference subspace* of $\mathbf{R}(t)$ is expected to be unity for all t, a rank one interference subspace results in a large ratio between the two principle eigenvalues $\delta(t) = \frac{\lambda_1(t)}{\lambda_2(t)}$ when the interference-to-noise ratio is high. The presence of receiver mismatch destroys the uniformity in spatial structure with respect to frequency bin $k = 1, 2, .., K$ over the PRI, its presence therefore manifests itself as a reduction in the eigenvalue ratio which can also be interpreted as a reduction in the spatial dynamic range of the array.

To illustrate this, Curves 1 and 2 in Figure 6.6 show the eigenvalue ratios $\delta(t)$ and $\tilde{\delta}(t)$ respectively as a function of slow-time (t). The ratio $\tilde{\delta}(t)$ has been derived in identical manner to $\delta(t)$ by using the "raw" or uncalibrated array data $\tilde{\mathbf{x}}_k(t)$ instead of $\mathbf{x}_k(t)$. Note that on average $\tilde{\delta}(t)$ is approximately 25 dB smaller than $\delta(t)$, this significant loss in spatial dynamic range illustrates the impact of real receiver mismatch.

Curve 3 in Figure 6.6 shows the eigenvalue ratio when the compensation estimated according to Eqn.(6.8) was applied to all 32 receiver passbands of the "raw" or uncalibrated array. A comparison of Curves 1 and 3 in Figure 6.6 clearly shows that the eigenvalue ratio has been restored to the level seen by the array after calibration with the Jindalee system. The value of receiver mismatch compensation is later quantified in terms of the improvement in interference cancellation performance.

Figure 6.7 compares the results achieved by different estimators, Curves 1 and 2 are obtained using the estimator proposed in Eqn.(6.8) and the unconstrained least squares estimator in Eqn.(6.6) respectively. (Curve 1 in Figure 6.7 is a replica of Curve 3 in Figure 6.6 and is included here for comparison) It is clear that the proposed estimator greatly outperforms the unconstrained least squares method which does not improve on the uncalibrated array (Curve 2 in Figure 6.7). Curve 3 in Figure 6.7 is calculated by omitting the weighting term $\mathbf{z}^H(t)\mathbf{z}(t)$ in Eqn.(6.8), the 5 to 10 dB loss in performance relative to Curve 1 in Figure 6.7 demonstrates the need for including this weighting term to decrease estimation errors.

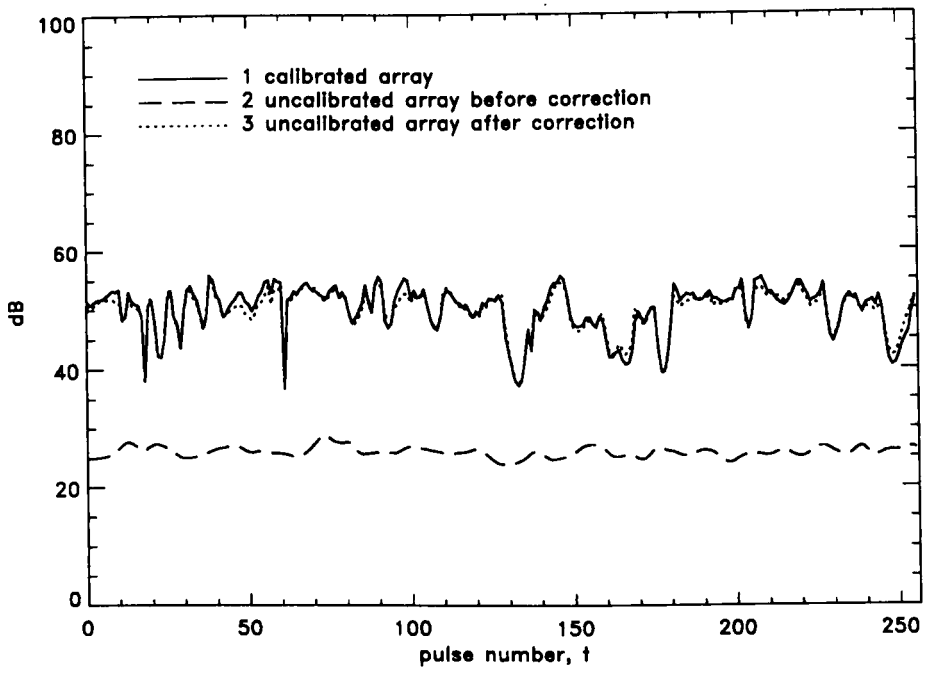

Figure 6.6: Curve 1 and Curve 2 show the ratios $\delta(t)$ (calibrated array) and $\tilde{\delta}(t)$ (uncalibrated array) respectively. Curve 3 shows the ratio when compensation estimated from the source of opportunity is applied to the uncalibrated array

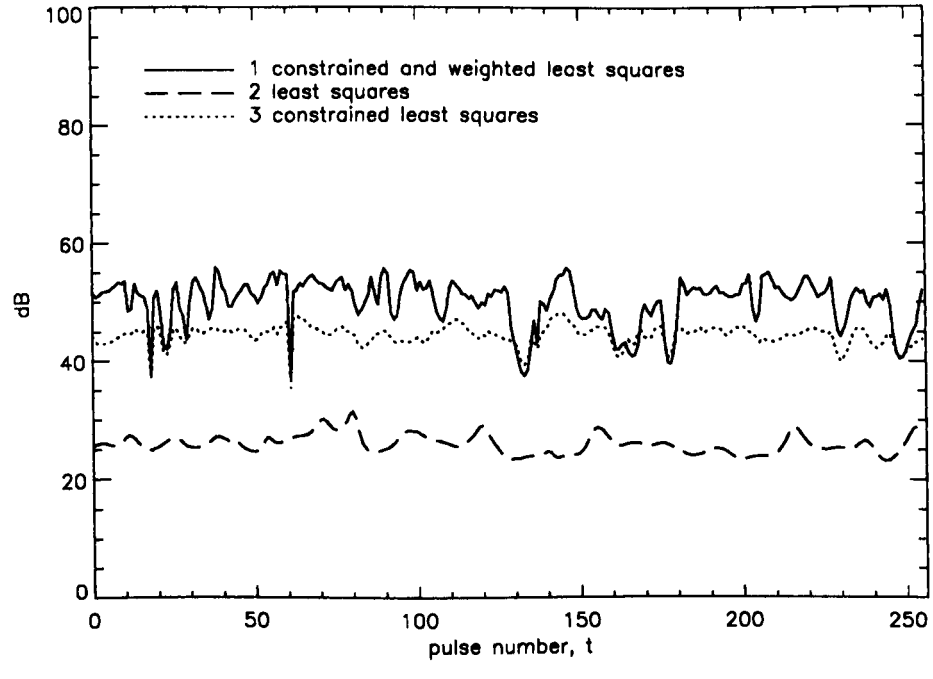

Figure 6.7: Curve 1 is a replica of Curve 3 in Figure 6.6. Curve 2 shows the ratio achieved by the applying compensation estimated according to the unconstrained least squares criterion on Eqn.(6.6). Curve 3 shows the ratio when the weighting term $\mathbf{z}^H(t)\mathbf{z}(t)$ is *omitted* from the proposed estimator in Eqn.(6.8).

As an aside, the interference model assumed that the fluctuations of the ionospheric propagation channel were "frozen" over the PRI with a duration of less than one tenth of a second. If this assumption is inaccurate the eigenvalue ratio of the array would be low even after the application of receiver mismatch compensation. However, the eigenvalue ratio increases by more than 25 dB over most of the coherent processing interval after compensation is applied, this very large increase indicates that the assumption of a "frozen" ionosphere is justifiable in our application for PRI shorter than one tenth of a second.

6.5.3 Application to adaptive spatial processing

To quantify the effect of compensation on subsequent radar processing, data from experiment B was used where the Jindalee array was tuned to receive broadband interference at a carrier frequency of 12.877 MHz 12 minutes prior to recording the AM source of opportunity. The spatial processing weight vector $\mathbf{w}$ for an adaptive sidelobe canceller (SLC) was calculated according to the sample matrix inverse technique (Reed et al. 1974) by using snapshots known to contain interference and noise only.

$$\hat{\mathbf{w}} = \frac{\hat{\mathbf{R}}^{-1}\mathbf{s}}{\mathbf{s}^H\hat{\mathbf{R}}^{-1}\mathbf{s}}\ ,\ \hat{\mathbf{R}} = \frac{2}{KP}\sum_{t=1}^{P}\sum_{k=1}^{\frac{K}{2}}\mathbf{x}_k(t)\mathbf{x}_k^H(t) \tag{6.11}$$

where the N-dimensional vector $\mathbf{s} = [1\ 0\ \cdots\ 0]^T$ implies that the first receiver is chosen as the reference receiver.

Before applying the SLC to the broadband interference, it is first shown that receiver mismatch is independent of carrier frequency and remains approximately constant over time intervals in the order of ten minutes. Curves 1 and 2 in Figure 6.8 show the amplitude responses of the reference channel measured by the Jindalee calibration system immediately prior to receiving the AM source of opportunity (05:59 UT) and the broadband interference (05:47 UT) respectively. Curve 3 in Figure 6.8 shows that variations in the ratio between the two amplitude responses is hardly noticeable over the passband of interest. Note that this example, which is representative of the other reception channels in the array, suggests that compensation for *receiver mismatch* estimated at one carrier frequency will remain effective at another.

Curve 3 in Figure 6.9 shows an analogous result for the phase variation of the reference channel. The absolute phase difference of approximately -23 degrees occurs because the time delay associated with the signal path in the reference channel translates to a phase shift which is proportional to the difference in carrier frequency. This carrier frequency dependence is represented by the term $\Phi_n(f_c)$ and is an array manifold error which can be corrected if necessary using the calibration methods proposed by (Solomon 1998).

To illustrate the directional characteristics of the broadband interference, MUSIC

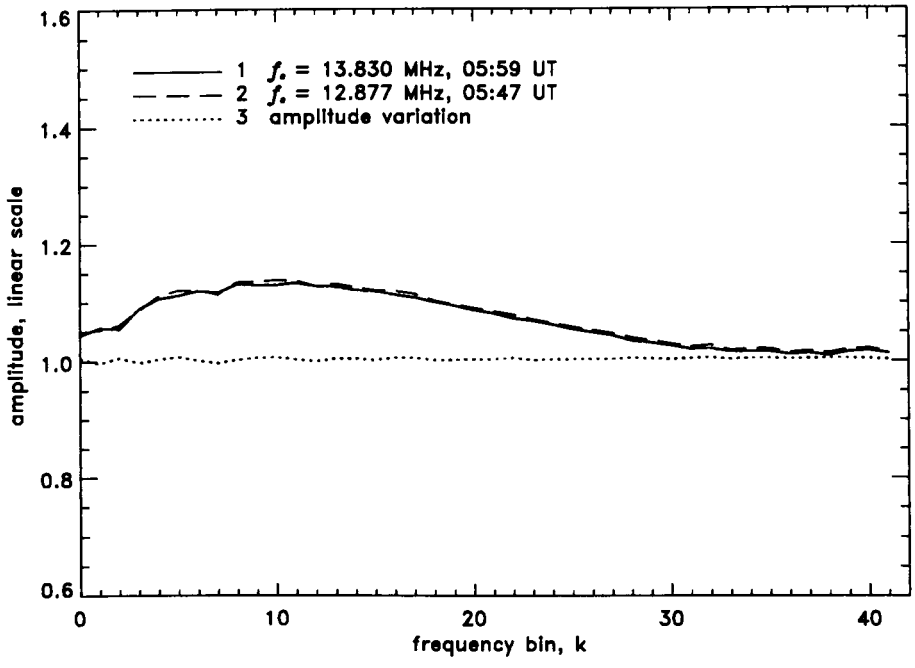

Figure 6.8: Curve 1 and Curve 2 show the amplitude of the reference channel transfer function prior to collecting the source of opportunity and broadband interference respectively. Curve 3 shows the amplitude variation over the passband of interest

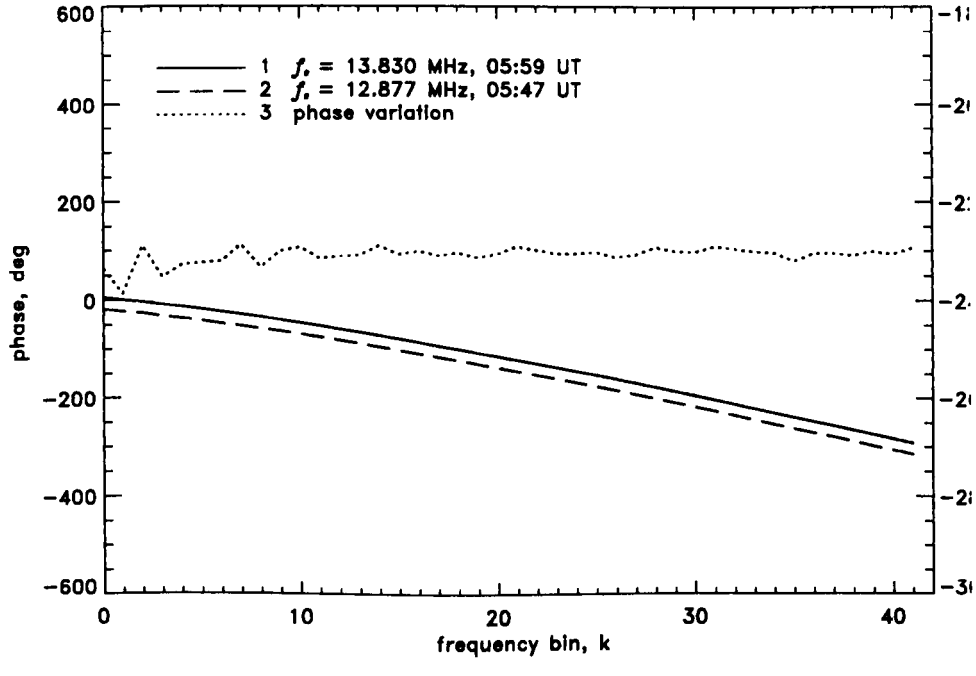

Figure 6.9: Curve 1 and Curve 2 show the phase of the reference channel transfer function prior to collecting the source of opportunity and broadband interference respectively. Curve 3 shows the phase variation observed over the passband of interest

spectra (Schmidt 1979) were computed for the matrix $\mathbf{R} = \sum_{t=1}^{P} \mathbf{R}(t)$ assuming different numbers of signals. Curves 1 and 2 in Figure 6.10 show the MUSIC spectrum resulting when five and six interference signals were assumed respectively. The existing peaks in Curve 1 become broader when six signals are assumed (Curve 2), but a sixth peak is not observed. A possible cause for this broadening is the angular spread imposed on the five dominant signals by the motion of irregularities in the ionospheric propagation medium during the coherent processing interval.

The scalar SLC output $y_k(t)$ corresponding to the broadband interference data after calibration with the Jindalee system is given by;

$$y_k(t) = \hat{\mathbf{w}}^H \mathbf{x}_k(t) \begin{cases} t &= 1, 2, .., P \\ k &= \frac{K}{2} + 1, \frac{K}{2} + 2, .., K \end{cases} \tag{6.12}$$

where the weight vector $\hat{\mathbf{w}}$ is calculated using Eqn.(6.11). Curve 1 in Figure 6.11 shows the Doppler spectra of the scalar SLC output $y_k(t)$ for a frequency or range bin known to contain a hardware (analog) generated desired signal at a Doppler frequency of 5 Hz. This signal was injected at the same time as receiving the broadband interference and has the range-Doppler characteristics of a target echo propagated via a stable ionosphere. Curve 2 in this figure shows the spectrum resulting when the data $\tilde{\mathbf{x}}_k(t)$ corresponding to the "raw" (uncalibrated) array is processed in identical manner. It is observed that the desired signal is no longer clearly distinguishable from the broadband interference and noise when receiver mismatch is present (Curve 2).

Curve 3 in Figure 6.11 shows the SLC output derived from the same data after applying the receiver passband corrections estimated from the AM source of opportunity. A comparison of curves 2 and 3 demonstrates that applying the frequency response corrections estimated by Eqn.(6.8) improves the output signal-to-noise ratio (SNR) of the SLC by approximately 10 dB. This improvement in output SNR allows the desired signal to be easily detected against the interference and noise. After applying compensation, both the signal and interference-plus-noise levels are similar to those seen by the array after calibration with the Jindalee system (Curve 1). This comparison also demonstrates that compensation estimated from an AM source of opportunity can be applied to effectively cancel broadband interference signals with different directions of arrival recorded at a different time and carrier frequency.

6.6 Chapter summary

To improve the interference cancellation performance of adaptive spatial processing in narrowband antenna arrays it is often necessary to compensate for degradations caused by reception channels with different frequency responses. In the context of high frequency (HF) antenna arrays, it is of great interest and potential importance to estimate this

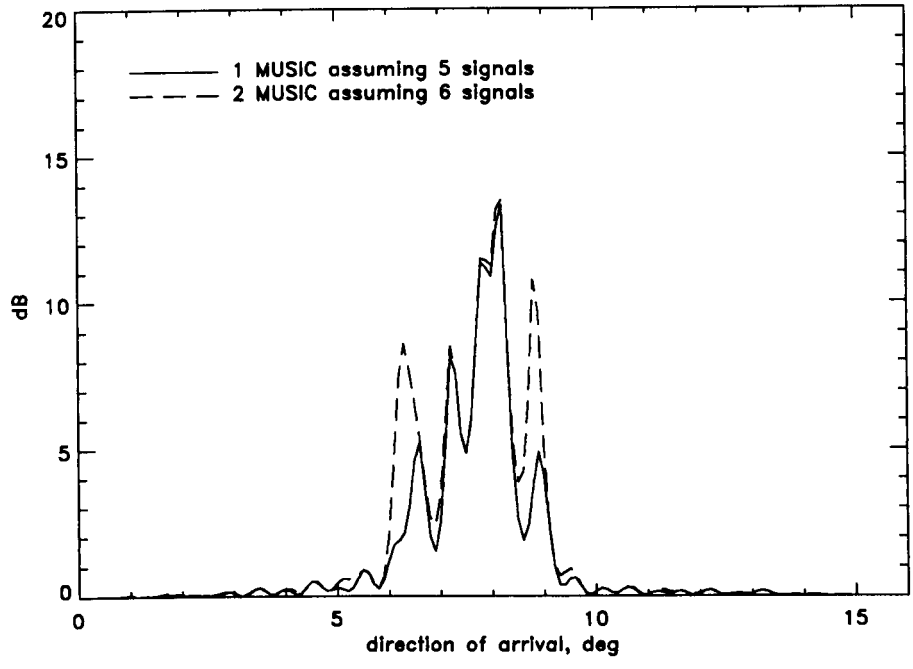

Figure 6.10: MUSIC spectra corresponding to the broadband interference. Curve 1 and Curve 2 show the MUSIC spectra when five and six signals respectively are assumed to be present.

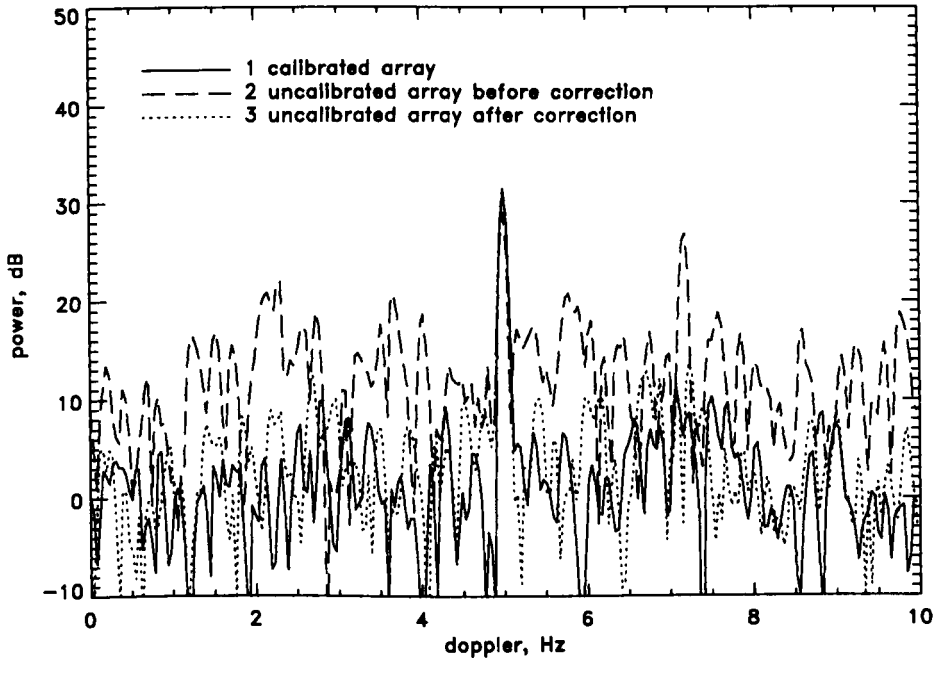

Figure 6.11: Curve 1 and Curve 2 show the Doppler spectra corresponding to the calibrated and uncalibrated array respectively. Curve 3 shows the Doppler spectrum resulting when the estimated compensation for channel mismatch is applied to the uncalibrated array.

compensation from external sources of opportunity. This chapter has proposed a space-time model for suitable interference sources of opportunity, and a data-dependent least squares (LS) algorithm based on this model, to estimate digital compensation for receiver mismatch. The introduced algorithm may be used in combination with the techniques described in (Solomon 1998) to calibrate for both array manifold errors and receiver mismatch in HF antenna arrays.

The performance of the proposed frequency response correction algorithm has been demonstrated and compared with other methods using experimental data. In the first experiment, an ionospherically-propagated AM signal of opportunity was used to estimate digital compensation for 32 reception channels of the Jindalee antenna array. Application of this digital compensation to the "raw" (uncalibrated) receiver passbands resulted in a significant improvement in the spatial dynamic range of the array. Due to the presence of multipath components and uncertain propagation effects, the compensation estimated from the source of opportunity by the commonly used (unconstrained) least squares technique was not able to improve on the spatial dynamic range observed for the uncalibrated array.

In the second experiment, an adaptive sidelobe canceller was used to mitigate broadband interference signals with different directions of arrival. The output signal-to-noise ratio of the adaptive sidelobe canceller improved by approximately 10 dB after applying the receiver mismatch compensation estimated from the AM source of opportunity. This improvement was comparable with that achieved by sophisticated software and hardware sub-systems normally used for calibrating the Jindalee array. In addition, this experiment demonstrated that digital compensation estimated from a source of opportunity can be applied to effectively cancel other interference signals recorded at a different time and carrier frequency.

The application of the proposed technique was successfully demonstrated for HF arrays. It should be noted that the multipath signal model upon which the proposed technique is based has quite general statistical properties, and for this reason, such a technique may be suitable in other adaptive sensor array applications which stand to benefit from receiver mismatch compensation prior to adaptive spatial processing.

CHAPTER 7

Conclusion

This thesis has presented the results of theoretical and experimental research concerned with the space-time characterisation and adaptive processing of ionospherically-propagated HF signals received by a very wide aperture antenna array. The first component of this research focussed on the theoretical derivation and experimental validation of mathematical models to describe the space-time characteristics of the HF channel over time-scales ranging from a few seconds to several minutes. The second component of this research exploited the information contained in the experimentally validated models to enhance the performance of adaptive beamformers in HF arrays. The central theme in both components of research was the application of modern and novel array signal processing techniques to experimental data for the purpose of quantifying the fine structure of ionospheric propagation as well as the limitations it imposes on the performance of adaptive beamformers in the HF environment. A summary of the experimental data which has been processed and the key contributions resulting in each of the two above-mentioned components of research follows to conclude the thesis.

7.1 Experimental data processed

The experimental HF propagation data for this study were collected on a 1265 km mid-latitude ionospheric path using several transmit and receive facilities. An oblique sounder system was utilised to monitor the mode content of the HF link so that the number of propagation modes and the ionospheric layers which reflected them could be identified. The 2.8 km long aperture of the Jindalee OTH radar receiving ULA was utilised to record coherent narrowband HF signals propagated over the same ionospheric link. This data, sometimes referred to as the channel scattering function (CSF) data, enabled the *space-time* characteristics of the narrowband HF channel to be analysed and modelled on a mode separated basis. The above-mentioned data was processed in chapters 2, 3, and 4 to address the requirements of the first research component.

The Jindalee OTH radar receiver array was also utilised to record a cooperative source

of radio frequency interference (RFI) propagated over the same HF link shortly after and in a nearby frequency channel to the CSF experiment. The data recorded from this RFI source permitted the cancellation performance of various adaptive beamforming schemes to quantified and compared with predictions made by a statistical HF channel model estimated from the CSF data. A non-cooperative amplitude modulated (AM) radio broadcast of opportunity and broadband interferer were recorded a few minutes apart on different frequency channels by the Jindalee receiver array. These non-cooperative signals were used to quantify the limitations imposed by real receiver frequency response mismatches on the interference cancellation performance of an adaptive sidelobe canceller as well as to test the effectiveness of a novel technique designed to compensate for such instrumental errors using AM sources of opportunity. The cooperative and non-cooperative interference data was processed in chapters 5 and 6 to address the requirements of the second research component.

7.2 Space-time characterisation of HF signals

A preliminary analysis of the space-time CSF data revealed that the spatial structure of individual HF signal modes reflected by the ionosphere exhibited a planar gross structure with some degree of time-varying amplitude and phase distortions superimposed. Mode wavefront crinkles have been observed with other HF arrays and are thought by some investigators to arise from the interference between relatively few specularly reflected rays. However, the resolution of ray parameters from a complex-valued mode wavefield is not readily achieved and generally requires the use superresolution methods in conjunction with a well calibrated very wide aperture antenna array that can receive ionospherically-propagated HF signals on a mode separated basis. Perhaps as a result of these difficulties, quantitative information regarding the ability of the wave-interference model to represent such wavefields at a high temporal resolution (less than 0.02 seconds) over typical OTH radar CIT (in the order of a few seconds) was not previously available. The accuracy and domain of validity of this model is of practical interest as it influences the selection of signal processing strategy for use within the CIT.

The MUSIC space-time superresolution algorithm was described and applied in chapter 2 to resolve the fine structure of signal modes recorded by the Jindalee array on a controlled mid-latitude ionospheric circuit. Comparisons between the real wavefields and those generated from the estimated wave interference model parameters showed that fitting accuracies greater than 90 percent could be obtained for CIT of about 4 seconds duration with four rays or less over a large percentage of the data analysed. Note that the wave interference model involves four parameters per ray which were fixed to model a CIT of data containing $30 \times 256 = 7680$ complex space-time samples of the wavefield produced by a single mode.

The time-variation of the ray parameters observed for a particular mode from one

CIT to another implies that as the time interval increases the number of rays required to maintain a certain modeling accuracy will also increase. Consequently, it was concluded that a deterministic ray interference model incorporating relatively few rays is best suited for representing mode fine structure over time scales which do not exceed a few seconds. Such a model is not considered appropriate for the characterisation of a complete data set received over an interval of a few minutes. The characterisation of longer data sets is useful for the purpose of optimising the selection of carrier frequency which to a large extent determines the effectiveness of a particular signal processing strategy.

To deal with data sets of several minutes, the space-time modulations imposed by the HF reflection channel on individual propagation modes were treated as a two-dimensional *random process*. A wide-sense stationary statistical model of this random process may be justified if attention is restricted to narrowband HF channels (less than 10-20 kHz bandwidth) over relatively small time intervals (less than 5-10 minutes). A one-dimensional Gaussian distributed stationary random process model for the temporal (i.e., Doppler) characteristics of narrowband HF channels reflected by the ionosphere has already been developed and experimentally validated using a single receiver system. A multi-sensor generalisation of this type of model is required to aid frequency management as well as the design and analysis of spatial and space-time adaptive signal processing algorithms in HF antenna arrays.

The broad physical principles which govern the reflection of radio waves from a dynamic and spatially irregular ionospheric plasma surface were described in chapter 3 in order to model the space-time second order statistics of HF signals reflected by a statistically rough ionospheric layer. Two analytical auto-correlation functions for the received signals (i.e., Gaussian and decaying exponential envelopes with linear phase) were derived from the physical model and compared against the sample auto-correlation functions measured for individual propagation modes in the spatial-only, temporal-only and space-time dimensions. Under the Gaussian scattering assumption, the sampling distributions for these measurements were also derived and evaluated in order to construct hypothesis tests which could be used to validate or reject the postulated statistical models.

It was found that there was no good reason to reject the assumption of a Gaussian shaped temporal auto-correlation function for a signal mode at the output of each receiver in the array. These results also indicated that the temporal second order statistics of the HF channel may be considered spatially homogeneous over apertures in the order of 2-3 km. The assumption of spatial stationarity across the very wide aperture was experimentally confirmed for the fully resolved modes along with a plane wave model for the mean wavefront of these modes. An exponentially decaying envelope was also accepted for the spatial auto-correlation function of all the resolved modes. It was shown that the space-time auto-correlation functions estimated for the resolved modes could be accurately predicted from the estimated models of the temporal-only and spatial-only auto-correlation functions. This result indicated a high level of space-time separability in

the signal second order statistics arising from the ionospheric reflection process.

Although the space-time wave interference model and wide sense stationary statistical models are based on physical principles, such principles may be transformed into signal processing models which can simulate ionospherically propagated HF signals received at multiple antenna sensors. A suitable signal processing framework for generating synthetic samples in accordance with the deterministic or statistical space-time HF channel models has been proposed in the literature and was adopted in chapter 4. However, a joint space-time parameter estimation technique for this model was not supplied and may be valuable for systems which are incapable of separating the individual propagation modes. While algorithms such as MUSIC can be used to estimate the parameters of the wave interference model the problem becomes significantly more complicated when it is required to estimate the parameters of distributed signals which exhibit Doppler and angular spread. The problem of parametrically localising space-time distributed sources from convolved signal mixtures was addressed in chapter 4.

If the modulations imposed by the ionosphere on different signal modes are mutually uncorrelated and accurately described by a first order auto-regressive process then the superposition of such modes gives rise to a signal which is statistically described by a special auto-regressive moving-average process. An explicit connection was made between estimating the parameters of such a process and estimating the frequencies and decay rates of superimposed exponentially damped cisoids in noise. A novel closed-form technique based on the least squares criterion was proposed for jointly estimating the mean and spread parameters of all modes in a computationally attractive manner from the space-time sample auto-correlation function of the signal mixture received by a uniform linear array.

It was necessary to use this technique to estimate the model parameters of two sporadic-E modes which could not be resolved in time-delay by the array but whose presence was certified by ionogram records from the oblique sounder. Assuming the presence of two space-time distributed signal modes, the model parameters were estimated using the proposed technique in order to regenerate the space-time auto-correlation function of the signal mixture. The remarkable similarity between the modelled and sample auto-correlation functions across 900 space-time lag points experimentally demonstrated the validity of the auto-regressive moving-average representation and the effectiveness with which the parameters of this process were estimated by the proposed technique.

7.3 Adaptive processing of HF signals

Previous analysis of the spatial properties of ionospheric modes have shown that signal distortions caused by ionospheric reflection do not greatly affect the reception of desired signals in the *main lobe* of the beampattern of a very wide aperture array. However, the influence of such distortions when the signal is received through the relatively steep

nulls of the beampattern (i.e., when the signal is considered interference) has received insufficient attention in the literature. The first aim of chapter 5 was to redress this balance by quantifying the effect of ionospheric propagation on the interference cancellation performance of various adaptive beamforming schemes operating on a very wide aperture antenna array. The second aim was to determine the accuracy with which the previously validated multi-sensor HF channel model could predict the performance improvement gained by adaptive beamforming over conventional beamforming as a function of the CIT length in a statistical sense.

It was found that the relative improvement in interference cancellation gained through the use of the sample matrix inverse adaptive beamforming technique over a tapered conventional beamformer was highly dependent on the time interval over which the adaptive beamforming weight vector was held constant. As the CIT length increased from a fraction of a second to approximately one minute the relative improvement dropped significantly for all schemes tried. For some schemes the degradation was so severe at long CIT lengths (50 seconds) that conventional beamforming actually outperformed adaptive beamforming. Such experimental results demonstrate that space-time distortions imposed on interference modes by the ionospheric reflection process can have a very pronounced influence on the effectiveness of adaptive cancellation algorithms and hence cannot be ignored in the design and evaluation of adaptive beamformers intended for operational use.

The previously estimated statistical HF channel model for the HF link was used to simulate the received interference signal assuming temporal-only distortions first and then space-time distortions. As expected, adaptive beamformer performance was not dependent on the CIT length when no spatial distortions were imposed on the simulated signals. After the introduction of spatial distortions the performance of the adaptive beamformer relative to the conventional beamformer dropped by over 25 dB as the CIT was increased from a fraction of a second to 50 seconds. Moreover, it was noted that the falloff in both the mean and deciles of the relative SINR improvement distribution with respect to CIT length was very similar to the curves derived from experimental interference data. An existing adaptive beamforming algorithm which is designed to reduce degradations in interference cancellation with respect to CIT length without effecting signal detection was described and its performance was illustrated to motivate further research in this area.

The performance of an adaptive array is not always limited by the capabilities of the adaptive processor or the complexity of the interference scenario; in many practical applications significant limitations may be encountered as a result of instrumental uncertainties such as receiver mismatch. While the problem of calibrating for array manifold errors using ionospherically-propagated HF sources of opportunity has been addressed the complimentary problem of correcting for receiver mismatch with HF sources of opportunity has received little if any attention. A mathematical model with quite general statistical properties was developed in chapter 6 for the special case of *amplitude modu-*

lated (AM) radio signals propagated by the ionosphere, this model was then exploited to estimate corrections for receiver mismatch from ionospherically-propagated AM broadcasts of opportunity.

The proposed algorithm was tested for the case of real receiver mismatch using an actual AM source of opportunity. The Jindalee calibration system provided independent calibration corrections, these corrections represented ground-truth data used to assess the performance of the proposed algorithm. It was found that the adaptive cancellation of a *broadband interference* was improved by 10 dB after applying the compensation estimated by the proposed algorithm from the AM source of opportunity. This improvement restored the performance of the uncalibrated array to the level observed after the application of the Jindalee system calibration weights. Commonly used unconstrained least squares techniques are not designed for the HF environment and were shown to be incapable of estimating effective corrections from the AM source of opportunity.

7.4 Recommendations for future research

Recommendations for future research in this area include a full generalisation of the multi-sensor HF channel model which could additionally incorporate wave polarisation, wave propagation in the azimuth-elevation domain and the frequency dispersive effects of ionospheric propagation encountered in broadband HF applications. The Jindalee array is narrowband and consists of uniformly spaced vertically polarised antenna elements arranged in a line. Consequently, it was only possible to measure the vertical component of polarisation of narrowband HF signals while the azimuth and elevation could not be measured independently as a one-dimensional array allows only variations in cone angle to be detected. Hence, the full generalisation of the HF channel model requires measurements made on wideband two-dimensional (or three-dimensional) arrays that have complete polarisation diversity.

It would be of interest to determine whether the stationary HF channel model proposed for single-hop mid-latitude ionospheric paths is valid for multi-hop propagation and if such a model is suitable (over perhaps shorter time scales) for propagation involving reflections from the equatorial and auroral ionosphere. The latter point is especially relevant for the design and development of adaptive beamforming routines which are sometimes required to cancel interference signals propagated via these regions. The concept of intra-CIT adaptive beampattern re-adjustments was introduced but requires further research especially for situations when the backscattered clutter model is unknown or if the interference-only array snapshots are not available.

APPENDIX A

Complex sample ACS distribution

Consider a continuous one-dimensional complex random process which is sampled every Δ seconds and let $z(t)$ be a complex random variable which takes on the value of the process at different sampling instants $t\Delta$ for $t = 0, 1, .., P-1$.

$$z(t) = x(t) + jy(t) = m(t)e^{j\theta(t)} \tag{A.1}$$

In equation Eqn.(A.1), the scalars $x(t)$ and $y(t)$ are the real and imaginary parts of $z(t)$ respectively while $m(t)$ and $\theta(t)$ are the associated magnitude and phase. It is assumed that $x(t)$ and $y(t)$ are *zero mean* Gaussian distributed random variables with the same variance σ^2. It is further assumed that $x(t)$ and $y(t)$ are independent and stationary random processes with the same second order statistics (i.e., auto-correlation function).

$$r_x(\tau) = E\{x(t)x(t+\tau)\} \ , \quad r_y(\tau) = E\{y(t)y(t+\tau)\} \ , \quad r_x(\tau) = r_y(\tau) = r(\tau) \tag{A.2}$$

For such a process it can be shown that the magnitude $m(t)$ is Rayleigh distributed and the phase $\theta(t)$ is uniformly distributed over the interval $[-\pi, \pi)$, see (Papoulis 1984). This general statistical model of a complex random process is suitable for the description of HF signals received at a single antenna sensor after reflection from the ionosphere, as experimentally verified by (Watterson et al. 1970).

The maximum likelihood estimator of the second order statistics or auto-correlation function is often referred to as the *unbiased* sample auto-correlation function $\hat{r}_z(\tau)$ and is calculated as the average of a sum of lagged products,

$$\hat{r}_z(\tau) = \frac{1}{P-\tau} \sum_{t=0}^{P-\tau-1} z(t)z^*(t+\tau) \tag{A.3}$$

where P is the number of available samples of the process $z(t)$. The various samples $\tau = 0, 1, ..., Q-1$ $(Q < P)$ of this *discrete* auto-correlation function are collectively referred to as an auto-correlation sequence (ACS) (Marple 1987). The estimator in Eqn.(A.3) is statistically consistent in the sense that the sample ACS $\hat{r}_z(\tau)$ tends to the statistically

expected ACS $r_z(\tau) = E\{z(t)z^*(t+\tau)\}$ as the number of samples P tends to infinity.

By substituting Eqn.(A.1) into Eqn.(A.3) the sample ACS can be decomposed into the following real and imaginary parts,

$$\hat{r}_z(\tau) = [\hat{r}_x(\tau) + \hat{r}_y(\tau)] + j[\hat{r}_{yx}(\tau) - \hat{r}_{xy}(\tau)] \tag{A.4}$$

where $\hat{r}_x(\tau) = M\{x(t)x(t+\tau)\}$, $\hat{r}_y(\tau) = M\{y(t)y(t+\tau)\}$, $\hat{r}_{xy}(\tau) = M\{x(t)y(t+\tau)\}$, $\hat{r}_{yx}(\tau) = M\{y(t)x(t+\tau)\}$ and $M\{\cdot\} = \frac{1}{P-\tau}\sum_{t=0}^{P-\tau-1}\{\cdot\}$. Since the sample ACS estimates are unbiased it is possible to define the following zero mean random variables.

$$\begin{aligned} e_x(\tau) &= \hat{r}_x(\tau) - r_x(\tau) \\ e_y(\tau) &= \hat{r}_y(\tau) - r_y(\tau) \\ e_{xy}(\tau) &= \hat{r}_{xy}(\tau) - r_{xy}(\tau) \\ e_{yx}(\tau) &= \hat{r}_{yx}(\tau) - r_{yx}(\tau) \end{aligned} \tag{A.5}$$

It is noted $r_{xy}(\tau) = E\{x(t)y(t+\tau)\}$ and $r_{yx}(\tau) = E\{y(t)x(t+\tau)\}$ are both equal to zero as the real and imaginary parts of $z(t)$ are independent. The asymptotic (large sample) variance of these random variables is given by (Muirhead 1982),

$$\begin{aligned} E\{e_x^2(\tau)\} &= E\{e_y^2(\tau)\} = [\sigma^4 + r^2(\tau)]/N \\ E\{e_{xy}^2(\tau)\} &= E\{e_{yx}^2(\tau)\} = \sigma^4/N \end{aligned} \tag{A.6}$$

where N is defined as the number of *independent* samples of $z(t)$ used to form the sample ACS according to Eqn.(A.3). In many practical situations the samples recorded from a random process will be correlated in which case the substitution of P for N in Eqn.(A.6) will not yield the asymptotic (large sample) variance of the error terms in Eqn.(A.5). One notable exception for which this substitution is valid occurs when the random processes $x(t)$ and $y(t)$ are *Gaussian distributed white noise* process as in this case the consecutive samples are uncorrelated and hence statistically independent. The effect of correlation in the samples of a random process is to reduce the number of independent observations which in turn increases the variance of the ACS estimates.

Fortunately, an *exact* result for the variances of the ACS estimation error terms in Eqn.(A.5) exists due to (Bartlett 1946). As explained in (Priestly 1981), the joint fourth order cumulant in the expression derived by (Bartlett 1946) vanishes for a Gaussian processes so the exact sample ACS error variance is given by the following expression.

$$\begin{aligned} E\{e_x(\tau)e_x(\tau+v)\} = &\frac{P}{(P-\tau)(P-\tau-v)} \sum_{m=-(P-\tau)+1}^{P-\tau-v-1} \\ &\left\{1 - \frac{\mu(m)+\tau+v}{P}\right\}[r(m)r(m+v) + r(m+\tau+v)r(m-\tau)] \end{aligned} \tag{A.7}$$

Note that $E\{e_y(\tau)e_y(\tau+v)\} = E\{e_x(\tau)e_x(\tau+v)\}$ as the two processes are statistically

identical, the term $\mu(m)$ is given by Eqn.(A.8).

$$\mu(m) = \begin{cases} m, & m > 0 \\ 0, & -v \leq m \leq 0 \\ -m - v, & -(P-\tau)+1 \leq m \leq -v \end{cases} \tag{A.8}$$

The cross-terms $e_{xy}(\tau)$ and $e_{yx}(\tau)$ of the sample ACS in Eqn.(A.4) are derived as the average of a sum of lagged products between the samples of *two independent* processes. Whereas the expression in Eqn.(A.7) has been derived for the average of a sum of lagged products between the samples of a *single* and potentially correlated random process. Consequently, the expression in Eqn.(A.7) cannot be used in strictly presented form to obtain the variances of these cross-terms.

If the processes $x(t)$ and $y(t)$ are of finite bandwidth then $r(s) \rightarrow 0$ as $s \rightarrow \infty$. In other words, the samples of either process are uncorrelated and hence statistically independent when the separation between them is sufficiently large. Since $x(t)$ and $y(t)$ are independent identically distributed (i.i.d) Gaussian processes, it follows that $x(t+s)$ for $s \rightarrow \infty$ can be considered a valid realisation of $y(t)$ for the purpose of evaluating the variances of the cross terms. Stated another way, the statistical properties of a sum of $P - \tau$ lagged products between the samples of $x(t)$ and $y(t+\tau)$ are equivalent to the statistical properties of the sum of $P - \tau$ lagged products between the samples of $x(t)$ and $x(t+s+\tau)$. Hence, by substituting $P+s$ for P and $\tau+s$ for τ in Eqn.(A.7) yields the following expression for the variance of the cross-terms as $s \rightarrow \infty$.

$$\begin{aligned} E\{e_{xy}(\tau)e_{xy}(\tau+v)\} &= E\{e_{yx}(\tau)e_{yx}(\tau+v)\} \\ &= \frac{P}{(P-\tau)(P-\tau-v)} \sum_{m=-(P-\tau)+1}^{P-\tau-v-1} \left\{1 - \frac{\mu(m)+\tau+v}{P}\right\} r(m)r(m+v) \end{aligned} \tag{A.9}$$

Note that if the processes $x(t)$ and $y(t)$ are white so that $r(\tau) = \delta(\tau)\sigma^2$ and $N = P$ then as $P \rightarrow \infty$ the variances which are predicted by Eqn.(A.7) and Eqn.(A.9) for $v = 0$ coincide with the asymptotic variances reported by (Muirhead 1982) which appear in Eqn.(A.6). It may also be observed from Eqn.(A.7) and Eqn.(A.9) that for non-white Gaussian processes the correlation between samples serves to increase the variance of the ACS estimates. This increase in variance is interpreted in terms of a decrease in the effective number of statistically independent samples used to estimate the ACS (Priestly 1981).

Before proceeding to determine the sampling distributions for the magnitude and phase of the ACS estimation error, a few points are worthy of mention. A more compact expression for the variance of the *complex* ACS estimation error exists, see (Thierren 1992), but this expression has not be used as nothing can be deduced about the variances of the real and imaginary parts of the ACS estimation error and this information is required to

evaluate the statistics of the sample ACS magnitude and phase. For Gaussian process which are stationary up to order four, the variances given by Eqn.(A.7) and Eqn.(A.9) are exact for any number of samples P but the *distributions* of the error terms in Eqn.(A.5) *tends* to the normal density as the number of samples P tends to infinity. As typically more than $P = 10,000$ samples are used to estimate the ACS in the experimental analysis, a normal distribution for these random variables is assumed in the analysis which follows. Although the theoretical expression for the variances will not be exact for non-Gaussian distributed processes they are known to provide a good approximation providing that $|\tau| \ll P$ (Thierren 1992).

The complex ACS estimation error $e_z(\tau)$ corresponding to Eqn.(A.4) can be written in the following form,

$$e_z(\tau) = \hat{r}_z(\tau) - r_z(\tau) = a(\tau) + jb(\tau) \tag{A.10}$$

where $a(\tau) = e_x(\tau) + e_y(\tau)$ and $b(\tau) = e_{yx}(\tau) - e_{xy}(\tau)$. The zero-mean random variables $e_x(\tau)$ and $e_y(\tau)$ have the same variance $\sigma_1^2(\tau)$ given by Eqn.(A.7) and are normally distributed in the asymptotic case. Similarly, the zero-mean normally distributed random variables $e_{xy}(\tau)$ and $e_{yx}(\tau)$ have a common variance $\sigma_2^2(\tau)$ given by Eqn.(A.9).

It is shown by (Muirhead 1982) that the random variables $e_x(\tau)$ and $e_y(\tau)$ are uncorrelated $E\{e_x(\tau)e_y(\tau)\} = 0$ so the random variable $a(\tau)$ is normally distributed with zero mean and a variance of $\sigma_a^2(\tau) = 2\sigma_1^2(\tau)$. The cross terms $e_{yx}(\tau)$ and $e_{xy}(\tau)$ are correlated so the variance of the zero-mean and normally distributed random variable $b(\tau)$ is equal to $\sigma_b(\tau) = 2[\sigma_2^2(\tau) - E\{e_{xy}(\tau)e_{yx}(\tau)\}]$. The random processes $x(t)$ and $y(t)$ are identically distributed so the random variables $e_{yx}(\tau)$ and $e_{xy}(-\tau)$ have the same *statistical* properties. The interchangeability of these two variables, as far as their statistical properties are concerned, is exploited to derive an expression for $E\{e_{xy}(\tau)e_{yx}(\tau)\}$

$$E\{e_{xy}(\tau)e_{yx}(\tau)\} = E\{e_{xy}(\tau)e_{xy}(-\tau)\} = E\{e_{xy}(\tau)e_{xy}(\tau + v)\}\ ,\ \ v = -2\tau \tag{A.11}$$

From Eqn.(A.11) the term $E\{e_{xy}(\tau)e_{yx}(\tau)\}$ is calculated by substituting $v = -2\tau$ in Eqn.(A.9). Note that for $\tau = 0$ the variance of $b(\tau)$ falls to zero which implies that $e_z(0)$ does not have an imaginary component or equivalently there is no phase error in the sample ACS. This is expected because both $\hat{r}_z(\tau)$ and $r_z(\tau)$ are real when $\tau = 0$.

It is shown by (Papoulis 1984) that the joint probability density function $p(a, b)$ of the random variables a and b (the dependence on τ has been dropped for notational convenience) is given by,

$$p(a,b) = \frac{1}{2\pi\sigma_a\sigma_b\sqrt{1-\rho^2}} \exp\left\{\frac{-1}{2(1-\rho^2)}\left[\frac{a^2}{\sigma_a^2} - \frac{2\rho ab}{\sigma_a\sigma_b} + \frac{b^2}{\sigma_b^2}\right]\right\} \tag{A.12}$$

where $\rho = E\{ab\}/(\sigma_a\sigma_b)$ is defined as the *correlation coefficient.* The normal random

variables a and b are uncorrelated ($\rho = 0$) in this case because the error terms in the real part (e_x, e_y) are mutually uncorrelated with those in the imaginary part (e_{xy}, e_{yx}) (Muirhead 1982). The Cartesian random variables a and b may be related to the polar random variables r (magnitude) and ϕ (phase) by the transformations $a = r\cos\phi$ and $b = r\sin\phi$. The joint probability density function of the variables r and ϕ is given by,

$$f(r,\phi) = J(a,b)p(r\cos\phi, r\sin\phi) = rp(r\cos\phi, r\sin\phi) \tag{A.13}$$

where $J(a,b) = r$ is the Jacobian of the transformation between Cartesian and polar coordinates (Papoulis 1984). By setting $\rho = 0$ in Eqn.(A.12) and substituting the result into Eqn.(A.13) the polar joint density function $f(r,\phi)$ can be derived as,

$$f(r,\phi) = \frac{r}{2\pi\sigma_a\sigma_b}\exp\frac{-1}{2}\left[\frac{r^2\cos^2\phi}{\sigma_a^2} + \frac{r^2\sin^2\phi}{\sigma_b^2}\right] \tag{A.14}$$

where r and ϕ are the magnitude and phase of the complex ACS estimation error. The marginal densities $f_1(\phi)$ and $f_2(r)$ can then be derived from Eqn.(A.14).

$$f_1(\phi) = \int_{r=0}^{\infty} f(r,\phi)dr = \int_{r=0}^{\infty} Cr\exp\left[\frac{-Ar^2}{2}\right]dr \tag{A.15}$$

The constants C and A in Eqn.(A.15) are given by $C = (2\pi\sigma_a\sigma_b)^{-1}$ and $A = \cos\phi^2/\sigma_a^2 + \sin\phi^2/\sigma_b^2$. This integral is readily evaluated to give the marginal density for the phase error.

$$f_1(\phi) = \left[\frac{-C}{A}\exp\{\frac{-Ar^2}{2}\}\right]_0^{\infty} = \frac{C}{A} = \frac{\sigma_a\sigma_b}{2\pi(\cos\phi^2\sigma_b^2 + \sin\phi^2\sigma_a^2)} \tag{A.16}$$

Note that in the special case where $\sigma_a = \sigma_b$ the phase becomes uniformly distributed, $f_1(\phi) = 1/2\pi$, as expected. The marginal density for the magnitude $f_2(r)$ is given by,

$$f_2(r) = \int_{\phi=-\pi}^{\pi} f(r,\phi)\,d\phi = \int_{\phi=-\pi}^{\pi} F\exp\left(G\cos 2\phi\right)\,d\phi \tag{A.17}$$

where after some manipulation the constants F and G can be written in the following way.

$$F = \frac{r}{2\pi\sigma_a\sigma_b}\exp\left\{\frac{-r^2(\sigma_a^2+\sigma_b^2)}{4\sigma_a^2\sigma_b^2}\right\}, \quad G = \frac{-r^2(\sigma_b^2-\sigma_a^2)}{4\sigma_a^2\sigma_b^2} \tag{A.18}$$

The integral in Eqn.(A.17) can be evaluated by first forming a Taylor series expansion of the integrand,

$$f_2(r) = F\int_{\phi=-\pi}^{\pi}\sum_{n=0}^{\infty}\frac{G^n(\cos 2\phi)^n}{n!}d\phi \tag{A.19}$$

and then deriving an expression for the following generic term of this expansion.

$$\int_{\phi=-\pi}^{\pi} \cos^n 2\phi \, d\phi = \int_{\phi=-\pi}^{\pi} \frac{1}{2^n}[e^{j2\phi} - e^{-j2\phi}]^n d\phi = \int_{\phi=-\pi}^{\pi} \frac{1}{2^n} \sum_{k=0}^{n} C_k^n e^{j2\phi k} e^{j2\phi(n-k)} d\phi$$

$$= \frac{1}{2^n} C_{n/2}^n 2\pi = \frac{1}{2^n} \frac{n!}{(n/2)!(n/2)!} 2\pi \quad \text{(for } n \text{ even)} \tag{A.20}$$

The odd terms in the Taylor series expansion do not contribute to the marginal density in Eqn.(A.19) which may be simplified to the form shown in Eqn.(A.21)

$$f_2(r) = F \sum_{n}^{\infty} \frac{1}{2^n} C_{n/2}^n 2\pi \frac{G^n}{n!} \quad \text{for} \quad n = 0, 2, 4, ..., \tag{A.21}$$

Note that if $\sigma_a = \sigma_b$ then $F = \frac{r}{2\pi\sigma_a^2} \exp -r^2/2\sigma_a^2$ while $G = 0$. Substituting these values in Eqn.(A.21) yields the density,

$$f_2(r) = \frac{r}{\sigma_a^2} e^{-r^2/2\sigma_a^2} \tag{A.22}$$

which is, of course, the Rayleigh density. The marginal densities derived above allow us to construct statistical tests for validating or rejecting a hypothesised ACS model in terms of real and imaginary components or magnitude and phase from a sample ACS with a known level of confidence.

APPENDIX B

Space-time separability of ACS

For a general ARMA(p,q) model the current output $\mathbf{c}_m^{[n]}(t)$ can be written as a linear combination of the current and past inputs $\epsilon_m^{[n]}(t)$ which drive the process;

$$\mathbf{c}_m^{[n]}(t) = \sum_{k=0}^{\infty} \alpha_m(k)\epsilon_m^{[n]}(t-k) \tag{B.1}$$

where $\alpha_m(k)$ denote the complex coefficients of the linear combination. Note that these coefficients are independent of receiver number (n) since in the model the temporal second order statistics of the processes which describe Doppler spread are assumed to be the same in all receivers. In accordance with the presented model, the inputs $\epsilon_m^{[n]}(t)$ have the following correlation properties,

$$E\{\epsilon_m^{[n]}(t)\epsilon_m^{[n-j]*}(t-i)\} = \rho_s(j)\,\delta(i) \tag{B.2}$$

where $\rho_s(j)$ is the spatial ACS of the driving noise process normalised such that $\rho(0) = 1$. Using Eqn.(B.1) and Eqn.(B.2) it can be shown that the temporal ACS of the modulations $\mathbf{c}_m^{[n]}(t)$ is given by,

$$E\{\mathbf{c}_m^{[n]}(t)\mathbf{c}_m^{[n]*}(t-i)\} = E\{\epsilon_m^{[n]}(t)\epsilon_m^{[n]*}(t)\}\sum_{k=0}^{\infty}\alpha_m(k+i)\alpha_m^*(k) = \rho_t(i) \tag{B.3}$$

where $\rho_t(i) = \sum_{k=0}^{\infty}\alpha_m(k+i)\alpha_m^*(k)$ since $E\{\epsilon_m^{[n]}(t)\epsilon_m^{[n]*}(t)\} = 1$. As the power of mode m is modelled by the square of the amplitude term A_m in Eqn.(4.1) it follows that the power of the modulations $\mathbf{c}_m^{[n]}(t)$ is also unity (i.e., $\rho_t(0) = 1$). This implies that $\sum_{k=0}^{\infty}|\alpha_m(k)|^2 = 1$ and that the spatial ACS of the modulations $\mathbf{c}_m^{[n]}(t)$ is equal to the spatial ACS of the driving noise process given by Eqn.(B.2).

$$E\{\mathbf{c}_m^{[n]}(t)\mathbf{c}_m^{[n-j]*}(t)\} = E\{\epsilon_m^{[n]}(t)\epsilon_m^{[n-j]*}(t)\}\sum_{k=0}^{\infty}|\alpha_m(k)|^2 = \rho_s(j) \tag{B.4}$$

Similarly to Eqn.(B.1), the output $\mathbf{c}_m^{[n-j]}(t-i)$ of the process taken at a different receiver $n-j$ and time instant $t-i$ is given by Eqn.(B.5).

$$\mathbf{c}_m^{[n-j]}(t-i) = \sum_{k=0}^{\infty} \alpha_m(k)\epsilon_m^{[n-j]}(t-i-k) \tag{B.5}$$

The space-time correlation sequence $r(i,j)$ is defined as;

$$r(i,j) = E\{\mathbf{c}_m^{[n]}(t)\mathbf{c}_m^{[n-j]*}(t-i)\} = E\{\epsilon_m^{[n]}(t)\epsilon_m^{[n-j]*}(t)\} \sum_{k=0}^{\infty} \alpha_m(k+i)\alpha_m^*(k) \tag{B.6}$$

where $E\{\epsilon_m^{[n]}(t)\epsilon_m^{[n-j]*}(t)\} = \rho_s(j) = E\{\mathbf{c}_m^{[n]}(t)\mathbf{c}_m^{[n-j]*}(t)\}$ from Eqn.(B.2) and Eqn.(B.4) respectively while $\sum_{k=0}^{\infty} \alpha_m(k+i)\alpha_m^*(k) = \rho_t(i) = E\{\mathbf{c}_m^{[n]}(t)\mathbf{c}_m^{[n]*}(t-i)\}$ from Eqn.(B.3). In other words,

$$E\{\mathbf{c}_m^{[n]}(t)\mathbf{c}_m^{[n-j]*}(t-i)\} = E\{\mathbf{c}_m^{[n]}(t)\mathbf{c}_m^{[n-j]*}(t)\}E\{\mathbf{c}_m^{[n]}(t)\mathbf{c}_m^{[n]*}(t-i)\} = \rho_t(i)\rho_s(j) \tag{B.7}$$

which indicates that the space-time ACS $r(i,j) = \rho_t(i)\rho_s(j)$ of the model is separable as a product of the temporal ACS $\rho_t(i)$ and the spatial ACS $\rho_s(j)$. For first order AR process the normalised correlation functions are given by $\rho_t(i) = \alpha^i$ and $\rho_s(j) = \beta^j$ where α and β are the coefficients of the temporal and spatial AR(1) processes respectively.

APPENDIX C

Modal decomposition of ACS

As described by (Scharf 1991), the discrete time impulse response $h(iT)$ of an ARMA(M, $M-1$) process can be expressed as the superposition of M modes;

$$h(iT) = \sum_{m=1}^{M} c_m z_m^i \tag{C.1}$$

where T is the sampling interval (Nyquist rate of the ARMA process) and $h(iT) = 0$ for $i < 0$ by definition for a causal system. The modes z_m are constructed from the roots of the AR characteristic equation,

$$A(z) = a_0 z^M + a_1 z^{M-1} + \cdots + a_M = \prod_{m=1}^{M} (z - z_m) \tag{C.2}$$

where $a_0, a_1, .., a_M$ are the AR process coefficients and z_m are the poles of the ARMA transfer function $H(z)$ which is given by the Z-transform of the impulse $h(iT)$. The residues c_m are constructed from the following partial fraction expansion evaluated at $z = z_m$,

$$c_m = [(1 - z_m z^{-1}) \frac{B(z)}{A(z)}]_{z=z_m} \tag{C.3}$$

where the moving average characteristic polynomial is defined as $B(z) = \sum_{k=0}^{M-1} b_k z^{-k}$.

The power spectral density $S(z)$ of the ARMA(M, $M-1$) process is equal to the modulus squared of the associated transfer function $H(z) = B(z)/A(Z)$ scaled by the sampling interval T.

$$S(z) = T|H(z)|^2 = H(z)H^*(z) \tag{C.4}$$

and is typically evaluated as a function of frequency f with $z = e^{j2\pi fT}$ on the unit circle.

The auto-correlation sequence (ACS) of the process $r(iT)$ is given by the inverse Fourier transform of the (periodic) power spectral density function $S(e^{j2\pi fT})$. Using

Eqn.(C.4) and the convolution theorem, the ACS of the process can be expressed in terms of the modal impulse response.

$$r(iT) = h(iT) \oplus h^*(-iT) = \sum_{j=0}^{\infty} h(j)h^*(j+i) \tag{C.5}$$

where $h^*(-iT)$ is the inverse Fourier Transform of $H^*(z)$ and the symbol $\otimes$ denotes convolution. The sampling interval T has been omitted from the discrete convolution sum in Eqn.(C.5) for notational convenience. Substituting Eqn.(C.1) into Eqn.(C.5) and expanding the terms yields,

$$r(iT) = \sum_{m=1}^{M} g_m z_m^{*i} \ , \ g_m = \sum_{m'=1}^{M} \frac{c_{m'} c_m^*}{1 - z_{m'} z_m^*} \tag{C.6}$$

where the identity for the geometric sum $\sum_{j=0}^{\infty}(z_{m'}z_m^*)^j = (1 - z_{m'}z_m^*)^{-1}$ has been used to simplify the expansion. Note that the poles z_m are inside the unit circle (i.e., $|z_m| < 1$ for $m = 1, 2, .., M$) in the assumed ACS model.

Hence, the ACS of an ARMA$(M, M-1)$ model can also be represented as modal decomposition, and as shown by Eqn.(C.6), the modes of $r(iT)$ are the complex conjugates of the modes of $h(iT)$. This result, which does not explicitly appear in (Scharf 1991) or (Marple 1987), can be exploited to *jointly* estimate the parameters g_m and z_m which provide a least squares fit to the sample ACS. Once the parameters g_m and z_m have been estimated from a finite length sample ACS it is possible to extend the ACS to an infinite number of lags to estimate the power spectral density as,

$$S(z) = T \sum_{i=-\infty}^{\infty} r(iT) z^{-i} = \sum_{m=1}^{M} \frac{g_m}{\|1 - z_m^* z^{-1}\|^2} \tag{C.7}$$

where $S(z) = S(e^{j2\pi fT})$.

APPENDIX D

Receiver mismatch compensation

The problem is to find the argument $\hat{\mathbf{c}}_a$ which minimises the quadratic cost function $f(\mathbf{c}_a)$ in Eqn.(D.1) subject to the linear constraint $\mathbf{c}_a^H\mathbf{e} = 1$.

$$f(\mathbf{c}_a) = \sum_{t=1}^{P}\{\mathbf{z}^H(t)\mathbf{z}(t)\,[\alpha(t)\mathbf{z}(t) - \mathbf{Y}(t)\mathbf{c}_a]^H[\alpha(t)\mathbf{z}(t) - \mathbf{Y}(t)\mathbf{c}_a]\} \tag{D.1}$$

This problem is similar to the weighted constrained least squares optimisation problems treated in (Albert 1972). However, it differs slightly from these problems because two different types of data-dependent weights are involved, namely $\mathbf{z}^H(t)\mathbf{z}(t)$ and $\alpha(t)$.

Let $\alpha_{opt}(t)$ be the value of $\alpha(t)$ which minimises $\mathbf{z}^H(t)\mathbf{z}(t)\,\|\alpha(t)\mathbf{z}(t) - \mathbf{Y}(t)\mathbf{c}_a\|_F$ for an arbitrary vector $\mathbf{c}_a$ subject to the constraint $\mathbf{c}_a^H\mathbf{e} = 1$. The value of $\alpha_{opt}(t)$ for $t = 1, 2, .., P$ is given by,

$$\alpha_{opt} = \arg\min \tilde{f}(\alpha)\,, \quad \tilde{f}(\alpha) = (\alpha\mathbf{z} - \mathbf{Y}\mathbf{c})^H(\alpha\mathbf{z} - \mathbf{Y}\mathbf{c}) \tag{D.2}$$

where the t-dependence and subscripts have momentarily been dropped for notational convenience. The cost function $\tilde{f}(\alpha)$ can alternatively be written in expanded form.

$$\tilde{f}(\alpha) = \alpha\alpha^*\mathbf{z}^H\mathbf{z} - \alpha^*\mathbf{z}^H\mathbf{Y}\mathbf{c} - \alpha\mathbf{c}^H\mathbf{Y}^H\mathbf{z} + \mathbf{c}^H\mathbf{Y}^H\mathbf{Y}\mathbf{c} \tag{D.3}$$

To find $\alpha_{opt}(t)$ we define $\frac{\partial\tilde{f}(\alpha)}{\partial\alpha} = \left[\frac{\partial\tilde{f}(\alpha)}{\partial\alpha_{re}} + j\frac{\partial\tilde{f}(\alpha)}{\partial\alpha_{im}}\right]$ as the partial derivative of $\tilde{f}(\alpha)$ with respect to the complex scaler variable $\alpha = \alpha_{re} + j\alpha_{im}$. The value of α_{opt} is found by setting the partial derivative $\frac{\partial\tilde{f}(\alpha)}{\partial\alpha}$ to zero.

$$\frac{\partial\tilde{f}(\alpha)}{\partial\alpha} = \alpha\mathbf{z}^H\mathbf{z} - \mathbf{z}^H\mathbf{Y}\mathbf{c} = 0 \tag{D.4}$$

The value of α_{opt} is readily derived from Eqn.(D.4).

$$\alpha_{opt} = \frac{\mathbf{z}^H\mathbf{Y}\mathbf{c}}{\mathbf{z}^H\mathbf{z}} \tag{D.5}$$

Substituting $\alpha_{opt}(t)$ for $\alpha(t)$ in Eqn.(D.1) and simplifying the terms yields the following cost function.

$$f(\mathbf{c}_a) = \sum_{t=1}^{P} \{\mathbf{z}^H(t)\mathbf{z}(t)\,\mathbf{c}_a^H\mathbf{Y}^H(t)\mathbf{Y}(t)\mathbf{c}_a - \mathbf{c}_a^H\mathbf{Y}^H(t)\mathbf{z}(t)\mathbf{z}^H(t)\mathbf{Y}(t)\mathbf{c}_a\} \tag{D.6}$$

The vector $\mathbf{c}_a$ is fixed with respect to t so it can be taken out of the summation in Eqn.(D.6). This leads to the following linearly constrained quadratic optimization problem,

$$\hat{\mathbf{c}}_a = \arg\min \mathbf{c}_a^H\mathbf{Q}\mathbf{c}_a \quad \text{subject to } \mathbf{c}_a^H\mathbf{e} = 1 \tag{D.7}$$

where $\mathbf{Q} = \sum_{t=1}^{P}\{\mathbf{z}^H(t)\mathbf{z}(t)\mathbf{Y}^H(t)\mathbf{Y}(t) - \mathbf{Y}^H(t)\mathbf{z}(t)\mathbf{z}^H(t)\mathbf{Y}(t)\}$. This problem can be solved using the method of Lagrangian multipliers (Frost 1972).

$$\hat{\mathbf{c}}_a = \frac{\mathbf{Q}^{-1}\mathbf{e}}{\mathbf{e}^T\mathbf{Q}^{-1}\mathbf{e}} \tag{D.8}$$

Bibliography

Abramovich, Y., Anderson, S. and Spencer, N.: 2000, Stochastic-constraints method in nonstationary hot-clutter cancellation - part 2: Unsupervised training applications, *IEEE Trans. on Aerospace and Electronic Systems* **AES-36**(1), 132–150.

Abramovich, Y. I.: 1993, Experimental efficiency research of adaptive spatial unpremeditated noise compensation in HF radars for distance sea surface diagnostics, *Radioteknika i Electronika* **38 (4)**, 664–671. In Russian.

Abramovich, Y. I., Anderson, S. J., Frazer, G. J. and Solomon, I. S. D.: 1995, Measurement and interpretation of phase fluctuations in HF radar echoes propagated via sporadic E layers, *Proceedings of the IPS/DSTO Conference on Solar and Terrestial Physics*, Adelaide, Australia, pp. 152–155.

Abramovich, Y. I., Gorokhov, A. Y. and Demeure, C.: 1996, Experimental verification of a general multivariate propagation model for ionospheric HF signals, *Proc. EUSIPCO-96*, Trieste.

Abramovich, Y. I., Gorokhov, A. Y., Mikhaylyuvov, V. N. and Malyavin, I. P.: 1994, Exterior noise adaptive rejection for OTH radar implementations, *Proc. ICASSP 94*, Vol. 6, Adelaide, pp. 105–107.

Abramovich, Y. I. and Kachur, V. G.: 1987, Effectiveness of adaptive tuning of correcting filters for cyclic convolution, *Soviet Journal of Communication Technology and Electronics* **32**(4), 180–186.

Abramovich, Y. I., Kachur, V. G. and Struchev, V. F.: 1984, Methods of digital channel correction in multichannel radar receivers, *Radio Engineering and Electronic Physics* **29**(9), 62–68.

Abramovich, Y., Spencer, N. and Anderson, S.: 1998, Stochastic-constraints method in nonstationary hot-clutter cancellation - part 1: Fundamentals and supervised training applications, *IEEE Trans. on Aerospace and Electronic Systems* **AES-34**(4), 1271–1292.

Albert, A.: 1972, *Regression and the Moore-Penrose pseudoinverse*, Academic Press, New York and London.

Anderson, S. J. and Abramovich, Y. I.: 1998, A unified approach to detection, classification, and correction of ionospheric distortion in HF skywave radar systems, *Radio Science* **33**(4), 1055–1067.

Anderson, S. J., Abramovich, Y. I. and Fabrizio, G. A.: 1997, Stochastic constraints in nonstationary hot clutter cancellation, *IEEE International Conference on Acoustics, Speech and Signal Processing (ICASSP97)*, Munich, Germany, pp. 3753–3756.

Applebaum, S. P.: 1976, Adaptive arrays, *IEEE Trans. on Antennas and Propagation* **AP-24**(5), 585–598.

Arato, M.: 1961, On the sufficient statistics for stationary Gaussian random processes, *Theo. Prob. Appl.* **6**, 199–201.

Aurand, J. F.: 1987, An algorithm for computing the roots of a complex polynomial, *IEEE Trans.* **AC-32**, 164–166.

Balser, M. and Smith, W.: 1962, Some statistical properties of pulsed oblique HF ionospheric transmissions, *J. Res. Nat. Bur. Stand. Sect.D* **66-D**, 721–730.

Barnes, R. I.: 1990, Modelling the horizontal structure of mid-latitude Es from its refraction effects on F-region echoes, *Journal of Atmospheric and Terrestial Physics* **53**(1/2), 105–114.

Barnes, R. I.: 1992, Spread-Es structure producing apparent small scale structure in the F-region, *Journal of Atmospheric and Terrestial Physics* **54**(3/4), 373–389.

Bartlett, M. S.: 1946, On the theoretical specification of the sampling properties of autocorrelated time series, *J. Roy. Statist. Soc. Suppl.* **8**, 27–41.

Beex, A. A. and Scharf, L. L.: 1981, Covariance sequence approximation for parametric spectrum modelling, *IEEE Trans. on Acoustics, Speech and Signal Processing* **ASSP-29**(5), 1042–1052.

Besler, Y. and Macovski, A.: 1986, Exact maximum likelihood parameter estimation of superimposed exponential signals in noise, *IEEE Trans. on Acoustics, Speech and Signal Processing* **ASSP-34**(5), 1081–1089.

Booker, H., Ratcliffe, J. and Shinn, D.: 1950, Diffraction from an irregular screen with applications to ionospheric problems, *Philos. Trans.* **A242**, 579–609.

Bourdillon, A. and Delloue, J.: 1994, Phase correction of a HF multi-receiver antenna array using a radar transponder, *Proceedings of ICASSP-94*, Vol. 6, Adelaide, Australia, pp. 125–128.

Bowhill, S.: 1961, Statistics of a radio wave diffracted by a random ionosphere, *Journal of Research of the National Bureau of Standards-D. Radio Propagation* **65D**(3), 275–292.

Boys, J.: 1968, Statistical variations in the apparent specular component of ionospherically reflected radio waves, *Radio Science* **3**(10), 984–990.

Bramley, E. N.: 1951, Diversity effects in spaced-aerial reception of ionospheric waves, *Proc. IEE, Part III* **98**, 19–25.

Bramley, E. N.: 1955, Some aspects of the rapid directional fluctuations of short radio waves reflected at the ionosphere, *Proc. Inst. Elec. Engrs. (London)* **122b**(4), 533–540.

Briggs, B. H. and Phillips, G. J.: 1950, A study of the horizontal irregularities of the ionosphere, *Proc. Phys. Soc.* **B63**, 907–923.

Bruzzone, S. and Kaveh, M.: 1984, Information tradeoffs in using the sample autocorrelation function in ARMA parameter estimation, *IEEE Trans. ASSP* **ASSP-32**(4), 701–715.

Budden, K. G.: 1985, *The propagation of radio waves*, Cambridge University Press, U.K.

Cadzow, J.: 1982, Spectral estimation: An overdetermined rational model equation approach, *Proc. IEEE* **70**, 907–938.

Cadzow, J. A. e. a.: 1983, Singular-value decomposition approach to time series modelling, *IEE Procedings Pt.F* **130**(3), 332–340.

Capon, J.: 1969, High-resolution frequency-wavenumber spectrum analysis, *Proc IEEE* **57**(8), 2408–2418.

Carlson, B. D.: 1988, Covariance matrix estimation errors and diagonal loading in adaptive arrays, *IEEE Trans. on Aerospace and Electronic Systems* **AES-24**(4), 397–401.

Carter, G. C.: 1971, *Coherence Estimation*, Naval Underwater Systems Centre, Newport Laboratory, Rhode Island.

CCIR: 1970, 12th plenary assembly, New Delhi, *Volume II, part 2* pp. 197–213.

Cheremisin, O. P.: 1982, Efficiency of adaptive algorithms with regularised sample covariance matrix, *Radioteknika i Electronika* **27 (10)**, 1933–1941. In Russian.

Clark, M. and Scharf, L.: 1994, Two-dimensional modal analysis based on Maximum Likelihood, *IEEE Trans. Signal Processing* **SP-42**(6), 1443–1452.

Clark, R. H. and Tibble, D. V.: 1978, Measurement of the elevation angles of arrival of multi-component HF skywaves, *Proc. IEE* **125**, 17–24.

Compton, R. T.: 1982, The effect of random steering vector errors in the applebaum adaptive array, *IEEE Transactions on Aerospace and Electronic Systems* **18**(5), 392–400.

Compton, R. T.: 1988a, *Adaptive Antennas - concepts and performance*, Prentice Hall, Englewood Cliffs, NJ.

Compton, R. T.: 1988b, The relationship between tapped delay-line and FFT processing in adaptive arrays, *IEEE Trans. on Aerospace and Electronic Systems* **36**(1).

Creekmore, J., Bronez, T. and Keizer, R.: 1993, Experimental results on high frequency direction finding with modern methods, *MILCOM 93* **1**, 73–77.

Davies, K.: 1990, *Ionospheric Radio*, Peter Peringrinus, London, United Kingdom.

de Prony, B. G. R.: 1795, Essai experimental et anlaytique: sur les lois de la dilatabilite de fluides elastiques et sur celles de la force expansive de la vapour de l'eau et de la vapeur de l'alkool, a differentes temperatures, *J.E. Polytech* **1**(2), 24–76.

Earl, G. F. and Ward, B. D.: 1986, Frequency management support for remote sea-state sensing using the Jindalee sky-wave radar, *IEEE Journal of Ocean Eng.* **OE-11**, 164–172.

Fabrizio, G. A., Abramovich, Y. I., Gray, D. A., Anderson, S. J. and Turley, M. D.: 1998, Adaptive cancellation of nonstationary interference in HF antenna arrays, *IEE Proceedings Radar, Sonar and Navigation* **145**(1), 19–24.

Fabrizio, G. A., Gray, D. A., Turley, M. D. and Anderson, S. J.: 1998, Modelling the spatial characteristics of ionospherically propagated HF signals, *Proceedings of the International Radar Symposium*, Munich, Germany, pp. 1187–1197.

Fante, R. L. and Vacarro, J. J.: 1998, Cancellation of jammers and jammer multipath in a GPS receiver, *IEEE AES Systems Magazine*, pp. 25–28.

Farina, A.: 1992, *Antenna-based signal processing techniques for radar systems*, Artech House, Norwood, MA, USA.

Felgate, D. G. and Golley, M. G.: 1971, Ionospheric irregularities and movements observed with a large aerial array, *Journal of Atmospheric and Terrestial Physics* **33**, 1353–1369.

Frost, O. L.: 1972, An algorithm for linearly constrained adaptive array processing, *Proceedings of the IEEE* **60**, 926–935.

Games, R., Townes, S. and Williams, R.: 1991, Experimental results for adaptive sidelobe cancelellation techniques applied to a HF array, *Conference Record of the 25th Asilomar Conf. Sigs, Sys, Comp.*, Pacific Grove, CA, pp. 153–159.

Gersham, A., Mecklenbrauker, C. and Bohme, J.: 1997, Matrix fitting approach to direction-of-arrival estimation with imperfect spatial coherence of wavefronts, *IEEE Trans. on Signal Processing* **SP-45**(7), 1894–1899.

Gething, P. J. D.: 1991, *Radio Direction Finding and Superresolution*, Peter Peregrinus Ltd, 2nd Edition, London, U.K.

Goldberg, J. and Messer, H.: 1998, A polynomial rooting approach to the localisation of coherently scattered sources, *Proceedings of ICASSP98*, pp. 2057–2060.

Goodman, N. R.: 1963, Statistical analysis based on a certain multivariate complex gaussian distribution (An introduction), *Ann. Math. Statist.* **34**, 152–177.

Griffiths, L. J.: 1976, Time-domain adaptive beamforming of HF backscatter radar signals, *IEEE Trans. on Antennas and Propagation* **AP-24**(5), 707–720.

Griffiths, L. J.: 1996, Linear constraints in hot clutter cancellation, *Proc. ICASSP 96*, Atlanta.

Griffiths, L. J. and Buckley, K. M.: 1987, Quiescent pattern control in linearly constrained adaptive arrays, *IEEE Trans. on Acoustics, Speech and Signal Processing* **ASSP-35**(7), 917–926.

Hanuise, C., Villain, J., Gresillon, D., Cabrit, B., Greenwald, R. and Baker, K.: 1993, Interpretation of HF radar ionospheric doppler spectra by collective wave scattering theory, *Annales Geophysicae* **11**, 29–39.

Harris, F. J.: 1978, On the use of windows for harmonic analysis with the descrete Fourier transform, *Proc. IEEE* **66**(1).

Hayden, E. C.: 1961, Instrumentation for propagation and direction finding measurements, *J. Res. Natl Bur. Stand.* **65D**(3).

Hayward, S. D.: 1997, Effects of motion on adaptive arrays, *IEE Proceedings Radar, Sonar and Navigation* **144**(1), 15–20.

Hua, Y.: 1992, Estimating two-dimensional frequencies by matrix enhancement and matrix pencil, *IEEE Trans. Signal Processing* **SP-40**(9), 2267–2280.

Hudson, J. E.: 1981, *Adaptive array principles*, Perengrinus, Stevenage.

Hughes, C. J. and Morris, D. W.: 1963, Phase characteristics of HF radio waves received after propagation by the ionosphere, *Proc. IEE* **110**, 1720–1734.

Hughes, D. T. and McWhirter, J. G.: 1996, Sidelobe control in adaptive beamforming using a penalty function, *In Proc. ICASSP96*, pp. 200–203.

Johnson, J. R., Fenn, A. J., Aumann, H. M. and Willwerth, F. G.: 1991, An experimental adaptive nulling receiver utilising the sample matrix inversion algorithm with channel equlisation, *IEEE Transactions on Microwave Theory and Techniques* **39**(5), 798–808.

Kay, S. M.: 1987, *Modern Spectral Estimation*, Prentice-Hall, Inc., Englewood Cliffs, N. J.

Kay, S. M.: 1993, *Fundamentals of statistical signal processing: estimation theory*, Prentice-Hall, Inc., Englewood Cliffs, N. J.

Kelly, E. J.: 1989, Performance of an adaptive detection algorithm, *IEEE Transactions on Aerospace and Electronic Systems* **25**(2), 122–133.

Kreyszig, E.: 1988, *Advanced Engineering Mathematics, Sixth Edition*, John Wiley and Sons, New York, USA.

Krim, H. and Viberg, M.: 1996, Two decades of array signal processing research, *IEEE Signal Processing Magazine* pp. 67–94.

Kumaresan, R., Scharf, L. and Shaw, A.: 1986, An alogorithm for pole-zero modeling and spectral analysis, *IEEE Trans. ASSP* **ASSP-34**(3), 637–640.

Lees, M. L.: 1987, An overview of signal processing for over-the-horizon radar, *Proceedings of the international symposium on signal processing and applications*, Adelaide, Australia.

Lewis, B. L., Kretschmer, F. F. and Shelton, W. W.: 1986, *Aspects of radar signal processing*, Artech House, Norwood, MA, USA.

Li, J., Stoica, P. and Zheng, D.: 1997, One-dimensional MODE algorithm for two dimensional frequency estimation, *Multidimensional Systems and Signal Processing* **8**, 449–468.

Marple, S. L.: 1987, *Digital spectral analysis with applications*, Prentice Hall signal processing series.

McNamara, L. F.: 1991, *The ionosphere: communications, surveillance and direction finding*, Krieger Publishing Company, Malabar, Florida.

Meng, Y., Stoica, P. and Wong, K.: 1996, Estimation of the directions of arrival of spatially dispersed signals in array processing, *IEE Proceedings - Radar, Sonar and Navigation* **143**(1), 1–9.

Monzingo, R. and Miller, T.: 1980, *Introduction to adaptive arrays*, Wiley and Sons Publications, New York, USA.

Moyle, D. E. and Warrrington, E. M.: 1997, Some superresolution DF measurements within the HF band, *10th International Conference on Antennas and Propagation*, pp. 71–73.

Muirhead, R. J.: 1982, *Aspects of multivariate statistical theory*, John Wiley and Sons, Inc., New York, USA.

Ng, B. P., Er, M. H. and Kot, C.: 1994, Array gain/phase calibration techniques for adaptive beamforming and direction finding, *IEE Proceedings Radar, Sonar and Navigation* **141**(1), 25–29.

Ottersten, B., Viberg, M., Stoica, P. and Nehorai, A.: 1993, *Analysis of subspace fitting and ML techniques for parameter estimation from sensor array data*, Radar array processing, Springer-Verlag, pages 99-151, Berlin.

Papoulis, A.: 1984, *Probability, Random variables and stochastic processes*, McGraw-Hill, New York, USA.

Paulraj, A. and Kailath, T.: 1988, Direction of arrival estimation by eigenstructure methods with imperfect spatial coherence of wavefronts, *J. Acoust. Soc. Am.* **83**, 1034–1040.

Pillai, S. U.: 1989, *Array signal processing*, Springer-Verlag, New York, USA.

Porat, B. and Friedlander, B.: 1985, Aymptotic analysis of the bias of the modified Yule-Walker estimator, *IEEE Trans. Autom. Control.* **AC-30**, 765–767.

Priestly, M. B.: 1981, *Spectral Analysis and Time Series, Volume 1*, Academic Press, Harcourt Brace Publishers, San Diego, CA, USA.

Reed, I. S., Mallet, J. D. and Brennan, L. E.: 1974, Rapid convergence rate in adaptive arrays, *IEEE Transactions on Aerospace and Electronic Systems* **10**(6), 853–863.

Rice, D. W.: 1973, Phase characteristics of ionospherically-propagated radio waves, *Nature Physical Science* **244**, 86–88.

Rice, D. W.: 1976, High resolution measurement of time delay and angle of arrival over 911 km HF path, *in BLACKBAND, W.T. (Ed), 'Radio systems and the Ionosphere', AGARD conference Proc. No 173, Advisory group for aerospace research and development*, p. 33.

Rice, D. W.: 1982, HF direction finding by wave front testing in a fading signal environment, *Radio Science* **17**(4), 827–836.

Ringelstein, J., Gershman, A. and Bohme, J.: 1999, Sensor array processing for random inhomogeneous media, *SPIE'99, Advanced Signal Processing: Algorithms, Architectures and Implementations IX* **3807**, 267–276.

Sacchini, J., Steedly, W. and Moses, R.: 1993, Two-dimensional prony modelling and parameter estimation, *IEEE Trans. Signal Processing* **SP-41**(11), 3127–3137.

Scharf, L.: 1991, *Statistical signal processing, detection, estimation and time series analysis*, Addison-Wesley Publishing Company, USA.

Schmidt, R. O.: 1979, Multiple emitter location and signal parameter estimation, *Proceedings RADC Spectral Estimation Workshop, Rome, NY* pp. 243–258.

Schmidt, R. O.: 1981, *A signal subspace approach to multiple emitter location and spectral estimation*, Ph.D. thesis, Standford University, Standford, CA, USA.

Sennitt, A. G. and Kuperus, B.: 1997, *World radio TV handbook*, Glen Heffernan Billboard Books.

Shan, T. J., Wax, M. and Kailath, T.: 1985, On spatial smoothing for direction of arrival estimation of coherent signals, *IEEE Trans. on Acoustics Speech and Signal Processing* **ASSP-33**(4), 806–811.

Shepherd, A. and Lomax, J.: 1967, Frequency spread in ionospheric radio propagation, *IEEE Trans. on Communication Technology* **COM-15**(2), 268–275.

Sherill, W. and Smith, G.: 1977, Direcional dispersion od sporadic-E modes between 9 and 14 MHz, *Radio Science* **12**(5), 773–778.

Shunjun, W. and Yingjun, L.: 1995, Adaptive channel equalisation for space-time adaptive processing, *IEEE International Radar Conference*, pp. 624–628.

Sinnott, D. H.: 1987, Jindalee - DSTO's over-the-horizon radar project, *IREE, Digest of papers, 21st International Electronics Convention and Exhibition*, Sydney, Australia, pp. 661–664.

Solomon, I. S. D.: 1998, *Over-the-horizon radar array calibration*, Ph.D. thesis, The University of Adelaide, Adelaide, Australia.

Solomon, I. S. D., Gray, D. A., Abramovich, Y. I. and Anderson, S. J.: 1998, Over-the-horizon radar array calibration using echoes from ionised meteor trails, *IEE Proceedings Radar, Sonar and Navigation* **145**(3), 173–180.

Steinhardt, A. O. and Van Veen, B. D.: 1989, Adaptive beamforming, *International Journal of Adaptive Control and Signal Processing* **3**, 253–281.

Stoica, P. and Nehorai, A.: 1989, MUSIC, Maximum Likelihood and Cramer-Rao lower bound: further results and comparisons, *IEEE Trans. ASSP* **ASSP-37**, 720–741.

Stoica, P. and Sharman, K. C.: 1990, Novel eigenanalysis method for direction estimation, *IEE Proceedings, Pt. F* **137**(1), 19–26.

Sweeney, L. E.: 1970, *Spatial properties of ionospheric radio propagation as determined with half degree azimuthal resolution*, Ph.D. thesis, Stanford University, CA, USA.

Tarran, C. J.: 1997, Operational HF DF systems employing real-time super resolution processing, *HF Radio Systems and Techniques*, Nottingham UK, pp. 311–319.

Teitelbaum, R.: 1991, A flexible processor for a digital adaptive array radar, *Proceedings of the National Radar Conference*, Los Angeles, USA, pp. 103–107.

Thierren, C. W.: 1992, *Descrete random signals and statistical signal processing*, Prentice-Hall, Inc., Englewood Cliffs, New Jersey.

Treharne, R. F.: 1967, Vertical triangulation using skywaves, *Proc Int. Radio electron. Eng., Aust.* **28**, 419–423.

Trump, T. and Ottersten, B.: 1996, Estimation of nominal direction of arrival and angular spread using an array of sensors, *Signal Processing* **50**(9), 57–69.

Turley, M. D.: 1999, Skywave radar spatial adaptive processing with quiescent pattern control, *Fifth International Symposium on Signal Processing and its Applications, ISSPA99*, Brisbane, Australia, pp. 337–340.

Valaee, S., Champagne, B. and Kabal, P.: 1995, Parametric localisation of distributed sources, *IEEE Trans. Signal Processing* **SP-43**(9), 2144–2153.

Van Veen, B. D.: 1991, Minimum variance beamforming with soft response constraints, *IEEE Trans. on Signal Processing* **SP-39**(9).

Van Veen, B. D. and Buckley, K. M.: 1988, Beamforming: A versatile approach to spatial filtering, *IEEE ASSP Magazine* pp. 4–24.

Viberg, M. and Ottersten, B.: 1991, Sensor array processing based on subspace fitting, *IEEE Trans. Signal Processing* **SP-39**(5), 1110–1121.

Villain, J., Andre, R., Hanuise, C. and Gresillon, D.: 1996, Observation of high latitude ionosphere by HF radars: interpretation in terms of collective wave scattering and characterization of turbulence, *Journal of Atmospheric and Terrestial Physiscs* **58**(8), 943–958.

Warrington, E. M., Thomas, E. C. and Jones, T. B.: 1990, Measurements on the wavefronts of ionospherically-propagated HF radio waves made with a large aperture antenna array, *Proc. IEE* **137H**(1), 25–30.

Washburn, T. W. and Sweeney, L. E.: 1976, An on-line adaptive beamforming capability for HF backscatter radar, *IEEE Trans. on Antennas and Propagation* **AP-24**(5), 721–732.

Watterson, C. C., Juroshek, J. R. and Bensema, W. D.: 1970, Experimental confirmation of an HF channel model, *IEEE Trans on Communication* **18**(6), 792–803.

Wax, M. and Kailath, T.: 1985, Detection of signals by information theoretic criteria, *IEEE Trans. on Acoustics Speech and Signal Processing* **ASSP-33**, 387–392.

Whale, H. and Gardiner, C.: 1966, The effect of a specular component on the correlation between the signals received on spaced antennas, *Radio Science* **1**(5), 557–570.

Widrow, B., Mantey, P., Griffiths, L. and Goode, B.: 1967, Adaptive antenna systems, *Proc. IEEE* **55**(12), 2143–2159.

Zatman, M. A. and Strangeways, H. J.: 1994, Measurements on multi-moded signals using single snapshot data, *Proc. IEEE Antennas and Propagation, (4)*, pp. 1934–1937.